TECHNISCHE UNIVERSITÄT DRESDEN

Leibniz-Institut für Festkörper- und Werkstoffforschung Dresden

Magnetic studies on lanthanide-based endohedral metallofullerenes

DISSERTATION
for obtaining the academic degree
Doctor of Philosophy
(Ph. D.)

submitted to the
Faculty of Physics
Technical University Dresden

by
M. Sc. Georgios Velkos
born on June 13, 1990 in Thessaloniki, Greece

Defence date: 11.10.2021

Academic advisors:

1. Prof. Dr. Bernd Büchner, Technical University of Dresden
2. Dr. Alexey Popov, Leibniz Institute for Solid State and Materials Research (IFW Dresden)

Reviewers:

1. Prof. Dr. Bernd Büchner, Technical University of Dresden
2. Prof. Dr. Thomas Greber, University of Zurich

Contents

Chapter 3. Single-molecule magnets (SMMs)

Chapter 4. Magnetic studies on lanthanide dimetallofullerenes

Chapter 5. Magnetic studies on Dy-oxide clusterfullerenes

Outlook

Bibliography

Statement of originality

Acknowledgements

The opportunity to conduct scientific research in the framework of my PhD thesis at the Leibniz Institute for Solid State and Material Research (IFW Dresden), was a complete privilege for me. I am deeply grateful to Prof. Dr. Bernd Büchner who trusted me to become a member of a large professional community and collaborate with warm and friendly people.

I consider myself extremely fortunate to work and learn next to my scientific advisor, Dr. Alexey Popov. Without his guidance, support and advice, nothing would be possible. I am also thankful to him for giving me the chance to present our scientific work at the biggest conferences, attend seminars, and participate in synchrotron visits for experiments, gaining valuable experience and skills. In personal level, I felt that I could rely on him and ask for help in any issue that could arise.

Moreover, I would like to thank all the nice people that I collaborated with. First of all, Dr. Anja-Wolter-Giraud who allowed me to perform the magnetic measurements in the lab and Sebastian Gaß for his constant technical support. My warm acknowledgements go to all present and former colleagues, with special reference to my tutor on the SQUID magnetic measurements, Dr. Denis Krylov. Also, I appreciate the great collaboration with my chemist colleagues: Dr. Fupin Liu, Dr. Lukas Spree, Dr. Chia-Hsiang Chen, Dr. Ariane Brandenburg, Yaofeng Wang and Wei Yang, who were always providing me with plenty of samples to study. Furthermore, I would like to thank Dr. Stanislav Avdoshenko, Vasilii Dubrovin and Svetlana Sudarkova, for their theoretical work input and many fruitful discussions. Also, my acknowledgements go to Dr. Evgenia Dmitrieva, Marko Rosenkranz, Sandra Schiemenz, Alexander Beger, Frank Ziegs and Emmanouil Koutsouflakis for their valuable contribution in our studies. In addition, my special thanks are given to our external collaborators, Prof. Dr. Thomas Greber and Aram Kostanyan, from the University of Zurich. Apart from strictly PhD-related topics, I have to mention the sport activities with my colleague Vasilii (IFW ping pong table), accompanied with interesting discussions on science in general.

Last but not least, I would like to express my gratitude to my family and friends for their constant ethical and emotional support, despite the long distance between us. Especially I thank from the bottom of my heart my parents for our deep discussions and their great help to all my problems. This work is dedicated to my beloved grandmother.

Publication list

1. **Magnetic Hysteresis at 10 K in Single Molecule Magnet Self-Assembled on Gold**
   Chen, Chia-Hsiang; Spree, Lukas; Koutsouflakis, Emmanouil; Krylov, Denis S.; Liu, Fupin; Brandenburg, Ariane; Velkos, Georgios; Schimmel, Sebastian; Avdoshenko, Stanislav M.; Fedorov, Alexander; Weschke, Eugen; Choueikani, Fadi; Ohresser, Philippe; Dreiser, Jan; Buchner, Bernd; Popov, Alexey A.
   Published: Mar 2021 in Advanced Science
   DOI: 10.1002/ADVS.202000777

2. **Magnetic hysteresis and strong ferromagnetic coupling of sulfur-bridged Dy ions in clusterfullerene $Dy_2S@C_{82}$**
   Krylov, Denis; Velkos, Georgios; Chen, Chia-Hsiang; Buechner, Bernd; Kostanyan, Aram; Greber, Thomas; Avdoshenko, Stanislav M.; Popov, Alexey A.
   Published: Oct 2020 in Inorganic Chemistry Frontiers
   DOI: 10.1039/D0QI00771D

3. **Shape-adaptive single-molecule magnetism and hysteresis up to 14 K in oxide clusterfullerenes $Dy_2O@C_{72}$ and $Dy_2O@C_{74}$ with fused pentagon pairs and flexible Dy-(μ_2-O)-Dy angle**
   Velkos, Georgios; Yang, Wei; Yao, Yang-Rong; Sudarkova, Svetlana M.; Liu, XinYe; Buechner, Bernd; Avdoshenko, Stanislav M.; Chen, Ning; Popov, Alexey A.
   Published: May 2020 in Chemical Science
   DOI: 10.1039/D0SC00624F

4. **Substrate-Independent Magnetic Bistability in Monolayers of the Single-Molecule Magnet $Dy_2ScN@C_{80}$ on Metals and Insulators**
   Krylov, Denis S.; Schimmel, Sebastian; Dubrovin, Vasilii; Liu, Fupin; Nhung Nguyen, T. T.; Spree, Lukas; Chen, Chia-Hsiang; Velkos, Georgios; Bulbucan, Claudiu; Westerstrom, Rasmus; Studniarek, Michal; Dreiser, Jan; Hess, Christian; Buechner, Bernd; Avdoshenko, Stanislav M.; Popov, Alexey A.
   Published: Mar 2020 in Angewandte Chemie International Edition
   DOI: 10.1002/ANIE.201913955

5. **Single Molecule Magnetism with Strong Magnetic Anisotropy and Enhanced Dy…Dy Coupling in Three Isomers of Dy-Oxide Clusterfullerene $Dy_2O@C_{82}$**
   Yang, Wei; Velkos, Georgios; Liu, Fupin; Sudarkova, Svetlana M.; Wang, Yaofeng; Zhuang, Jiaxin; Zhang, Hanning; Li, Xiang; Zhang, Xingxing; Buechner, Bernd; Avdoshenko, Stanislav M.; Popov, Alexey A.; Chen, Ning
   Published: Oct 2019 in Advanced Science
   DOI: 10.1002/ADVS.201901352

6. **High Blocking Temperature of Magnetization and Giant Coercivity in the Azafullerene $Tb_2@C_{79}N$ with a Single-Electron Terbium-Terbium Bond**

   Velkos, Georgios; Krylov, Denis S.; Kirkpatrick, Kyle; Spree, Lukas; Dubrovin, Vasilii; Buechner, Bernd; Avdoshenko, Stanislav M.; Bezmelnitsyn, Valeriy; Davis, Sean; Faust, Paul; Duchamp, James; Dorn, Harry C.; Popov, Alexey A.

   Published: Apr 2019 in Angewandte Chemie International Edition

   DOI: 10.1002/ANIE.201900943

7. **Air-stable redox-active nanomagnets with lanthanide spins radical-bridged by a metal-metal bond**

   Liu, Fupin; Velkos, Georgios; Krylov, Denis S.; Spree, Lukas; Zalibera, Michal; Ray, Rajyavardhan; Samoylova, Nataliya A.; Chen, Chia-Hsiang; Rosenkranz, Marco; Schiemenz, Sandra; Ziegs, Frank; Nenkov, Konstantin; Kostanyan, Aram; Greber, Thomas; Wolter, Anja U. B.; Richter, Manuel; Buechner, Bernd; Avdoshenko, Stanislav M.; Popov, Alexey A.

   Published: 2019 in Nature Communications

   DOI: 10.1038/S41467-019-08513-6

8. **Single-Electron Lanthanide-Lanthanide Bonds Inside Fullerenes toward Robust Redox-Active Molecular Magnets**

   Liu, Fupin; Spree, Lukas; Krylov, Denis S.; Velkos, Georgios; Avdoshenko, Stanislav M.; Popov, Alexey A.

   Published: 2019 in Accounts of Chemical Research

   DOI: 10.1021/ACS.ACCOUNTS.9B00373

9. **Giant exchange coupling and field-induced slow relaxation of magnetization in $Gd_2@C_{79}N$ with a single-electron Gd-Gd bond**

   Velkos, G.; Krylov, D. S.; Kirkpatrick, K.; Liu, X.; Spree, L.; Wolter, A. U. B.; Buechner, B.; Dorn, H. C.; Popov, A. A.

   Published: Mar 2018 in Chemical Communications

   DOI: 10.1039/C8CC00112J

10. **A diuranium carbide cluster stabilized inside a C_{80} fullerene cage**

    Zhang, Xingxing; Li, Wanlu; Feng, Lai; Chen, Xin; Hansen, Andreas; Grimme, Stefan; Fortier, Skye; Sergentu, Dumitru-Claudiu; Duignan, Thomas J.; Autschbach, Jochen; Wang, Shuao; Wang, Yaofeng; Velkos, Giorgios; Popov, Alexey A.; Aghdassi, Nabi; Duhm, Steffen; Li, Xiaohong; Li, Jun; Echegoyen, Luis; Schwarz, W. H. Eeugen; Chen, Ning

    Published: 2018 in Nature Communications

    DOI: 10.1038/S41467-018-05210-8

Introduction

The progress in the field of single-molecule magnetism has experienced unparalleled evolution over the last 30 years. It is by definition an interdisciplinary field of science, which requires the collaboration between chemists, physicists, material scientists and engineers. The ultimate goal is the synthesis of molecules with suitable magnetic properties for incorporation in applications like high-data storage and spintronic devices. In parallel, understanding of the physical principles governing the magnetism in molecular level constitutes a great challenge.

Among the myriads of single-molecule magnets existing in the literature, endohedral fullerenes with embedded magnetic ions have great perspective, and there are many reasons behind. The robust carbon cage can accommodate different magnetic ions in very close distance to each other that gives rise to unprecedented interactions. Repulsive ions reside in limited space, despite their natural tendency to break apart, and obtain unconventional charge states. As we have witnessed from recent studies, endohedral fullerenes exhibit superior magnetic properties. In combination with the high chemical stability of the carbon cage, these molecules become excellent candidates for application in devices. Therefore, magnetic endohedral fullerenes deserve our attention.

In this work, we report the advance of our understanding on the magnetic behavior of various endohedral species. First chapter is a basic introduction to the physical principles governing the *4f*-magnetism and single-molecule magnets. In the second chapter, the synthesis of endohedral fullerenes and a selection of characterization techniques are described, with focus on the specific magnetic methods we use in our experimental studies. Third chapter contains a retrospective of single-molecule magnetism history, and special reference to two molecules studied recently in our group. Chapters four and five describe the magnetic studies completed in the framework of my PhD thesis. Chapter four refers to the big family of the air-stable $Ln_2@C_{80}(CH_2Ph)$ (Ln_2: Gd_2, Tb_2, Ho_2, Er_2 and TbY) lanthanide dimetallofullerenes, featuring a single-electron Ln-Ln bond. The lanthanide moments are glued together by very strong exchange interactions mediated through the single electron residing on the Ln-Ln bonding orbital. Chapter five describes a different story, where we explore the magnetic properties of five Dy_2O-clusterfullerenes ($Dy_2O@C_{2n}$: C_{72}, C_{74}, C_{82}-three isomers). In this study, we explore the effect of the carbon cage size and shape on the magnetic properties of the Dy_2O cluster (two magnetically coupled Dy^{3+} ions via the O^{-2} ion).

To summarize, in this work we discuss the first in-depth magnetic study on two different families of endohedral metallofullerenes, the lanthanide-dimetallofullerenes $Ln_2@C_{80}(CH_2Ph)$ and the Dy-oxides $Dy_2O@C_{2n}$. With the very interesting results acquired in this work, we were able to extend the knowledge in the field of molecular magnetism, which could help in understanding better the physical phenomena behind and open new possibilities for magnetic device applications.

Chapter 1

Magnetism of lanthanides

Lanthanides, named after the ancient Greek -*λανθάνειν*- ("lanthanein"- to be hidden), include 15 elements, with atomic numbers ranging from 57 (Lanthanum) to 71 (Lutetium). Together with Scandium (21) and Yttrium (39), they comprise the rare-earth metal group with similar chemical behavior. The electronic configuration of lanthanide atoms in the ground state is $[\mathrm{Xe}]6s^2 4f^n 5d^0$, except from (La, Ce, Gd and Lu) with $[\mathrm{Xe}]6s^2 4f^{n-1} 5d^1$ ground configuration [1]. For that reason, the most stable lanthanide ions appear with 2+/3+ oxidation states.

1.1 Nature of *4f*-orbitals

The paramagnetic properties of lanthanide compounds derive from their unpaired *4f*-electrons. There are seven *4f*-orbitals in total, which barely participate in chemical bonding because they are well buried within the *5s* and *5p* orbitals. In first approximation, *4f*-orbitals of a lanthanide ion resemble those of a free ion.

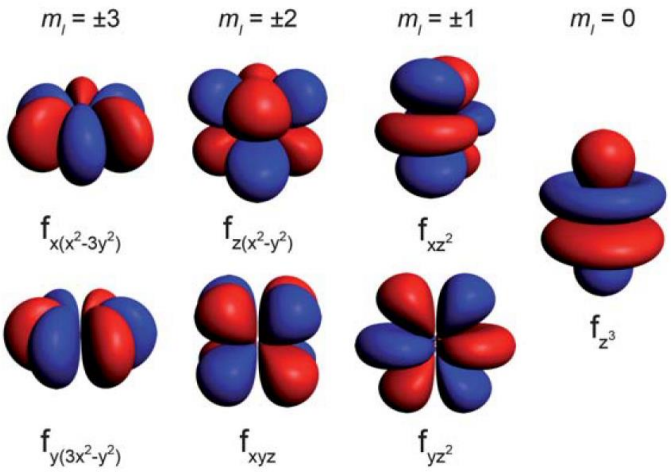

Figure 1.1.1 Representation of a free ion *4f*-shells from the highest magnitude m_l (most oblate shape) to the lowest magnitude m_l (most prolate shape). Reproduced from ref. [2] with permission from The Royal Society of Chemistry.

Interaction between spin and orbital momentum (spin-orbit coupling), in combination with the core-like character of the *4f*-shells, leave the orbital momentum largely unquenched, leading to strong single-ion magnetic anisotropies. As a result, lanthanide compounds are considered today as excellent candidates for the realization of the concept of single-molecule magnet (SMM).

1.2 Spin-orbit coupling

There are two sources of atomic electron magnetism: the orbital motion of electrons around the nucleus giving rise to the orbital momentum ***l***, and the intrinsic property of spin, resulting to spin momentum ***s***. According to quantum theory, confinement of electrons in atomic orbitals leads to quantization of their energies [3]. Coulomb repulsions between them induce secondary splitting on their energy levels, in the order of ≈10^4 K ($\Delta E_{ee}/k_B$) [4]. Coupling between spin and orbital momentum, derived from the relativistic nature of moving electrons [5], separates further their energy levels. According to *L-S* coupling scheme [6], orbital and spin momenta of the electrons are coupled into total orbital $L = \sum l_i$ and spin $S = \sum s_i$ momenta, giving a set of energy states called 'term' ${}^{2S+1}X$, where X is a capital letter denoting the *L* quantum number (*X: S, P, D, F, G, H* for *L*= 0, 1, 2, 3, 4, 5). Taking into account the spin-orbit coupling, the 'sum' of the orbital and spin momentum (***L*** and ***S***) gives rise to the total momentum ***J*** and each term is split into *J* states, also known as 'multiplets' ${}^{2S+1}X_J$. Every multiplet contains (2*J*+1) degenerated m_J states with energy:

$$E\left({}^{2S+1}X_J\right) = \lambda/2[J(J+1) - L(L+1) - S(S+1)] \qquad (1.2.1)$$

where λ is the spin-orbit coupling constant [7], proportional to the effective nuclear charge Z^4, meaning that the heavier is the element and the closer are the electrons to the nucleus, spin-orbit coupling becomes stronger. Every multiplet is characterized by a unique triad of *L, S* and *J* numbers and their values can be predicted for the energetically lowest multiplet (called ground state) following the Hund's rules and Pauli's exclusion principle [7]. The value of *J* can vary from I*L-S*I to *L+S* and for the ground multiplet is equal to I*L-S*I for lanthanides before Gd (less than half-filled *4f*-shells, *n<7*) and equal to *L+S* for lanthanides after Gd (more than half-filled *4f*-shells, *n>7*). For Gd, *4f*-shells are exactly half-filled (*L*=0 and *J*=*S*). The physical meaning of that difference is that I*L-S*I refers to antiparallel ***L*** *and* ***S*** vectors while *L+S* to parallel.

Generally for the *4f*-elements except Eu^{3+} and Sm^{3+}, the ground multiplet is well separated from the first excited one, in the order of at least ≈10^3 K ($\Delta E_{SO}/k_B$) [4]. As a result, magnetic behavior of some lanthanides can be explained by considering only the ground multiplet. Light lanthanides (*n<7*) show small values of ground state total momentum *(J=IL-SI)* and consequently smaller energy splitting (eq. 1.2.1), in contrast to heavier lanthanides (*n>7*, *J=L+S)*. Special cases are the isotropic Gd^{3+}/Eu^{2+} ($4f^7$, *L*=0, *S*=*J*=7/2) and the Eu^{3+}/Sm^{2+} ($4f^6$, *L*=*S*=3, *J*=0) with diamagnetic ground state.

1.3 Ligand-field

For atoms not isolated from their surrounding environment, Coulomb interactions with the neighboring charges, better known as crystal/ligand field (CF/LF) interactions, are always present. In a given ligand field, the electronic charge cloud reorients to obtain an energetically favorable direction and a magnetic anisotropy type. In case of lanthanide elements, ligand field compared to the spin-orbit coupling is a small perturbation on the electronic energy levels which lifts the (2*J*+1)-fold degeneracy of every multiplet. The energetically lowest energy level becomes the new ground state of the system. The energy gap with the first excited state is usually in the order of ~10^2 K for lanthanides, so often it can be considered as the only occupied state at relatively low temperatures [4].

Crystal-field theory was originally developed for the magnetic ions embedded into crystalline environments [8], and decades later was expanded to ligand molecules [9]. The easiest approach to describe a crystal field environment is the point-charge electrostatic model (PCEM) [10], where the surrounding electronic cloud is represented by single point charges, located at the atomic positions of ligand molecules. Stevens formalism simplifies the problem with the calculation of the operator equivalents for the CF potential $\hat{O}_k^q$ (Stevens operators) [6] leading to the simplified Hamiltonian:

$$\widehat{H}_{CF}^{St} = \sum_{k=2,4,6} \beta^k \sum_{q=-k}^{k} A_k^q \langle r^k \rangle_{4f} \hat{O}_k^q \tag{1.3.1}$$

where *k* is the operator rank (must be even due to the CF potential inversion symmetry), *q* is the operator range between (*k, –k)*, β^k is the Stevens equivalent coefficient, A_k^q an adjustable parameter and *r* the *4f*-cloud radius. The number of the non-zero CF parameters estimated in this model is quite high (27), so it is very helpful to recognize the symmetry operations under which the CF Hamiltonian remains invariant. In case of symmetric environments around the lanthanide ion, some independent parameters can become zero (i.e. for tetragonal symmetry only the q = 0, ± 4 terms are non-zero). Moreover, Stevens approach allows to identify the shape of the *4f*-cloud as prolate, oblate, or spherical, based on the sign of the quadrupole moment Q_2 [6]:

$$Q_2 = a_J \langle r^2 \rangle_{4f} (2J^2 - J) \tag{1.3.2}$$

where α_J is the second-order Stevens coefficient and r^2 the squared *4f*-shell radius. Stevens' method estimates with great success the energy splitting in systems with well-separated ground multiplets, but fails to predict the optical transitions between excited states. A more complete description of lanthanides spectroscopy is Wyborne notation [11], including electron correlation, spin-orbit coupling and CF splitting.

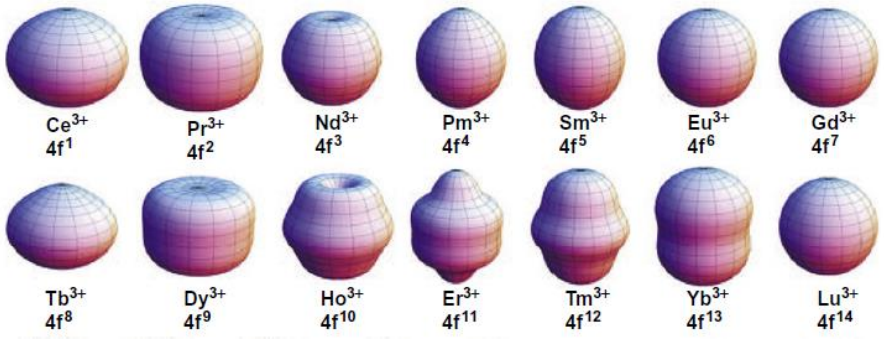

Figure 1.3.1 Representation of the *4f*-charge density of the Ising states (m_J=± J) for all the lanthanide ions. Those with negative Q_2 (Ce^{3+}, Pr^{3+}, Nd^{3+}, Tb^3, Dy^{3+} and Ho^{3+}) exhibit more oblate shape, whereas those with negative Q_2 (Pm^{3+},Sm^{3+}, Er^{3+}, Tm^{3+}, Yb^{3+}) more prolate. The spherical isotropic shape for Eu^{+3}, Gd^{+3} and Lu^{+3}, corresponds to Q_2=0. Reproduced from ref. [12] with permission from The Royal Society of Chemistry.

Simple electrostatic models like those of Long et al. [2] and Chilton et al. [13] predict with great success for many single lanthanide ions the ligand architectures that lead to strong magnetic anisotropies. For example, an elongated crystal-field induces easy-plane anisotropy to lanthanide ions with prolate electron distribution like Tm^{3+} and Yb^{3+}, and easy-axis anisotropy for ions with oblate shape such as Dy^{3+} and Tb^{3+}. However, it is not always possible to predict precisely the ligand-field effect on molecular complexes, relating the geometry and electronic structure, based on a simple electrostatic model. Different approaches have been developed, including high level ab initio calculations [14], which are more precise but on the other hand are computationally expensive and by no means trivial. One important parameter regarding the energy splitting between the electron states is the time reversal symmetry. According to Kramers theorem [15], in a system with odd number of fermions the energy levels are degenerated. Consequently, for lanthanides with odd number of *4f*-electrons (Kramers ions), acted by a crystal field (electrostatic fields are symmetric under time reversal), each energy level must be two-fold degenerate, at least. For non-Kramers ions (even number of *4f*-electrons), the (2*J*+1)-fold degeneracy can be lifted completely by the crystal field.

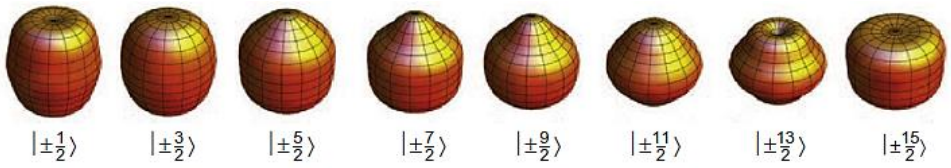

Figure 1.3.2 Representations of the *4f*-electron densities of the eight Kramers doublets of Dy^{3+} ground multiplet, going from prolate shape (m_J = ± 1/2) to a more oblate one (m_J = ± 15/2). Reproduced from ref. [12] with permission from The Royal Society of Chemistry.

1.4 Lanthanide ion in a magnetic field

An external stimuli (i.e. application of a magnetic field) breaks the time-reversal symmetry and lifts the degeneracy of the Kramers doublets. The atomic orbital and spin magnetic moments are given by the equations:

$$\boldsymbol{\mu_L} = -\mu_B g_L \boldsymbol{L} \qquad \text{and} \qquad \boldsymbol{\mu_S} = -\mu_B g_S \boldsymbol{S} \tag{1.4.1}$$

where μ_B is the magneton Bohr constant and g_L/g_S are the g-factors which relate the quantum numbers *L* and *S* to the corresponding values of magnetic moments μ_L/μ_S. The total magnetic moment $\boldsymbol{\mu}_{tot}$ is the sum:

$$\boldsymbol{\mu}_{tot} = \boldsymbol{\mu}_L + \boldsymbol{\mu_S} = -\mu_B g_L \boldsymbol{L} - \mu_B g_S \boldsymbol{S} = -\mu_B (g_L \boldsymbol{L} + g_S \boldsymbol{S}) \tag{1.4.2}$$

For an atom, $g_L = 1$ and $g_S = 2$ so

$$\boldsymbol{\mu}_{tot} = -\mu_B (\boldsymbol{L} + 2\boldsymbol{S}) \tag{1.4.3}$$

Therefore, the $\boldsymbol{\mu}_{\text{tot}}$ vector is not collinear with the total momentum $\boldsymbol{J} = \boldsymbol{L} + \boldsymbol{S}$, but tilted towards the spin momentum $\boldsymbol{S}$. Projection of $\boldsymbol{\mu}_{\text{tot}}$ onto $\boldsymbol{J}$ is given by the equation:

$$\boldsymbol{\mu}_J = -\mu_B g_J \boldsymbol{J} \tag{1.4.4}$$

where g_J is the *Lande*-factor: $$g_J = \frac{3}{2} + \frac{S(S+1) - L(L+1)}{2J(J+1)} \tag{1.4.5}$$

For an induced axial magnetic field (i.e along the z-axis), the Zeeman energy E_H is:

$$E_H = \boldsymbol{\mu_{tot}} \cdot \boldsymbol{H} = -\mu_B (\boldsymbol{L} + 2\boldsymbol{S}) \cdot \boldsymbol{H} \tag{1.4.6}$$

Supposing that the *L+2S* multiplet is a pure *J* state, the previous Zeeman term, using the Wigner-Eckart theorem, can be expressed as:

$$E_H = -\mu_B g_J \boldsymbol{J} \cdot \boldsymbol{H} \tag{1.4.7}$$

In general, the response of a lanthanide ion under an external magnetic field is anisotropic and *Lande*-factor is not a number but a tensor (known as g-tensor), a symmetric 3x3 matrix. Upon the application of an electrostatic (i.e. crystal field), the total momentum $\boldsymbol{J}$ is split into doublets, with different projections $\boldsymbol{J}_z$ along the z-axis. An applied magnetic field along the z-axis (*H//z)* splits further each doublet with energy difference equal to $-\mu_B g_J J_z H$.

1.5 Magnetic interactions

A magnetic ion, besides the interaction with an external magnetic field (Zeeman effect), can also interact with other magnetic ions through exchange and dipolar interactions [15-17]. There are also the hyperfine interactions between electron and nuclear spins.

Exchange interactions

The total wavefunction of two identical particles must be symmetric or antisymmetric under the exchange of the particles with respect to their spatial and spin coordinates. This property can be described by the introduction of the exchange interactions, which have no classic analogue, and are responsible for coupling between particle spins. The degree of overlap of the wavefunctions determines their effectiveness. Only in a short distance, for example between electrons of the same atom (intra-atomic) or neighbor atoms (inter-atomic), exchange interactions are effective. Interestingly, exchange interactions can be mediated in longer range via orbitals of neighboring atoms (super-exchange interactions) [18]. In lanthanides, *4f*-shells are so localized that exchange interactions are usually only intra-atomic. However, in molecular complexes with two or more lanthanide ions, it is important to understand the extent of the exchange coupling between them. The exchange Hamiltonian for two interacting spins (Heisenberg model) is:

$$\widehat{H}_{ex} = -2j_{12} \cdot \boldsymbol{S}_1 \cdot \boldsymbol{S}_2 \tag{1.5.1}$$

The sign of the exchange coupling constant j_{12} shows if the coupling is ferromagnetic (j_{12}>0) or antiferromagnetic (j_{12}<0), while its magnitude describes the strength of interaction between the spins. For more than two interacting spins and anisotropic exchange interactions characterized by the tensor j_{12}, eq. 1.5.1 becomes:

$$\widehat{H}_{ex} = -2\sum_{i>j}(j_{x,ij}\boldsymbol{S}_x^i \cdot \boldsymbol{S}_x^j + j_{y,ij}\boldsymbol{S}_y^i \cdot \boldsymbol{S}_y^j + j_{z,ij}\boldsymbol{S}_z^i \cdot \boldsymbol{S}_z^j) \tag{1.5.2}$$

In studies on lanthanides magnetism, where the orbital momentum $\boldsymbol{L}$ is not quenched, the above equations can be generalized by replacing the spin momentum $\boldsymbol{S}$ with the total momentum $\boldsymbol{J}$, where j_{12} is a tensor. If single-ion magnetic anisotropy is of Ising-type (along one direction, i.e. z-axis), then $j_x = j_y = 0$. This condition can apply in cases of coupled lanthanide ions too, when magnetic anisotropy tends to be axial along the direction of the bond.

Dipolar interactions

Unlike exchange interactions, dipolar are purely magnetic with long-range action. The energy of the dipole-dipole interaction is described by the equation:

$$\widehat{H}_{dip} = \frac{\mu_0}{4\pi}\sum_{i\neq j}\left(\frac{\vec{\mu}_i\vec{\mu}_j}{r_{ij}^3} - 3\frac{(\vec{\mu}_i\vec{n}_r)(\vec{\mu}_j\vec{n}_r)}{r_{ij}^3}\right) \quad (1.5.3)$$

where $\vec{n}_r$ is the normal of the radius vector connecting two magnetic moments $\vec{\mu}_i$ and $\vec{\mu}_j$, and r_{ij} the distance between them. In lanthanide-SMMs, dipolar interactions cannot be ignored because they can be equal or larger than the exchange. Their contribution can be computed precisely using experimental or DFT-calculated atomic coordinates and ab initio derived orientations of the magnetization axes and g-tensors of individual Ln-centres.

Hyperfine interactions

The atomic nucleus can have magnetic moment derived from the intrinsic angular momentum of its components coupled to a non-zero spin. Hyperfine interactions describe the coupling between the nucleus and electron magnetic moments. However, nuclear moments are much smaller than electronic ones, as proton and neutrons are much heavier than electrons. In our magnetic studies their role is less crucial comparing to the rest of the magnetic interactions.

1.6 Spin Hamiltonian for lanthanides

The Hamiltonian operator which produces the energy levels of the *4f*-electrons in a lanthanide ion can be written as the sum of the Hamiltonian operators of all the possible interactions:

$$\hat{H} = \hat{H}_{p-e} + \hat{H}_{e-e} + \hat{H}_{SO} + \hat{H}_{CF} + \hat{H}_{B} + \hat{H}_{N} \qquad (1.6.1)$$

Each term can be considered as a perturbation to the previous one (fig. 1.6.1).The terms from left to right describe proton-electron attractive forces, electron-electron repulsions, spin-orbit coupling, crystal-field effect, magnetic interactions (Zeeman, exchange and dipolar) and last the hyperfine interactions.

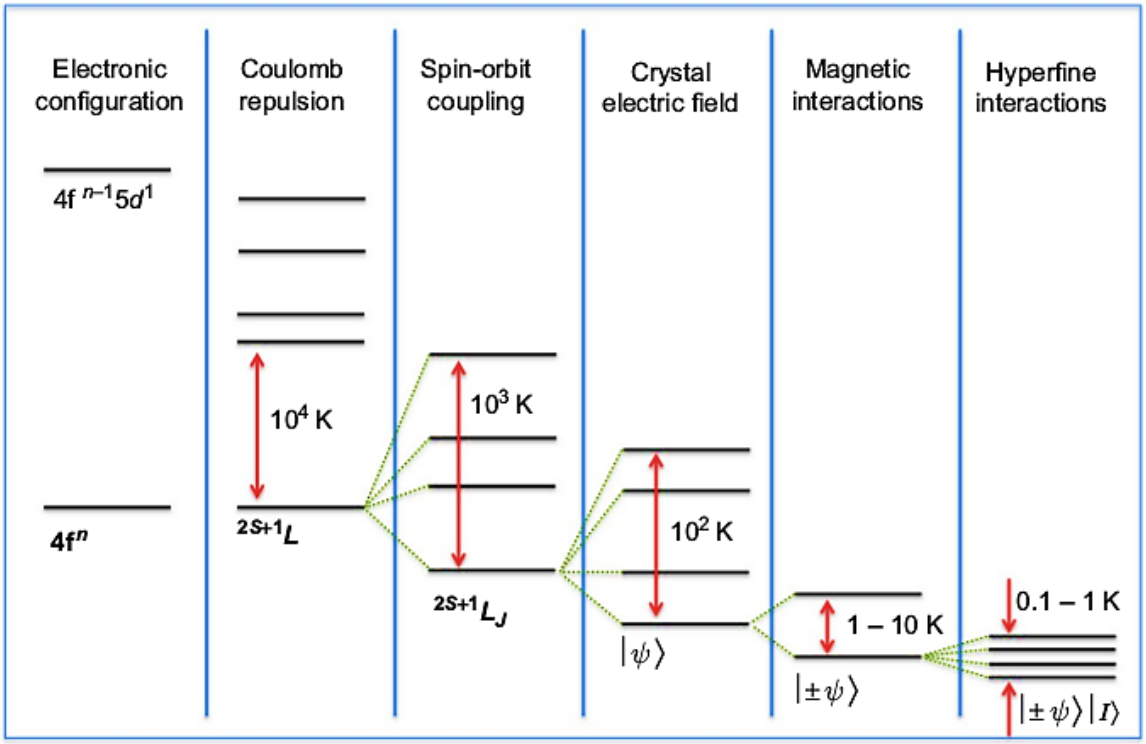

Figure 1.6.1 Typical energy level structure of a lanthanide ion, evidencing the effect of the progressively weaker interactions presented in eq.1.6.1. Reproduced from ref. [19]

To describe the magnetic properties of two or more coupled lanthanide ions in a molecule, it is usually sufficient to consider only the crystal field and magnetic interactions Hamiltonian terms because the large crystal-field splitting (≈10^2 K) allows the occupancy of the lowest states only in temperatures up to 300 K. Hyperfine interactions can be neglected at temperatures over 1 K.

1.7 Single-molecule magnetism (SMM)

Macroscopic magnetic particles exhibit multi-domain structure in which every domain contains magnetic moments that are parallel to one direction (Weiss theory 1907) [20]. In the absence of an external magnetic field, domains are oriented randomly so the macroscopic magnetization of the particle is zero. Under reduction of the particle size, when the radius becomes smaller than the Bloch wall depth (Bloch walls separate the domains), the particle turns into single-domain to minimize its magnetic energy [21]. With further decrease of the size, there is a critical value of radius (between ≈2-30 nm, depending on the nature of the material) below which the particle turns into a superparamagnet, which means that magnetization can randomly flip direction under the influence of temperature [15].

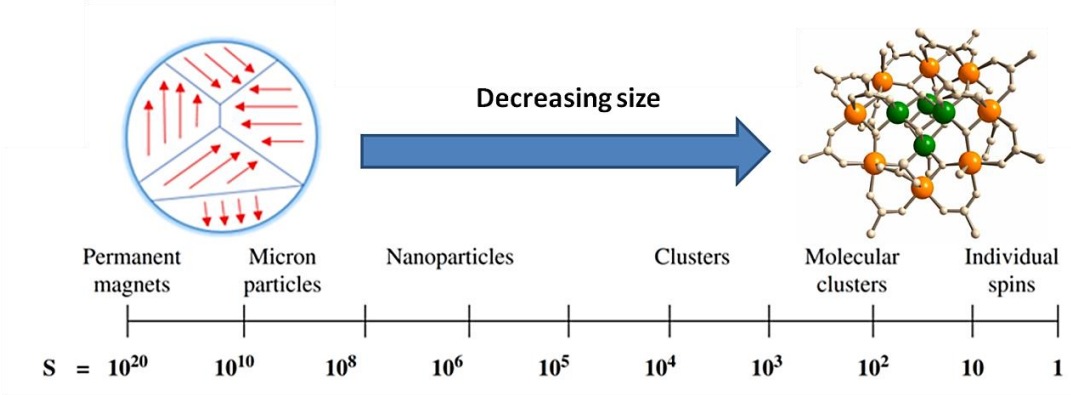

Figure 1.7.1 Miniaturization of bulk magnets (ca 10^{20} spins) to multi and single-domain nanoparticles (ca 10^6 spins) and ultimately to single-molecule magnets (ca 1-10^2 spins).

A single-molecule magnet is considered as the extreme case of a magnetic particle reduced to the size of one molecule. It contains a relatively small number of magnetic ions (1-10^2) coupled together, resulting in a single magnetic moment. If we take the example of an SMM with easy-axis magnetic anisotropy (Ising model), the magnetic behaviour can be easily described by the concept of bistability. As fig. 1.7.2 shows, in the absence of a magnetic field, there are two energy minima corresponding to the opposite directions of the magnetic moment along the same anisotropy axis. The energy states are divided into doublets (or pseudo-doublets) for Kramers (or non-Kramers) ions. In equilibrium, the probability of each ground state to be populated is equal (50%), so in a compound the net magnetization would be zero. The states are separated by an energy (or anisotropy) barrier, induced by the ligand-field interactions of the magnetic ion with the surrounding environment. With the application of a magnetic field with direction parallel to the easy-axis, every doublet is split by ΔE_{ZEE}. Thus, the degeneracy is removed and the ground state where the orientation is parallel to the field takes the lower energy while the one with the orientation opposite to the field the higher. As a result, the population of the lower energy state is increased and can eventually reach ≈100%.

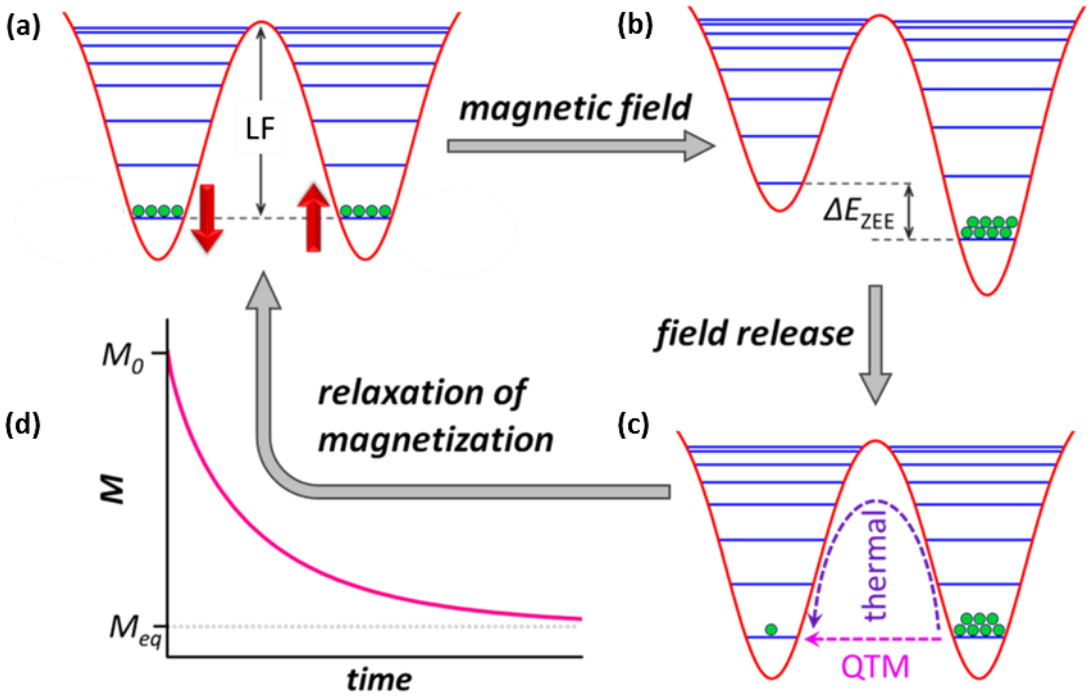

Figure 1.7.2 Schematic illustration of spin bistability and relaxation of magnetization concept for an Ising-type SMM. The energy spectrum is pictured as a double-well potential with $\pm m_J$ doublets, and the spin states population as green circles. In the absence of a magnetic field (and at relatively low temperatures combined with strong LF splitting) only the spin states of the ground doublet are populated (a). Application of a magnetic field removes the time-reversal symmetry, and induces energy splitting on each doublet, equal to ΔE_{ZEE} (b). The lowest spin state is populated. Field release allows the system to return to the initial equilibrium after some time period (c). This process is called relaxation of magnetization and schematically is the restoration of M_{eq} value from the initial M_0 value (d). Reproduced with permission from Dr. A. Popov.

Field removal allows the degeneracy to appear again for each $\pm m_J$ doublet (or pseudo-doublet), and the system can return to its initial state where both ground states are equally populated. However, this process needs some time to complete because of the energy barrier existence. This phenomenon is called relaxation of magnetization and is characterized by the relaxation time τ_m. In the simplest theoretical description of relaxation, magnetization reaches equilibrium with an exponential function of time ($M = M_0 \exp(-t/\tau) + M_{eq}$). For single-domain particles and superparamagnets, there is a competition between thermal energy and magnetic field strength. For SMMs the situation is in principle the same but more complicated as relaxation proceeds via mechanisms obeying the quantum laws. Thermal relaxation appears as phonon-spin interaction where several processes can take place that allow to overcome the energy barrier. Besides these, there is also a pure temperature independent quantum mechanism named as quantum tunneling of magnetization (QTM). The SMM relaxation mechanisms are discussed next in more details.

1.8 Magnetic relaxation mechanisms in SMM

For a single-molecule magnet, relaxation proceeds via different mechanisms which are in general dependent on temperature and magnetic field. One great goal is to design molecular systems with very long-living metastable magnetic states in high temperatures. The subject of magnetic relaxation has been studied thoroughly for decades. Classical references for thermal relaxation are Van Vleck [22, 23], Orbach [24] and Stevens [25], while relaxation via quantum tunneling is descripted in publications like Garanin [26] and Gatteschi [27]. However, a universal theoretical framework providing an unambiguous description for the experimental observations in SMM-field does not exist. Today, the study of physical principles underlying the magnetic relaxation continues with great interest as many new systems often question the existing theory.
Currently accepted theory describes thermal relaxation processes which proceed via energy exchange with lattice vibrations, where electronic transitions emit or absorb acoustic phonons below the cutoff at Debye frequency [15, 17]. Main spin–lattice relaxation mechanisms known today are Direct, Raman and Orbach, involving one, two and multiple phonons respectively. Tunneling of magnetization is the only non-temperature dependent process but combination with thermal process is also possible (thermally-assisted tunneling).

Direct process (one phonon)

The molecule makes a direct transition from one crystal-field state to another with emission or absorption of one acoustic phonon with energy equal to the difference between the initial and final state [15, 17]. Therefore, direct mechanism does not occur between states of the same energy (i.e. Kramers doublets) but a finite magnetic field is necessary to lift the degeneracy and allow the transition. Resonant phonon will have energy equal to the Zeeman splitting between the two states ($\hbar\omega_k=\mu_0 H$) and for high-temperature regime ($k_B T>>\hbar\omega_k$) the relaxation rate is given by the following approximate equation, where k=1 for non-Kramers ion and k=2 for Kramers:

$$\tau_{Direct}^{-1} = AH^{2k}T \tag{1.8.1}$$

Raman process (two-phonon)

In the first order Raman phenomenon, spin relaxes through a virtual non-stationary state of the lattice via two-phonon process [15, 17]. In the second-order Raman effect, not only the lattice but also the spin system undergoes a transition via a virtual intermediate state. The mechanism can be expressed by the temperature-dependent formula:

$$\tau_{Raman}^{-1} = CT^{n} \tag{1.8.2}$$

Raman process is expected to be predominant with respect to the direct at temperatures above 20 K.

Orbach process (multi-phonon)

Similar to Arrhenius behavior of superparamagnets, single-molecule magnets follow the same motif overpassing the anisotropy barrier with the energy contribution of several phonons [15, 17]. In principle, every multi-phonon process requires relatively high temperatures to appear. Therefore, Orbach mechanism dominates at higher temperatures as a large number of phonons becomes available. The equation is:

$$\tau_{Orbach}^{-1} = \tau_0^{-1} exp\left(-\frac{U^{eff}}{k_B T}\right) \quad (1.8.3)$$

The exponential term includes the competition between the CF-induced effective barrier (U^{eff}) and the thermal energy $k_B T$. The pre-exponential factor τ_0 is described as the attempt time of relaxation from the phonon bath and its value is within the range of 10^{-7}-10^{-10} s for molecular species [15, 17]. Temperature dependence of relaxation time in a constant field is often plotted in Arrhenius coordinates ($log\tau$-T^{-1}), hence the Orbach mechanism appears as a straight line of experimental points with gradient equal to the effective barrier (U^{eff}).

Phonon-bottleneck effect

Phonon-bottleneck is the situation when phonon relaxation slows down considerably as the energy dissipation to the lattice becomes insufficient [15, 17]. Phonons of the required energy are not able to transfer energy to the phonon bath fast enough, inducing a warming up of the lattice. The emitted phonons are prone to be re-absorbed thus delaying the relaxation. The process can be described by the same equation as Raman process, but with smaller power for temperature ($2 \leq m \leq 4$):

$$\tau_{PB}^{-1} = CT^m \quad (1.8.4)$$

The basic hypothesis for the interpretation of the thermally-activated relaxation processes in SMMs is that the lattice phonon-spectrum is approximated by the Debye model. As a result, the density of phonon states depends quadratically on the phonon frequency up to a maximum value, called Debye frequency. Acoustic phonon wavelengths are larger than the interatomic distances (i.e. 300 nm for 10 GHz frequency), a fact that raises the question up to which extent is the Debye model suitable for SMMs. In addition to acoustic, optical phonons can also participate in relaxation. Low energy librational, like small oscillatory rotational motions of molecules, can generate a quasi-continuum of optical phonons. All these open topics question the existing theory, accompanied by many cases of modern SMMs in which obtained fitting parameter values deviate from those predicted from classical theory.

Quantum tunneling of magnetization (QTM)

At sufficiently low temperatures, the occupation probability of the excited magnetic states is so small that the system can be described only by considering the ground state. Spin-reversal with a shortcut through the energy barrier is defined as Quantum Tunneling of Magnetization (QTM) [27]. For non-Kramers ions (even number of *4f*-electrons), energy states are not degenerate and as a result, tunneling between the two states of the ground pseudo-doublet under zero-field is allowed. For Kramers ions (odd number of *4f*-electrons), zero-field tunneling is forbidden because the eigenstates are stationary and degenerate (pure Kramers-doublets). However, a transverse component to the easy-axis magnetic field, induced by external stimuli or magnetic interactions (exchange, dipolar and/or hyperfine) is able to open the door for QTM. The general formula for QTM mechanism is:

$$\tau_{QTM}^{-1} = \frac{B_1}{1+B_2H^2} \quad (1.8.5)$$

where B_1 and B_2 are temperature-independent fitting parameters. In zero-field, relaxation rate equals B_1, whereas upon field application it decreases fast with the field increase. Tunneling is completely temperature independent as no phonons are involved and at low temperature and zero-field is usually the most efficient relaxation path. Phonon-assisted (or thermally activated) QTM is also possible, where a combination of thermal and quantum relaxation occurs.
Zero-field tunneling is very ubiquitous in molecular magnets containing a single lanthanide ion, resulting in the characteristic "butterfly" shape [28, 29] of hysteresis curves at low temperatures. For two or more coupled lanthanide ions, zero-field tunneling is often quenched. However, exchange interactions can favor tunneling in some finite field. This type of tunneling appears as a step or deflection in the magnetization curves.

Combination of relaxation mechanisms

In principle, a single-molecule magnet can relax simultaneously via all the mechanisms described so far. However, temperature and external magnetic field conditions define the magnitude of the relaxation rates of each mechanism involved. Often, one of them prevails in certain (*B*, *T*) regime. The general equation that is used to fit the experimental data of relaxation time as a function of magnetic field and temperature, is the sum of all the relaxation mechanisms mentioned above:

$$\tau^{-1} = \tau_{QTM}^{-1} + \tau_{Direct}^{-1} + \tau_{Raman}^{-1} + \tau_{Orbach}^{-1} = \frac{B_1}{1+B_2H^2} + AH^{2k}T + CT^n + \tau_0^{-1}exp\left(-\frac{U^{eff}}{k_BT}\right) \quad (1.8.6)$$

The processes are written in the order of expected dominance from low to high temperature and magnetic field. As the equation contains eight fitting parameters, it is preferred to fit tau (τ) as a function of field or temperature separately. Once we understand which relaxation mechanisms are involved, we can try to design molecules where these factors are taken into account.

Chapter 2

Synthesis and characterization of endohedral metallofullerenes

Fullerenes, the spherical-like closed carbon structures, possess the unique ability to encapsulate small atomic clusters within their empty space. Such fullerenes are called “endohedral” after combination of the Greek words ένδον (“endon”-within) and έδρα (“hedra”-face of a geometrical figure). In the chemical formulae, endohedral species are written first, followed by the symbol “@” and then the type of carbon cage. For example, La@C_{60} denotes an endohedral fullerene where one lanthanum atom is inside the C_{60} cage.

2.1 Brief history of fullerenes

Until 1985, it was widely accepted that carbon can exist only in two allotropic forms, diamond and graphite. That year, Harold W. Kroto et al. discovered a new class of self-organizing carbon structures, by reporting the existence of the first fullerenes, C_{60} and C_{70} (fig. 2.1.1) [30]. The same year, the ability of them to host foreign atoms inside their empty space was also introduced [31]. Eleven years after, Harold W. Kroto, Robert F. Curl and Richard E. Smalley were awarded the Nobel Prize in Chemistry for their discovery of fullerenes. The spherical-like polyhedral shapes and the potential to form ‘endohedral’ structures with various species inside, draw immediately the scientific interest. Nevertheless, further studies in the first years after the discovery, were hampered by the extremely poor yields of the available synthesis methods at that time [32]. The situation changed completely in 1990, when Wolfgang Krätschmer et al. [33] developed the arc-discharge synthesis method allowing the production of macroscopic quantities of fullerenes (grams) in a reasonable time scale. This decisive step resulted in the great boom in the fullerene research area.

In recent past, organic chemistry developed successfully a plethora of surface functionalization reactions which inherit new physical and chemical properties to the fullerenes, and allow them to polymerize and attach onto surfaces [34]. Another area of interest has been the exohedral fullerenes (or fullerides), which are chemical compounds with foreign cations located among the hollow fullerenes (fig. 2.1.2). The highlight of this research area has been the discovery of unconventional high critical temperature (T_c) superconductivity in alkali fullerides [35], with $RbCs_2C_{60}$ holding the record among them (T_c=33 K in ambient conditions) [36]. Finally, in the field of endohedral fullerenes, encapsulated magnetic ions can transform the fullerene into a single molecule magnet. The last two decades, a shift of interest towards the magnetic behavior of lanthanide clusters inside fullerenes has arisen with high prospective.

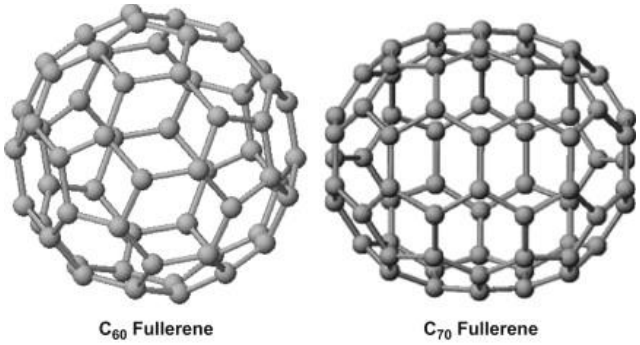

Figure 2.1.1 Structures of C_{60} and C_{70} fullerenes. Reproduced from ref. [37]

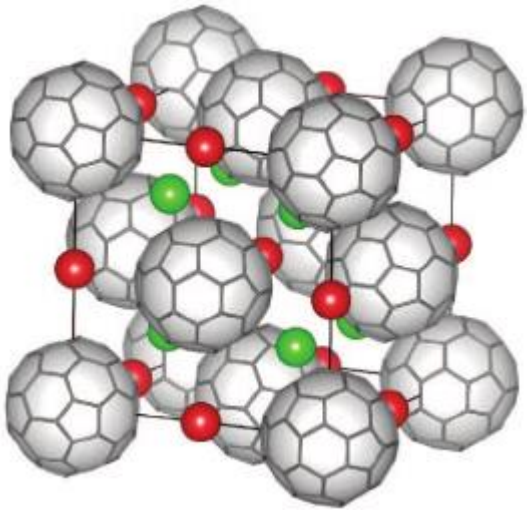

Figure 2.1.2 Crystal structure of fcc A_3C_{60} (A: alkali metal, green spheres represent cations on tetrahedral, and red on octahedral sites, respectively). From ref. [38]. Reprinted with permission from AAAS.

2.2 Categories of endohedral metallofullerenes (EMFs)

Fullerenes can become the host environment for a great variety of combinations of different atomic species. For endohedral metallofullerenes (EMFs), the internal unit can comprise from one to four metal ions (depending on the size of the ions and the carbon cage), usually lanthanide and/or transition metals typically in their trivalent oxidation state (M^{3+}), and possibly up to three electronegative non-metal ions (like N/O/C/S) to compensate the Coulomb repulsions between the cations. When metallic and non-metallic species coexist in the carbon cage, the molecule is called clusterfullerene [32]. The name of the clusterfullerene is derived from the negative charge unit, such as "nitride clusterfullerene" when a nitride ion (N^{3-}) is located in the center of an M_3N cluster [39, 40] or "sulfide clusterfullerene" with sulfide ion (S^{2-}) in the M_2S cluster [41]. Other types are the carbide, carbonitride and oxide clusterfullerenes [42, 43].

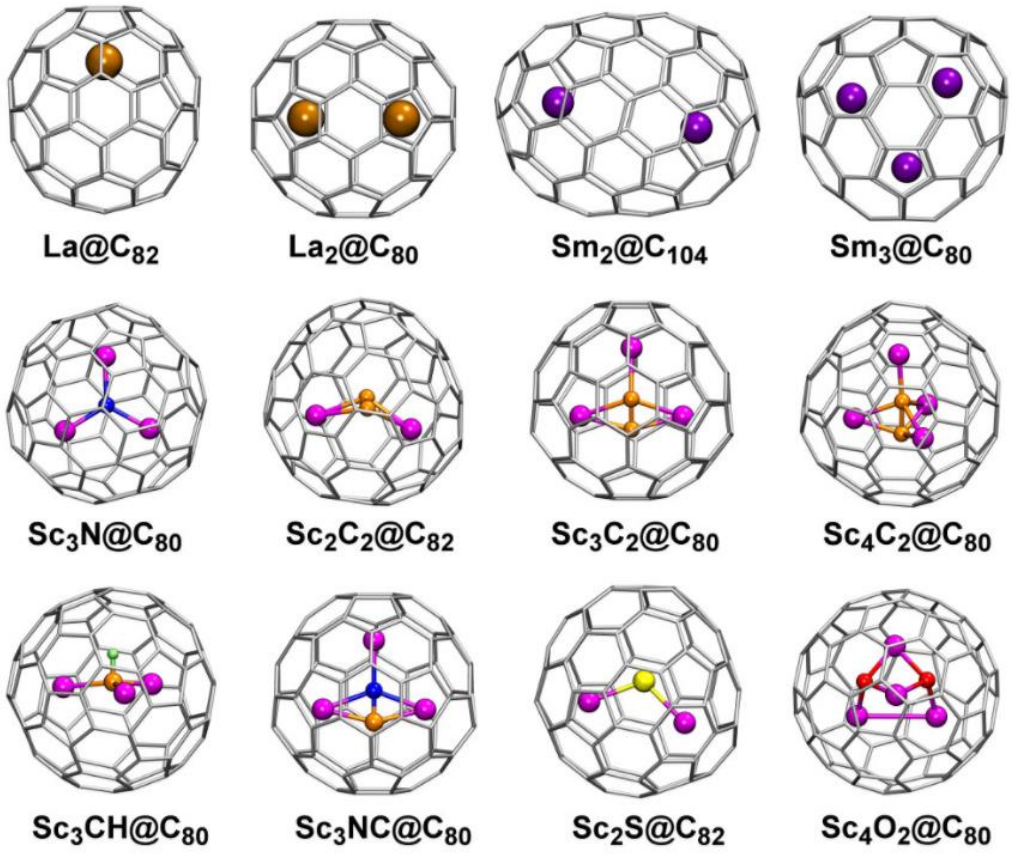

Figure 2.2.1 Variant types of endohedral metallofullerenes and their carbon cages. Reproduced from ref. [32]. Copyright (2013) American Chemical Society.

2.3 Synthesis and separation techniques of EMFs

Two conceptual pathways for the synthesis of endohedral fullerenes exist: either foreign atoms are “implanted” through the walls of the already existing carbon cages (ion bombardment [44-46], high pressure treatment [47, 48] and molecular surgery [49, 50]), or encapsulation takes place along with the fullerene formation [32, 33]. The vast majority of endohedral metallo-fullerenes can be produced only via the Krätschmer-Huffman method [51]. A strong electric current, typically around 120 A, is generated between two graphite rods which evaporate under inert atmosphere, (50−100 Torr of He gas). The rods are filled before with metal or metal-oxide powder required as a precursor material for the formation of EMFs. Various carbon structures are produced during and after the arc discharge. Among them, decent amounts of empty and filled fullerenes can be formed. The synthesis process is rather chaotic so it does not allow the monitoring of the formed products with in situ probes. Hence, it remains a challenge today to find ways to study the formation mechanism of EMFs inside the arc discharge apparatus. The yield depends sensitively on the He gas pressure in the chamber and other parameters like the size and composition of the graphite electrodes, the distance between them, the DC current etc. Generally EMFs are found in yields of 2% or less, but precise control over the relative quantities of the added materials and the physical conditions inside the chamber enable fine optimization of the production yields for each type of the endohedral fullerenes.

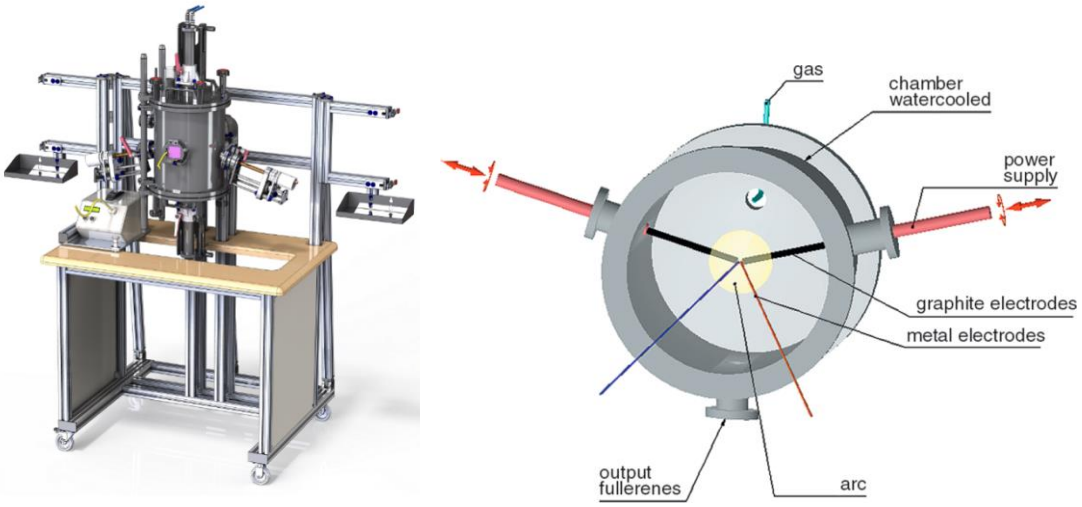

Figure 2.3.1 Modern Krätschmer-Huffman generator used in IFW-Dresden and schematic view of the interior of the apparatus during arc discharge. Reproduced from ref. [32]. Copyright (2013) American Chemical Society.

.

Carbon soot is collected from the chamber and fullerenes are extracted with suitable organic solvents (carbon disulfide, toluene and dichlorobenzene). Next step requires high-performance liquid chromatography (HPLC) to obtain the endohedral metallofullerenes in compositionally pure forms [52, 53]. When the formation takes place in He-atmosphere, mono, di, and rarely trimetallofullerenes (but in considerably lower amounts) are mainly formed. Presence of N_2 gas benefits the creation of nitride clusterfullerenes. Other reactive gases like CH_4, SO_2, CO_2 and H_2 benefit the synthesis of different types of clusterfullerenes with sulfur, oxygen, CH, CN, etc [43, 54]. Solid organic sources such as guanidium thiocyanate, reduce dramatically the yield of empty fullerenes simplifying the separation procedures [55, 56].

2.4 Structural analysis techniques of EMFs

The presence of the carbon cage is not completely "innocent", because it acts as an electron acceptor forming bonds with the endohedral unit. These interactions play an important role on the structure parameters like symmetry of the fullerene cage and cluster position with respect to the cage. Knowledge of the structure is important in order to interpret the physical and chemical properties in depth. A complete structural analysis includes recognition of the type of the fullerene (number of carbon atoms and cage symmetry) plus specification of the type and position of the cluster inside. For this reason, several techniques are usually employed.

Mass-spectrometry provides valuable information on the sample composition, and UV-Vis-NIR spectroscopy helps to distinguish the cage isomer. Light absorption is dominated by the π-π^* excitations of the carbon cage, thus the absorption spectra of different EMFs with the same cage symmetry and in the same charge state are almost identical regardless their inner species [32].

Detailed structural analysis can be accomplished via X-ray diffraction technique. Single crystals are required and rarely is an easy task for fullerene samples. A limiting factor is the presence of several possible cluster positions and orientations with respect to the cage with low energy barriers of inter-conversion. Consequently, structure elucidation with XRD on single crystals can be rather challenging [32].

In certain cases, nuclear magnetic resonance (NMR) and Raman spectroscopy can provide additional information on the fullerene structure. The vast majority of NMR studies are dedicated to the determination of the cage structure by ^{13}C NMR spectroscopy in solution [57-59]. However, the low natural abundance of the ^{13}C isotope, the relatively small gyromagnetic ratio and long relaxation times in fullerenes, require extended capacity for ^{13}C NMR technique in the spectroscopic studies, usually unavailable in most of the labs. Besides, the method gives only the carbon cage symmetry, and therefore the structure remains ambiguous when several isomers are possible.

2.5 Magnetic characterization techniques of EMFs

A broad spectrum of techniques are employed for the study of materials with different magnetic properties. Standard magnetometry is the most popular method, sometimes combined with special techniques like magnetic torque measurement [60], in order to recognize the magnetic anisotropy of the material. Additionally, static heat capacity measurements [61] can provide information on the electronic levels and phonon energies. Magnetic resonance techniques, like electronic, nuclear and muon [62-64], are widely employed to identify the electronic structure of the ground multiplet. Neutron techniques [65] are particularly useful to determine the energy splitting in zero field.

Nowadays, SQUID (Superconducting Quantum Interference Device) magnetometer is one of the most commonly used devices for macroscopic magnetic studies [66]. Commercially available by Quantum Design, Magnetic Property Measurement System 3 (MPMS 3) ensures fast acquisition of high-quality data and precise temperature and magnetic field control.

Figure 2.5.1 MPMS 3 SQUID commercially available by Quantum Design. This type of magnetometer was used in the majority of the magnetic measurements conducted in the framework of this thesis, thanks to the permission of Dr. Anja Wolter-Giraud. The image is reproduced from *www.qdusa.com*

2.6 SQUID magnetometer

In the third generation of MPMS SQUID-magnetometer produced by Q.D., all major components (cryogenic Dewar, control electronics and magnet power supply) are integrated into a single unit.

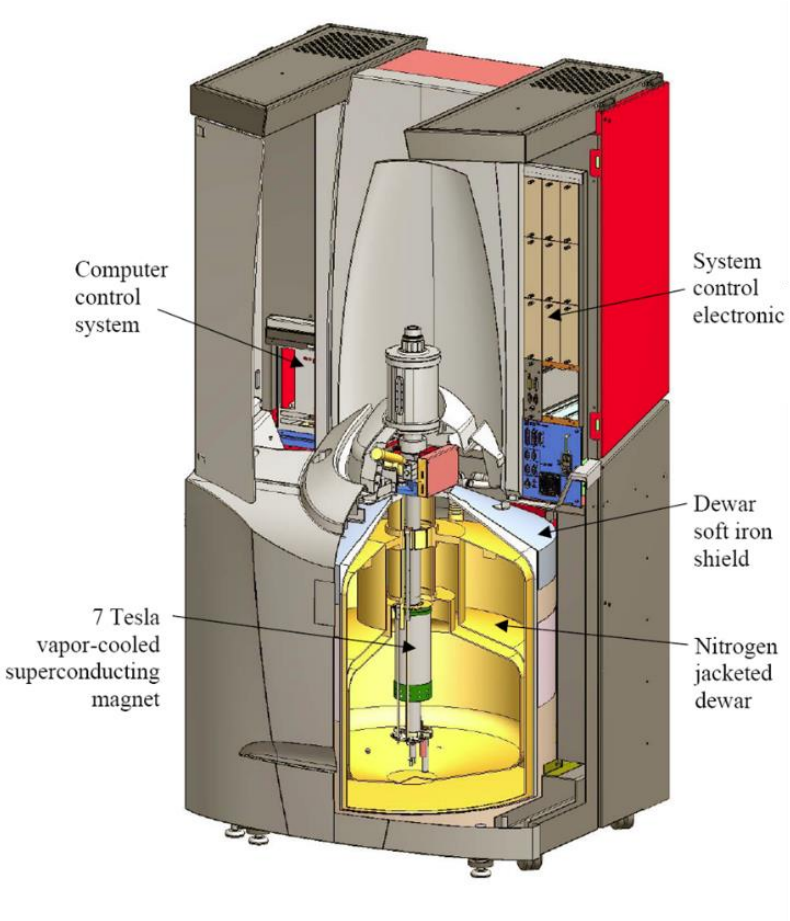

Figure 2.6.1 Cutaway view of MPMS 3 SQUID-magnetometer. Reproduced from www.qdusa.com

The temperature control insert of the MPMS 3 is a vacuum-insulated chamber into which cold helium is drawn through a variable flow valve, for the purpose of cooling the sample chamber with pumped helium, down to 1.5 K. However, 1.8 K is the lowest stable temperature where continuous operation is possible. Heaters on the sample chamber can raise the temperature up to 400 K. Temperature control allows to cool the sample chamber from room temperature to 1.8 K in typically less than 15 minutes with maximum sweep rate of 50 K/min. If it is important to conduct magnetic measurements at sub-Kelvin temperatures, SQUID magnetometers offer this possibility by extending even to milli-Kelvin range, but the techniques are more expensive and demanding in terms of experimental setup and data acquisition (less automated).

The 7-Tesla superconducting magnet is helium vapor-cooled and as a result the magnet is very "quiet", contributing to the great signal to noise ratio performance of the system. The most sensitive part of the magnetometer is the SQUID sensor which is kept constantly under liquid ^{4}He temperature (4.23 K) in order to remain in superconductive state. Precision in the magnetic measurements requires the SQUID sensor operating smoothly so it is placed further away from the magnet, which reduces the interference with the magnetic field even at its maximum of 7 T. SQUID is inductively coupled to a closed-loop control circuit [66] and operates as an extremely sensitive flux-to-voltage converter. It measures the changes in the magnetic flux as the sample moves through the superconductive detection coils (or pick-up coils). According to Faraday's law, time-varying magnetic flux creates a proportional electromotive force on the closed-looped circuit, which contains four detection coils (fig. 2.6.2). They have 17 mm diameter and two of them are located in the middle consisting of 2N parallel windings, while the two outer coils have N windings each, in the opposite direction of the central ones. This is a second-order gradiometer designed to enhance sensitivity by minimizing the background magnetic signal.

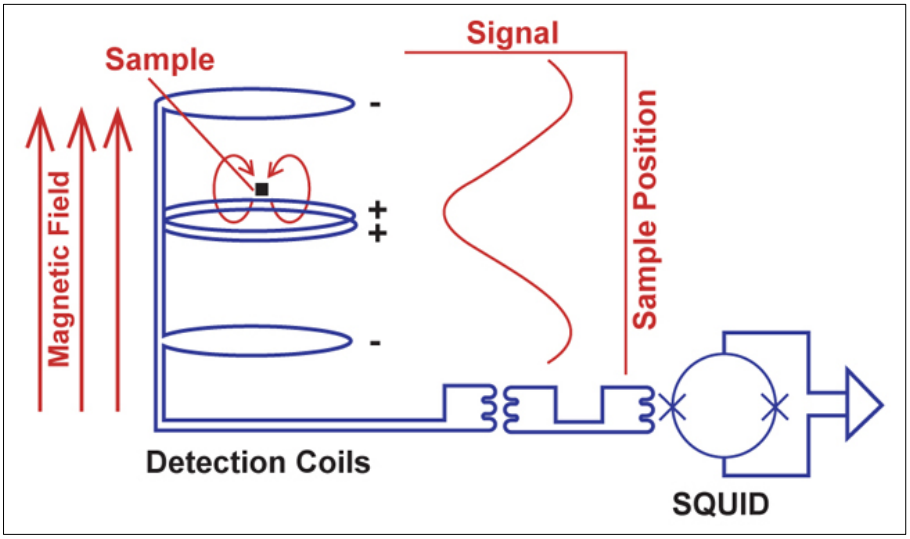

Figure 2.6.2 Schematic description of a SQUID magnetometer working principle. During a measurement scan, transport mechanism moves the sample through the detection coils creating a voltage vs position waveform. Software performs a curve fitting to the raw waveform to obtain sample's magnetic moment value. Reproduced from *www.qdusa.com*

A standard SQUID magnetometer offers the option to record magnetization as a function of the external field or temperature. Applied magnetic field can go up to 7 Tesla with maximum sweep rate 700 Oe/s. It is also possible to measure time evolution of magnetization to study relaxation. MPMS 3 comes with three measurement modes: DC scan mode, VSM and AC susceptibility mode. DC scan mode provides continuous plotting and capture of raw data points at static or sweeping fields/temperatures. Scan range is from 3 to 6 cm with variable speed. Further improvement of

the signal to noise ratio can be achieved by the vertical vibration of the sample around the center position. This is possible with the VSM mode where the motor provides a sinusoidal motion at a fixed frequency with available amplitude from 0.1 to 8 mm. Since VSM signal is proportional to the 2nd power of vibration amplitude, improvement of the signal to noise ratio would require full vibration amplitude, but on the other hand, larger amplitude may induce frictional heat that leads to temperature instability and noisy data. An optimal choice usually ranges between 3-6 mm. AC susceptibility mode uses a weak magnetic field, harmonically oscillating, in order to follow the fast relaxation of the studied sample. Available frequency ranges are 0.01-1.000 Hz for MPMS-XL, 0.1-1.000 Hz for MPMS-3 and 10-10.000 Hz for PPMS models. The amplitude of the applied oscillating field can reach 10 Oe while DC field (up to 7 T) can be also present. SQUID sensor offers the advantage of measuring with frequency-independent sensitivity, enabling very low frequency measurements. The advantage of MPMS 3 design is that DC/AC and VSM measurements can be conducted within the same single platform, without having to remove/re-installing the VSM motor.

2.7 SQUID magnetic measurements

Sample preparation

Magnetic characterization of our samples is a multi-stage procedure, utilizing the abilities of the available MPMS 3 SQUID-magnetometer for VSM and AC measurements, and the MPMS-XL for AC only. Our samples are often in powder form (and rarely in single-crystalline) with randomly oriented endohedral fullerenes. In VSM magnetometry, tiny amount of sample (<0.1 mg) without mass knowledge, is drop-casted on a quartz holder from CS_2 solution, forming a spot of 2-3 mm diameter (fig. 2.7.1). The solvent evaporates fast in room temperature, leaving a dense fullerene film on the holder. Multiple tests showed that for a sample mass of less than 0.1 mg, the adhesion of the film is strong enough and does not require the use of glue to prevent detachment of the sample during measurements. However, we always cover the quartz holder with a low-signal straw as precaution meter. The advantage of this kind of sample preparation is that it is fast and straightforward. Quartz holders and straws have an extremely low diamagnetic signal, hence it is possible to detect weak magnetic signals without significant background contribution.
AC measurements require larger amounts of sample to get a measurable response. For that reason, we use the whole sample available (usually 1-2 mg), which is placed inside a propylene capsule of low diamagnetic signal. The sample is drop-casted into the capsule from CS_2 solution and let dry under vacuum before the measurement. The precise knowledge of the sample mass inside the capsule, allows to determine the absolute magnetic moment of our molecule, by measuring the saturated magnetization at 1.8 K and 7 T field. The capsule is closed tightly, so that the sample is packed as much as possible to improve the signal intensity. Then, the capsule is fitted inside a brass holder to conduct the AC measurements. The diamagnetic signal of the brass holder is higher (10^{-6} emu) comparing to the quartz holder, but the sample signal is also usually 2-3 orders of magnitude higher (10^{-4} emu at least).

Figure 2.7.1 Quartz (up) and brass (down) holders with drop-casted sample and sample in capsule resp.

Blocking temperature of magnetization (T_B)

The first and very important parameter for the evaluation of a SMM performance is the blocking temperature of magnetization T_B. It is the temperature where the transition from hysteretic to paramagnetic behavior occurs. There are two determination methods of blocking temperature, and as it is a kinetic parameter the value depends on the experimental conditions. In one definition, T_B is the highest temperature where hysteresis loop remains open. The opening of hysteresis is dependent on the magnetic field sweep rate and so the T_B value. In the second definition (fig. 2.7.2), T_B is the temperature where the maximum of magnetization appears during the in-field warm up of a previously zero-field cooled sample. The field should be 'weak' enough (i.e. 2.000 Oe) to avoid fast increase of magnetization of the sample at low temperatures, in the time scale of the experiment.

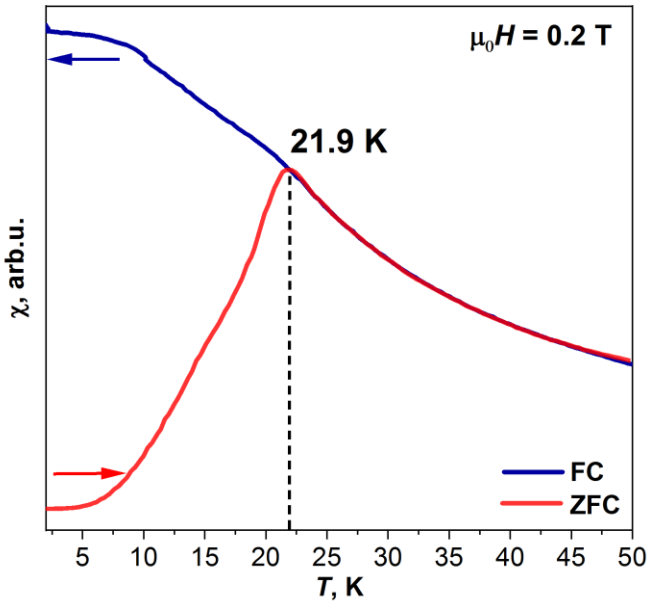

Figure 2.7.2 Standard method for determination of blocking temperature of magnetization. The χ_{ZFC} curve (red) is measured during warm-up (5 K/min) in the field of 0.2 T. The χ_{FC} curve (blue) is recorded during cooling down in-field (0.2 T, 5 K/min). The vertical bar denotes T_B. In this example, $T_{irrev}=T_B$. The χ_{ZFC} and χ_{FC} curves presented here, were measured for $Dy_2@C_{80}(CH_2Ph)$ [67]

After the sample is cooled down in zero-field, a finite magnetic field is applied and magnetization increases to reach its equilibrium value. But when relaxation of magnetization is slow, the process of approaching the equilibrium value may be rather long. As temperature increases fast (5 K/min), the time required to reach equilibrium magnetization diminishes, and when the sample approaches the blocking temperature, the relaxation is 'unblocked' and thus magnetization starts increasing very fast and reaches the equilibrium value. When temperature increases further, the magnetization starts decreasing (equilibrium paramagnetic behavior), and as a result a peak appears, corresponding to the blocking temperature T_B. Cooling down the sample in the same

field that it was warmed up before (i.e. 2.000 Oe), the in field-cool curve deviates from the field-warmed curve, after a point which is called irreversibility temperature T_{irr} and does not necessarily coincide with T_B.

As already mentioned, blocking temperature is a kinetic parameter and therefore is dependent on the magnetic field and temperature sweep rates. Fig. 2.7.3 shows the measurement of T_B with different temperature sweep rates, and illustrates the variation of T_B between 18.3 at 1 K/min to 21.9 K at 5 K/min and 22.9 K at 20 K/min.

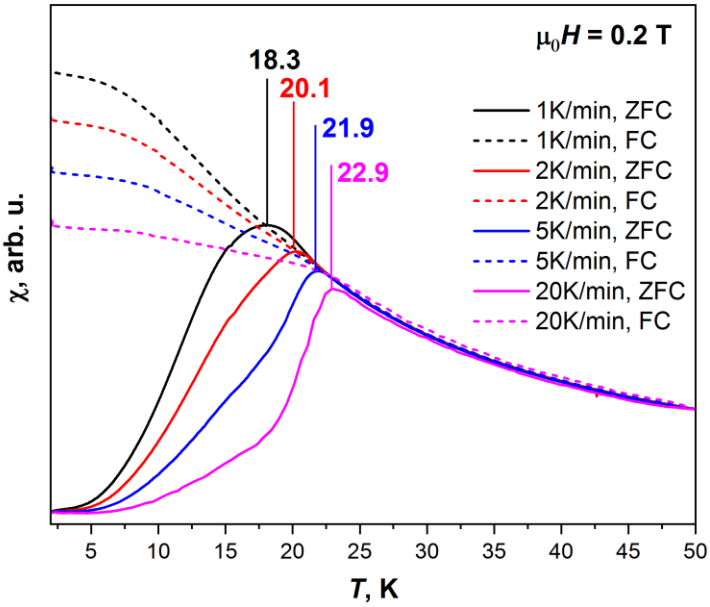

Figure 2.7.3 Determination of blocking temperature (T_B) of $Dy_2@C_{80}(CH_2Ph)$ for different temperature sweep rates. Vertical bars denote T_B. The values become higher with increase of the temperature sweep rate. Reproduced from ref. [67]

Comparison of T_B values measured in different experimental conditions can be misleading. For that reason, Gatteschi et al. [27] suggested a more quantitative description, the 100-sec blocking temperature $T_{B(100)}$. This is the temperature where the relaxation time τ is equal to 100 s. The global scientific community today is mainly focused on rising the value of blocking temperature of magnetization, ideally to room temperature. This achievement would minimize the cost and practical difficulties for operating SMMs into magnetic devices.

Field dependence of magnetization (*M* vs *H*)

When a constant field *H* is applied, the sample is magnetized and the value of the macroscopic magnetization *M* can be measured. Given enough time, the sample reaches the thermodynamic equilibrium, but if the field is swept before that, then the out-of-equilibrium magnetization is recorded. In this case, magnetic hysteresis is observed, meaning deviation from the equilibrium curve or equally, opening of the magnetization loop in *M*-*H* coordinates, which depends also on

the sweep rate of the magnetic field. Hysteresis curves at low temperatures provide important information on magnetic properties. Manifestation of SMM behavior is an open hysteresis loop. A sudden drop of magnetization in zero or non-zero field indicates QTM as the main relaxation process.

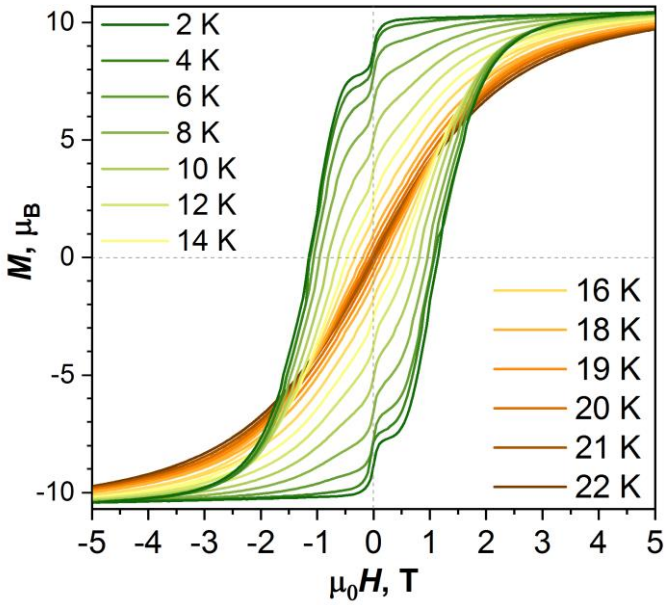

Figure 2.7.4 $Dy_2@C_{80}(CH_2Ph)$ magnetization curves measured at various temperatures with our standard field sweep rate (2.9 mT/s). Reproduced from ref. [67]

Temperature dependence of magnetization (M vs T)

Direct measurement of magnetic susceptibility as a ratio between the recorded magnetization divided by the value of the applied magnetic field ($\chi_{dc}=M/H$) is possible. However, in principle it does not coincide with the differential susceptibility ($\chi=dM/dH$). Also, the assumption that the field experienced by the spin system is equal to the applied field is generally wrong, because a magnetized sample has magnetic poles which create an additional field with opposite direction to the external, known as demagnetizing or Maxwell field. For molecular magnets though, the demagnetizing field is very weak and can be neglected.

Temperature dependence of the product $\chi_{dc} \cdot T$ gives information on the type and strength of the exchange interactions in the system. In lower temperature regime, where the ground state is mainly populated, strong ferromagnetic (FM) coupling is manifested by the presence of a sharp peak in $\chi_{dc}T$-T coordinates, while antiferromagnetic (AFM) does not (fig. 2.7.5). At higher temperatures where excited states are populated too, $\chi_{dc}T$-T curves measured in different constant fields, gradually converge to the same value, the high-temperature limit. When the Curie law is obeyed, the product of molar susceptibility and temperature is constant and is related to the effective magnetic moment ($\mu_{eff} \sim \sqrt{\chi T}$).

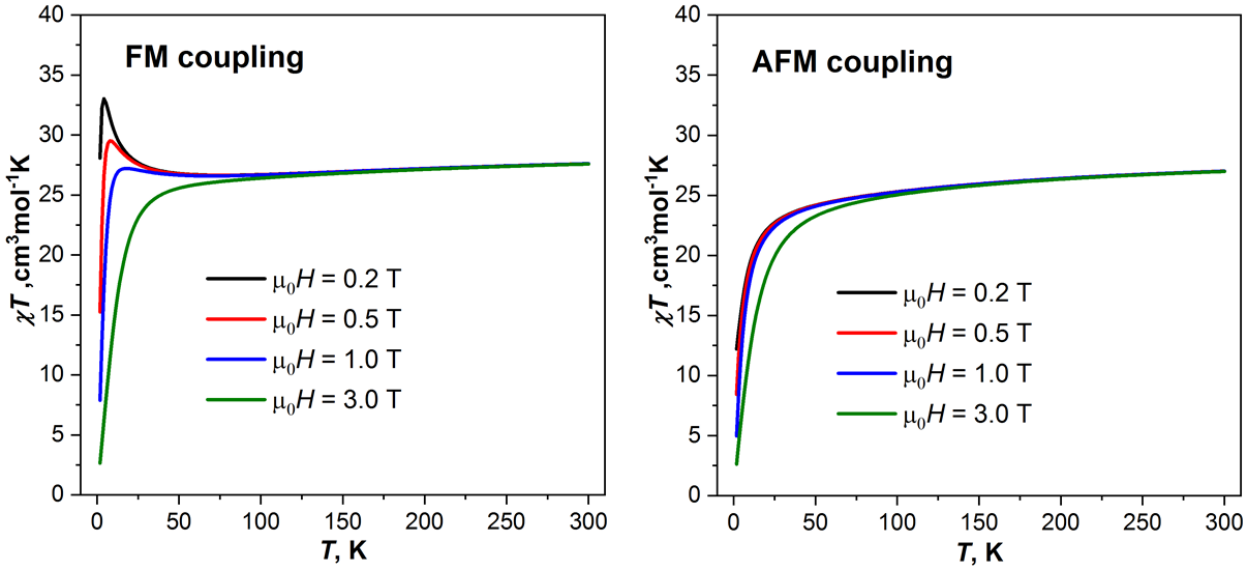

Figure 2.7.5 Calculated χT-T curves in the fields of 0.2 T, 0.5 T, 1 T and 3 T for ferromagnetic coupling (FM) and antiferromagnetic coupling (AFM) of two Dy ions. Reproduced from ref. [68]

Magneto-dynamics (relaxation)

One of the most interesting and challenging tasks in SMM research field is the experimental characterization and interpretation of the magnetic behavior in respect with time. It can reveal intrinsic properties like the anisotropy barrier and preferred relaxation pathways in different temperature and magnetic field regimes, like quantum tunneling of magnetization. The complete time period is needed for a system to reach a new equilibrium state after leaving the initial one because of some external perturbation (change in the external field or temperature) is hard to measure precisely. In praxis, the parameter that is experimentally determined and used in the discussion, is the relaxation time τ, defined as a parameter of the exponential decay discussed in section 1.7. Its value can be determined by direct current (DC) relaxation measurements for $\tau >$ 10 s and by alternating current (AC) measurements for $\tau <$ 1 s. The gap between 1-10 s cannot be covered by conventional SQUID magnetometry.

DC relaxation measurements (static susceptibility)

The standard procedure to record relaxation in DC magnetometry, prerequisites that the sample is first magnetized in a relatively strong external field where the equilibrium state is established, optionally in a temperature $T_1 > T_B$ (higher than the blocking). The sample is then cooled down to the temperature T_2 where we are interested to measure relaxation, and the field is ramped as fast as possible to the desired value H_2 and the decay of magnetization is recorded.

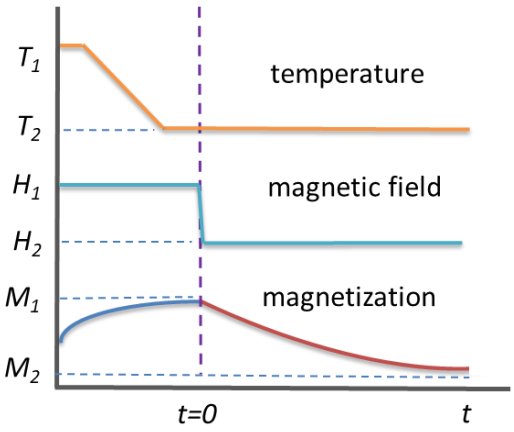

Figure 2.7.6 Schematic view of the procedure to measure the time decay of remnant magnetization. The time dependence of temperature (top), applied magnetic field (middle), and the measured magnetization (bottom) are reported.

The magnetization decay curve usually cannot be fitted well with a single exponential function because relaxation rate over the time is not uniform. For that reason, the stretched exponential function is usually applied:

$$M(t) = M_2 + (M_1 - M_2)\exp[-(t/\tau)^{\alpha}] \qquad (2.7.1)$$

where α is ranging from zero (infinite number of exponential relaxation pathways) to one (single exponential), M_1, M_2 are the initial and final equilibrium-states of magnetization respectively. In our measurements, α is usually found to be between 0.7 and 0.8, hence, stretched exponential fit gives an average relaxation time. While M_1 is easy to detect, it is important that the experiment lasts long enough to get a good estimation of M_2. Reliable estimation of τ requires recording of the decay for ca 3 times τ or longer. For low temperature measurements, this requirement cannot be properly fulfilled because relaxation times are usually too long. If decay time is considerably shorter than 3 x τ, the fit with eq. 2.7.1 gives rather ambiguous results because τ is strongly dependent on M_2, which is not well defined. Although M_2 should be zero for a paramagnet in zero field, a small remnant magnetization is present even in zero field (e.g. diamagnetic contribution, small magnetization caused by deviation of the field from zero etc.).
To avoid these ambiguities, M_2 values can be determined in separate measurement. Namely, the temperature can be increased above blocking temperature to cause complete relaxation of magnetization, and then decreased again to the required temperature (as shown in fig. 2.7.6). Magnetization of the demagnetized sample is then measured over certain time, giving estimation of the M_2 parameter. Using M_2 values determined this way, eliminates ambiguity in M_2 and gives more reliable estimation of relaxation times even when the measurement time is considerably shorter than τ.

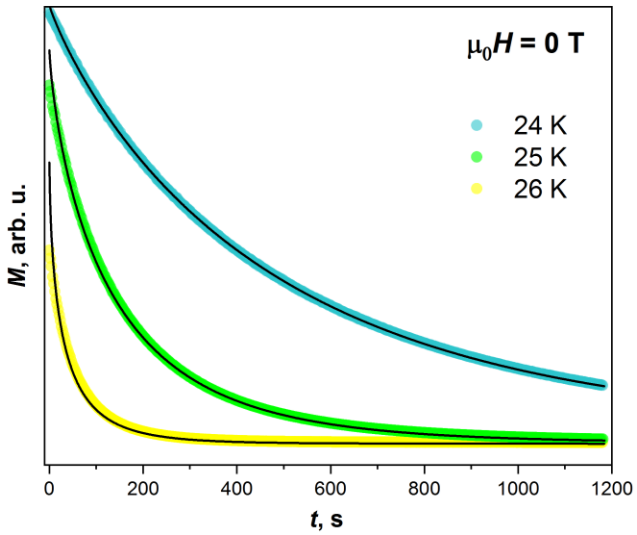

Figure 2.7.7 Example of magnetization decay curves measured by first magnetizing the sample in the field of 7 Tesla, then sweeping the field fast to 0 T (or a finite field in general) and measuring the decay (colored dots). The curves are fitted with stretched exponential black solid lines.

AC relaxation measurements (differential susceptibility)

In AC relaxation measurements, a small (max. 10 Oe) oscillating magnetic field $hcos(\omega t)$ is applied on top of a constant H_0 field (which can be also 0):

$$H = H_0 + hcos(\omega t) \tag{2.7.2}$$

Measured ac susceptibility (χ_{ac}) at a given temperature is a complex value containing the real (in-phase) *χ'(ω)* and imaginary (out-of-phase) *χ''(ω)* components. Typically, relaxation process is not characterized by a single τ but rather a distribution where χ_{ac} is given by the equation:

$$\chi(\omega) = \chi' + i\chi'' = \chi_S + \frac{(\chi_T - \chi_S)}{1+(i\omega\tau)^{(1-a)}} \tag{2.7.3}$$

where α denotes the width of distribution. The χ_T is the isothermal susceptility ($\omega\tau \ll 1$) and χ_S the adiabatic ($\omega\tau \gg 1$). In practice, χ_S can be interpreted as the susceptibility of an isolated magnetic molecule while χ_T corresponds to the equilibrium susceptibility. When $\omega\tau = 1$, an inflection in *χ'(ω)* and a maximum in *χ''(ω)* are observed. In this case, the magnetic relaxation time τ can be determined by the position of the maximum of *χ''(ω)* curve. The real and imaginary parts of the non-static susceptibility of eq. 2.7.3 are:

$$\chi'(\omega) = \chi_S + (\chi_T - \chi_S)\frac{1 + (\omega\tau_m)^{1-\alpha}\sin\left(\frac{\pi\alpha}{2}\right)}{1 + 2(\omega\tau_m)^{1-\alpha}\sin\left(\frac{\pi\alpha}{2}\right) + (\omega\tau_m)^{2-2\alpha}} \tag{2.7.4}$$

$$\chi"(\omega) = (\chi_T - \chi_S)\frac{(\omega\tau_m)^{1-\alpha}\cos(\pi\alpha/2)}{1 + 2(\omega\tau_m)^{1-\alpha}\sin(\pi\alpha/2) + (\omega\tau_m)^{2-2\alpha}} \quad (2.7.5)$$

where α is the parameter, accounting for the distribution of relaxation times (α=0 when only one process is present), and χ_S/χ_T are the adiabatic and isothermal susceptibilities.

In our AC measurements, the frequency f of the oscillating magnetic field is scanned between 0.1-1.000 Hz (in MPMS) and 100-10.000 Hz (in PPMS) and the in-phase (χ') and out-of-phase (χ") magnetic susceptibilities are recorded.

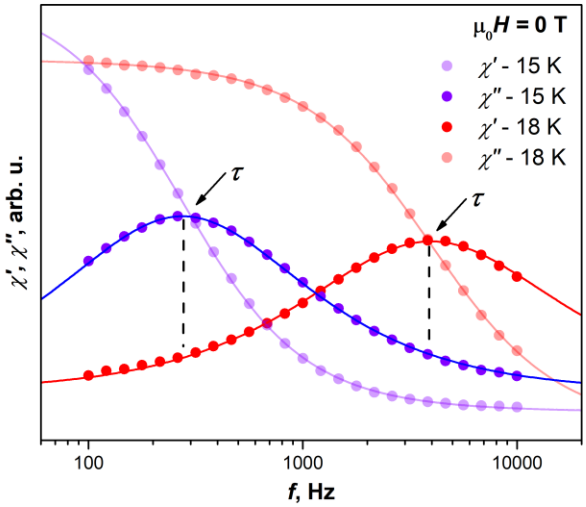

Figure 2.7.8 Frequency dependence of the real (in-phase) χ' and imaginary (out-of-phase) component χ'' of magnetic susceptibility in semi-log scale, in two different temperatures.

Another way to represent the AC-susceptibility data is the Cole-Cole plot used for dielectrics [69], where *χ''(ω)* is plotted as function of *χ'(ω)*.

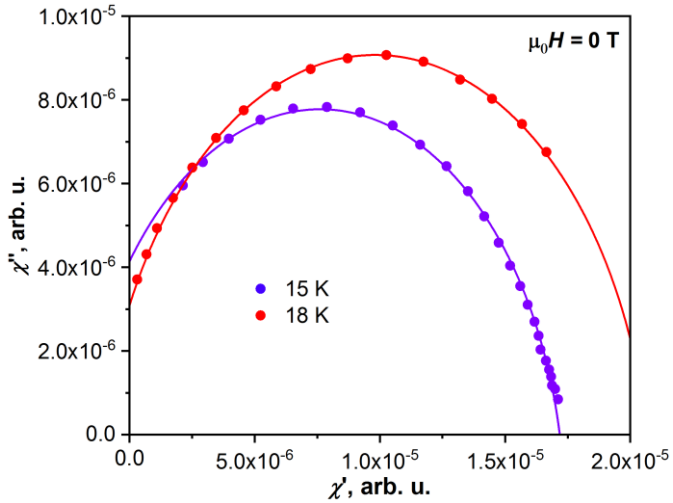

Figure 2.7.9 Cole-Cole plot (χ'' versus χ' for each frequency).

Chapter 3

Single-molecule magnets (SMMs)

A single-molecule magnet consists of one or more metal ions with unpaired electrons, acting as magnetic centres. Below blocking temperature, SMMs display slow relaxation of magnetization due to the presence of intrinsic magnetic anisotropy. Their magnetic bistability opens the way to employ them as building blocks in applications like high-density information storage, magnetic qubits and spintronic devices. The two main criteria to judge the performance of a SMM are the blocking temperature of magnetization T_B and the anisotropy barrier U^{eff}. Therefore, the main research direction is the design of molecules with maximum T_B and U^{eff} values.
In the first part of this chapter we explore the history of molecular magnetism research field by pointing out the highlights from the start of this era until today. In the second part, we introduce the idea of endohedral fullerenes with encapsulated lanthanide ions as possible single-molecule magnets, with two characteristic example systems studied by our group in the recent past.

3.1 Towards the perfect SMM

Over the past three decades, a huge number of single-molecule magnets with distinct magnetic properties have been synthesized and studied in detail. Early efforts focused on testing existing theoretical models of solid-state magnetism and understanding physical phenomena like intra-molecular exchange interactions [70]. Very soon, research expanded into a plethora of magnetic materials with different topologies and dimensionalities, until the landmark discovery of the first SMM, known as Mn_{12}-acetate (1993) [71]. In this complex, twelve manganese ions (four Mn^{4+} and eight Mn^{3+}) are coupled together via oxo-bridges, forming the high-spin ground state of $S=\pm 10$.

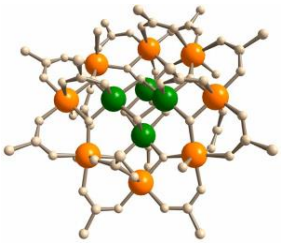

Figure 3.1.1 Structure of Mn_{12}-acetate ($Mn_{12}O_{12}(OAc)_{16}(H_2O)_4$) molecule, the first SMM. Reproduced from ref. [71]

The observed magnetic hysteresis has totally different origin from the traditional bulk magnets, and is the result of the spin-reversal anisotropy barrier between the two bistable ground states, with energy of 51 cm^{-1} (fig. 3.1.2a). In the absence of a magnetic field, quantum tunneling of magnetization (QTM) between the S=±10 states is possible, and appears as step in the hysteresis loops (fig. 3.1.2b) [72]. Upon the application of a magnetic field, QTM is quenched and relaxation proceeds by overcoming the anisotropy barrier. The discovery of Mn_{12}-ac SMM behavior is considered today as the beginning of the single-molecule magnetism era.

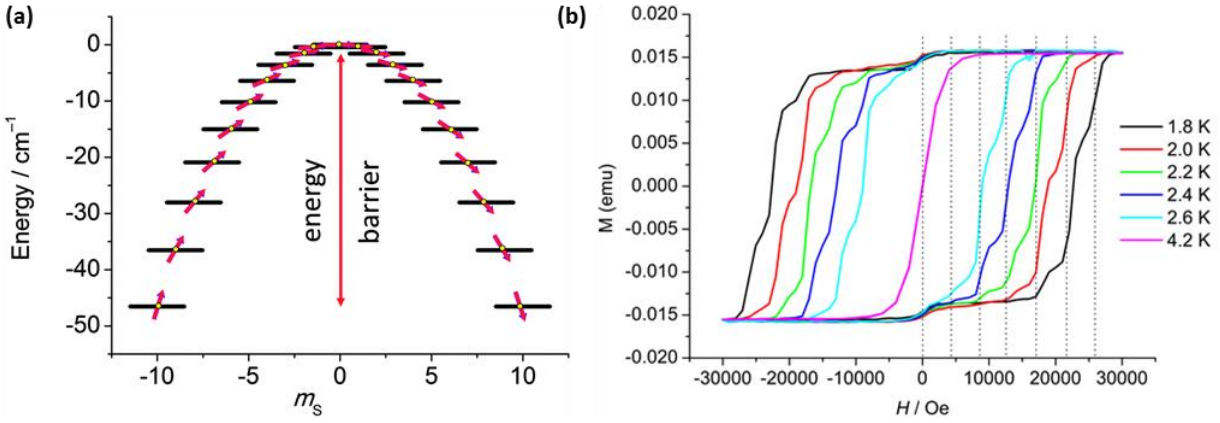

Figure 3.1.2 (a) Potential energy as a function of the m_s quantum number and (b) hysteresis loops of Mn_{12}-ac. Reproduced from ref. [9] and [72]

The energy of the Mn_{12} anisotropy barrier is equal to DS^2, where D is the axial zero-field splitting (ZSF) parameter and S the ground state spin. Following efforts, focused on synthesizing SMMs with larger number of transition-metal ions in order to raise the energy barrier ΔE by increasing the ground state spin number S (which can be easier predicted than the parameter D). In 2006, the SMM with record high-spin ground state up to date (Mn_{19}, S=83/2) was reported by Ako et al. [73]. However, this molecule as the rest of the polynuclear Mn-complexes, suffered from low anisotropy because of the strong interactions among the spin centres, as a result of their spatial arrangement. The largest anisotropy barrier claimed for this type of SMM-series is 60 cm^{-1} for Mn_6 [74]. Except from Mn-SMMs, numerous others with different *3d*-metals, like oxo-bridged iron clusters [75, 76], or vanadium [77], cobalt [78, 79] and nickel-based [80] clusters were

studied. Nevertheless, their blocking temperature values and anisotropy barriers were usually lower than that of Mn_{12}-ac. In other approaches, different ligand molecules, like the cyano-group (CN^-), were tested. In this case, C≡N bond provides effective magnetic coupling between metal ions. In 2017, the record energy barrier of 44.9 cm^{-1} for cyano-bridged SMMs was reported for the tri-nuclear Mn_2Mo compound [81]. From the experimental results on the abundant high-nuclear transition-metal SMMs, it became clear that the spin value does not necessarily increase with the number of metal ions. In addition, the magnetic anisotropy usually degrades strongly due to the different orientations of the magnetic axes of different metal sites, which cancel out each other.

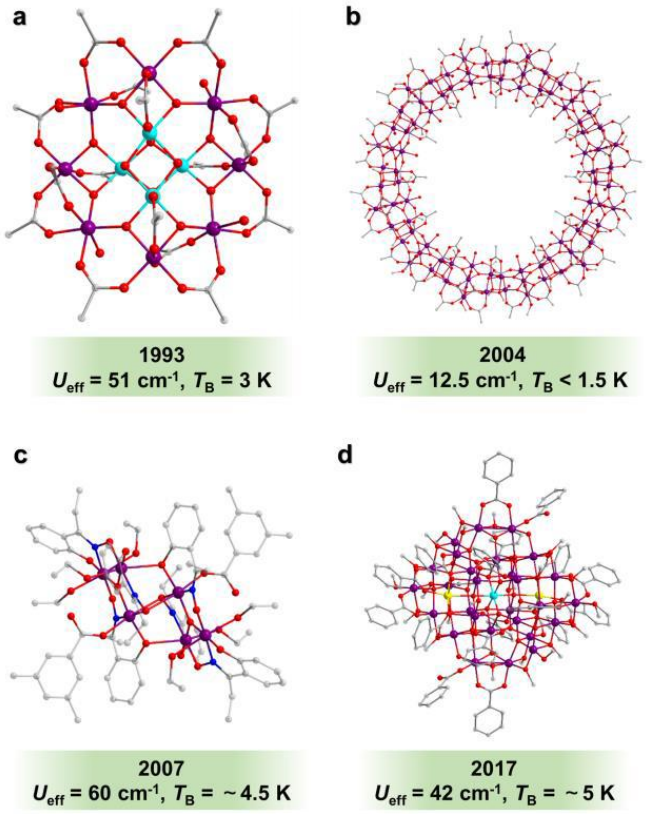

Figure 3.1.3 Molecular structures of Mn_{12} (a), Mn_{84} (b), Mn_6 (c), and Fe_8 (d), and their corresponding values of blocking temperature of magnetization T_B and anisotropy barrier U^{eff}. Reproduced from ref. [82]

With the beginning of the new century, the scientific interest had already expanded to lanthanide elements. Their magnetic properties are fundamentally different from those of transition metals, and maybe more suitable for application in the SMM field. Their big difference is the unquenched orbital momentum of the *4f*-orbitals which leads to effective spin-orbit coupling and in principle stronger intrinsic magnetic anisotropies. The first approach was the single-ion lanthanide SMMs (known as SIMs too). Here, the main challenge is the design of suitable ligand field environment to induce axial magnetic anisotropy and raise the effective barrier. In 2003, the discovery of slow

magnetic relaxation in a series of mononuclear phthalocyanine double-decker complexes $[LnPc_2]^-$ (Ln =Tb, Dy) was reported by Ishikawa and coworkers [83]. Remarkably, the Tb-complex exhibited the energy barrier of 230 cm^{-1}. After this great success, further studies followed leading to the energy barrier of 652 cm^{-1} [84], surpassing by one order of magnitude the respective barrier from Mn_{12}-ac molecule. The reason for such a high value is the axial magnetic anisotropy induced by the strong ligand field. In addition, the planar shape of phthalocyanine ligands make these double-decker SMMs suitable for surface deposition [85, 86] and favourable for application in spintronic devices [87, 88].

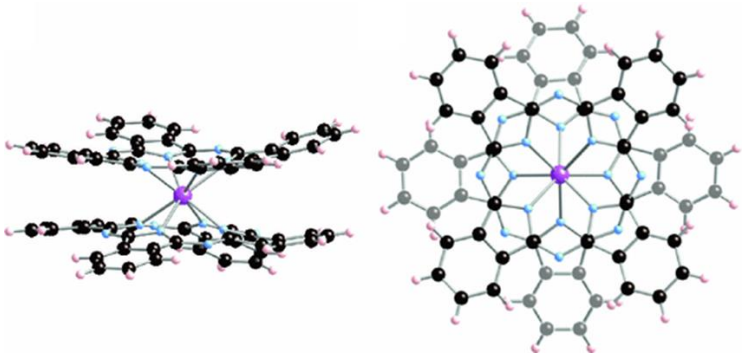

Figure 3.1.4 Side and top view of the mononuclear phthalocyanine double-decker complex $[TbPc_2]^-$. Color scheme: C (black), H (pink), N (light blue) and Tb (magenta). Reproduced from ref. [89]

Although the $[LnPc_2]^-$ molecules present large anisotropy, they suffer from fast relaxation in zero-field. The reason behind that, is the effective zero-field QTM which produces for all the SIMs the characteristic 'butterfly' shape in magnetization curves. This would be an obstacle if we consider application in magnetic-data storage devices. One approach to quench zero-field tunneling, is to combine *3d* and *4f* metals in the same molecule [90]. Several studies showed that zero-field QTM is suppressed by the induced *3d-4f* exchange interactions, like in $\{Co_2Dy_2\}$ [91], $\{Cr_8Dy_8\}$ [92] and $\{Tb_2Fe_3\}$ [93] SMMs.

A second strategy is the design of polynuclear *4f*- SMMs, with many of them and especially those with radical-bridged lanthanides exhibiting superior SMM performance. For non-radical-bridged systems, an interesting example is the trinuclear Dy^{3+}-complex reported by Luzon et al. in 2006 [94]. The Dy^{3+} ions lie on the vertices of a triangle at 120° one from each other axes, where the cancellation of the magnetic moments results in a nonmagnetic ground doublet, with a peculiar chiral nature. Another example is the $[Dy_4K_2O(OtBu)_{12}]$ complex [95], with large energy barrier (U^{eff}= 481 cm^{-1}) attributed to relaxation *via* the second excited Kramers doublet. The reason accounting for such behavior is the axial ligand field induced by the very short Dy-O bonds (≈2 *Å*). In a hypothetical $[DyO]^+$ (Dy-O=1.74 Å) complex, perfect magnetic axiality can be achieved, which might lead to extremely high U^{eff} values (> 3.000 cm^{-1}) and blocking temperature up to RT [96].

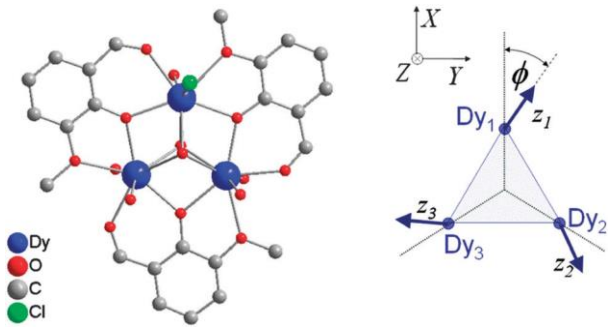

Figure 3.1.5 Molecular and spin structure of the Dy^{3+} triangular cluster $[Dy_3(\mu_3{-}OH)_2L_3Cl(H_2O)_5]Cl_3$. Reproduced from ref. [94]

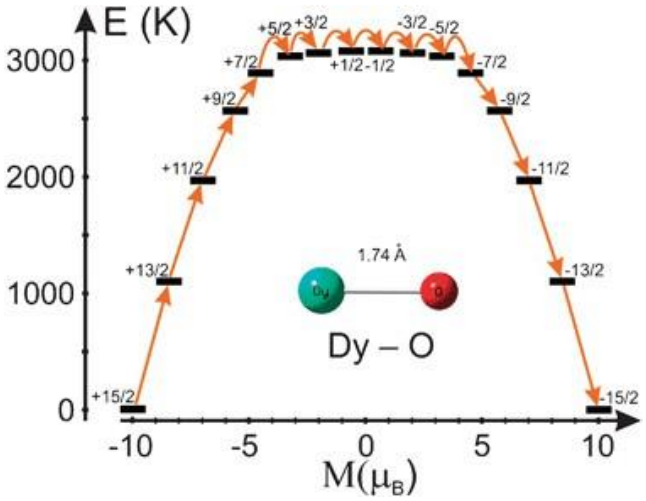

Figure 3.1.6 Energy barrier for reversal of magnetization in hypothetical $[DyO]^+$. Horizontal black lines are the energy levels and orange arrows show the path for the reversal of magnetization [96] with permission from The Royal Society of Chemistry.

Radical ligands between lanthanide ions seem to be of great importance, as their diffused orbitals penetrate the outer-shell electron clouds of Ln ions, which results in strong exchange coupling. Long and co-workers have reported several examples of radical bridged Ln-SMMs, with most famous the N_2^{3-} radical-bridged binuclear Ln-complexes. Particularly, Tb^{3+} with T_B= 14 K and U^{eff}=227 cm^{-1}, is the one which showed extremely broad hysteresis, that ranked it as the hardest molecular magnet at the time of discovery (2011) [97]. This unprecedented performance was attributed to the very strong exchange coupling provided via the N_2^{3-} radical.

In 2017, Mills et al. reported the Dysprosocenium-complex $[Dy(Cp^{ttt})_2]^+$, the first SMM to present open hysteresis up to 60 K, with U^{eff}=1.223 cm^{-1} [98]. The reason suggested for so good SMM performance is that the Cp^{ttt}-rings (fig 3.1.7) not only cause strong magnetic axiality to the Dy^{3+} ion, but also create constrained metal-ligand vibrational modes.

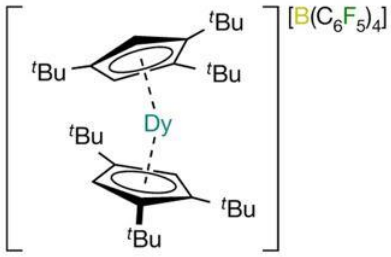

Figure 3.1.7 Molecular structure of Dysprosocenium-complex $[Dy(Cp^{ttt})_2]^+$, with selective atom labelling (B, yellow; C, grey; Dy, cyan; F, green). Reproduced from ref. [98]

In 2018, the goal of synthesizing a single-molecule magnet that can exhibit hysteresis over liquid-N_2 temperature (T_B >77 K) was achieved for first time. Layfield and co-workers [99] reported a new Dysprosocenium-complex with T_B=80 K, which remains up to date highest value ever recorded. The new molecule showed a higher energy barrier of 1541 cm^{-1}. The improved SMM behavior is mainly attributed to the stronger magnetic axiality originating from the shorter Dy-Cp distance.

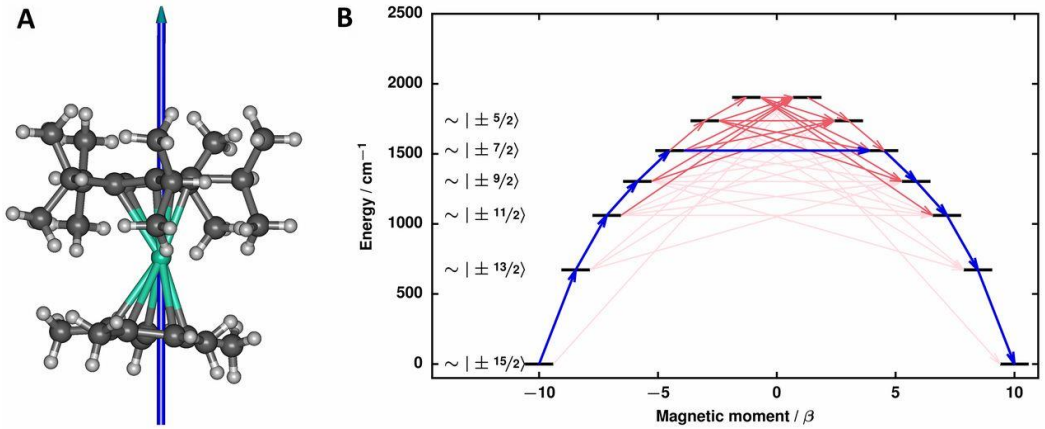

Figure 3.1.8 (a) The principal magnetic axis of the ground Kramers doublet. (b) Relaxation mechanism for Dy-5* cation. Blue arrows show the most probable relaxation route and red arrows show transitions between states with less probable but non-negligible matrix elements: darker shading indicates a higher probability. From ref. [99]. Reprinted with permission from AAAS.

Today, research in the field of single-molecule magnetism continues with great interest by the global scientific community. Among the numerous different types of SMMs, a promising one is the fullerene-based, where magnetic ions are encapsulated inside the vacant space of the carbon cage. The idea behind this strategy is that fullerene offers a safe environment for the stabilization of unique species that cannot be realized outside of it. Furthermore, considering the deposition of SMMs onto surfaces for devices, a common drawback is their chemical instability. However, carbon cage plays the role of the protector and preserving the magnetic properties.

3.2 Endohedral metallofullerenes as SMMs

A common drawback of the up-to-date SMMs is their chemical instability, a practical issue if we consider application in spin-devices. Endohedral metallofullerenes can overcome this obstacle because the carbon cage acts as a natural barrier against the external environment of the cluster. The first magnetic studies on EMFs were conducted for $Gd@C_{82}$ [100] and $La@C_{82}$ [101] in '94-'95. The synthesis and isolation of $Sc_3N@C_{80}$-I_h in 2001 [102], triggered further studies in tri-metallic nitride clusterfullerenes. In this category, the three metal ions are located on the vertices of a triangle with the nitride ion at the center of it (fig. 3.2.1), minimizing Coulomb repulsions. The cluster can donate up to six electrons and the C_{80} cage is the most suitable host as it needs six electrons to form a closed-shell electronic structure. Icosahedral symmetry (I_h) is proved to be the prevailing one.

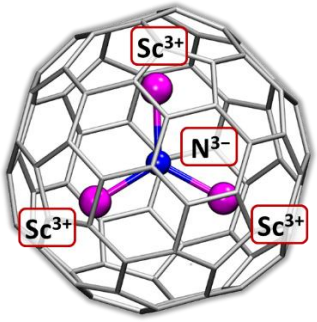

Figure 3.2.1 Molecular structure of $Sc_3N@C_{80}$-I_h. Reproduced with permission of Dr. A. Popov.

If we have lanthanide ions instead of transition metals inside the fullerene, the presence of the nitride anion in such short distance (ca 2 Å), induces very strong ligand field which results in large single-ion magnetic anisotropy. In case of Dy^{+3} ion, the magnetic anisotropy is axial with the magnetic moment aligned almost parallel to the Dy–N bond. Strong anisotropy results in large energy barriers of the thermally-activated Orbach process, the key factor for excellent SMM behavior. In 2012 was found that $DySc_2N@C_{80}$ exhibits slow relaxation of magnetization in a finite magnetic field of 0.2 T [103]. In zero field, magnetization of $DySc_2N@C_{80}$ relaxes fast via quantum tunnelling of magnetization (QTM), resulting in the characteristic butterfly shape of the magnetic hysteresis, typical for single-ion magnets. Further studies revealed single-molecule magnetism in other lanthanide-based EMFs including clusterfullerenes with nitride [40], sulphide [104], carbide [105] [106] and cyanide units [67, 107].

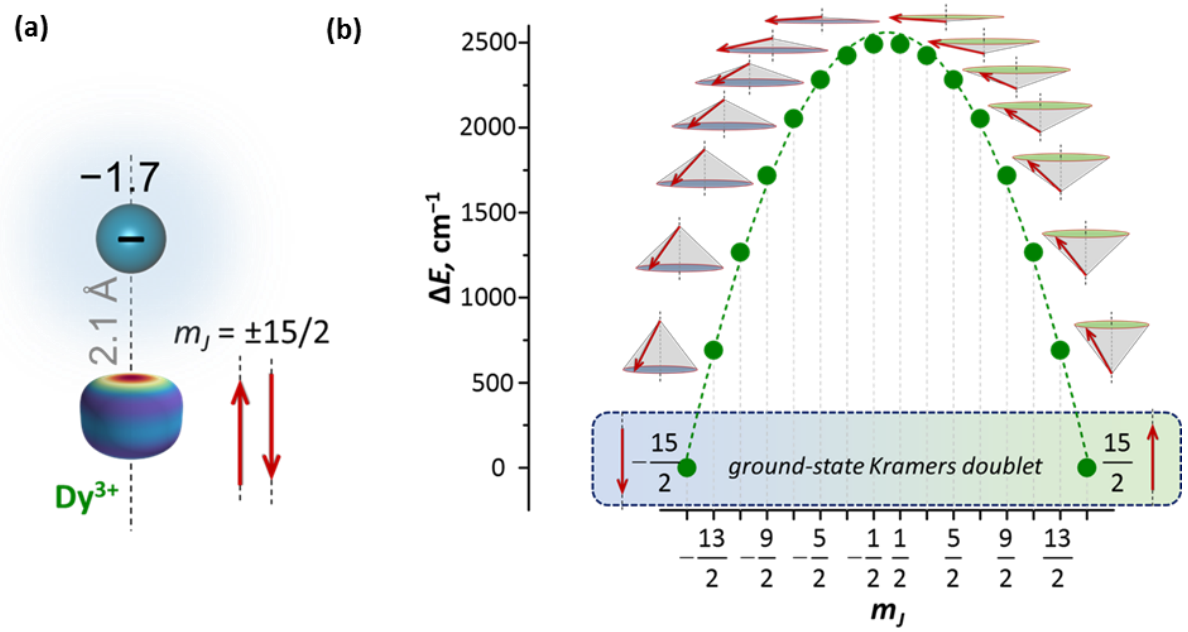

Figure 3.2.2 (a) *4f*-electron density flattened shape (m_J = ±15/2) of Dy^{3+} ion under the influence of a large negative charge in close distance; (b) Visualization of the eight Dy^{3+} Kramers doublets (m_J: ±15/2, ±13/2 … ±1/2). Red arrow represents the Dy magnetic moment and orientation is different for each state. Coulomb interactions between *4f*-electrons and the large negative charge of the nitride ion. Reproduced with permission of Dr. A. Popov.

For that reason, $Dy_xSc_{3-x}N@C_{80}$ family of magnetic molecules was among the first to be studied by our group, with $DySc_2N@C_{80}$ [108] and $Dy_2ScN@C_{80}$ [68], exhibiting clear SMM behavior at low temperatures. Moreover, they presented great divergence in their magnetic properties which derives from the different number of Dy ions [109].

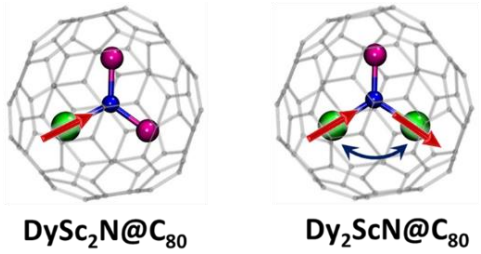

Figure 3.2.3 Molecular structures of $DySc_2N@C_{80}$ and $Dy_2ScN@C_{80}$ (green: Dy^{3+} ion, magenta: Sc^{3+} ion, blue: N^{3+} ion). Reproduced with permission of Dr. A. Popov.

3.3 $DySc_2N@C_{80}$ and $Dy_2ScN@C_{80}$

$DySc_2N@C_{80}$ was the first EMF to show long relaxation times [103], as evidenced by the detection of low-temperature hysteresis (fig. 3.3.1). Magnetization curves correspond to the powder form of the sample, drop-casted from CS_2 solution on a quartz holder. Each molecule and cluster have a random orientation frozen below some temperature, so every Dy ion 'feels' a magnetic field equal to the projection of the external field onto the direction of the anisotropy axis. With the standard field sweep rate of approximately 2.9 mT/s, hysteresis appears up to 7 K. The abrupt fall of magnetization near zero magnetic field derives from the fast quantum tunneling process, leading to the characteristic "butterfly" (or "waist-restricted") shape [108]. Zero-field tunneling is very common in single-ion molecular magnets.

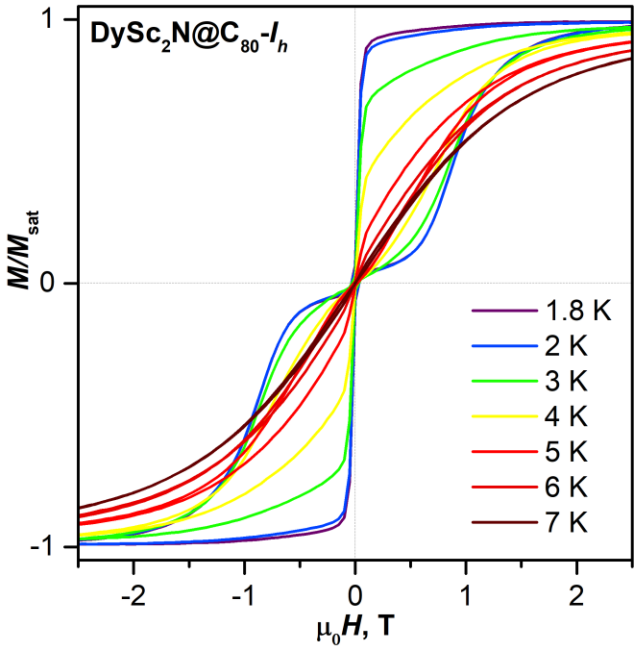

Figure 3.3.1. Magnetization curves of $DySc_2N@C_{80}$ measured at different temperatures between 1.8 and 7 K (sweep rate: 2.9 mT/s K). Reproduced from ref. [108]

Encapsulation of two Dy ions forming the $Dy_2ScN@C_{80}$ clusterfullerene changes the situation completely [110]. Magnetic behavior is very different from its mono-dysprosium counterpart, as manifested by the experimental hysteresis curves [68].

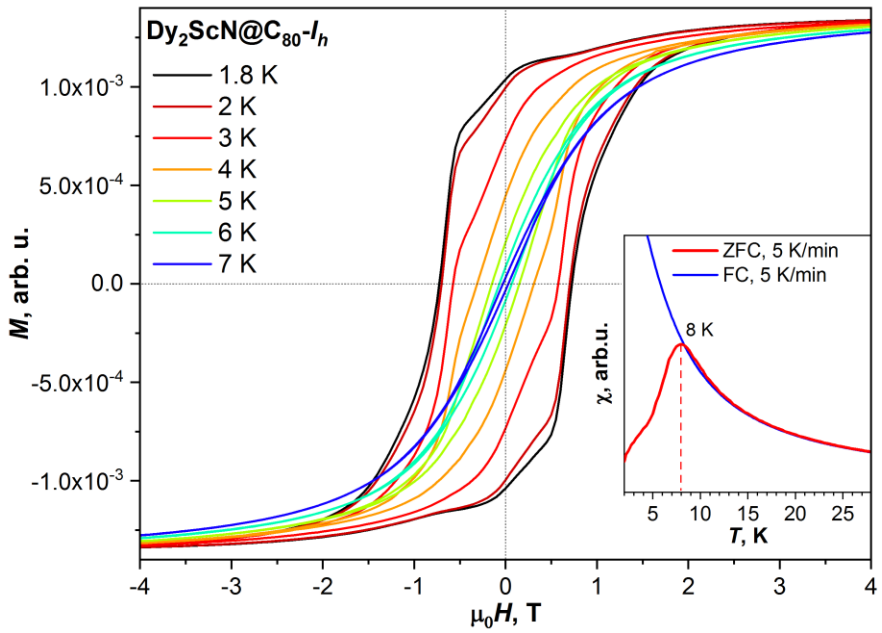

Figure 3.3.2 Magnetization curves of $Dy_2ScN@C_{80}$ measured from 1.8 to 7 K (2.9 mT/s sweep rate). The inset shows the blocking temperature of magnetization (T_B) as the peak in the temperature dependence of χ_{ZFC} curve, for the rate of 5 K/min. Reproduced from ref. [68]

Closing hysteresis temperature (7-8 K) is approximately the same with $DySc_2N@C_{80}$ (6 -7 K) and agrees well with the measured blocking temperature of magnetization with 5K/min sweep rate (fig. 3.3.2 inset). However, the shape of hysteresis curves is completely different from those of $DySc_2N@C_{80}$. Intramolecular exchange and dipolar interactions between the Dy ions suppress the single-ion zero-field tunneling by giving rise to a new ground state, which corresponds to either 'ferromagnetic' (FM) or 'antiferromagnetic' (AFM) coupling of Dy magnetic moments (fig. 3.3.3). In analogy with bulk materials, we name FM coupling the orientation of the magnetic moments which leads to the higher total moment while antiferromagnetic (AFM) to the lower.

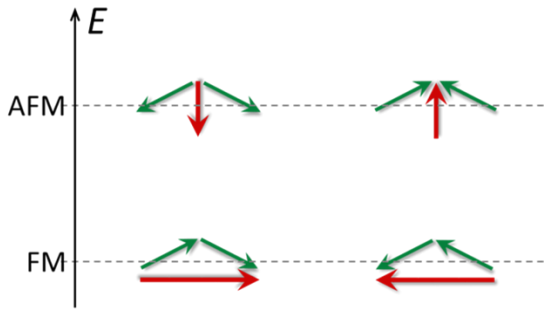

Figure 3.3.3 FM/AFM energy splitting of the ground state for a non-collinear two-lanthanide system. Green arrows are the magnetic moments of individual lanthanide ions and red arrows are total magnetic moments of the dinuclear system.

Chapter 4

Magnetic studies on lanthanide dimetallofullerenes

Metal-metal bonding is a well-known phenomenon in the chemistry of transition metals [111] but not for lanthanides as they rarely participate in Ln-Ln bonding in molecular compounds. Up to date, stabilization of lanthanide dimers has been realized only inside fullerenes as the carbon cage acts against the strong repulsive forces between the positive metal ions. In addition, such Ln-Ln interactions can create the unique situation where a localized unpaired electron becomes the connecting link between the two ions resulting in unconventional valence states [112]. The term single electron Ln-Ln bond refers to the situation where the lanthanide di-metallofullerene (di-EMF) features a single-occupied Ln-Ln bonding molecular orbital (MO).

The first lanthanide di-EMFs with single-electron Ln-Ln bonds were the azafullerenes $Ln_2@C_{79}N$ (Ln: Y, Tb, Gd), which were discovered in 2008 [113, 114]. DFT studies showed that single-electron Ln-Ln bond can exist in other di-EMFs too [115, 116]. Stable $La_2@C_{80}$ mono-adducts with single-electron Ln-Ln bond were obtained in 2015 and 2016 [117, 118]. Giant exchange coupling and promising SMM properties were predicted for $Ln_2@C_{79}N$ (Ln: Y, Gd, Dy) in 2015 [119, 120]. These very interesting preliminary results were the starting point for our group to explore further the lanthanide di-EMF systems, with first the $Dy_2@C_{80}(CH_2Ph)$ molecule (2017) [67]. Magnetic studies performed by Dr. Krylov, revealed superior SMM behavior, with T_B =21.9 K and U^{eff} =613 K.

This great success gave us the motivation to continue studying more $Ln_2@C_{80}(CH_2Ph)$ molecules with different encapsulated lanthanide dimers (Gd_2, Tb_2, TbY, Ho_2 and Er_2) between 2017–2019 [121], in the framework of my PhD thesis. The $Ln_2@C_{80}(CH_2Ph)$ compounds were synthesized in our lab by Dr. Liu, except from $Gd_2@C_{80}(CH_2Ph)$ synthesized by Dr. Spree. We also studied the magnetic performance of two azafullerene molecules, the $Gd_2@C_{79}N$ [122] and $Tb_2@C_{79}N$ [123], provided by Prof. H. C. Dorn*. All samples were characterized in their pristine powder form via

DC/AC SQUID magnetometry. The measurements were performed in IFW using VSM-MPMS 3, XL-MPMS and PPMS devices, under the supervision of Dr. Wolter-Giraud and technical support from S. Gaß and K. Nenkov.

The structure of this chapter is the following: Firstly, we explain the bonding situation between two lanthanides inside a fullerene, and how the single-electron Ln-Ln bond is realized (§ 4.1-4.2). Then, we introduce the spin Hamiltonian that we use to simulate and interpret the magnetic properties of our lanthanide di-EMF systems (§ 4.3). Detailed analysis of the experimental results is presented in sections § 4.4-4.9.

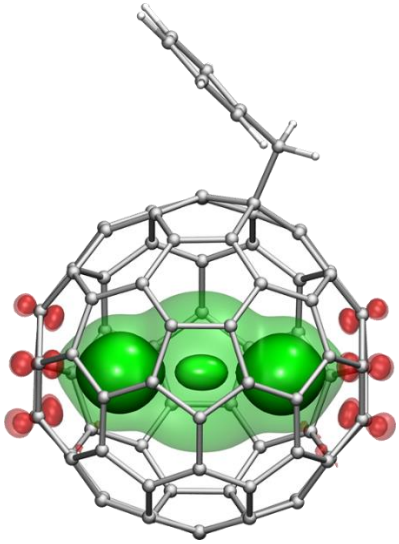

Figure 4.1 Molecular structure of an example $Ln_2@C_{80}(CH_2Ph)$ system. Green color represents the spin density distribution, with three well-seen maxima corresponding to the Ln *4f*-electrons and the unpaired electron spin residing on the Ln-Ln bonding orbital; Carbon atoms p-orbitals are illustrated with red color.

* Department of Chemistry, Virginia Polytechnic Institute and State University, Blacksburg, Virginia 24061, United States

4.1 Valence state of lanthanides in dimetallofullerenes

In lanthanide mono-metallofullerenes ($Ln@C_{2n}$), oxidation state of lanthanide ions is trivalent except from Sm, Eu, Tm, and Yb, which are divalent. Deviation origins from the third ionization potential (IP_3) of lanthanide atoms (fig. 4.1.1). The metals with IP_3>23 eV (Sm, Eu, Tm, and Yb) donate two electrons to the fullerene cage, whilst the rest with IP_3<23 eV donate three.

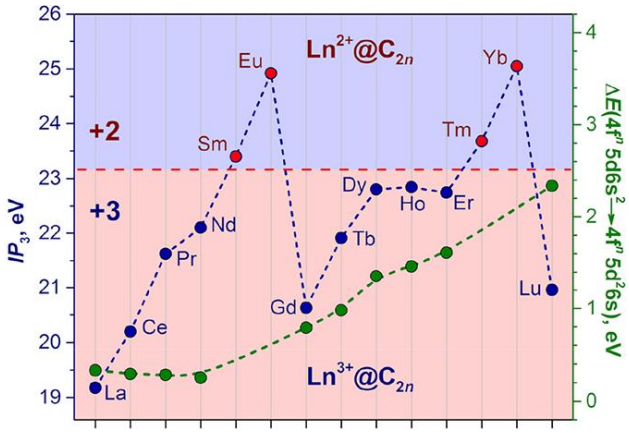

Figure 4.1.1 Third ionization potential (IP_3, blue dots) and energy of the $4f^n5d^16s^2 \rightarrow 4f^n5d^26s^1$ excitations (green dots) of lanthanides. The red dashed horizontal line marks the border between divalent and trivalent lanthanides in mono-metallofullerenes. Reproduced from ref. [121]. IP values were taken from *www.nist.gov*

The situation in lanthanide di-metallofullerenes is different from their mono-counterparts and cannot be explained with the concept of IP_3 threshold. For early lanthanides such as La and Ce (fig. 4.1.2), the 3+ oxidation state agrees with the abundancy of their di-EMF structure, $La_2@C_{80}$ and $Ce_2@C_{80}$, because the C_{80} cage has enhanced stability in the 6- oxidation state. However, for lanthanides in the end of the row, such as Lu and Er (fig. 4.1.2), typical host is the C_{82} cage with charge state 4-, implying 2+ oxidation state for each ion. The difference between La/Ce and Er/Lu is rooted to the MO structure of the Ln_2 dimers (fig. 4.1.3).

For La_2, the most suitable host is the C_{80} cage, because it needs six electrons to fill the unstable threefold-degenerate LUMO and form a closed-shell electronic structure. MO levels of La_2 are considerably higher in energy than the LUMO of C_{80}-I_h (fig. 4.1.3), so that six valence electrons of $(6s)\sigma_g^2(5d)\pi_u^4$ configuration are transferred to the cage. In contrast, the orbitals of Lu_2 with configuration $(6s)\sigma_g^2(6s)\sigma_u^2(5d)\pi_u^2$ are spread into a broader energy range of La_2 and the $(6s)\sigma_g^2$ level has lower energy than the LUMO of C_{80} (fig. 4.1.3). As a result, the Lu_2 dimer cannot transfer six electrons in $Lu_2@C_{80}$ and the C_{82} cage with two low-energy unoccupied MOs appears as more suitable host, as it is stabilized by the addition of four electrons. In $Lu_2@C_{82}$ four electrons from the $(6s)\sigma_u^2(5d)\pi_u^2$ levels of Lu_2 are transferred to the fullerene (fig. 4.1.3).

For lanthanides in the middle of the periodic row, the energy of the $(6s)\sigma_g^2$ MO in Ln_2 dimer is not low enough to stabilize the Ln^{2+} state, but also not high enough to ensure transfer of six electrons. Therefore, these lanthanides cannot produce di-EMFs with a closed-shell electronic structure. This seemingly simple conclusion was formulated in 2014 in a computational study of $Y_2@C_{80}$-I_h by Shinohara et al. [116] which showed that $Y_2@C_{80}$-I_h is a triplet with one electron populating the Y−Y bonding orbital and then formal charge distribution $(Y^{2.5+})_2@C_{80}^{5-}$. With one electron occupying the $(6s)\sigma_g^2$ Ln−Ln bonding orbital, such di-EMFs feature a single-electron Ln−Ln bond.

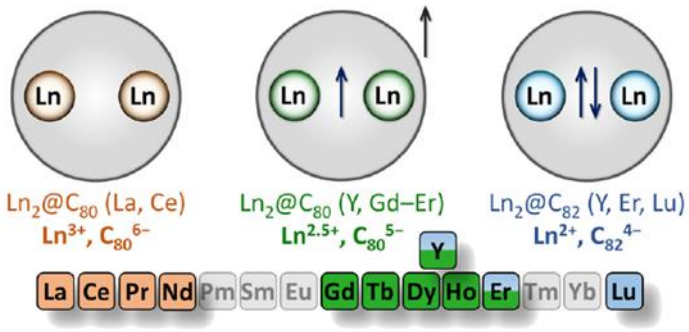

Figure 4.1.2 Oxidation states in lanthanide di-EMFs: Dimers of early lanthanides (light brown) transfer six electrons to the fullerene, leading to Ln^{3+} state and the Ln−Ln bonding. Dimers of lanthanides at the end of the *4f*-row (light blue) transfer only four electrons to the fullerene and keep the Ln−Ln bond in di-EMFs with 2+ state for the Ln ion. Finally, dimers of lanthanides in the middle of the row (light green) transfer five electrons to the hosting fullerene and form di-EMFs with a single-electron Ln−Ln bond and an oxidation state of $Ln^{2.5+}$. Reproduced from ref. [121].

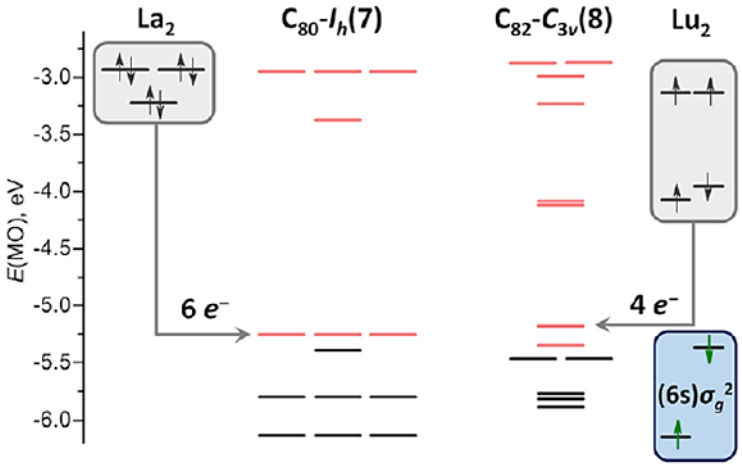

Figure 4.1.3 MO energy levels in C_{80}-I_h and C_{82}-C_{3v} carbon cages (black: occupied MOs; pink: vacant MOs) as well as in La_2 and Lu_2 dimers. Arrows show the electron transfer from La_2 and Lu_2 frontier orbitals to the LUMO of C_{80}-I_h of C_{82}-C_{3v} cages resp. Reproduced from ref [112]

4.2 Stabilization of single-electron Ln-Ln bond in dimetallofullerenes

Depending on the nature of the frontier orbitals in $Ln_2@C_{80}$, different strategies are employed to stabilize a single-electron Ln-Ln bond. In $(Ln^{3+})_2@C_{80}^{6-}$ formed by early lanthanides, reaction with benzyl bromide ($BrCH_2Ph$) under UV irradiation gives the non-charged benzyl monoadduct $Ln_2@C_{80}(CH_2Ph)$ (fig. 4.2.1). The unpaired electron produced by the attachment of the benzyl radical on the fullerene surface, is transferred to the Ln-Ln bonding orbital and yields a single-electron bond [118]. For $(Ln^{2.5+})_2@C_{80}^{5-}$ formed by the lanthanides in the middle of the *4f*-row (Gd, Tb, Ho, Er), the single-electron Ln-Ln bond is already present, but the fullerene has one unpaired electron which results in high reactivity and polymerization making them insoluble in CS_2 or aromatic solvents [124]. Addition of one electron leads to the radical anion $(Ln^{2.5+})_2@C_{2n}^{6-}$ (fig. 4.2.1), which can be extracted by dimethylformamide (DMF) [125]. After extraction, reaction with benzyl bromide yields the stable form of $Ln_2@C_{80}(CH_2Ph)$ monoadduct. Single-crystal X-ray diffraction study on $Dy_2@C_{80}(CH_2Ph)$ revealed selective addition of the benzyl group onto the pentagon/hexagon/hexagon ([5,6,6]) junctions (fig. 4.2.2) [67]. Alternatively, the single-electron Ln-Ln bond in $(Ln^{2.5+})_2@C_{80}^{5-}$, can be stabilized by the substitution of one carbon atom with a nitrogen, since $C_{79}N^{5-}$ is isoelectronic with C_{80}^{6-} cage. Then, the new form is called azafullerene $(Ln^{2.5+})_2@C_{79}N^{5-}$ and can be obtained by arc-discharge synthesis in the presence of nitrogen gas [113, 114]. Single-crystal X-ray diffraction studies on $Tb_2@C_{79}N$ and $Gd_2@C_{79}N$, co-crystallized with Ni(OEP) (fig. 4.2.2) [113], proved that their fullerene cages are based on C_{80}-I_h symmetry, but the exact position of the nitrogen atom cannot be determined. DFT computations showed that substitution of a [5,6,6] C atom in C_{80} cage by a N atom gives the most stable $Ln_2@C_{79}N$ structures [123].

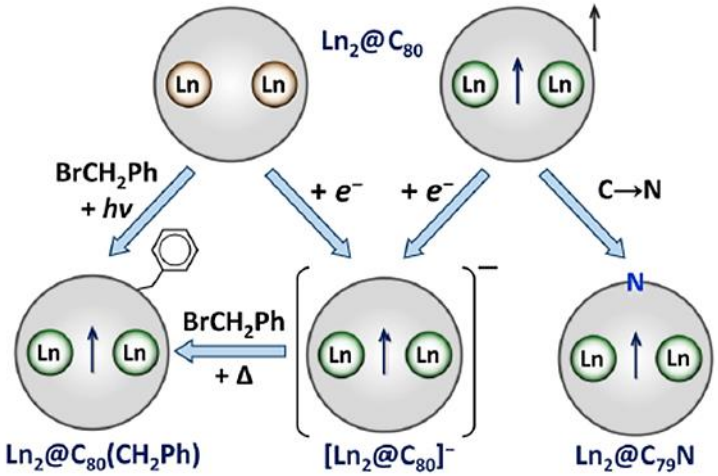

Figure 4.2.1 Stabilization of $Ln_2@C_{80}$ (light brown and light green for early and middle lanthanides resp.) with single-electron Ln-Ln bond in the form of $Ln_2@C_{80}(CH_2Ph)$, $[Ln_2@C_{80}]^-$ and $Ln_2@C_{79}N$.

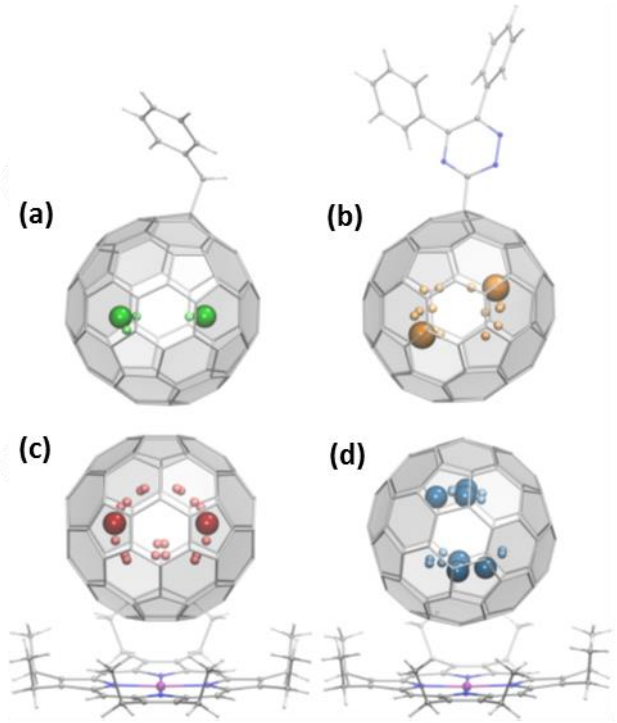

Figure 4.2.2 Molecular structures of di-EMFs with single-electron Ln-Ln bond from single-crystal X-ray diffraction: (a) $Dy_2@C_{80}(CH_2Ph)$ (green), (b) $La_2@C_{80}(C_3N_3Ph_2)$ (light brown), (c) $Tb_2@C_{79}N{\cdot}Ni(OEP)$ (red) and (d) $Gd_2@C_{79}N{\cdot}Ni(OEP)$ (blue). Large colored spheres show the Ln sites with the highest occupancies.

Despite the 2.5+ oxidation state of the lanthanide ions, both $Ln_2@C_{80}(CH_2Ph)$ and $Ln_2@C_{79}N$ compounds are air-stable, something that is not typical for compounds with lanthanides in unconventional oxidation states. Thus, the fullerene cage provides sufficient protection to the $(Ln^{2.5+})_2$ species with a single-electron Ln-Ln bond. Another important aspect, is the spatial confinement of Ln_2 dimers. Coulomb repulsion between lanthanide ions in di-EMFs is much stronger than the stabilization energy of the bonding interactions. Therefore, Ln ions tend to maximize the Ln-Ln distance, but since the extent of the Ln_2 dimer is limited by the fullerene, metal ions remain at distances allowing bond formation.

The most important benefit from the single-electron bond is on the magnetic properties of the system. Usually, exchange coupling in polynuclear lanthanide compounds is very weak because of the core nature of *4f*-electrons. However, when interactions between Ln centers are mediated by a radical bridge and ultimately, a single unpaired electron, the strength of the exchange coupling is increased dramatically. As a result, at low temperatures, the $[Ln^{3+}\text{-e-}Ln^{3+}]$ fragment behaves as a single giant spin.

4.3 Spin Hamiltonian for Ln^{3+}-e-Ln^{3+} systems

In this section, we introduce the spin Hamiltonian for lanthanide dimetallofullerenes, featuring single-electron Ln-Ln bond, that will be used extensively for the experimental data modeling and interpretation in this work. A complete description of the energy spectrum of two magnetically coupled lanthanide ions would require all the Hamiltonian terms included in eq. 1.6.1. However, in very good approximation, it is enough to define a simplified spin Hamiltonian to describe the magnetic properties of our systems in easier way. This Hamiltonian includes the single-ion ligand field terms $\widehat{H}_{\mathrm{Ln}}$, the magnetic interaction (exchange and dipolar) terms between the two ions $\widehat{H}_{\mathrm{Ln,Ln}}$ and between each ion and the unpaired electron $\widehat{H}_{\mathrm{Ln,e}}$, and finally the Zeeman term $\widehat{H}_{\mathrm{ZEE}}$:

$$\widehat{H}_{\mathrm{spin}} = \widehat{H}_{\mathrm{Ln}_1} + \widehat{H}_{\mathrm{Ln}_2} + \widehat{H}_{\mathrm{Ln}_1,\mathrm{Ln}_2} + \widehat{H}_{\mathrm{Ln}_1,e} + \widehat{H}_{\mathrm{Ln}_2,e} + \widehat{H}_{\mathrm{ZEE}} \qquad (4.3.1)$$

The single-ion LF parameters used further in this work, are computed by Dr. Avdoshenko (IFW Dresden) with the following method. First, the molecular structures are optimized at the PBE-D level using PAW pseudopotentials with standard recommended cutoffs [126]. The *4f*-shells of lanthanides do not contribute to chemical bonding, and therefore the *4f*-shells are included in the core potential (open-core approximation). This procedure is expected to provide realistic results for structures involving Ln ions. The pseudopotential configuration $5p^6 6s^2 5d^1$ was used for all the Ln ions. After DFT-optimization, the ab initio energies and wave-functions of LF multiplets are computed at the CASSCF/RASSI-SO level for each Ln center in the model of $\{LnY\}^-$ system. Substitution of one Ln ion with one Y is necessary to make calculations tractable because calculations for two Ln ions treated simultaneously is very "expensive" and cannot be performed at this moment for most of the lanthanides. Also, the use of $\{LnY\}^-$ anions instead of neutral {LnY} molecule, allows one to limit active space only to the *4f*-shell. Calculations for the neutral {LnY} molecule would require inclusion of the unpaired valence electron and corresponding valence orbital into the active space, which makes ab initio calculations less tractable. Besides, the crystal field parameters extracted from such calculations would then lose their clear physical meaning.
Regarding the magnetic interactions for anisotropic lanthanides, it is possible to calculate ab initio only the dipolar interactions (based on the DFT-optimized structures) and not the exchange term. For that reason, we select to include both exchange and dipolar interactions in a single term described by the equation:

$$\widehat{H}_{\mathrm{Ln}_1,\mathrm{Ln}_2} = -2j_{\mathrm{Ln}_1,\mathrm{Ln}_2}\left(\hat{J}_{\mathrm{Ln}_1} \cdot \hat{J}_{\mathrm{Ln}_2}\right) \qquad (4.3.2)$$

where the lanthanide moments $\hat{J}_{\mathrm{Ln}_i}$ are treated in full $|J, m_J\rangle$ basis. Magnetic interactions are in principle anisotropic, but in our calculations we assume they are isotropic (which is a reasonable approximation for easy-axis anisotropic systems, i.e. Ising spins), with coupling constant equal to the sum of the exchange and dipolar constants values: $j_{12} = j_{ex} + j_{dip}$. By definition, the sign of the exchange coupling constant is positive (j_{ex}>0) for ferromagnetic (FM) coupling and negative

(j_{ex}<0) for antiferromagnetic (AFM). By substituting the eq. 4.3.2 in eq. 4.3.1 for Ln-Ln and Ln-e interactions, and omitting the Zeeman term for simplicity, the spin Hamiltonian becomes:

$$\widehat{H}_{\mathrm{spin}} = \widehat{H}_{\mathrm{Ln}_1} + \widehat{H}_{\mathrm{Ln}_2} - 2j_{\mathrm{Ln}_1,\mathrm{Ln}_2}\left(\hat{J}_{\mathrm{Ln}_1} \cdot \hat{J}_{\mathrm{Ln}_2}\right) - 2j_{\mathrm{Ln}_1,\mathrm{e}}\left(\hat{J}_{\mathrm{Ln}_1} \cdot \hat{s}_{\mathrm{e}}\right) - 2j_{\mathrm{Ln}_2,\mathrm{e}}\left(\hat{J}_{\mathrm{Ln}_2} \cdot \hat{s}_{\mathrm{e}}\right) \quad (4.3.3)$$

The equation applies in the situation of two different lanthanides ions inside a molecule, hence two different $\hat{J}_{\mathrm{Ln,e}}$ coupling constants. For homo-metallic systems, the small difference between $j_{\mathrm{Ln}_1,\mathrm{e}}$ and $j_{\mathrm{Ln}_2,\mathrm{e}}$ values can be ignored in first approximation, and the eq. 4.3.3 is further simplified into:

$$\widehat{H}_{\mathrm{spin}} = \widehat{H}_{\mathrm{Ln}_1} + \widehat{H}_{\mathrm{Ln}_2} - 2j_{\mathrm{Ln,Ln}}\left(\hat{J}_{\mathrm{Ln}_1} \cdot \hat{J}_{\mathrm{Ln}_2}\right) - 2j_{\mathrm{Ln,e}}\hat{s}_{\mathrm{e}}\left(\hat{J}_{\mathrm{Ln}_1} + \hat{J}_{\mathrm{Ln}_2}\right) \quad (4.3.4)$$

Besides the assumptions, the effective spin Hamiltonians of eq. 4.3.3 and eq. 4.3.4 describe very well the experimental magnetic data and allow through simulation/fitting the determination of the exchange coupling constant. In our studies, we do not consider the possible intermolecular exchange and dipolar interactions because we assume we have an isolated molecule.
Further simplification of the spin Hamiltonian is based on the fact that Ln-e exchange interactions are much stronger than the direct Ln-Ln coupling (for Ln≡Gd, this also follows from computational studies discussed below). This allows to remove the term describing Ln-Ln interaction and replace $j_{\mathrm{Ln,e}}$ with the effective constant $j_{\mathrm{Ln,e}}^{eff}$:

$$\widehat{H}_{\mathrm{spin}} = \widehat{H}_{\mathrm{Ln}_1} + \widehat{H}_{\mathrm{Ln}_2} - 2j_{\mathrm{Ln,e}}^{eff}\hat{s}_{\mathrm{e}}\left(\hat{J}_{\mathrm{Ln}_1} + \hat{J}_{\mathrm{Ln}_2}\right) \quad (4.3.5)$$

The Hamiltonian of eq. 4.3.5 is used for the simulation and interpretation of the experimental data, presented in the next sections of this chapter. The single-ion ligand field parameters ($\widehat{H}_{Ln}$) were obtained from ab initio calculations by Dr. Avdoshenko, and the exchange constant $j_{\mathrm{Ln},e}^{\mathrm{eff}}$ is the only unknown parameter, considered as isotropic. Although the description of $j_{\mathrm{Ln},e}^{\mathrm{eff}}$ constant as isotropic is an oversimplification, for the Ising-type ground state with collinear spins, this approximation is essentially valid for the lower part of the energy spectrum. To determine the $j_{\mathrm{Ln},e}^{\mathrm{eff}}$ coupling constant and evaluate its reliability, we used the following strategy: *χT-T* curves were measured for a given {Ln_2} compound at different constant magnetic fields. The value of $j_{\mathrm{Ln},e}^{\mathrm{eff}}$ was varied to find the best fit to the experimental data for one particular field value (1 T usually). This value was then used to calculate *χT-T* curves measured in other magnetic fields too (0.5, 3, 5, and 7 T), as well as to calculate magnetization curves at different temperatures. All simulations are done with PHI code [127]. The agreement of the model and experiment is considered to be good when the $j_{\mathrm{Ln},e}^{\mathrm{eff}}$ value gives good agreement for the whole set of experimental data.

4.4 $Gd_2@C_{80}(CH_2Ph)$ and $Gd_2@C_{79}N$

It is reasonable to start the presentation of our results on $\{Ln_2\}$ systems with $\{Gd_2\}$, because it allows the analysis of intra-molecular exchange interactions without the influence of single-ion anisotropies (Gd^{3+}: L=0, S=7/2). The purpose of this study was to understand and compare the magnetic properties of $\{Gd_2\}$ system in the mono-adduct $Gd_2@C_{80}(CH_2Ph)$ and the azafullerene $Gd_2@C_{79}N$.

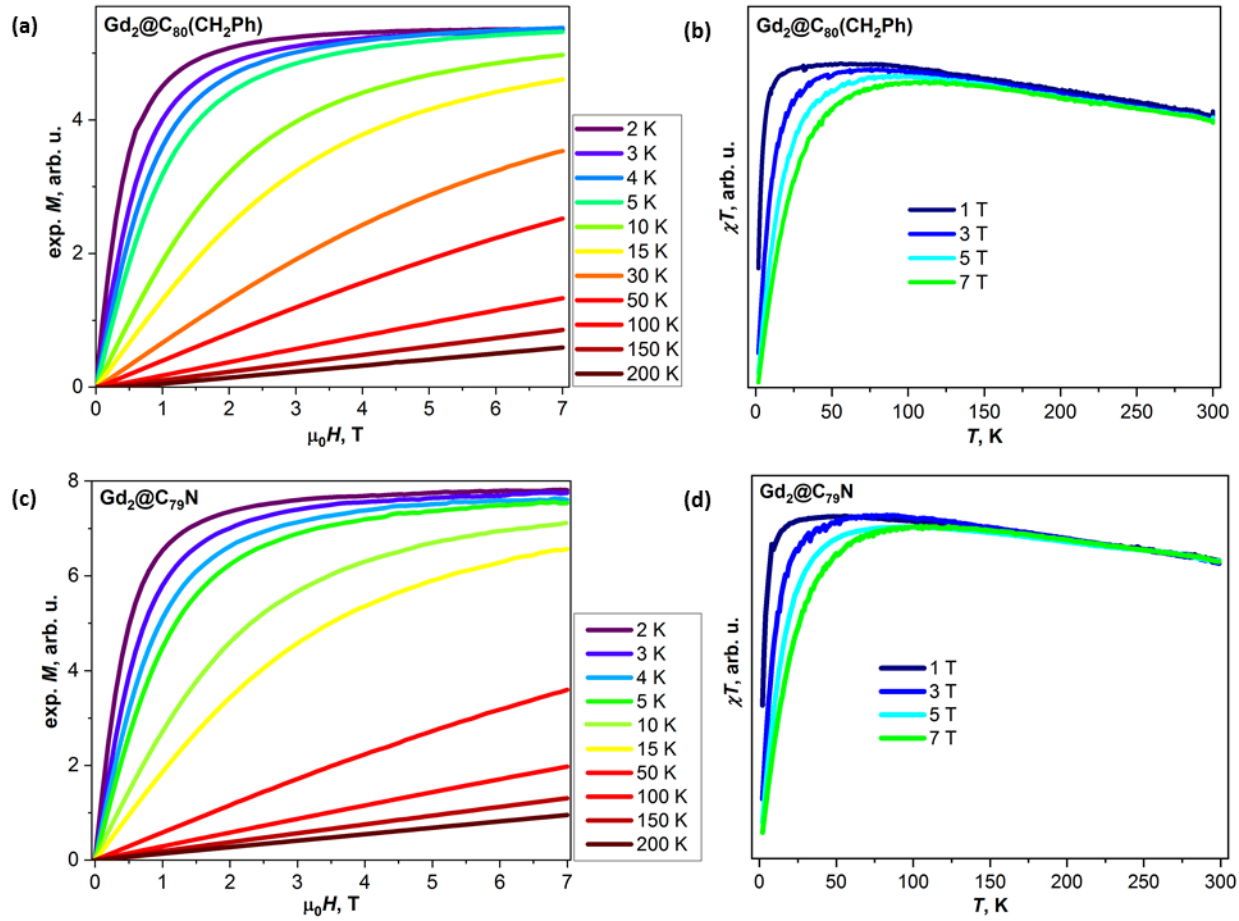

Figure 4.4.1 Experimental *M-H* and *χT-T* curves of (a-b) $Gd_2@C_{80}(CH_2Ph)$ and (c-d) $Gd_2@C_{79}N$.

Magnetization curves show no hysteresis down to 1.8 K. Thus, $\{Gd_2\}$ is not a strong SMM, which is not surprising since Gd ion is magnetically isotropic. For the two types of molecules, *M-H and χT-T* curves look almost identical. At high temperatures, *χT* values coincide independently of the applied field, and a gradual linear increase takes place with temperature decrease. Below ca 150 K, deviation between the *χT* curves measured in different fields starts, indicating that at lower temperatures the magnitude of Zeeman splitting affects the population of spin states.

The EPR studies on $Gd_2@C_{80}(CH_2Ph)$ performed by Dr. M. Zalibera (Bratislava) and M. Rosenkranz (IFW Dresden) revealed a ground state with the giant spin of S = 15/2, which points out clearly the ferromagnetic coupling between all the spins in Gd^{3+} (7/2)-e (1/2)-Gd^{3+} (7/2) system. At room

temperature and in toluene solution, {Gd_2} shows a single EPR line with g-factor of 1.987. Freezing the solution down to 100 K, results in a complex multiline structure in the X-band (9.4 GHz) EPR spectrum (fig. 4.4.2). The Q-band (34 GHz) spectrum of {Gd_2} measured under similar conditions has a simpler but still complex pattern. The low-temperature structure in the EPR spectra is an evidence of zero-field interactions in the large-spin ground state. The spin Hamiltonian of such a system can be written as:

$$\hat{H}_{spin} = D\left(\hat{S}_z^2 - \frac{1}{3}S(S+1)\right) + \frac{1}{2}E\left(\hat{S}_+^2 + \hat{S}_-^2\right) + g_{\mathrm{iso}}\mu_{\mathrm{B}}\boldsymbol{B}\hat{S} \qquad (4.4.1)$$

The first two terms describe the second-order zero-field splitting (ZFS) of rhombic symmetry, and the last term represents the Zeeman effect. The X- and Q-band EPR spectra of {Gd_2} in a frozen solution can be well reproduced by the parameters D = 1.00(2) GHz, E = 0.22(4) GHz, and g_{iso} = 1.987. The ZFS tensor of {Gd_2} is found to be similar to that of the previously reported $Gd_2@C_{79}N$ (D = 0.96(6) GHz, E = 0.14(1) GHz, g_{iso} = 1.99) [128] but shows somewhat larger rhombicity (i.e. larger E parameter), which is in line with the asymmetric geometry of {Gd_2} induced by the exohedral CH_2Ph group.

A schematic description of the Zeeman splitting of the 16 energy levels of the weakly anisotropic S = 15/2 system in {Gd_2} together with the transitions accessible in the X- and Q-band EPR spectra are shown in fig. 4.4.2. Our EPR studies on $Gd_2@C_{80}(CH_2Ph)$ agree with the results from previous EPR studies on $Gd_2@C_{79}N$ by Dorn et al. (2008) [113] and Gao et al. [128]. The fact that low-T EPR spectra are well descried by the spin S = 15/2 model indicate that magnetic moments of Gd ions and that of unpaired electron are coupled ferro-magnetically.

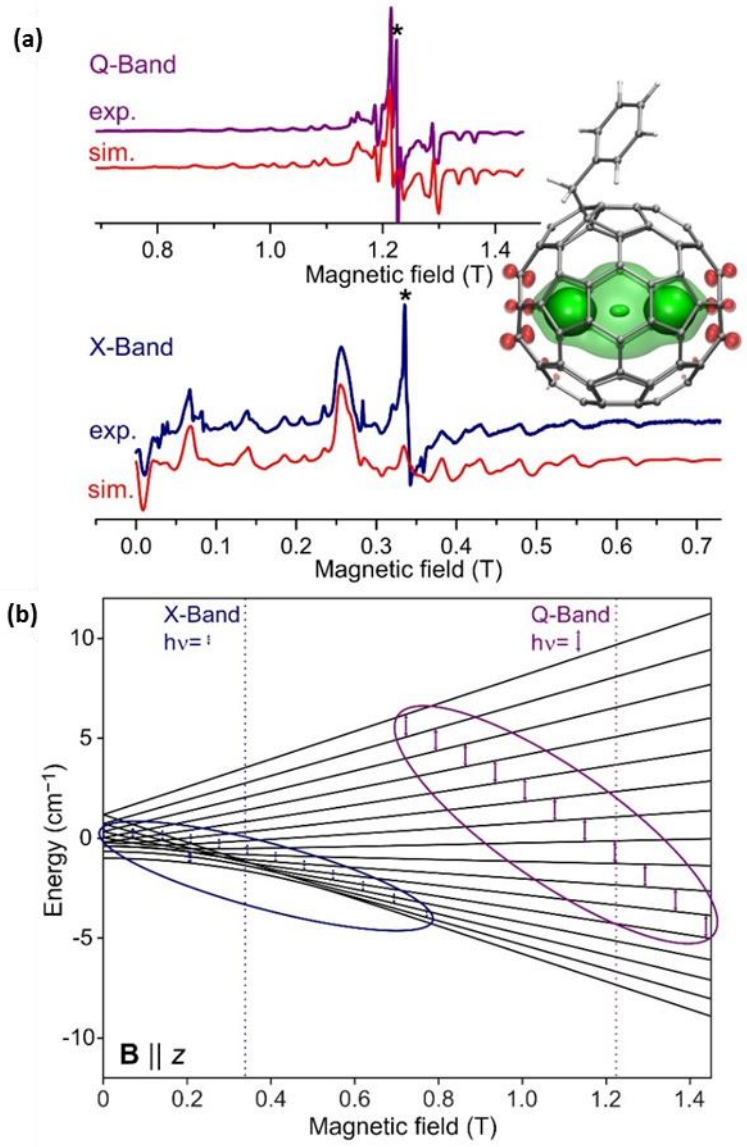

Figure 4.4.2 Electron paramagnetic resonance (EPR) spectroscopy of $Gd_2@C_{80}(CH_2Ph)$. (a) X-band and Q-band EPR spectra of frozen {Gd_2} solution in toluene near 100 K together with the spectra simulated for spin S = 15/2 with g_{iso} = 1.987 and zero field splitting (ZFS) parameters D = 1.00 GHz and E = 0.22 GHz (inhomogeneous broadening is accounted for by ZFS strain Str$D$ = 0.029 GHz and Str$E$ = 0.027 GHz); asterisks mark unidentified signals (presumably of low spin states or organic impurities), the inset shows the spin-density distribution in {Gd_2}; (b) Zeeman splitting for spin S = 15/2 with the above ZFS parameters (magnetic field is parallel to z-axis of the ZFS tensor); also shown are energies of the X-band (9.4 GHz) and Q-band (34 GHz) microwave photons, EPR-active transitions (ovals and small arrows), and the resonance fields corresponding to the g-factor of 1.987 (vertical dotted lines).

Now let's formulate the spin Hamiltonian to describe our Gd-e-Gd system. As Gd is isotropic, the eq. 4.3.4 can be further simplified by removing the single-ion ligand-field terms and by replacing the total angular momentum $\hat{J}$ with the total spin momentum $\hat{S}$:

$$\widehat{H}_{\text{spin}}(\{\text{Gd}_2\}) = -2j_{\text{Gd,Gd}}\left(\hat{S}_{\text{Gd}_1} \cdot \hat{S}_{\text{Gd}_2}\right) - 2j_{\text{Gd,e}}\hat{s}_{\text{e}}\left(\hat{S}_{\text{Gd}_1} + \hat{S}_{\text{Gd}_2}\right) \quad (4.4.2)$$

In good agreement with the EPR studies, DFT-calculations predict huge ferromagnetic coupling between the Gd spin and the unpaired electron spin with $j_{\text{Gd,e}}$ value of 177 cm^{-1} for $Gd_2@C_{80}^-$ [129], 181-184 cm^{-1} for $Gd_2@C_{80}(CH_2Ph)$ [67] and 200 cm^{-1} for $Gd_2@C_{79}N$ [119, 120]. On the other hand, direct Gd–Gd exchange coupling is estimated to be much smaller, in the order of -1 cm^{-1} (or less) [130].

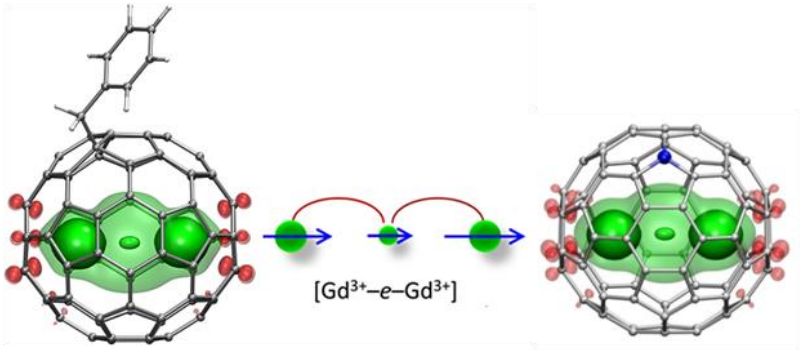

Figure 4.4.3 DFT-optimized structures and spin density distribution (green color) in $Gd_2@C_{80}(CH_2Ph)$ (left) and $Gd_2@C_{79}N$ (right) molecules. Three well-seen maxima of spin density correspond to the *4f*-electrons of Gd and the unpaired electron spin residing on the Gd-Gd bonding orbital; Carbon atoms p-orbitals are illustrated with red color and N atom with blue. Blue arrows show the spin of each center and demonstrate how we treat the molecule as a three-spin system.

The predicted $j_{\text{Gd,Gd}}$ value is two orders of magnitude smaller than that of $j_{\text{Gd,e}}$. To evaluate how important is the inclusion of the $j_{\text{Gd,Gd}}$ constant in our spin Hamiltonian, we calculated the spin Hamiltonian spectrum of the eq. 4.4.2 for different $j_{\text{Gd,Gd}}$ values and keeping $j_{\text{Gd},e}$=170 cm^{-1} (fig. 4.4.4). The Hamiltonian spectrum produced with $j_{\text{Gd,Gd}}$= 0 spans the energy range of 2550 cm^{-1}. The eigenstates are grouped into 15 "giant-spin" states with *S* = 15/2, 13/2, … 1/2, 1/2, 3/2, …, 13/2. The gaps between the states are all equal to $j_{\text{Gd,e}}$ except for the two *S*=1/2 states with the energy gap of $2j_{\text{Gd,e}}$. Red rectangle highlights the states with the reasonable population at room temperature. Thermal population of these states affects the shape of the $\chi \cdot T$-*T* function. As long as $j_{\text{Gd,Gd}}$ remains in the order of -1 cm^{-1}, the decay of the $\chi \cdot T$-*T* function in the 100-300 K range is still mainly determined by the thermal population of the *S* = 13/2 state (with smaller influence of *S* = 11/2). Therefore, it would not be possible to determine $j_{\text{Gd,Gd}}$ and $j_{\text{Gd,e}}$ separately. Instead, one can use a single-parameter model with effective $j_{\text{Gd},e}^{\text{eff}}$ coupling constant, which corresponds to the energy difference between these two states:

$$j_{\mathrm{Gd},e}^{\mathrm{eff}} \approx E_{13/2} - E_{15/2} = j_{\mathrm{Gd},e} + 14 j_{\mathrm{Gd,Gd}} \tag{4.4.3}$$

With the increase of $j_{\mathrm{Gd,Gd}}$, more and more spin states become accessible in the experimentally relevant temperature range, making the eq. 4.4.3 not valid for large $j_{\mathrm{Gd,Gd}}$ (such as the value of -10 cm^{-1} shown in fig. 4.4.4 below). But since the expected $j_{\mathrm{Gd,Gd}}$ value is rather small, we can safely neglect the $j_{\mathrm{Gd,Gd}}$ contribution and simplify our Hamiltonian of eq. 4.2.2 to the following form, with single unknown parameter, the effective $j_{\mathrm{Gd},e}^{\mathrm{eff}}$ coupling constant:

$$\hat{H}_{\mathrm{spin}}(\{\mathrm{Gd_2}\}) \approx -2 j_{\mathrm{Gd},e}^{\mathrm{eff}} \hat{s}_{\mathrm{e}} \left(\hat{S}_{\mathrm{Gd_1}} + \hat{S}_{\mathrm{Gd_2}}\right) \tag{4.4.4}$$

The g-factor value of 1.978 and the positive sign of $j_{\mathrm{Gd},e}^{\mathrm{eff}}$ are adopted from the EPR study.

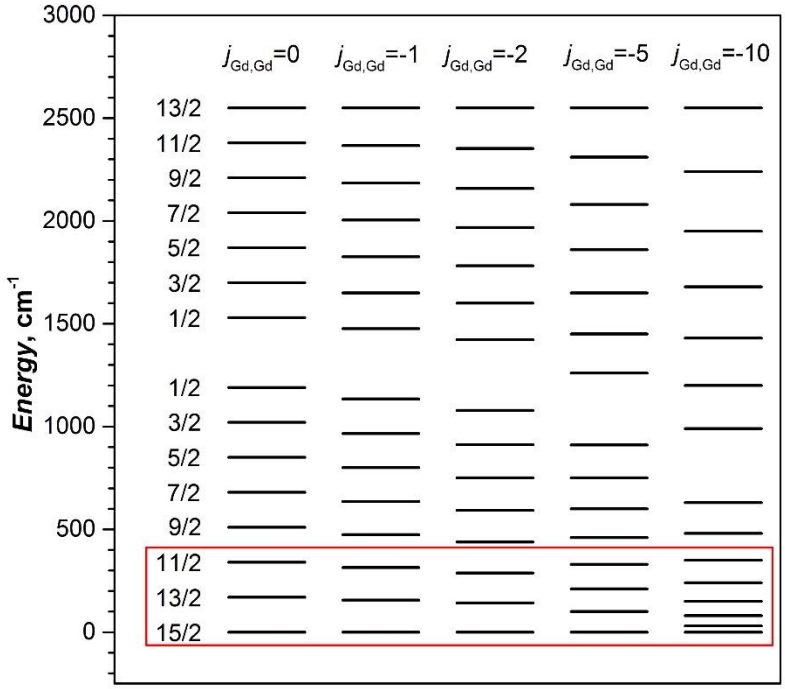

Figure 4.4.4 Computed Hamiltonian spectrum (eq. 4.4.2) with $j_{\mathrm{Gd},e}$ = 170 cm^{-1} and different values of $j_{\mathrm{Gd,Gd}}$. The $j_{\mathrm{Gd,Gd}}$ values in the figure are given in cm^{-1}, the left column gives the giant spin value for each manifold.

Furthermore, to test if in our calculations it is sufficient enough to consider completely isotropic spin 15/2 (although there is some anisotropy according to the EPR data), we simulated and compared the magnetization curves of a completely isotropic spin to a slightly anisotropic (fig. 4.4.5). The result show that completely isotropic spin is very good approximation to reproduce our experimental data.

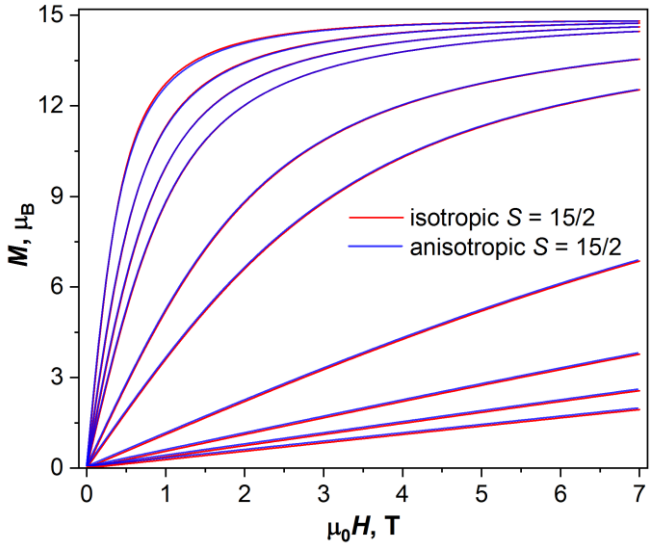

Figure 4.4.5 Magnetization curves simulated for the isotropic spin S = 15/2, and for the slightly anisotropic spin S=15/2 with zero field splitting parameter D = 0.01 cm^{-1} inferred from the EPR spectrum of $Gd_2@C_{79}N$. Temperatures are 2, 3, 4, 5, 10, 15, 50, 100, 150, and 200 K. Very small derivation can be seen only at 2 K, at all other temperatures the curves are indistinguishable.

Determination of the effective coupling constant $j^{\mathrm{eff}}_{\mathrm{Gd},e}$ is possible through comparison between the experimental and simulated χT-T curves, using the effective spin Hamiltonian of eq. 4.4.4.

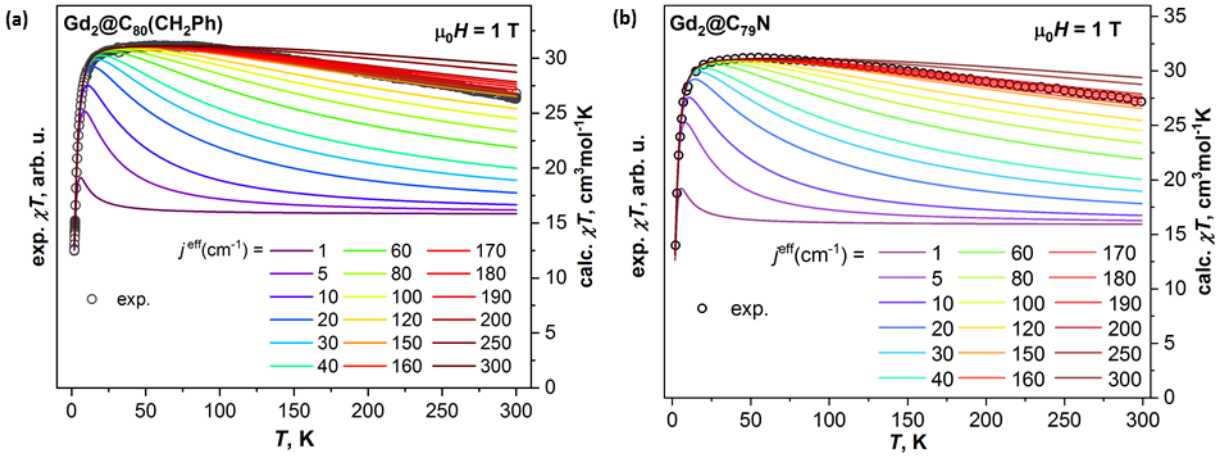

Figure 4.4.6 Experimental χT-T curves measured in the field of 1 T (open circles) for (a) $Gd_2@C_{80}(CH_2Ph)$ and (b) $Gd_2@C_{79}N$, compared to the calculated curves (lines) for different values of the $j^{\mathrm{eff}}_{\mathrm{Gd},e}$ constant.

According to the simulation curves, when $j^{\mathrm{eff}}_{\mathrm{Gd},e}$ is small, the χT curves exhibit a sharp peak at low temperatures, followed by a fast decay at higher temperatures. With the increase of $j^{\mathrm{eff}}_{\mathrm{Gd},e}$, the peak is growing and becomes less sharp, whereas the higher-temperature decay becomes less steep. Therefore, the temperature range where the fully-coupled spin system has the dominant contribution is increasing with the $j^{\mathrm{eff}}_{\mathrm{Gd},e}$ value. Likewise, the decay of χT caused by the thermal

population of the lower-spin states, becomes more gradual because the gap between the high-spin ground state and lower-spin excited states is also increasing.

For $Gd_2@C_{80}(CH_2Ph)$ and $Gd_2@C_{79}N$, the best convergence between the experimental and the calculated χT curves in the field of 1 T is reached for $j^{\mathrm{eff}}_{\mathrm{Gd},e}$=160±10 cm^{-1} and 170±10 cm^{-1} resp., the largest ever reported values for exchange coupling in lanthanide-based molecular magnets. This result comes in good agreement with the DFT-predictions and recent report by Gao et. al [131]. The largest Gd-radical coupling constant reported for other compounds in the past, were 6 cm^{-1} for Gd–nitroxide [132, 133], -10 cm^{-1} for Gd–bipyrimidyl [134] and -27 cm^{-1} for Gd-N_2 radical bridges [135]. More precise determination of $j^{\mathrm{eff}}_{\mathrm{Gd},e}$ value is hardly possible because the variation of computed curves within the interval is comparable to the experimental uncertainties. The values of 160 and 170 cm^{-1} were adopted to simulate all the χT curves measured in different fields and *M-H* curves as well (fig. 4.4.7). For all sets of data, very good agreement between experiment and theory is obtained.

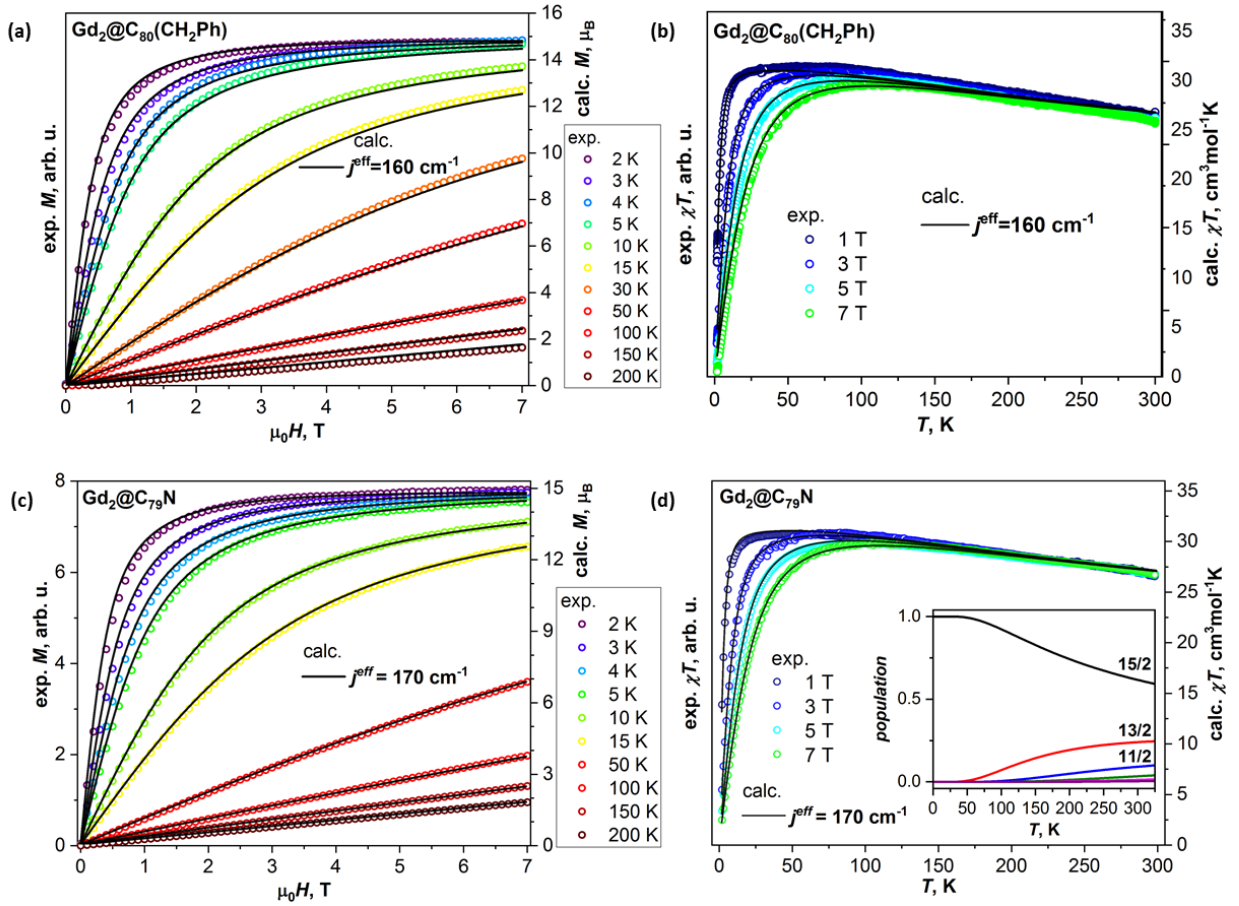

Figure 4.4.7 Experimental *M-H* and χT-*T* curves of (a-b) $Gd_2@C_{80}(CH_2Ph)$ and (c-d) $Gd_2@C_{79}N$ (open dots), compared to the results of calculations (black lines) for $j^{\mathrm{eff}}_{\mathrm{Gd},e}$ equal to 160 cm^{-1} and 170 cm^{-1} respectively. The inset shows the thermal population of the giant-spin states, in particular *S* = 15/2 (black), 13/2 (red), and 11/2 (blue).

Using determined $j_{\mathrm{Gd},e}^{\mathrm{eff}}$ coupling constant of 170 cm^{-1}, we calculated populations of the giant spin states in $Gd_2@C_{79}N$ as a function of temperature (fig. 4.4.7 inset). The only state to be considered below 50 K is the *S*=15/2, hence the giant-spin approximation is valid at these temperatures. The *S*=13/2 manifold gains significant population above 50 K, and the *S*=11/2 state should be also considered above 150 K, although the ground state is still the dominant one (>60%) up to 300 K.

{Gd_2} is not expected to behave as a single-molecule magnet, but available quantity of $Gd_2@C_{79}N$ sample allowed to test the AC response of it. Millisecond-long relaxation of magnetization was observed near 2 K and in the presence of the magnetic field, as shown in the graphs below.

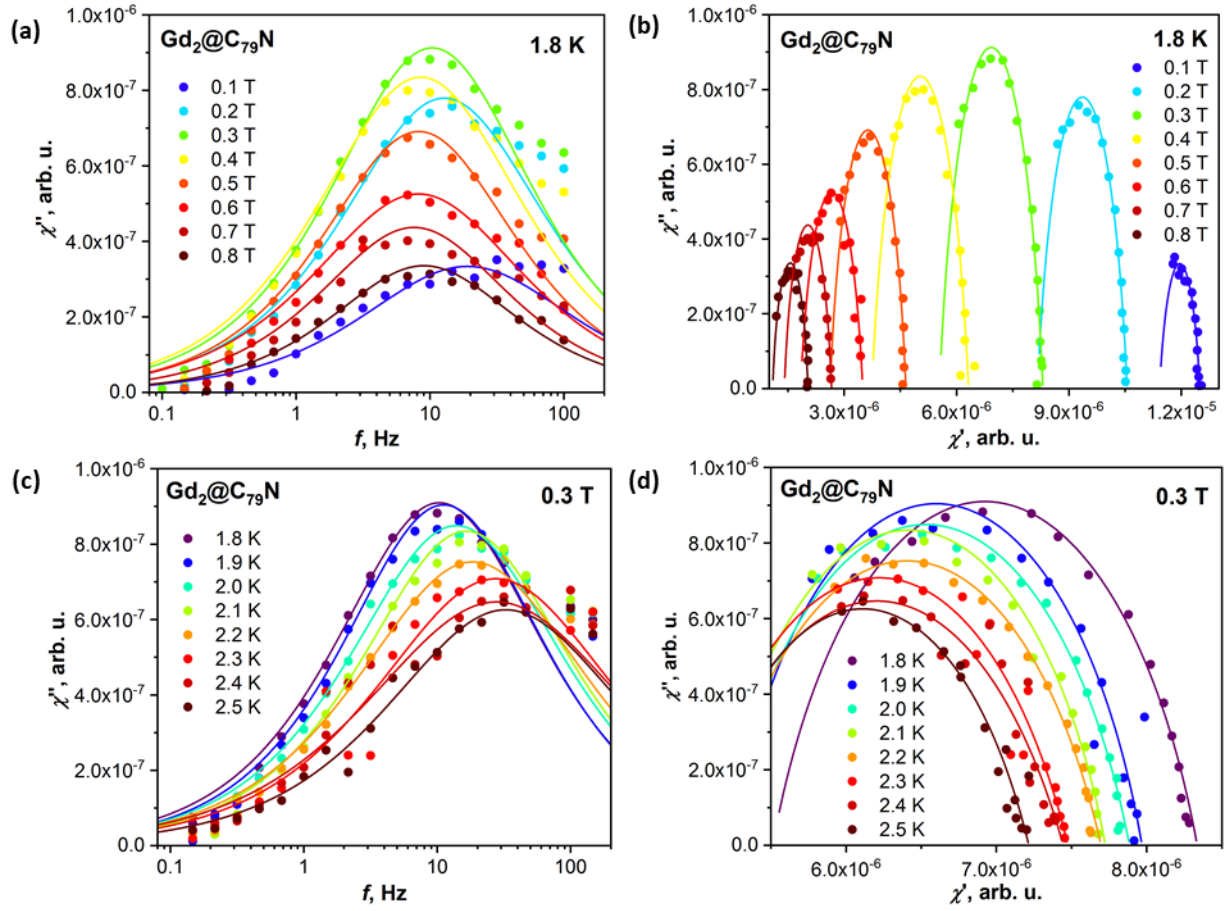

Figure 4.4.8 AC magnetometry studies of $Gd_2@C_{79}N$. (a) Out-of-phase susceptibility χ'' measured at 1.8 K in different constant fields; (b) Same as (a), but showing the out-of-phase susceptibility χ'' as a function of in-phase susceptibility χ' (Cole-Cole plots); (c) Out-of-phase susceptibility χ'' measured at different temperatures in the constant field of 0.3 T. (d) Same as (c), but showing the Cole-Cole plots. The dots are experimental values and lines are the fits with generalized Debye model.

AC measurements in zero-field did not give detectable *χ''(ω)* response, but the peak emerges in the field of 0.1 T. The peak amplitude grows with the field until the maximum at 0.3 T, and then

decreases again at higher fields. Fitting the data with generalized Debye model gave relaxation times (τ_m) from 8 ms (0.1 T) to 18–22 ms (0.4-0.8 T). After, the temperature dependence was measured in the field of 0.3 T, between 1.8 and 2.5 K. The signal could not be measured reliably at higher temperatures due to the amplifier disturbing the low-intensity signals at frequencies above 100 Hz. The relaxation times dropped from 16 ms (1.8 K) to 5 ms (2.5 K).

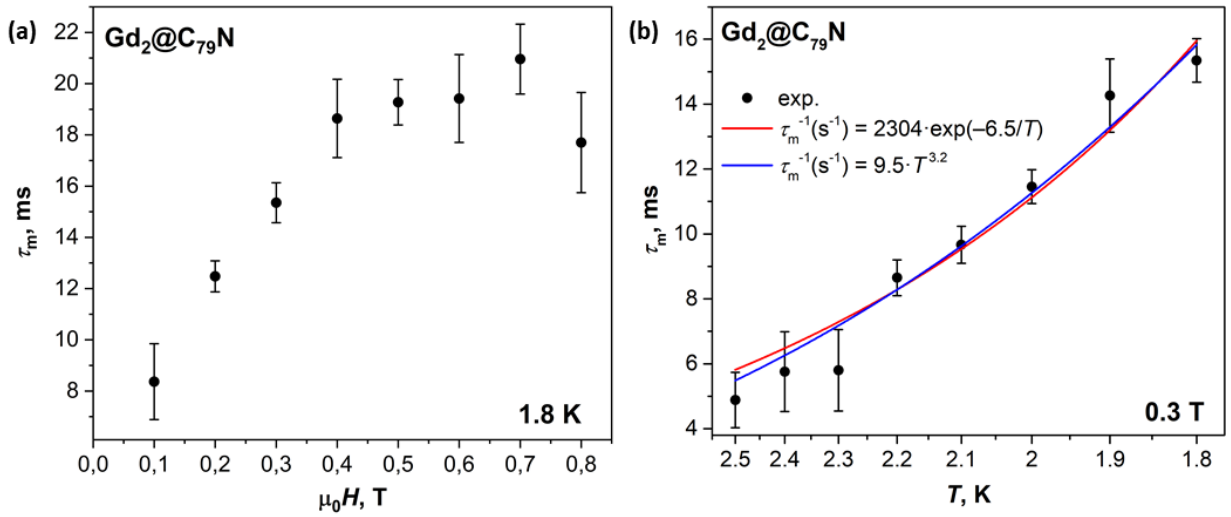

Figure 4.4.9 (a) Relaxation times of magnetization as a function of magnetic field at 1.8 K. (b) Relaxation times of magnetization in the field of 0.3 T as a function of temperature; the lines are fits to the Orbach relaxation mechanism (red, U^{eff} = 6.5 K) or to the power law (blue, n = 3.2).

Fitting of temperature dependence of τ_m shown in fig. 4.4.9, with both exponential and power law functions give comparable agreement. The exponential dependence $\tau^{-1} = \tau_0^{-1}\exp(-U^{\text{eff}}/T)$ corresponds to the Orbach relaxation mechanism with barrier U^{eff}= 6.5±0.5 K and attempt time τ_0= 4±1 10^{-4} s. The U^{eff} is larger than the zero-field splitting of S=15/2 manifold estimated from EPR data (~3 K), and Zeeman splitting in the field of 0.3 T (≈2.3 K). Fitting of the data with the power function of $\tau^{-1}\sim AT^n$ gives the n value of 3.2±0.2. At low temperatures, relaxation often follows the direct mechanism ($\tau^{-1}\sim T$), in which the spin flip is accompanied by the emission or absorption of a single phonon with frequency matching the splitting of the spin levels [136]. However, if the number of spins is much larger than the number of resonant phonons, then the energy dissipation is hampered resulting in phonon bottleneck effect [22] which elongates the relaxation with complex temperature dependence $\tau^{-1}\sim T^b$, ($1\leq b\leq 4$). Also, relaxation through Raman mechanism ($\tau^{-1}\sim T^9$) for Kramers systems is plausible at higher temperatures [136]. Thus, the value of n=3.2 determined for $Gd_2@C_{79}N$ may be indication of the bottlenecked direct relaxation mechanism near 2 K, but in the view of significant uncertainties of the values, this conclusion remains tentative.

4.5 $Tb_2@C_{80}(CH_2Ph)$ and $Tb_2@C_{79}N$

Study of $\{Gd_2\}$ gave us a first insight on the magnetic properties of a di-metallic system featuring single-electron bond between the two lanthanide ions. Now the question is how the same system but with anisotropic lanthanide ions would behave. The first di-EMF to be synthesized and magnetically characterized by our group was $Dy_2@C_{80}(CH_2Ph)$ in 2017 [67]. Excellent SMM properties were observed, and specifically high blocking temperature of magnetization (21.9 K), broad magnetic hysteresis and long relaxation times. Next anisotropic system to be studied, in the framework of my PhD thesis, was the $\{Tb_2\}$. In the same fashion with $\{Gd_2\}$, we magnetically characterized the mono-adduct and azafullerene version of $\{Tb_2\}$, $Tb_2C_{80}(CH_2Ph)$ and $Tb_2@C_{79}N$ respectively. Similar magnetic behaviour was observed for the two molecules, but with some differences presented below.

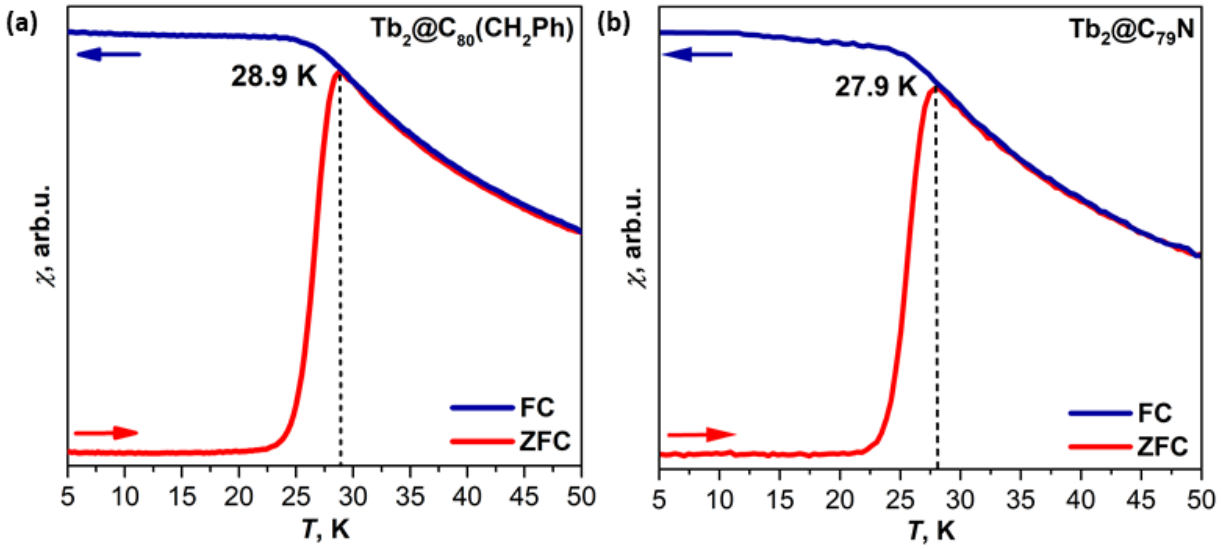

Figure 4.5.1 Blocking temperature of magnetization, T_B (sweep rate 5 K/min) for (a) $Tb_2C_{80}(CH_2Ph)$ (28.9 K) and (b) $Tb_2@C_{79}N$ (27.9 K).

Far beyond our expectations, $\{Tb_2\}$ surpassed the previous di-EMF champion ($\{Dy_2\}$, T_B = 21.9 K), by showing blocking temperature of magnetization of 28.9 K for $Tb_2@C_{80}(CH_2Ph)$, and 27.9 K for $Tb_2@C_{79}N$ (fig. 4.5.1). These T_B values rank among the highest ever recorded for single-molecule magnets (with the current record being today 80 K [99]). The only dinuclear SMM with similarly high blocking temperature is the Tb-complex with a N_2^{3-} radical bridge reported in 2017 [137]. Furthermore, $Tb_2@C_{80}(CH_2Ph)$ shows extremely broad hysteresis (H_c = 6.5 T at 5 K) (fig. 4.5.2a). Likewise, $Tb_2@C_{79}N$ exhibits also very broad but a little narrower hysteresis (H_c = 3.8 T between 1.8-10 K) (fig. 4.5.3a). These results show clearly that the presence of a N atom instead of the benzyl group produces a small deterioration in the magnetic properties.

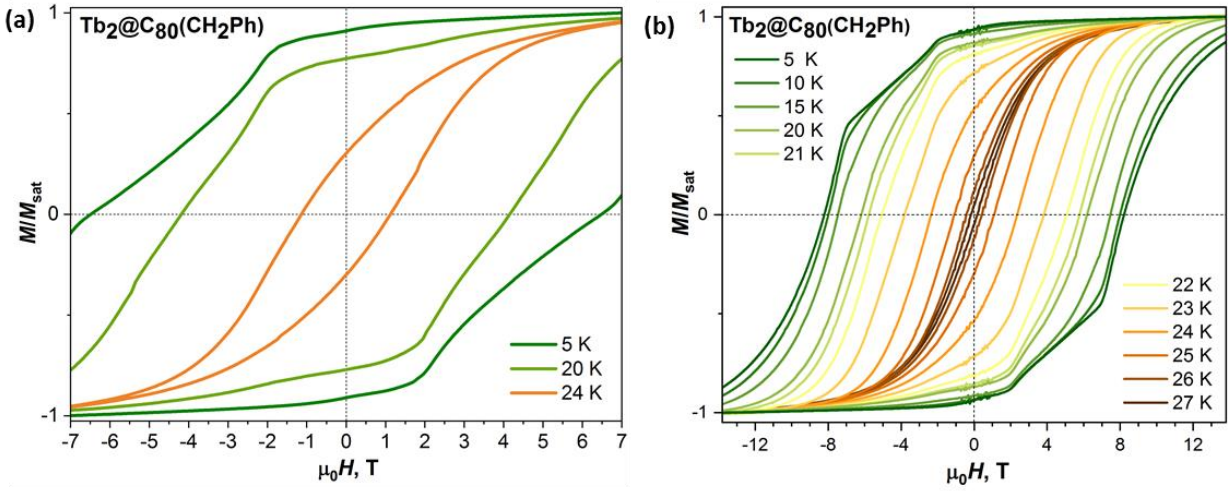

Figure 4.5.2 (a) Magnetization curves measured at the temperatures of 5, 20 and 24 K (sweep rate 2.9 mT/s), measured in the VSM-SQUID (MPMS 3); (b) Magnetic hysteresis curves between 5 and 27 K (sweep rate 9.5 mT/s), measured in the PPMS.

As we can see in fig. 4.5.2a, hysteresis is not closing in the range of ±7 T for the 5 and 20 K curves measured in the VSM-SQUID. For that reason, we decided to repeat the measurement of the magnetization curves in the available PPMS, where ±14 T field range is accessible (fig. 4.5.2b). Even at 14 T, the recorded hysteresis loop (field sweep rate: 9.5 mT/s) is open for temperatures below 15 K, with giant coercive fields of 8.2 T at 5 K and 8 T at 10 K. For $Tb_2@C_{79}N$, magnetization curves were measured only in the VSM-SQUID (field sweep rate: 2.9 mT/s) between 1.8-27 K (fig. 4.5.3a). Comparison with $Tb_2@C_{80}(CH_2Ph)$ magnetization curves at 5, 20 and 24 K, measured in the same magnetometer and field sweep rate (2.9 mT/s) is illustrated in fig. 4.5.3b.

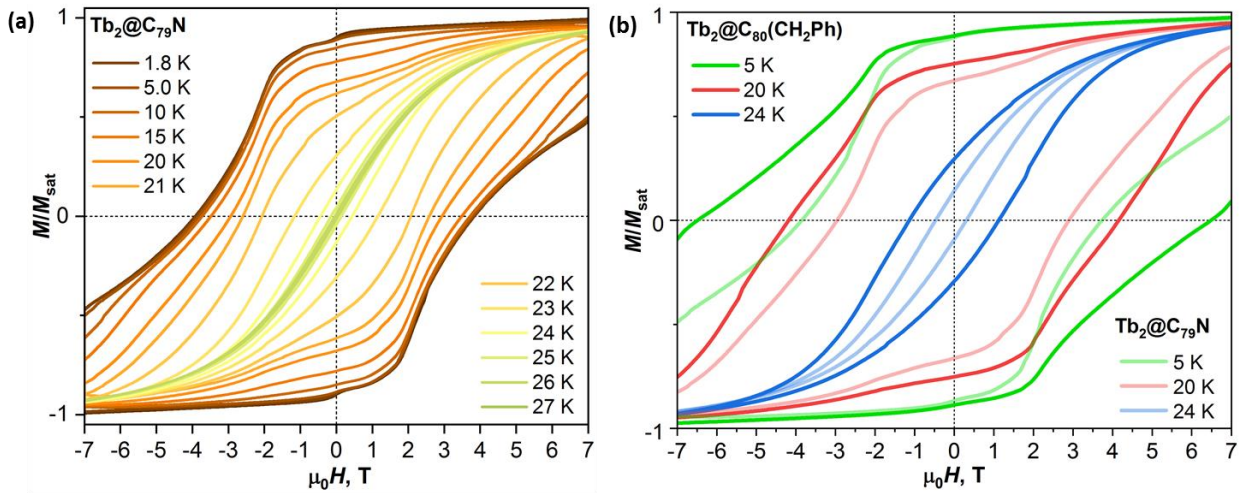

Figure 4.5.3 (a) $Tb_2@C_{79}N$ magnetization curves measured between 1.8 to 27 K in the VSM-SQUID and (b) comparison with the $Tb_2@C_{80}(Ch_2Ph)$ magnetization curves measured at 5, 10 and 24 K in the VSM-SQUID.

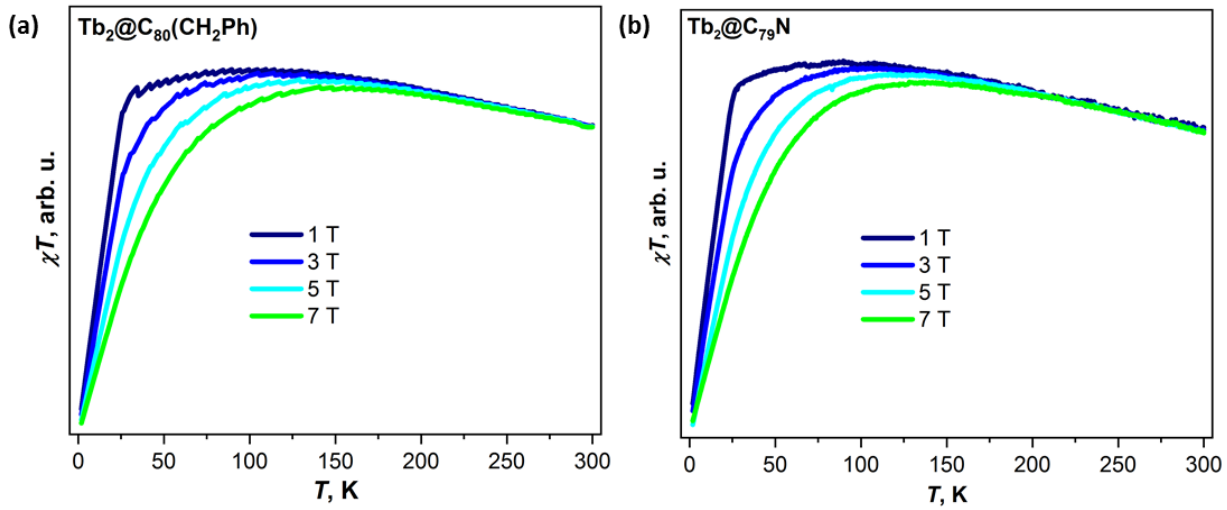

Figure 4.5.4 χT-T curves measured in the constant fields of 1, 3, 5 and 7 T (sweep rate 5K/min) for (a) $Tb_2@C_{80}(CH_2Ph)$ and (b) $Tb_2@C_{79}N$.

The spin Hamiltonian we use to describe the {Tb_2} system must include the magnetic anisotropy of Tb^{3+} ions. To understand the nature of magnetic anisotropy, ab initio calculations of single-ion properties in $TbY@C_{80}(CH_2Ph)^-$ and $TbY@C_{79}N^-$ were performed by Dr. S. Avdoshenko. For both molecules, calculations predicted strong ligand-field axiality. In $Tb_2@C_{80}(CH_2Ph)$, the quantization axes of both Tb^{3+} ions are parallel to the Tb-Tb axis. LF states are grouped into pseudo-doublets (pKDs) with a small splitting within each pKD, although Tb^{3+} is not a Kramers ion. In $|J, m_J\rangle$ basis, the low-energy pKD states have almost pure m_J composition (table 4.5.1), with the contribution of $|m_J|$ = 6 in the ground pKD being 99.9% (high-spin ground state, described as a $|\pm 6\rangle$ pseudo-doublet). The second pKD at 265 cm^{-1} is $|m_J|$ = 5 (99.6%), and the third pKD at 511 cm^{-1} is $|m_J|$ = 4 (98.9%). Since the relative energies of the first and second excited pseudo-doublets, pKD2 and pKD3 are predicted to be in the range of 300–500 cm^{-1}, only the lowest energy states contribute to the magnetic properties in the experimentally relevant temperature range. The overall LF splitting is 1014 cm^{-1}. For $Tb_2@C_{79}N^-$, analogous calculations revealed that Tb^{3+} ion has easy-axis magnetic anisotropy as well with the quantization axis aligned along the Tb-Tb bond, but tilted from it by ≈7° (fig. 4.5.6).

pKD	Tb1		Tb2	
	E, cm^{-1}	Composition, %	E, cm^{-1}	Composition, %
1	0.0 0.0	$100\|\pm6\rangle$ $100\|\pm6\rangle$	0.00 0.02	$100\|\pm6\rangle$ $100\|\pm6\rangle$
2	266.7 266.9	$100\|\pm5\rangle$ $100\|\pm5\rangle$	256.1 256.3	$100\|\pm5\rangle$ $100\|\pm5\rangle$
3	511.0 511.7	$99\|\pm4\rangle$ $99\|\pm4\rangle$	507.8 509.2	$99\|\pm4\rangle$ $100\|\pm4\rangle$
4	708.8 715.4	$99\|\pm3\rangle$ $99\|\pm3\rangle$	705.2 719.8	$99\|\pm3\rangle$ $98\|\pm3\rangle$
	847.6 869.1	$91\|\pm2\rangle + 8\|0\rangle$ $98\|\pm2\rangle$	839.3 865.1	$87\|\pm2\rangle + 13\|0\rangle$ $98\|\pm2\rangle$
	928.6 990.1	$97\|\pm1\rangle$ $94\|\pm1\rangle + 4\|0\rangle$	911.1 990.5	$96\|\pm1\rangle$ $91\|\pm1\rangle + 6\|0\rangle$

Table 4.5.1 CASSCF/SO-RASSI calculations summary for $\{TbY\}^-$ molecule. Energies and state compositions of pseudo Kramers doublets (pKDs) and singlet states of the Tb1 and Tb2 ions in single-ion frame. The contribution for the "$|\pm X\rangle$" state means a sum of contributions for $|+X\rangle$ and $|-X\rangle$ states.

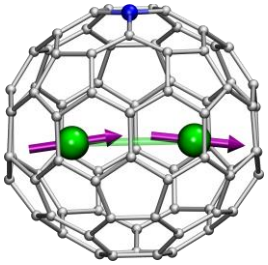

Figure 4.5.5 Orientation of quantization axes for individual Tb ions in $Tb_2@C_{79}N$ molecule, determined by ab initio calculations for $TbY@C_{79}N^-$.

As ab initio calculations predict for both molecules Ising-type magnetic ground state, we can use the following effective spin Hamiltonian:

$$\hat{H}_{\text{spin}}(\{\text{Tb}_2\}) = \hat{H}_{\text{Tb}_1} + \hat{H}_{\text{Tb}_2} - 2j^{eff}_{\text{Tb,e}}\hat{s}_{\text{e}}\left(\hat{J}_{\text{Tb}_1} + \hat{J}_{\text{Tb}_2}\right) \quad (4.5.1)$$

Here, based on the $\{Gd_2\}$ analogue, we assume that Tb-Tb coupling is much weaker than Tb-e interactions and thus can be ignored. Ligand-field parameters in eq. 4.5.1 are taken from ab initio calculations. Thus, our spin Hamiltonian has only one unknown parameter, the effective coupling constant $j^{eff}_{\text{Tb,e}}$. Similar to $\{Gd_2\}$, the value of $j^{\text{eff}}_{Tb,e}$ is estimated by calculating the *M-H* and *χT-T* curves using the eq. 4.5.1 and comparing them to experimental data.

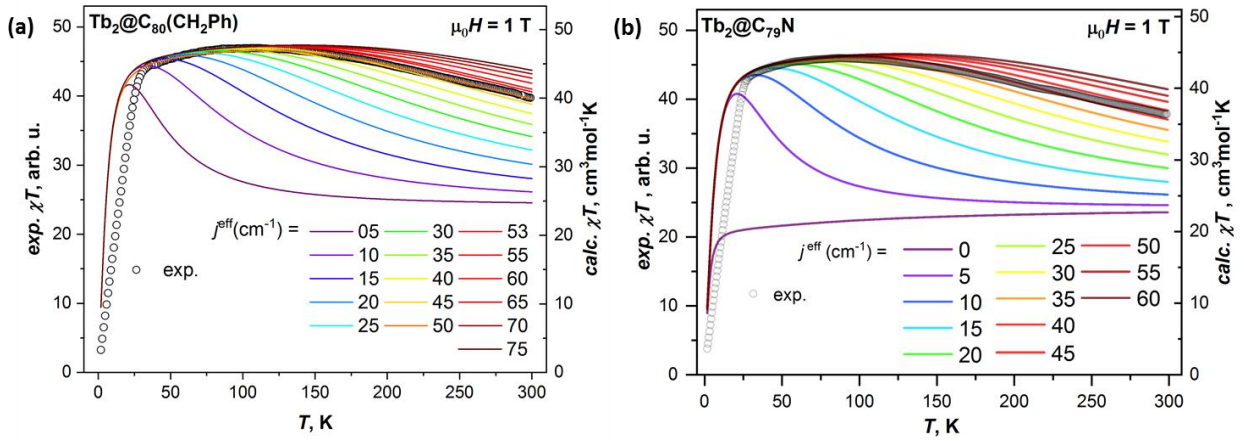

Figure 4.5.6 Experimental χT-T curves measured in the field of 1 T (open circles) for (a) $Tb_2@C_{80}(CH_2Ph)$ and (b) $Tb_2@C_{79}N$, compared to the calculated curves (lines) for different values of the $j^{\mathrm{eff}}_{Tb,e}$ constant.

Reasonable agreement between the experimental χT-T curve measured in the field of 1 T and the simulated one, is achieved for $j^{\mathrm{eff}}_{Tb,e}$ between 48-53 cm^{-1} for $Tb_2@C_{80}(CH_2Ph)$ and 40-45 cm^{-1} for $Tb_2@C_{79}N$. Magnetization curves and χT-T curves were then calculated for $j^{\mathrm{eff}}_{Tb,e}$ equal to 50 cm^{-1} for $Tb_2@C_{80}(CH_2Ph)$ and 45 cm^{-1} for $Tb_2@C_{79}N$. These coupling constant values determined for $\{Tb_2\}$, are the largest among all radical-bridged lanthanide SMMs. For comparison, in $[Ln^{3+}\text{-}N_2^{3-}\text{-}Ln^{3+}]$ systems, $j^{\mathrm{eff}}_{Tb,e}$ is -23.1 cm^{-1} for Tb [137].

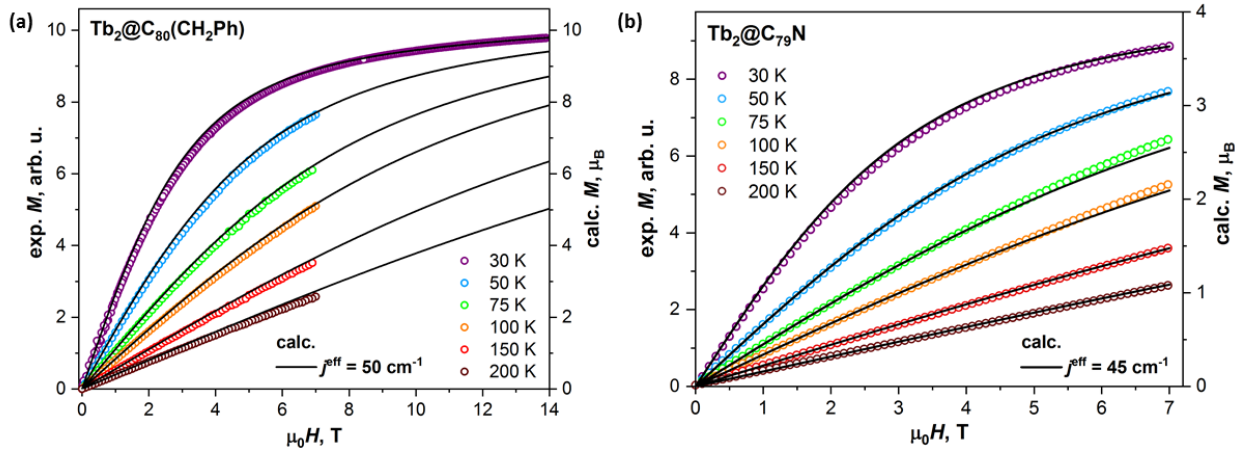

Figure 4.5.7 Experimental magnetization curves (open circles) above T_B for $Tb_2@C_{80}(CH_2Ph)$ and $Tb_2@C_{79}N$ molecules, measured in the SQUID-VSM (except from the 30 K M-H curve of $Tb_2@C_{80}(CH_2Ph)$, measured in the PPMS). The curves are compared to the results of calculations (black lines) for $j^{\mathrm{eff}}_{Tb,e}$ equal to 50 cm^{-1} for $Tb_2@C_{80}(CH_2Ph)$ and 45 cm^{-1} for $Tb_2@C_{79}N$.

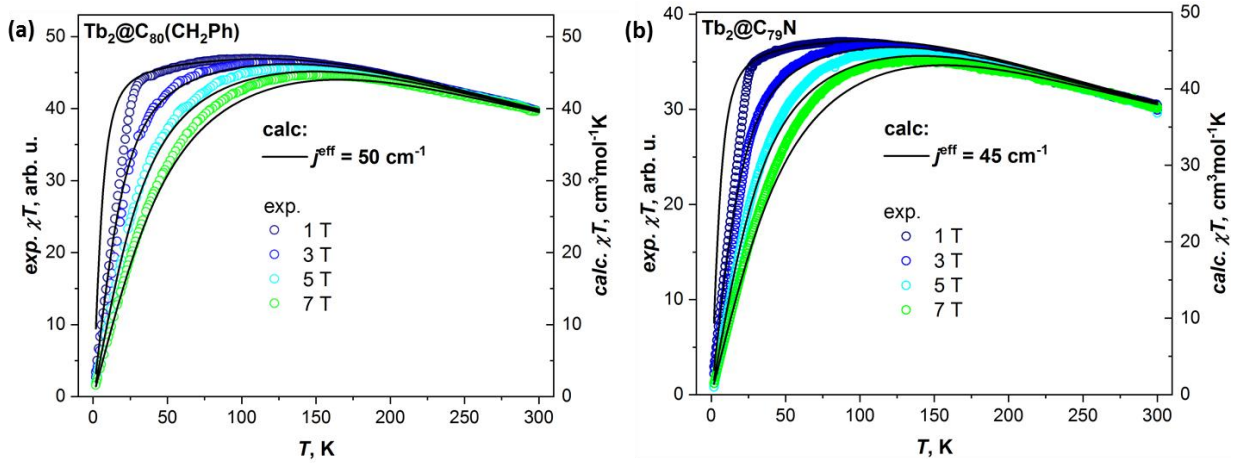

Figure 4.5.8 Experimental χT-T curves (open circles) of $Tb_2@C_{80}(CH_2Ph)$ and $Tb_2@C_{79}N$, measured in the SQUID-VSM, compared to the calculated curves (black lines) for $j^{\mathrm{eff}}_{Tb,e}$ equal to 50 cm^{-1} for $Tb_2@C_{80}(CH_2Ph)$ and 45 cm^{-1} for $Tb_2@C_{79}N$. Note that the part of the experimental χT-T values below the blocking temperature, does not correspond to the equilibrium values, especially in low fields, so they deviate from the calculated curves.

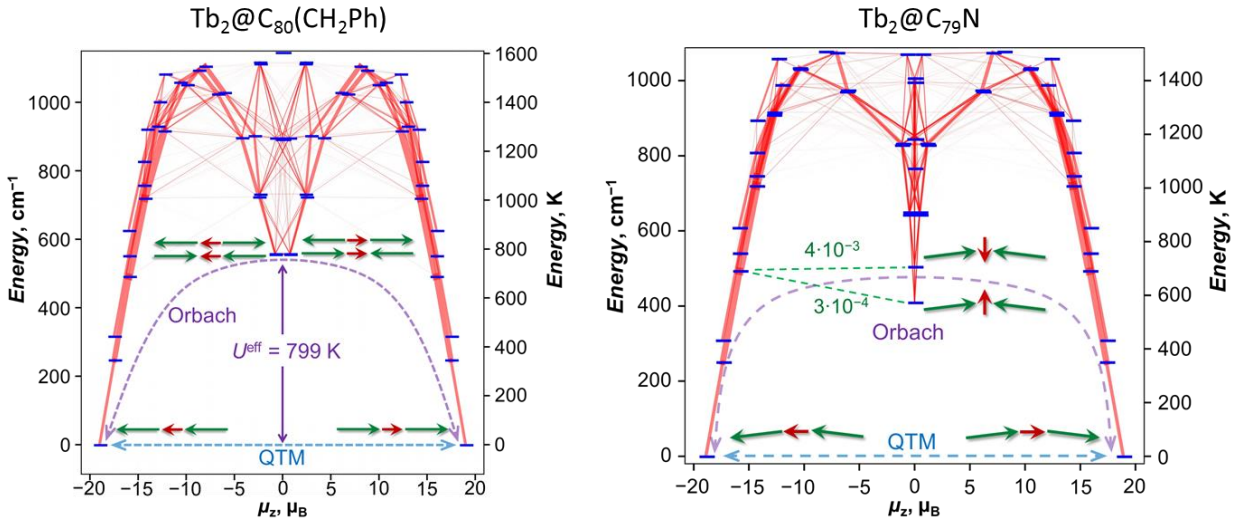

Figure 4.5.9 The low-energy part of the effective spin Hamiltonian spectrum for $Tb_2@C_{80}(CH_2Ph)$ ($j^{\mathrm{eff}}_{Tb,e}$= 50 cm^{-1}) and $Tb_2@C_{79}N$ ($j^{\mathrm{eff}}_{Tb,e}$=45 cm^{-1}). Transition probabilities for the low-energy range are visualized as lines of different thickness (thicker lines correspond to higher probabilities). The *x*-axis is the projection of magnetic moment upon the main anisotropy axis. Quantization axes of Tb ions are shown as green arrows, the red arrows represent the unpaired electron spin. Dashed arrows denote QTM and Orbach relaxation mechanisms, numbers are transition probabilities (in μ_B^2).

In accordance with the extremely broad hysteresis, relaxation times of {Tb_2} appeared to be quite long at low temperatures (and a great challenge to measure). Below blocking temperature (T_B), average magnetization relaxation times were determined by DC magnetometry. The sample was first magnetized to saturation, then the field was swept to a finite field (0/0.3 T) with the highest

possible sweep rate, and the decay of magnetization was recorded. Above blocking temperature, the relaxation times for both molecules were determined from AC susceptibility measurements. For $Tb_2@C_{80}(CH_2Ph)$, AC measurements were performed in the University of Zurich, with the help of Prof. Dr. Greber and Dr. A. Kostanyan.

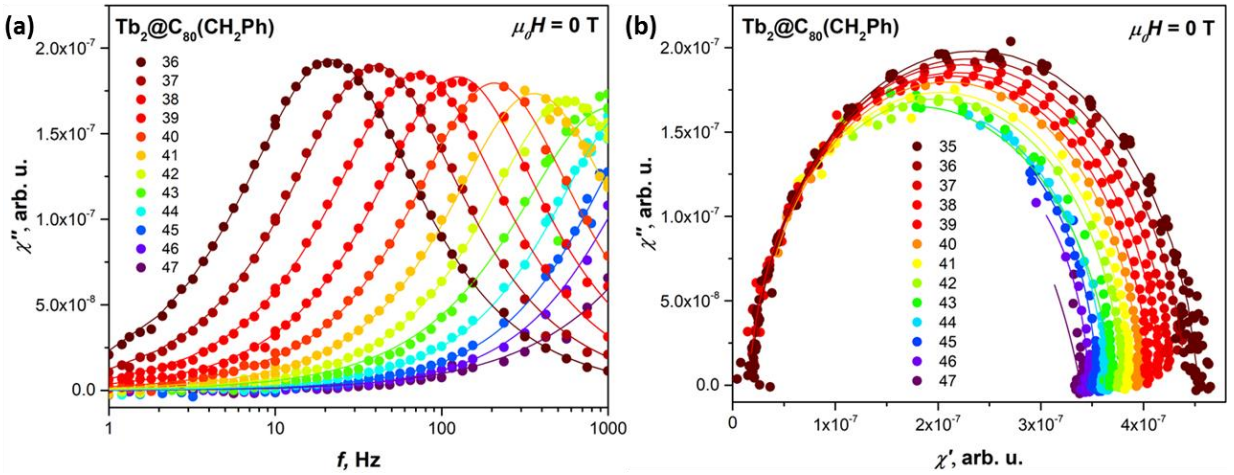

Figure 4.5.10 (a) Out-of-phase magnetic susceptibility of $Tb_2@C_{80}(CH_2Ph)$ measured in zero-field and different temperatures; (b) The corresponding Cole-Cole plots. Dots are experimental values, lines are fits with the generalized Debye model.

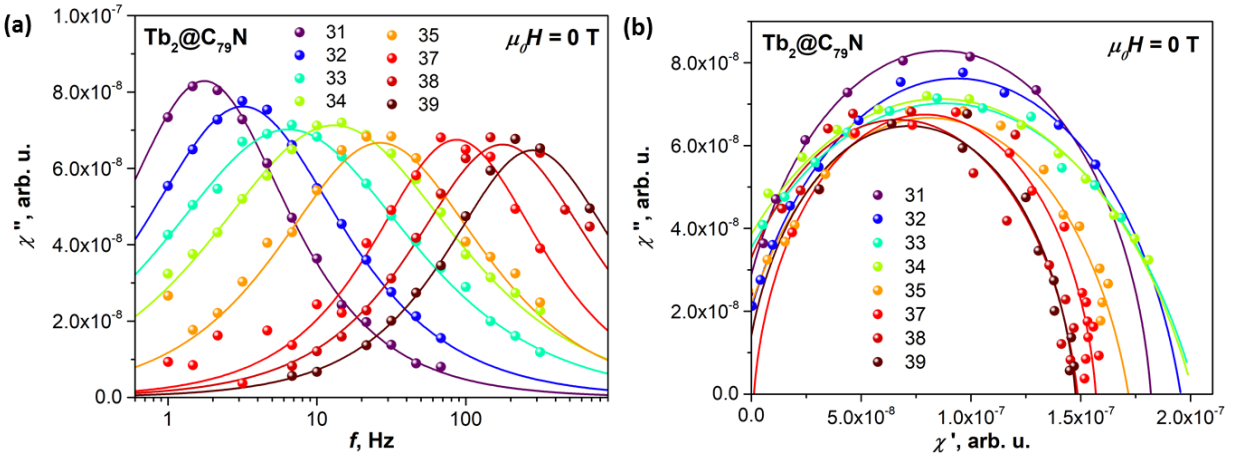

Figure 4.5.11 (a) Out-of-phase magnetic susceptibility of $Tb_2@C_{79}N$, measured in zero-field at different temperatures; (b) The corresponding Cole-Cole plots. Dots are experimental values, lines are fits with the generalized Debye model.

Collecting all the relaxation data (DC and AC) and plotting them in Arrhenius coordinates ($\log(\tau_m)$-$1/T$), we immediately observe the same temperature dependence for both molecules. However, the τ_m values of $Tb_2@C_{80}(CH_2Ph)$ are longer than those of $Tb_2@C_{79}N$, in agreement with broader hysteresis too.

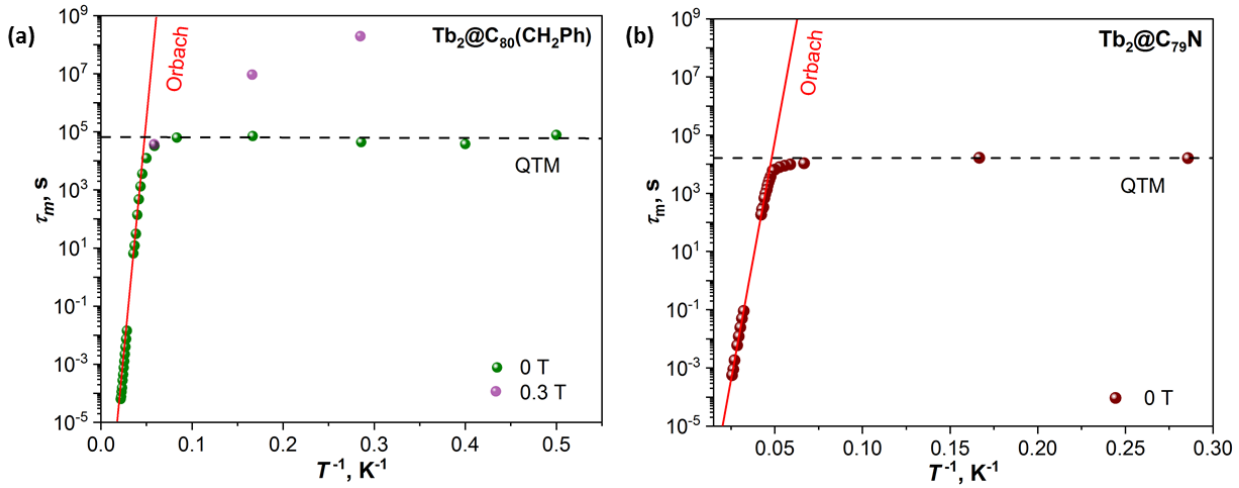

Figure 4.5.12 Magnetic relaxation times of (a) $Tb_2@C_{80}(CH_2Ph)$ and (b) $Tb_2@C_{79}N$; Dark green and red dots are zero-field data, light magenta dots are in-field data (0.3 T). Black dashed lines denote QTM and red solid lines Orbach process.

In the ca 2-15 K temperature regime, relaxation in zero-field exhibits a temperature-independent behaviour for both molecules. This is attributed to QTM mechanism, with characteristic times $\tau_{QTM} \approx 6.5 \cdot 10^4$ s (18 hrs) for $Tb_2@C_{80}(CH_2Ph)$ and $\tau_{QTM} \approx 4.5$ hrs for $Tb_2@C_{79}N$. This is uncommonly huge value for tunnelling (it is usually a very efficient way of relaxation) which could be explained only by the flip of the combined Tb-*e*-Tb spin as a single entity. When QTM is quenched by a finite magnetic field, relaxation times of $\{Tb_2\}$ are increased by orders of magnitude. A conservative estimation for relaxation time in the field of 0.3 T in case of $Tb_2@C_{80}(CH_2Ph)$ is reaching 6 years at 3 K. Above 20 K, the relaxation of magnetization shows linear temperature dependence in Arrhenius coordinates. The τ_m values found in DC measurements (below T_B), continue the linear regime over 35 K (AC measurements), which is described by Orbach relaxation mechanism $\tau^{-1} = \tau_0^{-1}\exp(-U^{\text{eff}}/T)$, with effective barrier U^{eff}=799±2 K for $Tb_2@C_{80}(CH_2Ph)$ and U^{eff}=757±4 K for $Tb_2@C_{79}N$. Between 15-20 K, the transition area from QTM to Orbach mechanism is more difficult to identify the involved relaxation processes (Raman is possible).

At this point, it is instructive to analyze the energy spectra shown in fig. 4.5.9. As a Kramers system, Tb^{3+}-e-Tb^{3+} has a rigorous two-fold degeneracy of the spin states in zero magnetic field. In the ground state doublet, all three spins are aligned along the Tb-Tb axis giving a total magnetic moment of 18.9 μ_B. This giant-spin state can be described as a pseudospin S = 1/2 with the g-tensor (0, 0, 37.789). Negligible transverse (*x*, *y*) components of the g-tensor and the large total spin result in the low efficiency of the QTM, in which the total spin flips as a whole (hence the long QTM relaxation time of ≈18 hours). The lowest energy excited states at 251 and 310 cm^{-1} correspond to the LF excitation in one of the Tb ions to the second pKD. Further states with LF excitations to the third pKD, or when both Tb centers are excited to the second pKD, are found

at 494, 541, and 609 cm^{-1}. All these states are characterized by negligible $g_{x,y}$ components and g_z values.

With two symmetry-equivalent and collinear Tb magnetic moments, ferro-magnetically coupled to the electron spin, the exchange-states with flipping of one Tb moment form a quartet (fig. 4.5.9α). But when Tb moments are tilted from the Tb-Tb axis, then the quartet is split into two doublets (fig. 4.5.9b). Furthermore, when one Tb moment is reversed, both Tb moments cancel each other in *z* direction, but tilting leads to the emergence of *y*-component (if tilting is defined as a rotation around the *x*-axis). Unpaired electron spin then orients itself along the *y*-axis either parallel or antiparallel to the projection of Tb moments as illustrated in fig. 4.5.9b. In particular, for $Tb_2@C_{79}N$ with a tilting angle of 7.2° and isotropic coupling constant j^{eff} = 45 cm^{-1}, the lowest-energy exchange-excited states are found at 410 cm^{-1} (g_y = 11.61) and 505 cm^{-1} (g_y = 0.79). With negligible g_z components, exchange excited states should be very efficient for the spin reversal.

When LF-excited and exchange-excited states have similar energies, transition probabilities between them can become sufficiently high (fig. 4.5.9), and this may be a relevant relaxation pathway for the Orbach relaxation mechanism. Alternatively, the system can be excited to the exchange states directly from the ground state. A rather simple spin Hamiltonian employed in this work gives very low transition probability for such a process. However, more refined treatment proposed by Chibotaru *et al.* for radical-bridged di-Tb complex, showed that exchange excitations may have a rather high transition probability [138]. In our case, if only the exchange term of the Hamiltonian (eq. 4.5.1) is considered, and the ground state lanthanide spins are of Ising type with $J_z = \pm J$ (here *J* is the total momentum of the lanthanide ion), the energy of the exchange-excited state and hence the relaxation barrier would be $U^{eff}=2\cdot J\cdot j^{eff}$. With j^{eff} of 50 cm^{-1} for $Tb_2@C_{80}(CH_2Ph)$ and 45 cm^{-1} for $Tb_2@C_{79}N$ (from PHI simulations), the corresponding energy barriers are calculated as 600 cm^{-1} (863 K) and 540 cm^{-1} (777 K) respectively. These values are very close to the experimentally observed 555 cm^{-1} (800 K) and 526 cm^{-1} (757 K), which makes it reasonable to assume that the two barriers match. Therefore, we suggest that relaxation in $\{Tb_2\}$ in high-temperature regime proceeds via the first exchange state corresponding to the flip of one of the Tb-ion moments. Based on this assumption, we can use the experimentally determined values of U^{eff} to make more precise estimation of the coupling constant values, using the equation $U^{eff}=2\cdot J\cdot j^{eff}$ (j^{eff} = 46.3 cm^{-1} for $Tb_2@C_{80}(CH_2Ph)$ and 43.8 cm^{-1} for $Tb_2@C_{79}N$).

It is interesting to compare the magnetic properties of $Tb_2@C_{80}(CH_2Ph)$ and $Tb_2@C_{79}N$, as these molecules have identical spin system encapsulated in the same fullerene cage but with different "defects" (one C-sp^3 atom in the benzyl adduct versus one nitrogen atom in the azafullerene). It appears that $Tb_2@C_{80}(CH_2Ph)$ is slightly stronger SMM. Thus, despite the overall similarity of the two SMMs, we can conclude that the fullerene cage is not just an inert container but has a certain influence on the SMM behavior.

4.6 TbY@$C_{80}(CH_2Ph)$

To answer the question if symmetry in the [Ln^{3+}-*e*-Ln^{3+}] spin system is essential for excellent SMM performance, in the sense if the same type of the Ln element is necessary, we studied the mixed-metal {TbY} compound. Substitution of one Tb ion with the non-magnetic Y, resulted in dramatic increase of the relaxation rate. {TbY} shows very narrow hysteresis only below 5 K. The opening is observed in the field range of 0.1-1.0 T, whereas near zero-field the hysteresis is closing.

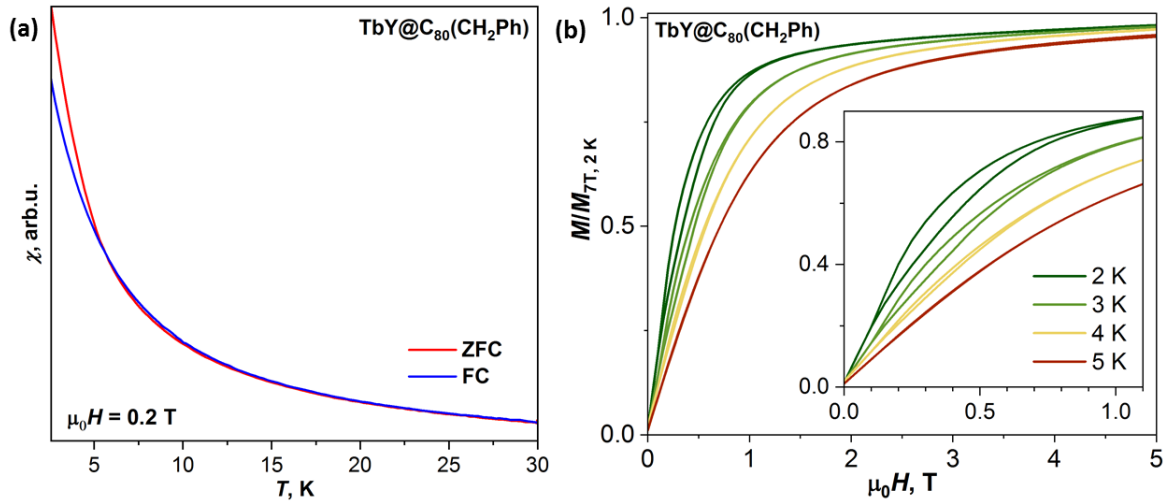

Figure 4.6.1 (a) Blocking temperature curves of {TbY}, showing divergence below 5 K; (b) In accordance, hysteresis is observed only below 5 K.

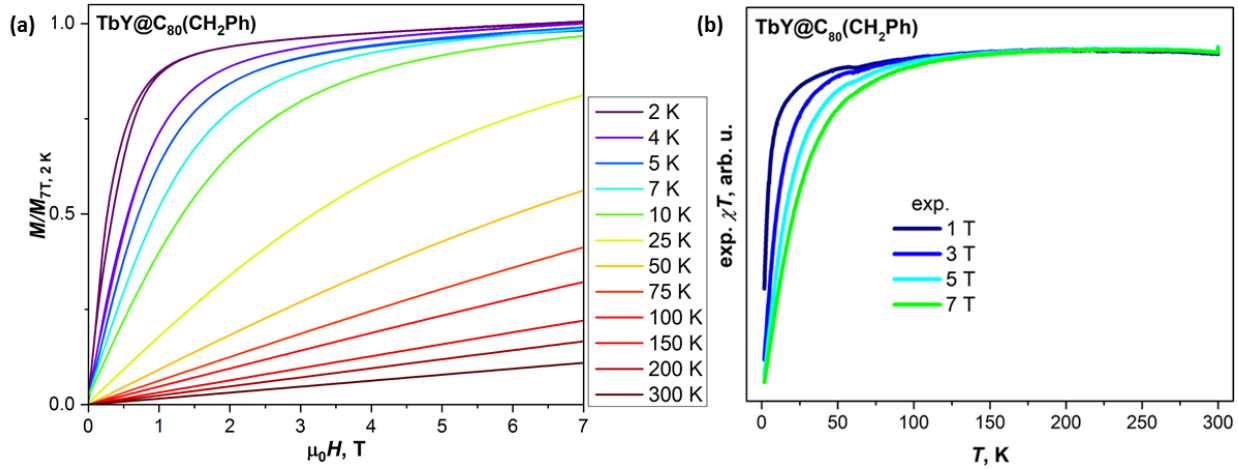

Figure 4.6.2 (a) Magnetization curves of {TbY} measured in the range of 2-300 K. The curves are normalized by the magnetization value of the sample measured at 7 T, 2 K; (b) χT-T curves measured in the constant fields of 1, 3, 5 and 7 T.

In our analysis, we tried to simulate the magnetic properties of {TbY} with the same Hamiltonian as for {Tb_2}, except now that we have only one Tb ion, which means only one single-ion LF term and no Tb-Tb interactions. The spin Hamiltonian is reduced to the following form:

$$\hat{H}_{\text{spin}}(\{\text{TbY}\}) = \hat{H}_{Tb} - 2j_{Tb,e}^{eff}\hat{s}_e \cdot \hat{J}_{\text{Tb}} \qquad (4.6.1)$$

Comparison between experimental and simulated χT curve at 1 T, gives best agreement for $j_{Tb,e}^{\text{eff}}$ in the range of 30-40 cm^{-1}. Absolute experimental χT values are not known and are scaled to reproduce the calculated data. The optimal $j_{Tb,e}^{\text{eff}}$ value is smaller than that for {Tb$_2$}, presumably because of the asymmetry of the unpaired electron distribution between Tb and Y.

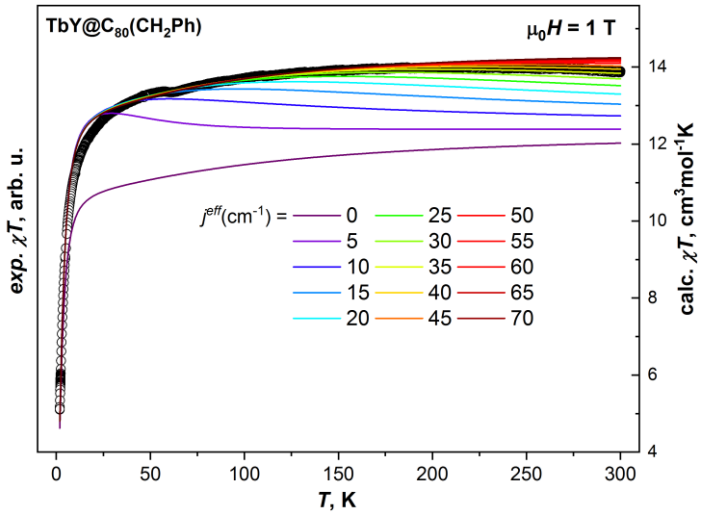

Figure 4.6.3 Experimental χT curve of {TbY} measured in the field of 1 T (dots), compared to the calculated curves for different values of the exchange parameter $j_{Tb,e}^{\text{eff}}$. Calculated curves approach the experimental data for $j_{Tb,e}^{\text{eff}}$ in the range from 30 to 40 cm^{-1}. However the low-temperature part is not reproduced well.

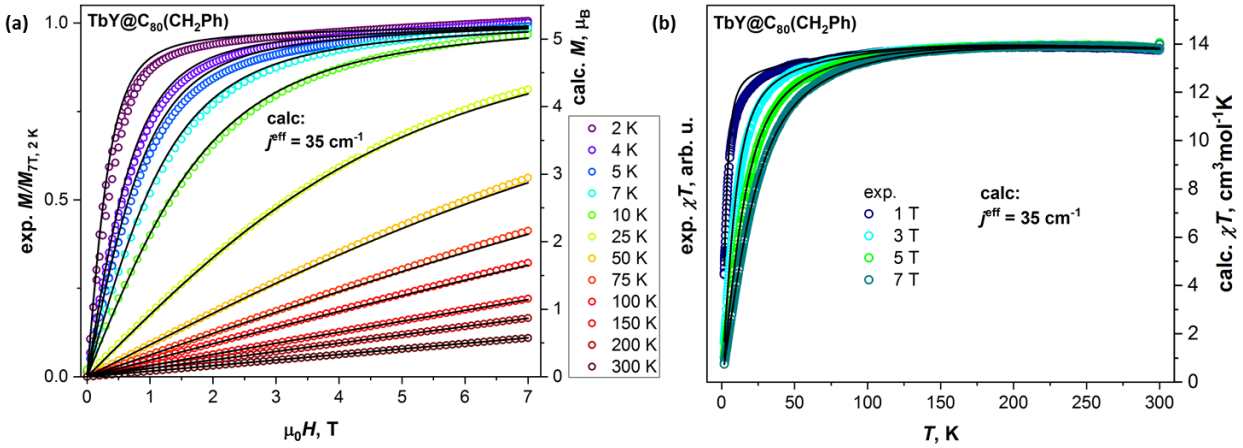

Figure 4.6.4 Magnetization curves of {TbY} (dots) compared to the results of calculations for $j_{Tb,e}^{\text{eff}}$ = 35 cm^{-1} (lines). Experimental points are normalized by the magnetization value measured at 7 T, 2 K. Low-temperature curves show a noticeable deviation from the calculated ones.

The calculated curves saturate at high fields, whereas experimental show continuous growth of magnetization in the whole accessible field range. We suggest that this is caused by the limited applicability of the spin Hamiltonian for {TbY}.

AC susceptibility measurements were performed. Temperature dependence in 0 T/0.3 T constant DC field was studied, between 1.5-35 K (0 T) and 2-18 K (0.3 T), and field dependence (0 to 1 T, with small step) in constant temperature (4 K).

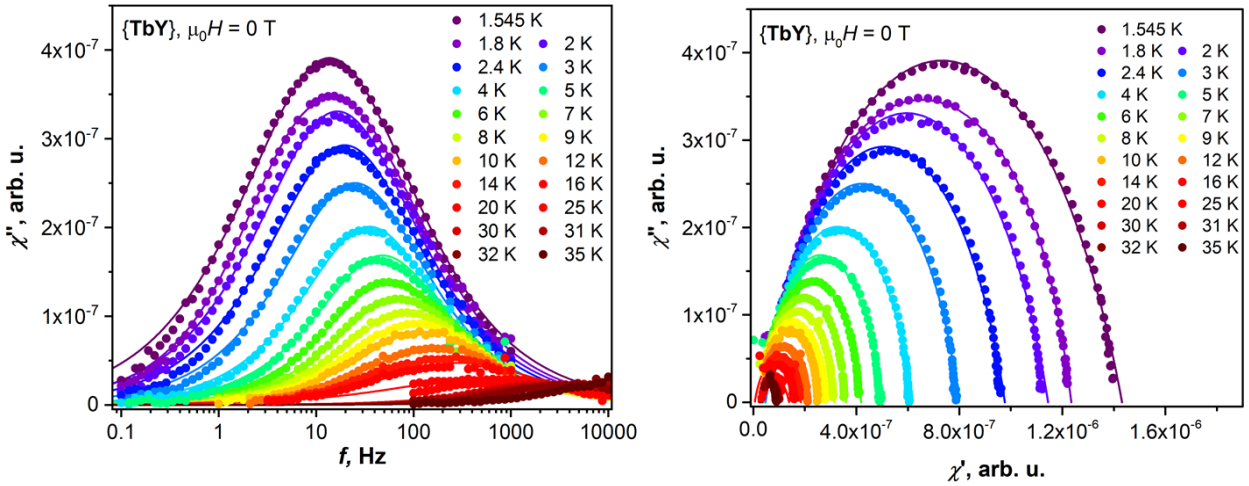

Figure 4.6.5 Temperature dependence of χ'' in zero field (left) and corresponding Cole-Cole plots (right). Dots are experimental data, lines are results of the fit with generalized Debye model.

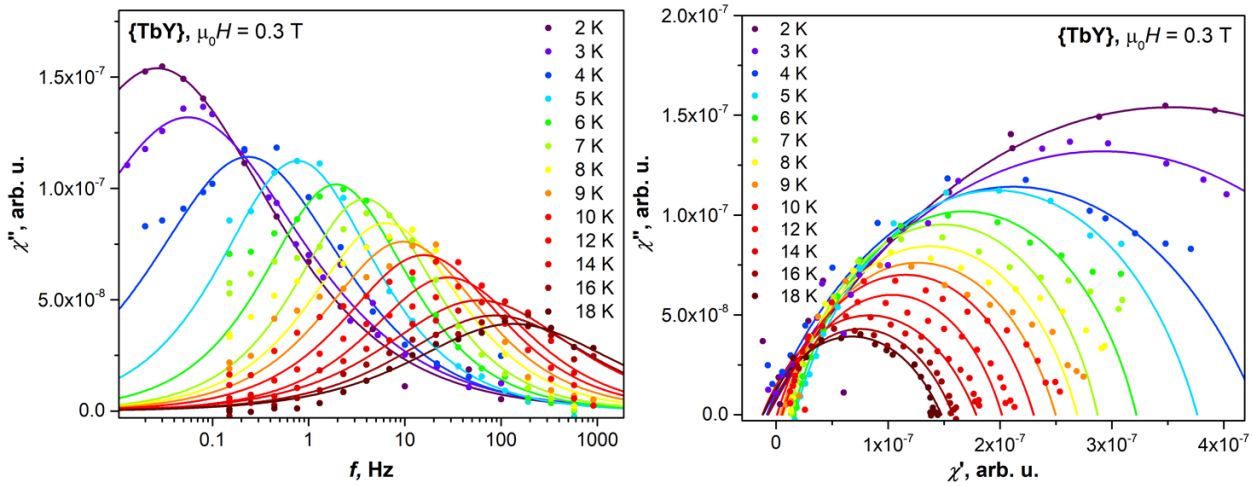

Figure 4.6.6 Temperature dependence of χ'' in the field of 0.3 T (left) and corresponding Cole-Cole plots (right). Dots are experimental data, lines are results of the fit with generalized Debye model.

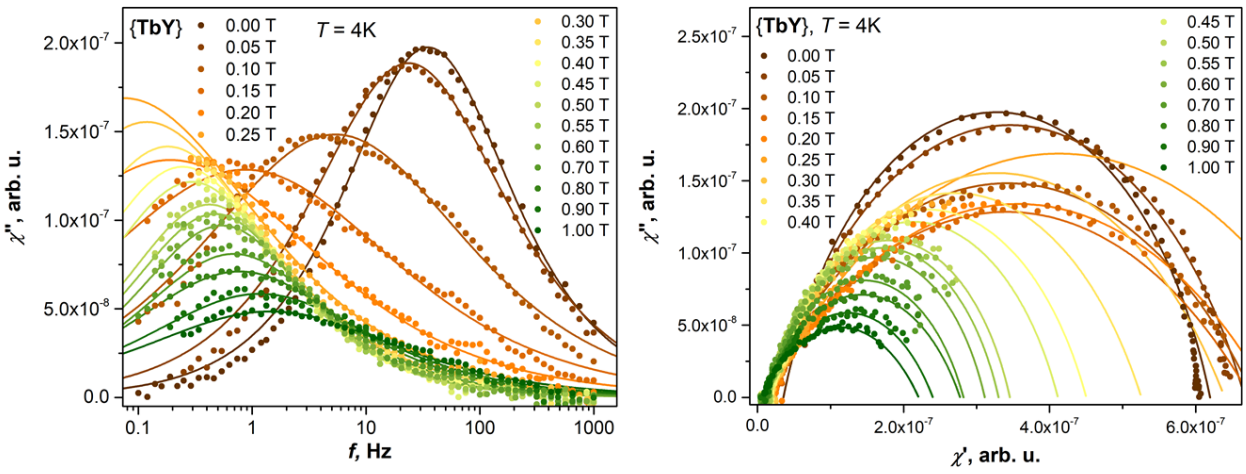

Figure 4.6.7 Field dependence of χ'' at 1.8 K (left) and Cole-Cole plots (right).

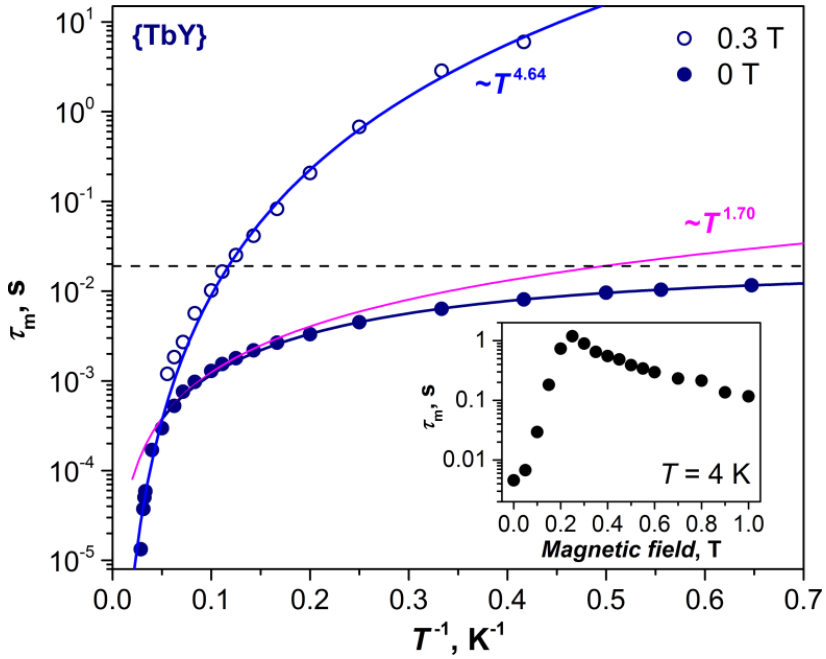

Figure 4.6.8 Magnetic relaxation times of {TbY}, dashed horizontal line is a QTM contribution to zero-field relaxation, magenta line is a low-power process (~$T^{1.70}$), dark blue line is a combination of both, light blue line is a Raman process (~$T^{4.64}$). The inset shows magnetic field dependence of relaxation times at 4 K;

AC measurements showed that in-field and zero-field magnetization relaxation times of {TbY} are considerably different below 15 K, and the difference is reaching a factor of 450 at 2 K (2.9 s at 0.3 T versus 6 ms in zero field). The field dependence of τ_m measured at 4 K has a sharp maximum at 0.25 T. Such a strong variation of relaxation time with magnetic field points to a considerable contribution of zero-field tunnelling at low temperatures. However, zero-field relaxation rate shows temperature dependence down to 1.8 K. The low-temperature part is well described by a combination of temperature-independent QTM and a power function of temperature, $\tau^{-1} =$

$\tau_{\mathrm{QTM}}^{-1} + AT^n$, with τ_{QTM} = 19.0±0.6 ms, A = 16±1 $s^{-1} K^{-n}$, and n = 1.70±0.04. The exponent of 1.7 is close to the expected value for a direct (n=1) or a bottleneck direct process (n=2). However, this temperature dependent process should be strongly linked to QTM because it is not observed anymore when the finite field of 0.3 T is applied. Temperature dependence of the in-field relaxation rate as well as high-temperature zero-field relaxation are well described by a power function with parameters A = 2.5±0.5 $ms^{-1} K^{-n}$, and n = 4.64±0.08.

Concluding, fitting of χT and magnetization measurements with the short version of Hamiltonian (eq. 4.6.1), including only single lanthanide ion exchange-coupled to electron spin, gives the optimal $j_{Tb,e}^{\mathrm{eff}}$ value of 35 cm^{-1}, thus being considerably smaller than the Tb-electron coupling constant in {Tb_2}. These results prove that coupling of the single lanthanide spin to a delocalized electron spin of the single-electron Tb-Y bond is not sufficient to create a strong SMM and that the presence of two local lanthanide spins in {Ln_2}, preferably both of uniaxial anisotropy type, is indeed essential.

4.7 $Ho_2@C_{80}(CH_2Ph)$

$Ho_2@C_{80}(CH_2Ph)$ was the next lanthanide di-EMF to study after the success of $\{Tb_2\}$ analogues. However, $\{Ho_2\}$ proved to be far inferior single-molecule magnet. Magnetization curves revealed typical paramagnetic behavior, while $\chi \cdot T$-T curves featuring an increase at low temperatures and fields, indicated FM coupling between the lanthanide moment and the delocalized electron spin.

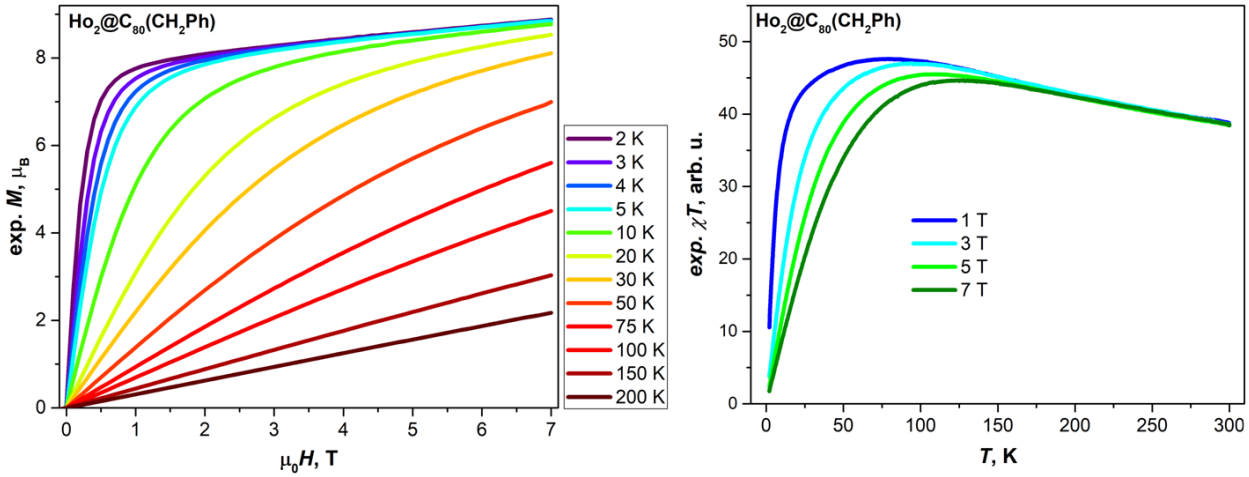

Figure 4.7.1 Experimental magnetization and χT-T curves of $\{Ho_2\}$ measured at different temperatures and mangetic fields respectively.

pKD	Ho1		Ho2	
	E, cm^{-1}	Composition, %	E, cm^{-1}	Composition, %
1	0.0	$64\|\pm8\rangle + 14\|\pm7\rangle + 10\|\pm6\rangle$	0.0	$63\|\pm8\rangle + 19\|\pm6\rangle + 9\|\pm4\rangle$
	0.1	$64\|\pm8\rangle + 14\|\pm7\rangle + 10\|\pm6\rangle$	0.6	$64\|\pm8\rangle + 19\|\pm6\rangle + 8\|\pm4\rangle$
2	165.6	$31\|\pm3\rangle + 20\|\pm2\rangle + 18\|\pm5\rangle$	130.1	$29\|\pm5\rangle + 29\|\pm3\rangle + 18\|\pm4\rangle$
	172.6	$34\|\pm3\rangle + 13\|\pm2\rangle + 18\|\pm5\rangle$	138.1	$27\|\pm5\rangle + 23\|\pm4\rangle + 22\|\pm3\rangle$
3	262.7	$40\|\pm7\rangle + 28\|\pm6\rangle + 20\|\pm4\rangle$	245.2	$63\|\pm7\rangle + 19\|\pm6\rangle + 6\|\pm3\rangle$
	268.0	$42\|\pm7\rangle + 32\|\pm6\rangle + 20\|\pm4\rangle$	246.9	$65\|\pm7\rangle + 16\|\pm6\rangle + 5\|\pm3\rangle$
4	305.6	$40\|\pm5\rangle + 22\|\pm2\rangle + 20\|\pm1\rangle$	292.9	$33\|\pm2\rangle + 29\|\pm5\rangle + 19\|\pm4\rangle$
	342.0	$58\|\pm5\rangle + 12\|\pm2\rangle + 12\|\pm4\rangle$	323.6	$36\|\pm2\rangle + 25\|\pm4\rangle + 22\|\pm5\rangle$
5	378.8	$27\|\pm7\rangle + 18\|\pm8\rangle + 14\|\pm5\rangle$	363.0	$38\|\pm4\rangle + 19\|\pm7\rangle + 17\|\pm3\rangle$
	399.8	$28\|\pm7\rangle + 20\|\pm8\rangle + 17\|\pm6\rangle$	377.1	$55\|\pm1\rangle + 15\|\pm3\rangle + 12\|\pm4\rangle$
	407.4	$40\|\pm1\rangle + 20\|0\rangle + 11\|\pm6\rangle$	405.3	$25\|\pm6\rangle + 24\|\pm7\rangle + 20\|\pm1\rangle$
	448.6	$32\|\pm6\rangle + 31\|\pm4\rangle + 16\|\pm1\rangle$	428.2	$25\|0\rangle + 19\|\pm6\rangle + 14\|\pm1\rangle$
	450.8	$29\|\pm4\rangle + 24\|0\rangle + 20\|\pm3\rangle$	436.0	$30\|\pm6\rangle + 20\|\pm5\rangle + 14\|\pm3\rangle$
	486.6	$42\|\pm3\rangle + 17\|\pm4\rangle + 15\|0\rangle$	451.0	$45\|\pm3\rangle + 22\|\pm5\rangle + 14\|\pm1\rangle$
	555.3	$39\|\pm3\rangle + 23\|\pm1\rangle + 16\|\pm2\rangle$	526.5	$42\|\pm2\rangle + 17\|0\rangle + 13\|\pm4\rangle$
	581.2	$29\|\pm2\rangle + 29\|0\rangle + 17\|\pm1\rangle$	534.2	$36\|0\rangle + 22\|\pm2\rangle + 13\|\pm1\rangle$

Table 4.7.1 CASSCF/SO-RASSI calculations summary for $\{HoY\}^-$ molecule. Energies and state compositions of pseudo-Kramers doublets (pKDs) and singlet states of the Ho1 and Ho2 ions in single-ion frame. The contribution for the "$|\pm X\rangle$" state means a sum of contributions for $|+X\rangle$ and $|-X\rangle$ states.

The magnetic moment of each Ho ion is predicted to be tilted from the Ho-Ho axis by 13.4°. Therefore, for a non-Ising type magnetic anisotropy our effective spin Hamiltonian of eq. 4.7.1 cannot capture the whole underlying physics. Nevertheless, we still choose to use it as a first approximation to simulate our experimental data.

$$\widehat{H}_{\mathrm{spin}}(\{\mathrm{Ho_2}\}) = \widehat{H}_{\mathrm{Ho_1}} + \widehat{H}_{\mathrm{Ho_2}} - 2j_{\mathrm{Ho,e}}^{eff}\hat{s}_{\mathrm{e}}\left(\hat{J}_{\mathrm{Ho_1}} + \hat{J}_{\mathrm{Ho_2}}\right) \qquad (4.7.1)$$

Comparison with the experimental 1 Tesla χT curve (fig. 4.7.2), shows best convergence with the simulated χT curve for $j_{Ho,e}^{eff}$ values between 35-45 cm^{-1}. The closest match is found for $j_{Ho,e}^{eff}$ equal to 40 cm^{-1}, and with this value adopted we simulate all the experimental curves (fig. 4.7.3).

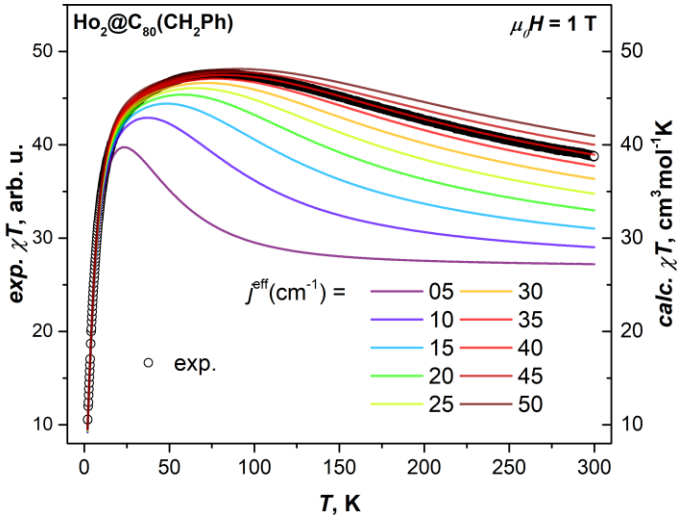

Figure 4.7.2 Experimental χT-T curve of {Ho_2} measured in the field of 1 T (open circles), compared to the calculated curves with different values of the exchange parameter $j_{Ho,e}^{\mathrm{eff}}$.

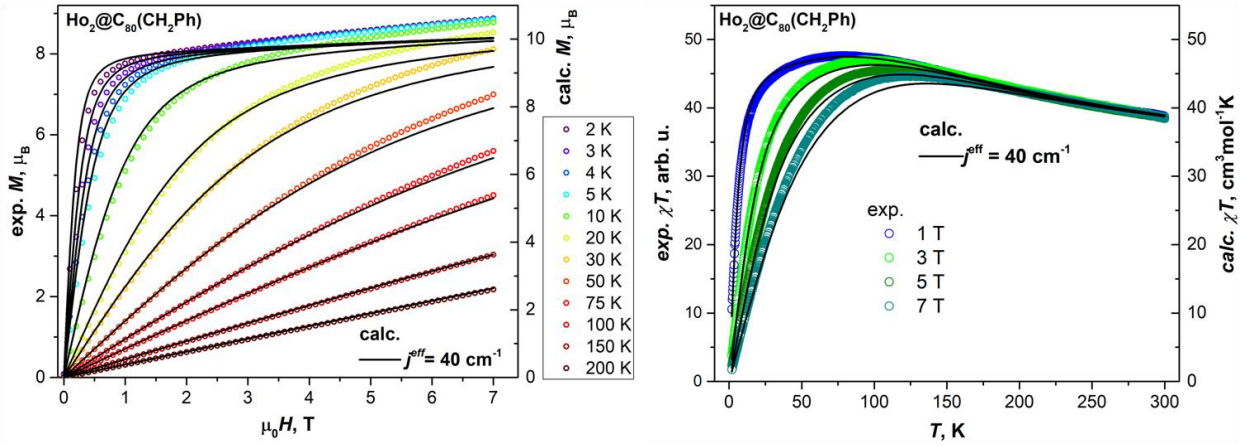

Figure 4.7.3 Exp. magnetization and χT-T curves of {Ho_2} (dots), compared to the calculated curves for the exchange parameter $j_{Ho,e}^{\mathrm{eff}}$= 40 cm^{-1} (black lines).

The deviation of the shape of experimental and calculated curves is seen at all temperatures and fields. In case of *M-H* curves, we see that at 2 K, the experimental curve show continuous growth of magnetization at high fields, whereas calculated curve saturates already at 2 T. This deviation in the shapes of experimental and calculated curves is more pronounced at low temperatures. Also, our attempt to reproduce the experimental χT curves gave poorer agreement than that for {Tb_2}. We suggest that this is caused by the limited applicability of the effective spin Hamiltonian for {Ho_2} with two non-collinear Ho spins.

The spin Hamiltonian spectrum was calculated for the value of $j^{\mathrm{eff}}_{Ho,e}$= 40 cm^{-1}. The lowest-energy exchange-excited state is predicted to be 374 K.

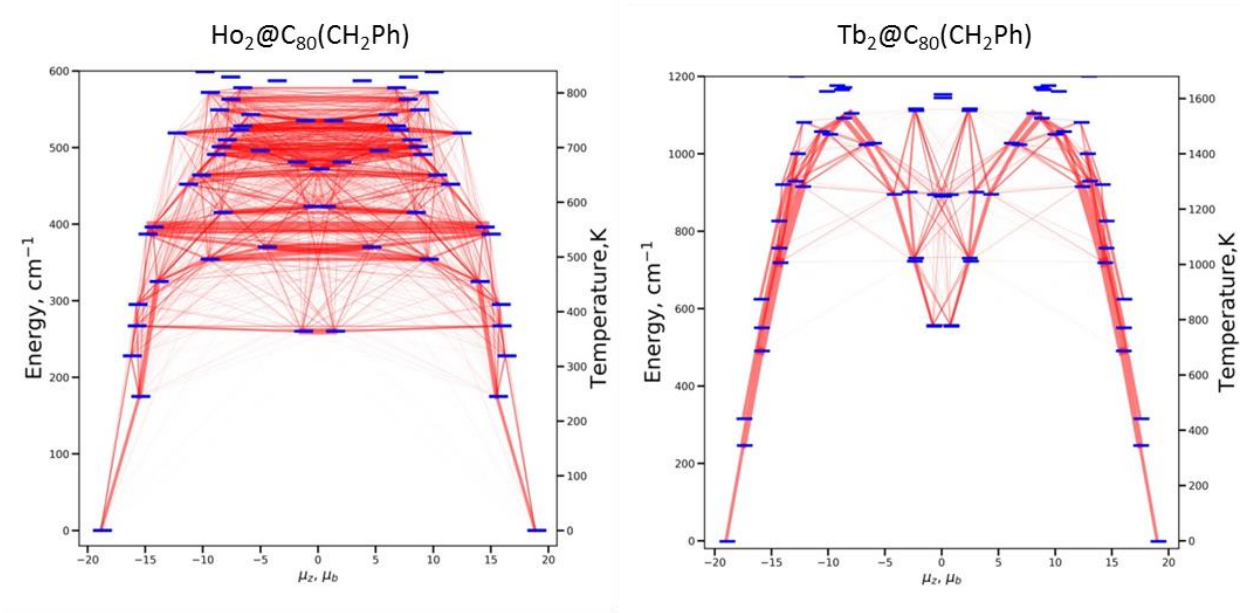

Figure 4.7.4 (a) Low-energy part of the spin Hamiltonian spectrum for {Ho_2} with $j^{\mathrm{eff}}_{Ho,e}$= 40 cm^{-1}; (b) for comparison, the low-energy part of the spin Hamiltonian spectrum for {Tb_2} with $j^{\mathrm{eff}}_{Tb,e}$= 50 cm^{-1} is also presented. Transition probabilities for the low-energy range are visualized as lines of different thickness (thicker lines correspond to higher probabilities).

It is instructive to compare the lower parts of {Ho_2} and {Tb_2} Hamiltonian spectra as calculated from their respective spin Hamiltonian equations. Since single-ion anisotropy of Ho in {Ho_2} is weaker, the first excited LF state in {Ho_2} occurs at lower energy than in {Tb_2}. Further, the lowest-energy exchange-excited states happen at roughly twice lower energy than in {Tb_2}. Altogether, the {Ho_2} spectrum is much more dense, meaning there are more relaxation pathways between the excited states and higher transition possibilities between them. Thus, a faster relaxation of magnetization can be expected in {Ho_2} based on this data, and indeed observed experimentally.

Magneto-dynamics was also studied for {Ho_2}. As blocking temperature of magnetization is below 1.8 K, it is possible to study the relaxation of {Ho_2} only via AC magnetometry. We performed a series of zero-field and in-field (0.1, 0.2, 0.3 and 0.4 T) susceptibility measurements between 1.8 and 19.9 K, in the MPMS-XL (0.1-1.000 Hz) and PPMS (100-10.000 Hz). We also studied the field-dependence of relaxation at 1.8 and 5 K. The results are presented below.

Temperature-dependence of {Ho_2} relaxation times at 0 and 0.2 T constant fields (MPMS):

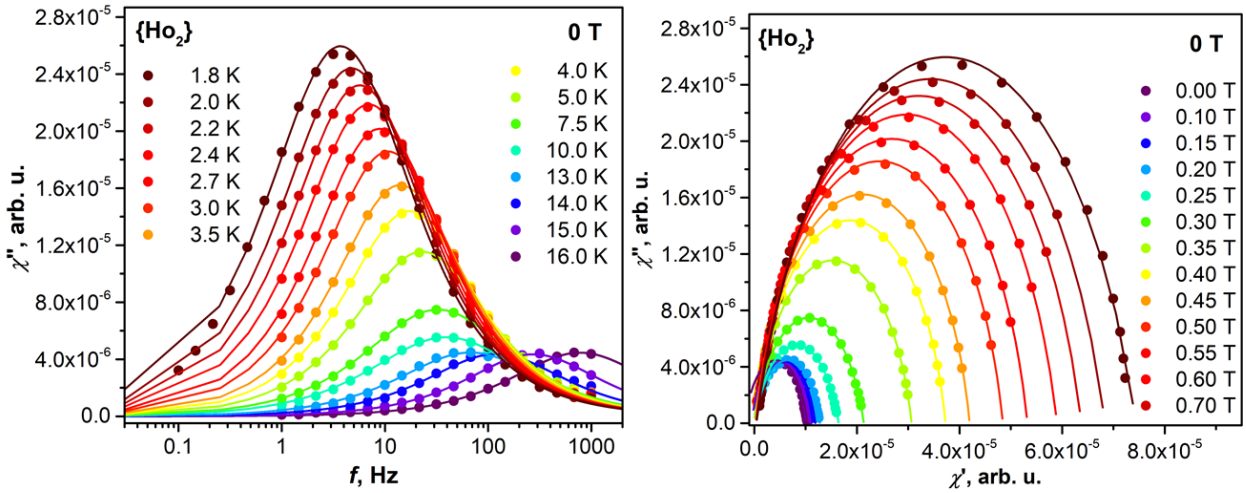

Figure 4.7.5 Temperature dependence of $\chi''(\omega)$ of {Ho_2} measured in zero-field (left) and corresponding Cole-Cole plots (right). Measurements are performed with MPMS-XL system between 1.9 and 16 K. Dots are experimental data, lines are results of the fit with generalized Debye model.

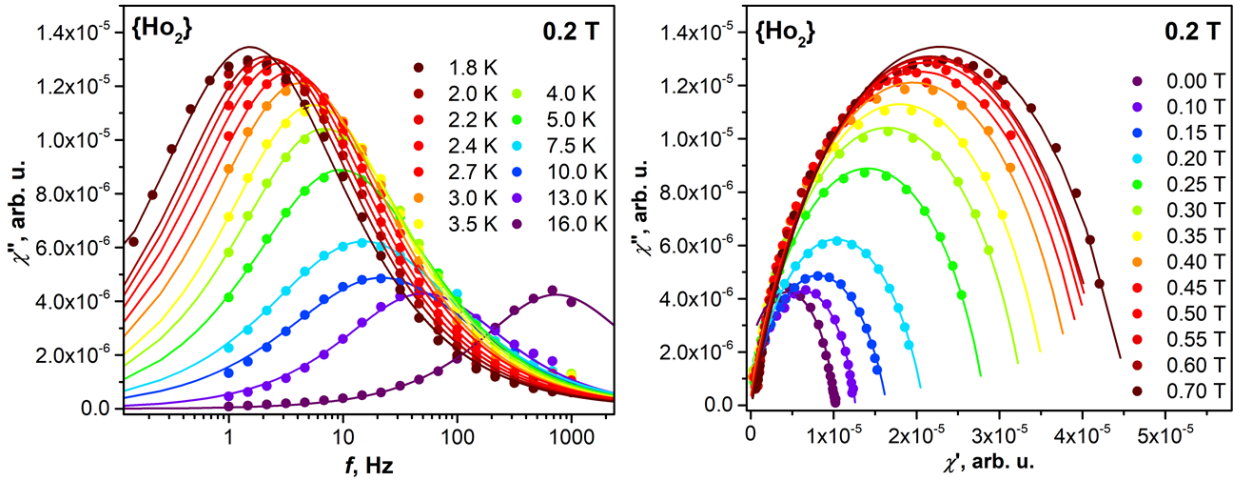

Figure 4.7.6 Temperature dependence of $\chi''(\omega)$ of {Ho_2} measured in 0.2 T field (left) and corresponding Cole-Cole plots (right). Measurements are performed with MPMS-XL system between 1.9 and 16 K. Dots are experimental data, lines are results of the fit with generalized Debye model.

Temperature-dependence of {Ho_2} relaxation times at 0 and 0.2 T constant fields (PPMS):

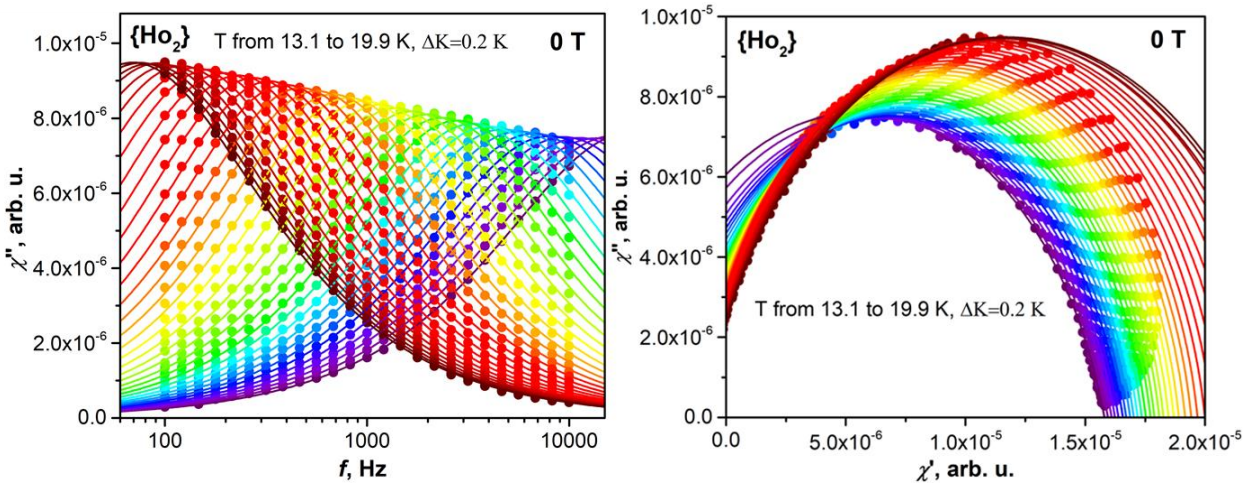

Figure 4.7.7 Temperature dependence of $\chi''(\omega)$ of {Ho_2} measured in zero-field (left) and corresponding Cole-Cole plots (right). Measurements were performed with PPMS system between 13.1 and 19.9 K. Dots are experimental data, lines are results of the fit with generalized Debye model.

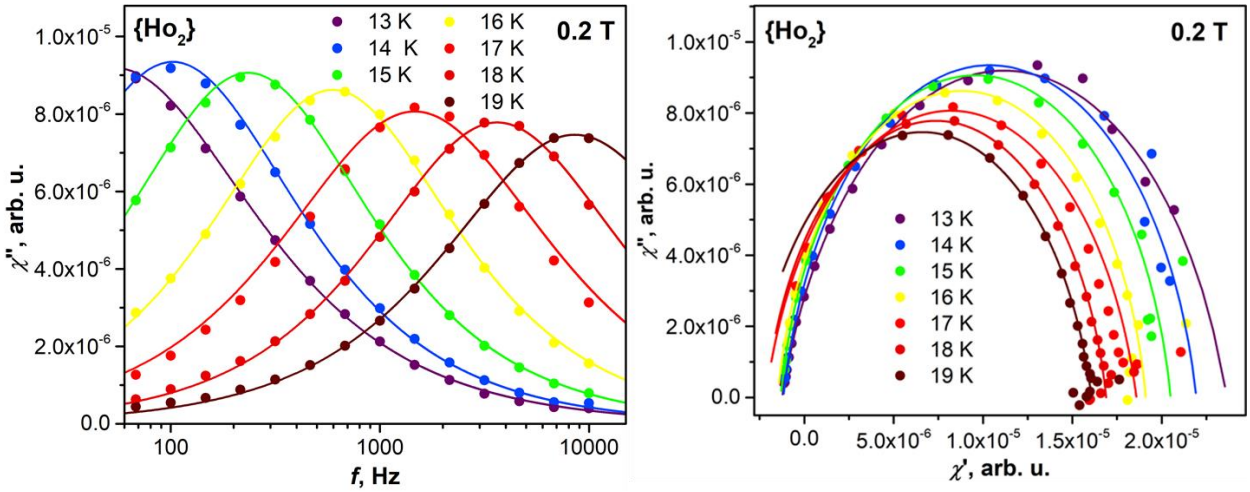

Figure 4.7.8 Temperature dependence of $\chi''(\omega)$ of {Ho_2} measured in 0.2 T (left) and the corresponding Cole-Cole plots (right). Measurements are performed with PPMS system between 13 and 19 K. Dots are experimental data, lines are results of the fit with generalized Debye model.

Field-dependence of {Ho_2} relaxation times at 1.8 and 5 K:

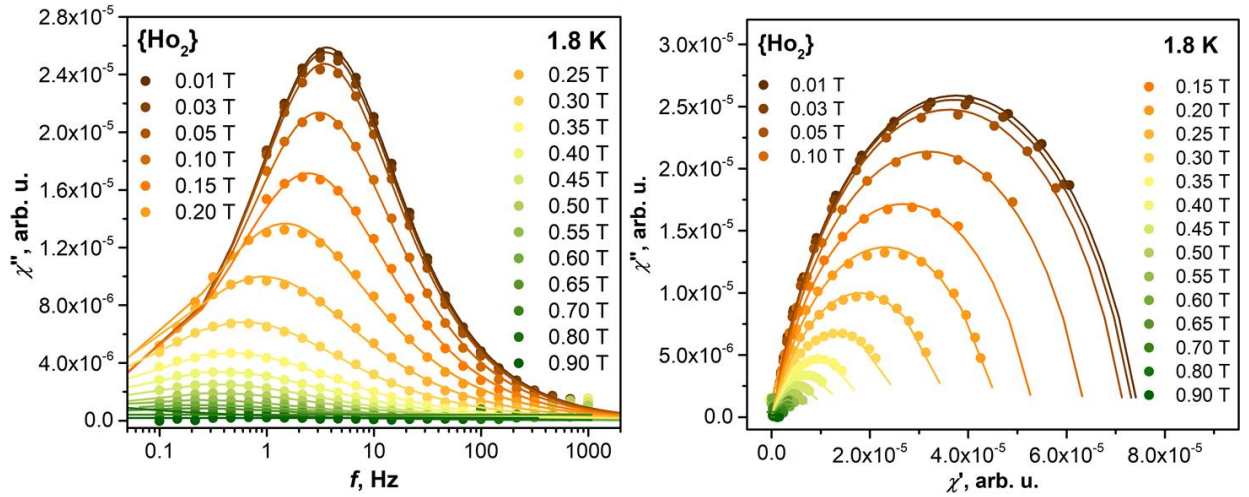

Figure 4.7.9. Field dependence of $\chi''(\omega)$ of {Ho_2} measured at 1.8 K (left) and corresponding Cole-Cole plots (right). Measurements are performed in MPMS system. Dots are experimental data, lines are results of the fit with generalized Debye model.

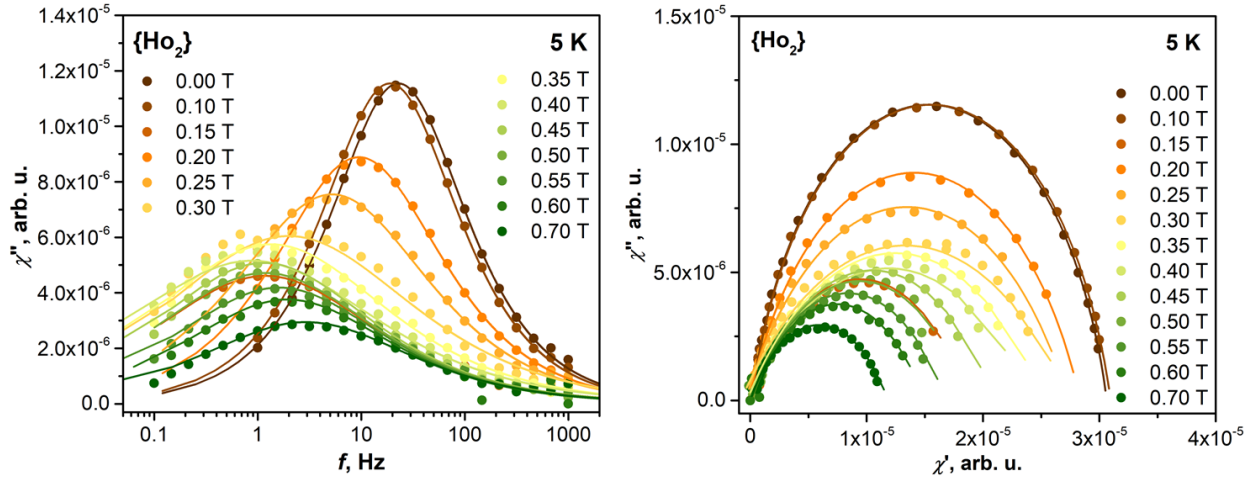

Figure 4.7.10 Field dependence of $\chi''(\omega)$ of {Ho_2} measured at 5 K (left) and corresponding Cole-Cole plots (right). Measurements are performed in MPMS system. Dots are experimental data, lines are results of the fit with generalized Debye model.

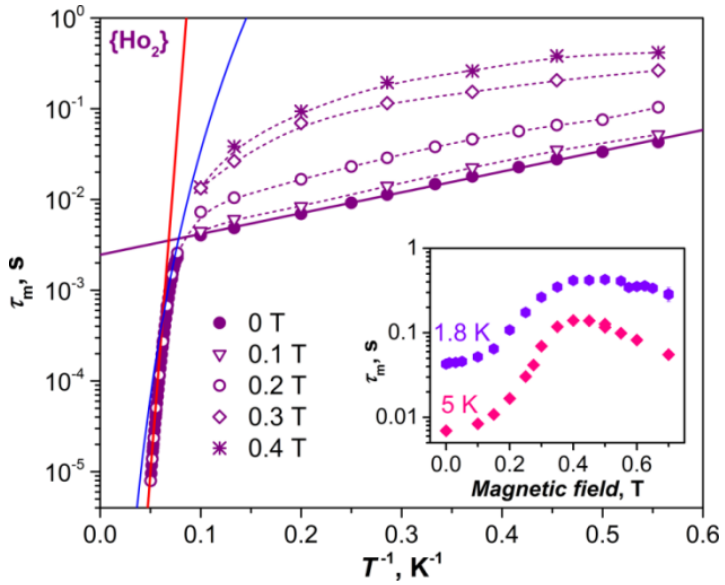

Figure 4.7.11 Magnetic relaxation times of $\{Ho_2\}$ in zero field (full dots) and in different fields between 0.1 and 0.4 T; red and purple solid lines are Orbach processes, blue line is a possible Raman contribution; the inset shows magnetic field dependence of relaxation times at 1.8 and 5 K.

Relaxation times of $\{Ho_2\}$ determined by AC magnetometry between 1.8 and 20 K show peculiar temperature and field dependencies (fig. 4.7.11). Between 1.8-10 K in zero field, the compound exhibits a linear $\log(\tau)$-vs-T^{-1} dependence described by the Orbach mechanism with U^{eff} of 5.3±0.1 K and τ_0 of 2.46±0.06 ms. With the increase of magnetic field up to 0.5 T, the relaxation decelerates and the linear dependence is gradually transformed into a curved one. Deceleration of relaxation with the application of a magnetic field is a typical characteristic of QTM, but the pronounced temperature dependence does not allow us to qualify it as such. Such a behavior may correspond to thermally-assisted QTM, i.e. QTM via an excited state. The nature of this state is not clear at this moment since the energy of 5.3 K is much smaller than the predicted ligand field splitting. If the magnetic field exceeds 0.5 T, the relaxation accelerates again (inset in fig. 4.7.11). The increase of the relaxation rate with the further increase of the magnetic field is an indication of the relaxation via the direct mechanism, which involves phonons of the frequency corresponding to the energy gap between the opposite spin states.

Above 10 K, the relaxation of magnetization becomes field-independent and exhibits rapid acceleration with temperature. The $\log(\tau)$-vs-T^{-1} dependence deviates from the linear form and cannot be assigned to a single Orbach process. The best fit to the data is obtained by combination of Orbach and Raman mechanisms with U^{eff}=334±10 K, τ_0=(5.6±2.6)·10^{-13} s, n_R=10.1±0.3, and A=(1.71±1.3) 10^{-9} s^{-1} $K^{-10.1}$. Similarly good fit is obtained for a combination of two Orbach processes with the following parameters: U_1^{eff}=324±5 K, τ_{01}=(0.8±0.2)·10^{-12} s and U_2^{eff}=136±5 K, τ_{02}=(1.1±0.4)·10^{-7} s. The estimated U^{eff} value of 324-334 K from the two different fittings probably corresponds to the first exchange excited state in the Hamiltonian spectrum (fig. 4.7.4a),

predicted near 370 K for $j_{Ho,e}^{\mathrm{eff}}$ value of 40 cm^{-1}. The interpretation with two Orbach processes leaves the question of the nature of the lower-energy state at 136 K, which has no clear correspondence in the Hamiltonian spectrum (fig. 4.7.4a). We thus conclude that the higher-temperature relaxation is most probably governed by a combination of Raman and Orbach mechanisms.

4.8 $Er_2@C_{80}(CH_2Ph)$

In contrast with {Tb_2} and {Ho_2} molecules, {Er_2} was expected to show single-ion easy-plane anisotropy, which probably would lead to inferior SMM properties. However, the study of {Er_2} was important to gain a complete view on the magnetic properties of heavier lanthanide di-EMFs.

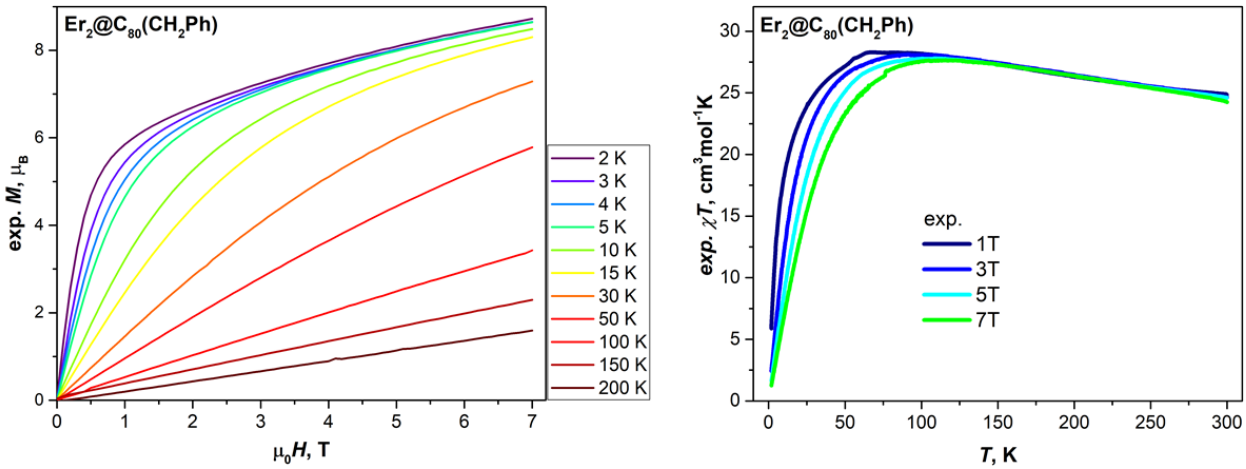

Figure 4.8.1. Experimental magnetization and χT-T curves measured at different temperatures and magnetic fields respectively.

As expected, {Er_2} exhibits typical paramagnetic behavior. M-H curves do not reach saturation at 7 T, while χT curves show some mere increase at low temperatures, indicating weak FM-coupling between the lanthanide ion and the delocalized electron spin ($j^{\mathrm{eff}}_{Er,e}$>0).

KD	Er1		Er2	
	E, cm^{-1}	Composition, %	E, cm^{-1}	Composition, %
1	0.0	$61\|\pm0.5\rangle + 19\|\pm1.5\rangle$	0.0	$38\|\pm0.5\rangle + 27\|\pm1.5\rangle + 16\|\pm2.5\rangle + 10\|\pm4.5\rangle$
2	96.4	$52\|\pm1.5\rangle + 15\|\pm2.5\rangle + 10\|\pm4.5\rangle$	85.4	$30\|\pm1.5\rangle + 26\|\pm0.5\rangle + 17\|\pm2.5\rangle + 16\|\pm3.5\rangle$
3	159.3	$26\|\pm5.5\rangle + 21\|\pm4.5\rangle + 21\|\pm2.5\rangle + 10\|\pm6.5\rangle$	123.9	$31\|\pm4.5\rangle + 24\|\pm5.5\rangle + 16\|\pm3.5\rangle + 11\|\pm1.5\rangle$
4	226.6	$19\|\pm2.5\rangle + 16\|\pm3.5\rangle + 16\|\pm6.5\rangle + 14\|\pm5.5\rangle + 13\|\pm4.5\rangle + 12\|\pm0.5\rangle$	193.2	$36\|\pm2.5\rangle + 25\|\pm3.5\rangle + 11\|\pm0.5\rangle$
5	255.7	$32\|\pm3.5\rangle + 26\|\pm2.5\rangle + 11\|\pm5.5\rangle$	229.9	$22\|\pm2.5\rangle + 19\|\pm3.5\rangle + 18\|\pm0.5\rangle + 15\|\pm1.5\rangle + 12\|\pm4.5\rangle$
6	342.0	$50\|\pm6.5\rangle + 19\|\pm7.5\rangle + 13\|\pm5.5\rangle$	315.6	$39\|\pm6.5\rangle + 30\|\pm7.5\rangle + 10\|\pm5.5\rangle$
7	429.1	$33\|\pm4.5\rangle + 28\|\pm3.5\rangle + 14\|\pm5.5\rangle$	420.8	$25\|\pm4.5\rangle + 21\|\pm5.5\rangle + 18\|\pm6.5\rangle + 18\|\pm7.5\rangle + 15\|\pm3.5\rangle$

Table 4.8.1 CASSCF/SO-RASSI calculations summary for {ErY}$^{-}$ molecule. Energies and state compositions of Kramers doublets of the Er1 and Er2 ions in single-ion frame.

Ab initio calculations predict an easy-plane character for the magnetic anisotropy of the ground state, and the simple spin Hamiltonian of eq. 4.8.1 cannot describe the spin exchange processes.

$$\widehat{H}_{\text{spin}}(\{\text{Er}_2\}) = \widehat{H}_{LF_{\text{Er}}} - 2j_{Er,e}^{eff}\hat{s}_e \cdot \hat{J}_{\text{Er}} \qquad (4.8.1)$$

Simulations showed that the shape of 1 T χT curve can be reproduced sufficiently well for $j_{Er,e}^{\text{eff}}$ ≈20 cm^{-1}. This value also gives reasonable but not perfect description of *M-H* curves. Thus, we can suggest that Er^{3+} moments are indeed coupled ferromagnetically and the coupling is still rather strong as in the rest of {Ln_2} systems.

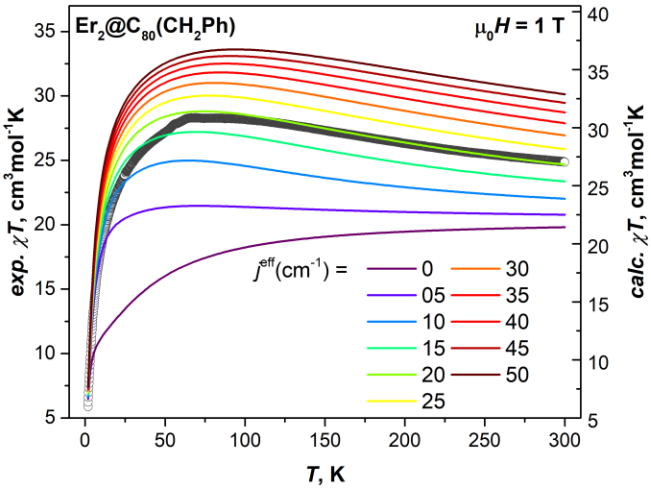

Figure 4.8.2 Experimental χT-*T* curve of {Er_2} measured in the field of 1 T (dots) compared to the calculated curves for different values of the exchange coupling constant $j_{Er,e}^{\text{eff}}$. Calculated curves are close to the experimental data for $j_{er,e}^{\text{eff}}$ = 20 cm^{-1}.

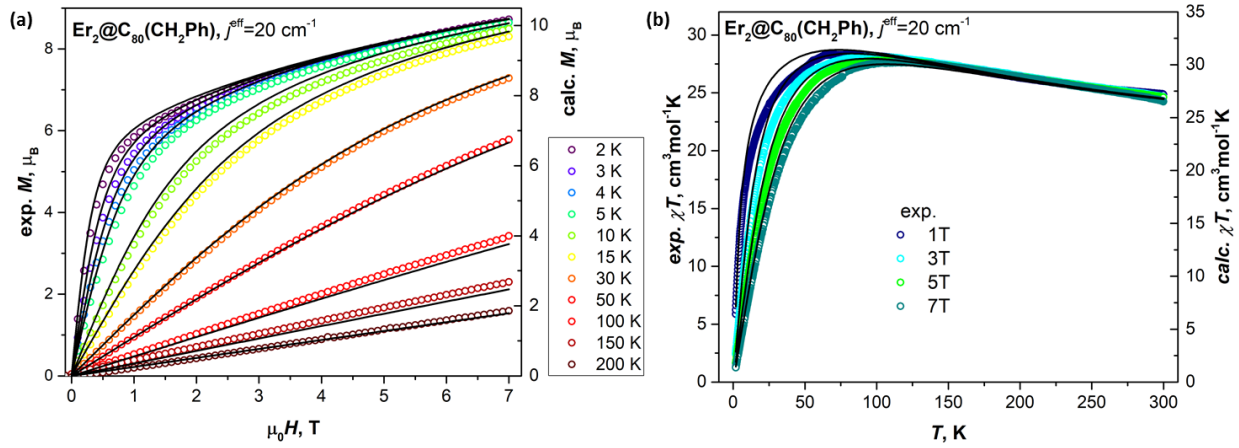

Figure 4.8.3 Exp. (a) *M-H* and (b) χT-*T* curves of {Er_2} (open circles), compared to the results of calculations for $j_{Er,e}^{\text{eff}}$=20 cm^{-1} (black lines). The deviation between experimental and calculated curves is caused by the limited applicability of the spin Hamiltonian (eq. 4.8.1) for {Er_2} (easy-plane anisotropy).

AC-magnetometry is the only method to give us more information on the magnetic relaxation of {Er_2}. It showed the out-of-phase χ'' response only at low temperatures and in the presence of a magnetic field. Field dependence of {Er_2} relaxation times at 1.8 K, and temperature dependence at 0.2 T are shown in figs. 4.8.4 and 4.8.5.

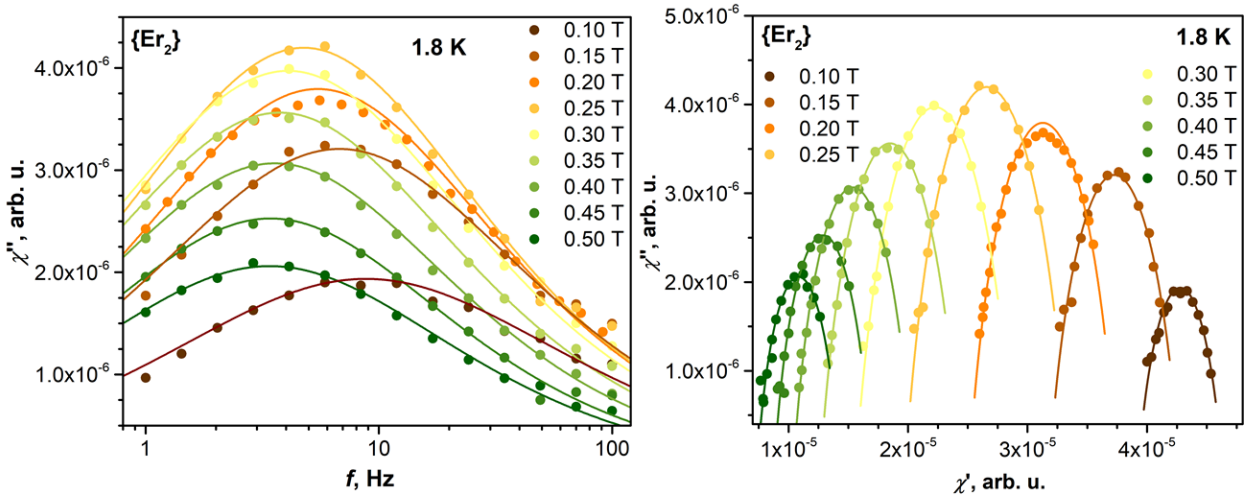

Figure 4.8.4 Field dependence of χ'' at 1.8 K (left) and Cole-Cole plots (right).

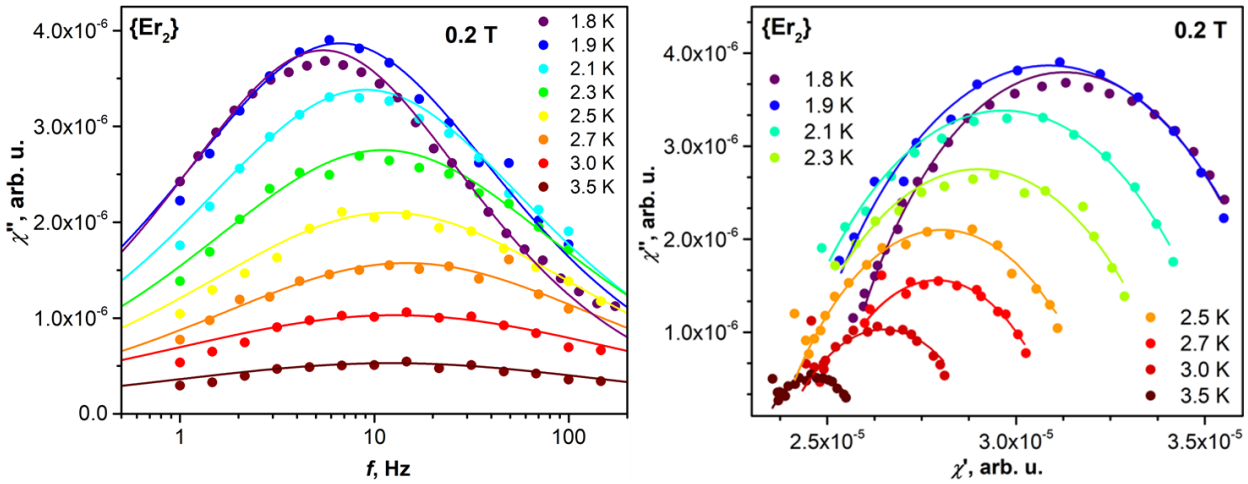

Figure 4.8.5 AC measurements of {Er_2}. Temperature dependence of χ'' in the field of 0.2 T (left) and Cole-Cole plots (right). Dots are experimental data, lines are results of the fit with generalized Debye model.

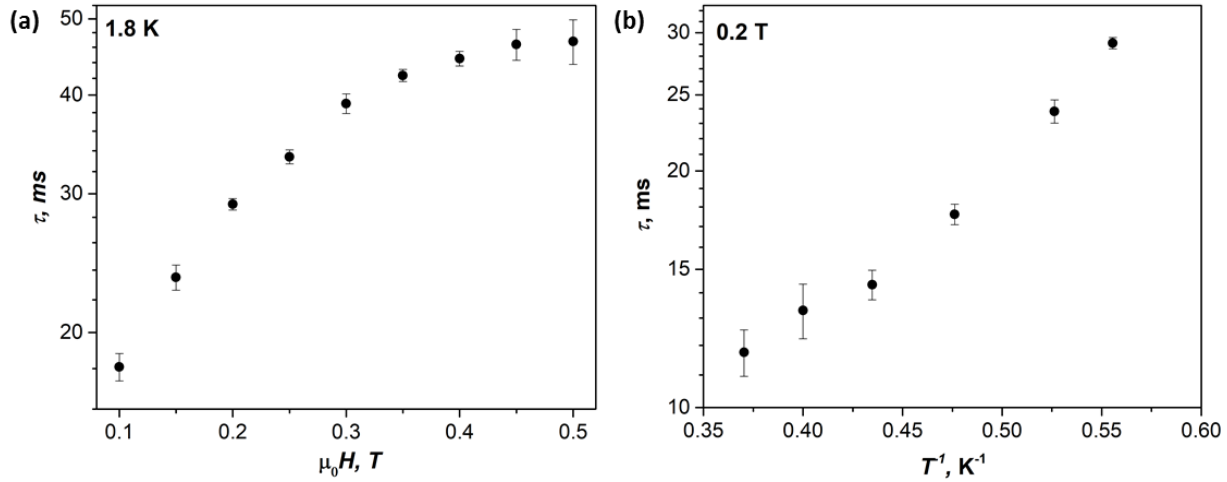

Figure 4.8.6 Relaxation times of {Er_2}: (a) field dependence at 1.8 K and (b) temperature dependence in the field of 0.2 T.

At 1.8 K, we could not detect χ" signal in zero field, but the signal appeared in the presence of an external field. The relaxation time increases with the field from 18 ms at 0.1 T to 47 ms near 0.5 T, but the χ" amplitude is the highest at 0.25 T. Temperature dependence measured in the field of 0.25 T revealed a decay of the relaxation time from 30 ms at 1.8 K to 10 ms near 3 K. Unfortunately, at higher temperatures the signal becomes too weak to be measured reliably. The assignment of the underlying relaxation processes to the SMM features of {Er_2} molecule is ambiguous because similar relaxation behavior at low temperatures may be also caused by the lattice-based phonon bottleneck. However, compared to the relaxation times measured for $Gd_2@C_{79}N$ (fig. 4.4.9) we can see the same trends in field and temperature dependence, and in the order of 10 ms for both molecules (for $Gd_2@C_{79}N$ are approximately half). Therefore, we can tentatively suggest that cooperative relaxation processes involving lattice (such as phonon-bottleneck) occur in {Ln_2} systems on the timescale of tens of ms, thus giving the low limit for SMM behaviour. As we cannot unambiguously assign this relaxation behaviour to single-molecule properties, it is likely that {Er_2} cannot be classified as a single-molecule magnet.

4.9 Summary

To summarize, our magnetic studies showed that delocalization of one unpaired electron spin in [Ln^{3+}–*e*–Ln^{3+}] system, acts as a connecting bridge between the lanthanides' magnetic moments. The strong ferromagnetic coupling emerging from the exchange interactions is responsible for the high-spin magnetic ground state in certain {Ln_2} molecules. The strong coupling alone though, is not enough to make an excellent molecular magnet. The type of single-ion anisotropy in certain ligand field environment plays crucial role. The isotropic character of Gd ion does not allow the {Gd_2} dimer to behave as superior SMM, despite the giant exchange coupling (160-170 cm^{-1}). Nevertheless, it was possible to detect in-field relaxation in the order of 20-50 ms, which gives us the idea on what one can expect in a weak SMM.

In total contrast, {Tb_2} appears to be an extremely hard single-molecule magnet. The reason behind is the strong easy-axis magnetic anisotropy of Tb^{3+} ions which leads to absolute collinearity for $Tb_2@C_{80}(CH_2Ph)$, and a small deviation of 7.2° in $Tb_2@C_{79}N$, without significant deterioration of the SMM properties. The axiality of the ligand field in {Ln_2} systems has several reasons. First, metal atoms transfer their valence electrons to the fullerene cage, resulting in accumulation of the negative charge on carbon atoms coordinated to the endohedral lanthanide ion. Note that this interaction has also considerable covalent contribution via overlap of π-electron density of the fullerene with vacant d-orbital of the lanthanide. Next, covalent Ln-Ln bonding results in a concentration of the electron density between two Ln ions. In ref. [130], the use of a simple point-charge model showed that even relatively small negative charge located between two lanthanide ions may induce rather high axial magnetic anisotropy. Thus, metal-metal bond is important not only for exchange interactions, but also to support the axial ligand field. Finally, lanthanide ions in di-EMFs have no "equatorial" ligands – the situation which also facilitates imposing of the axial ligand field.

Magnetic moments of Ho-ions appear to have larger deviation from the Ho-Ho bond-axis (13.4^0). In combination with the mixed nature of LF states, it makes {Ho_2} only a modest SMM. Finally {Er_2}, a completely different case from the previous, with easy-plane single-ion anisotropy is hardly an SMM at all. Furthermore, the coupling of a single lanthanide spin to the delocalized electron spin is also not sufficient as illustrated by the soft SMM behavior of the mixed-metal {TbY} system. Thus, homonuclear lanthanide di-EMFs with collinear spins and strong magnetic anisotropies give the best SMMs. In the table and graph next, we summarize the three types of anisotropies we met in our systems (collinear with Ln-Ln bond axis, tilted from Ln-Ln axis and easy-plane).

{Ln_2}	T_B (K)	H_C (2.9 mTs^{-1})	$j_{Ln\text{-}e}$ (cm^{-1})	Type of single-ion anisotropy
$Gd_2@C_{80}(CH_2Ph)$	< 1.8	-	170 ± 10	isotropic
$Gd_2@C_{79}N$	< 1.8	-	160 ± 10	isotropic
$Tb_2@C_{80}(CH_2Ph)$	29	6.5 T (5 K)	50 ± 3	easy-axis
$Tb_2@C_{79}N$	28	3.8 T (1.8 K)	45 ± 3	easy-axis
$TbY@C_{80}(CH_2Ph)$	5	-	35 ± 5	easy-axis
$Ho_2@C_{80}(CH_2Ph)$	< 1.8	-	40 ± 5	easy-axis
$Er_2@C_{80}(CH_2Ph)$	< 1.8	-	20 ± 5	easy-plane

Table 4.9.1 Summary of the most important SMM characteristics of {Ln_2} systems presented in this work.

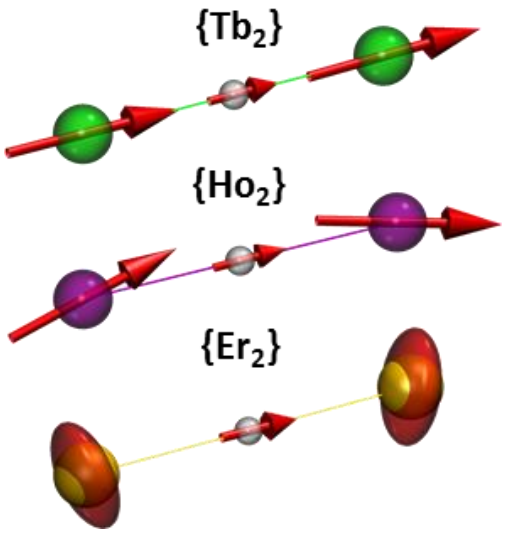

Figure 4.9.1 Schematic illustration of the alignment of Ln^{3+} magnetic moments and electron spin in {Ln_2} systems according to ab initio calculations: collinear in {Tb_2}, tilted moments in {Ho_2} (the arrows indicate directions of the single-ion quantization axis for each Ho), easy-plane in {Er_2}. In the latter the Ln moments are visualized as ellipsoids.

Chapter 5

Magnetic studies on Dy-oxide clusterfullerenes

The second family of endohedral metallofullerenes that was studied during my PhD work, is the Dy_2O-clusterfullerenes. Here, the two Dy ions are coupled via the O anion which acts like a bridge for the mediation of the exchange interactions between the two lanthanide ions. As described in Chapter 3, the encapsulation of more than one metal ions inside a fullerene opens an additional degree of freedom for tuning the magnetic properties, giving rise to FM and AFM states. Origin of the robust SMM behavior is the strong axial magnetic anisotropy of Dy ions induced by the presence of a negative ion in close distance. The type of the carbon cage hosting the Dy-cluster plays a certain role, but not fully understood yet. Significant influence of the fullerene isomerism is found for Dy nitride and sulfide clusterfullerenes [104, 139].

In this chapter, we present the first experimental study on the magnetic properties of a new class of single-molecule magnets, the $Dy_2O@C_{2n}$. Dy ions adopt their conventional 3+ oxidation state, forming ionic bond with the O^{2-}, and transferring four electrons to the carbon cage. The presence of O^{2-} in close distance to both Dy^{3+} ions (≈2 Å), imposes strong axial anisotropy to the latter. The motivation behind our work was the recent computational studies on endohedral fullerenes (2016) [140], which predicted that Dy_2O-clusterfullerenes can exhibit superior SMM properties, with thermal barriers up to 1400 cm^{-1}. The reason behind that is that the O^{2-} ionic radius is rather small, bringing the Dy ions in a very short distance, hence ensuring a strong axial ligand field, which is comparable or even larger than those observed in nitride clusterfullerenes. Following content includes a detailed analysis of the magnetic properties of five Dy_2O-clusterfullerenes, which differ only by the host carbon cage: $Dy_2O@C_{72}$-C_s/C_{74}-C_2/C_{82}-C_s/C_{82}-C_{2v}/C_{82}-C_{3v}. These molecules were synthesized by the group of Prof. Dr. N. Chen*. Hereafter, we demonstrate that

Dy_2O-clusterullerenes are molecular magnets with excellent magnetic properties depending sensitively on the size and symmetry of the host carbon cage.

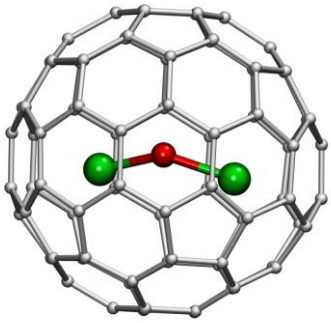

Figure 5.1 Example of a Dy_2O-clusterfullerene molecular structure (Dy^{3+} ions are represented with green color and O^{2-} with red color).

* College of Chemistry, Chemical Engineering and Materials Science, Soochow University, Suzhou, Jiangsu 215123, P.R. China

5.1 Dy-Dy exchange interactions

We already know that the presence of a negative charge near a Dy ion induces axial ligand-field. As a result, the Dy magnetic moments are aligned almost parallel to the Dy-O bond axis (similar to Dy-N). The question is how strong are the exchange interactions between the two Dy ions, and if they affect the SMM behavior. But first, we should define a way of description of the coupling between the Dy magnetic moments.

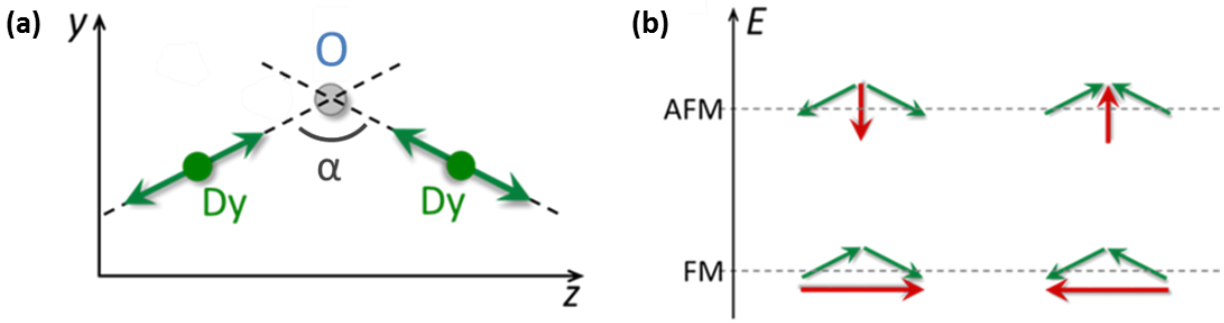

Figure 5.1.1 (a) Single-ion quantization axes (green lines) along the Dy-O bonds; Green arrows denote the two possible orientations of individual magnetic moments. In Dy_2O cluster (O is red, Dy is green) and α is the angle between the magnetic axes of Dy^{3+} ions (approximately equal to ∠Dy–O–Dy); (b) Schematic description of FM/AFM exchange states. Green arrows denote the individual magnetic moments and red arrows the total sum of them. Reproduced with permission from Dr. A. Popov.

There are only two possible orientations for each Dy magnetic moment aligned across the Dy-O axis (fig. 5.1.1a), which means we can have four possible combinations of them (fig. 5.1.b). When the two magnetic moments point towards the same direction of the Dy-Dy axis (defined as *z*-axis hereafter), the total moment (their sum) is aligned along the z-axis too. When the individual moments point to opposite directions along z-axis, the total magnetic moment is perpendicular to the Dy-Dy axis (defined as y-axis). In the following content, we will keep the convention that the two combinations that result in total moment along the z-axis correspond to ferromagnetic (FM) coupling, whereas the two combinations with total moment along the *y*-axis, describe the antiferromagnetic (AFM). This convention is selected because the magnetic moment of the FM coupling is larger than that of the AFM (length of the red arrows in fig. 5.1.1b), as long as ∠Dy–O–Dy angle exceeds π/2.

Exchange interactions between the Dy ions (or super-exchange as they are mediated via the O^{-2}) split the four possible moment configurations into two quasi-doublets, schematically shown in fig. 5.1.1b. These two quasi-doublets have in principle energy difference that acts as a barrier which prevents the quantum tunneling within the ground state quasi-doublet (FM in fig. 5.1.1). Flip of two moments as a single unity is possible though, but is a low-probability process with thermal-relaxation being more efficient. If one of the Dy moments is flipped, the di-nuclear

cluster changes state from FM to AFM (and *vice versa*). These two quasi-doublets can be described as the lowest-energy solution of the following Hamiltonian:

$$\widehat{H}_{\mathrm{spin}}(\{\mathrm{Dy_2O}\}) = \widehat{H}_{\mathrm{Dy_1}} + \widehat{H}_{\mathrm{Dy_2}} - 2j_{12}(\hat{J}_{Dy_1} \cdot \hat{J}_{Dy_2}) \quad (5.1.1)$$

where $\widehat{H}_{\mathrm{Dy_i}}$ are the Dy-ion ligand-field terms and j_{12} is the total coupling constant between the Dy moments, including the exchange and dipolar interactions. Again we assume j_{12} is isotropic, a very good approximation for Ising-type single-ion magnetic anisotropy. The sign of the coupling constant defines which of the FM/AFM state is lower in energy. The energy difference between FM and AFM states is given by the equation:

$$\Delta E_{\mathrm{AFM-FM}} = 225 j_{12} \cos(\alpha) \quad (5.1.2)$$

where α is the angle between the quantization axes (almost equal to ∠Dy–O–Dy angle). With application of an external magnetic field, both FM and AFM doublets experience energy splitting, and a crossing is possible between them at a finite field (high or low). This condition results to switching of the ground state from FM to AFM (or *vice versa*), and hence it changes dramatically the states populations. This shift is expected to be reflected in the shape of magnetization curves. To analyze it further, let's consider two cases, where in the first, the FM configuration is lower in energy than the AFM in zero-field, and in the second the opposite. Then, we examine what happens when we apply an increasing magnetic field along the z- or y-axis.

1. $E_{FM}<E_{AFM}$ (at zero-field)

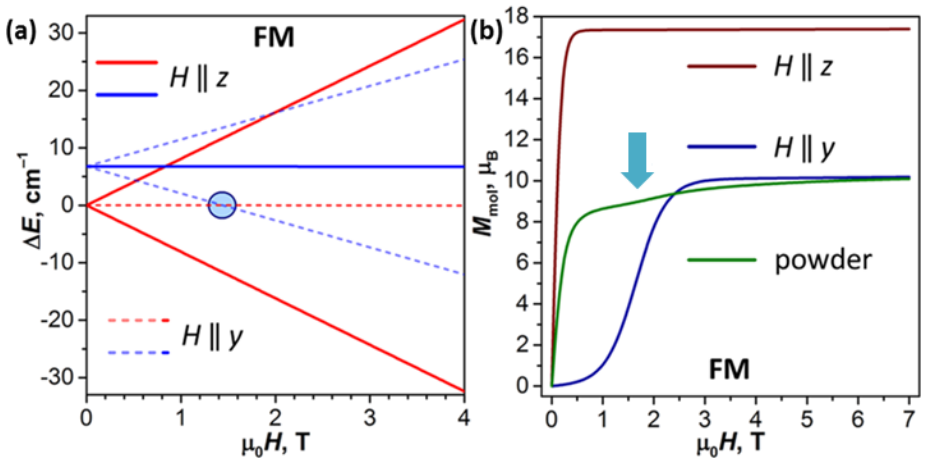

Figure 5.1.2 (a) Zeeman diagram for two orientations of the magnetic field (z and y). FM states are shown in red, AFM in blue; Field along z-axis is solid lines, and along y-axis dashed. (b) Calculated magnetization curves for the field along z (brown) and y (blue) axis, and the after powder averaging curve (green). Note the inflection area (pointed by the arrow) between 1-2 T.

In case of an applied magnetic field along the z-axis, the FM doublet is split into two energy states with parallel and antiparallel orientation of the total moment. In contrast, the AFM doublet does not experience Zeeman splitting because the total moment is oriented perpendicular to the field orientation, along the y-axis. Lower energy state becomes the one of the FM doublet with magnetic moment parallel to the external field. When the applied field is parallel to y-axis, then the FM states do not change their energy, whereas the AFM states do. At some field (marked by blue circle in fig. 5.1.2a), one of the AFM states becomes lower in energy than that of the FM doublet. The corresponding expected shapes of measured *M-H* curves are shown in fig. 5.1.2b. When the field is parallel to z-axis, the corresponding magnetization curve (brown in fig. 5.1.2b) reaches very fast the maximum value (saturation), as only the lower branch of the FM doublet is populated (100%). In the situation where *H* ∥ y, the sample does not show magnetization in small fields (blue curve in fig. 5.1.2b), because AFM states remain higher in energy so their population does not change significantly. Only when the field is beyond the point of the level crossing (blue circle), the rise of magnetization is observable, and magnetization will be saturated at a small value than for the H ∥ z case.

If we could measure magnetization of a well-ordered single-crystal, we should be able to see different magnetization curves for different orientations. But most of times we work with powder samples where the molecules are oriented in random directions. Consequently, field-averaging over all possible orientations is necessary to reproduce the experimentally measured curves (green curve in fig. 5.1.2b). We notice that an inflection appears between 1-2 T. This is the area of the fields where the crossing between FM and AFM states occurs, because depending on the

orientation of the molecule, level crossing appears in different field. Also, the saturation value of magnetization in the powder sample is smaller than the magnetic moment of the FM state, again because of the averaging over different angles.

2. $E_{AFM}<E_{FM}$ (at zero-field)

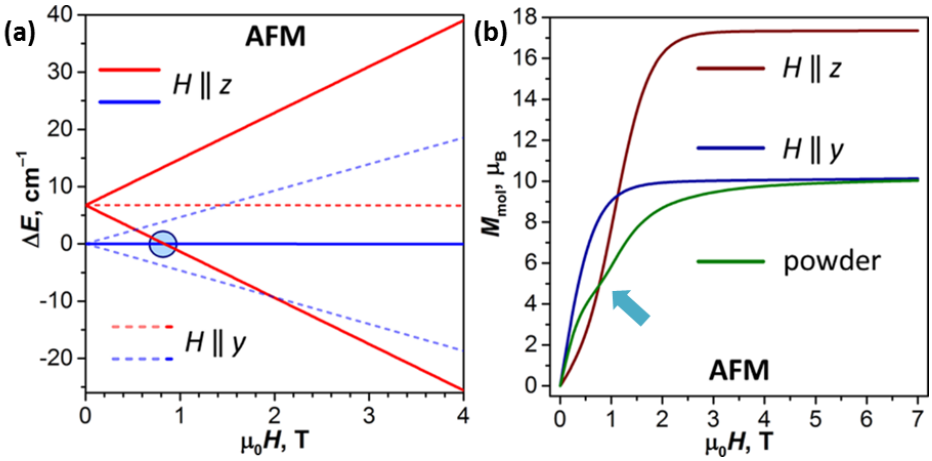

Figure 5.1.3 (a) Zeeman diagram for two orientations (z and y) of the magnetic field. FM states are shown in red, AFM in blue; Field along z-axis is solid lines, and along y-axis is dashed. (b) Calculated magnetization curves for the field along z (brown) and y (blue) axis, and the after powder averaging curve (green). Note the inflection area (pointed by the arrow) between 0.5-1.5 T.

Let' consider the opposite case, where the AFM state is lower in energy than the FM. In this case, if we apply a field long y-axis, FM state is not affected and AFM state experiences Zeeman splitting. We expect normal magnetization curve saturated at the magnetic moment of the AFM state. If we apply a field along z-axis, AFM state is not affected, and FM state shows Zeeman splitting. At some field, FM state will become lower in energy than AFM. Hence, in the magnetization curve measured along z-axis we will at first see no magnetization, and then magnetization will increase and saturate at the magnetic moment of FM state. Again, if we average it over all directions, we take a curve with some inflection, but this is roughly a field where FM states become more stable than AFM states.

To sum up, we saw with simple analysis that the energy difference between FM/AFM states has an effect on the shape of magnetization curves. Therefore, nature of Dy-Dy exchange coupling is valuable information for us in order to understand the SMM properties of our molecules. We can extract this information by measuring the *M-H* curves and fit them with proper Hamiltonian (eq. 5.1.1), to determine the sign and value of the j_{12} coupling constant.

5.2 $Dy_2O@C_{72}$

The smallest structure of the Dy_2O-clusterfullerenes that we have studied so far, is the one with 72 carbon atoms. Magnetic measurements revealed blocking temperature of magnetization near 3 K (peak of the χ_{ZFC} curve) but also an uncommon shape, with the ZFC curve being higher than the FC curve until the bifurcation point (T_{irrev} = 8.6 K), after which both curves coincide.

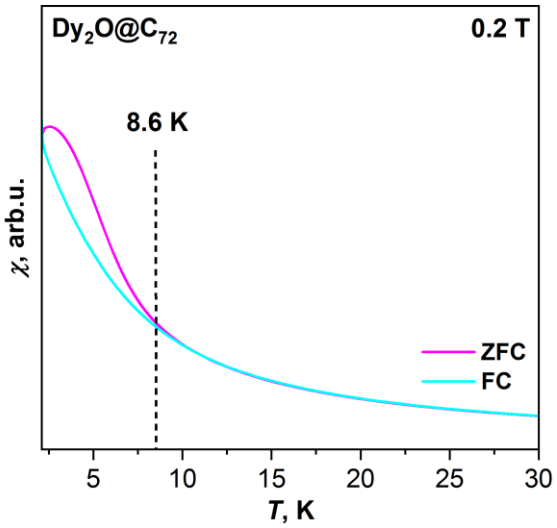

Figure 5.2.1 Comparison of χ_{FC} and χ_{ZFC} curves ($\mu_0 H$ = 0.2 T, temperature sweep rate 5 K/min); dashed black line denotes T_{irrev} (the temperature at which the two curves bifurcate).

This shape of ZFC/FC curves was caused by a temporary technical issue of temperature instability at low temperatures (below 4.2 K), in SQUID-VSM sample chamber. After cooling down to 2 K in zero-field, we apply the field of 0.2 T and when it is reached (after 2 s), then the warming up starts and the ZFC curve is recorded. However, the temperature stabilization delays the starting of warming up for a period varied randomly from 5 to 70 s. In combination with short relaxation times of $Dy_2O@C_{72}$, our sample starts with a relatively high value of initial magnetization, which results in a ZFC curve overcoming the FC curve measured after.

To test our hypothesis, we performed a series of blocking temperature measurements (ZFC/FC curves) in different fields, in the 2-20 K and 3-20 K regimes (fig. 5.2.2). Indeed, we see that for fields lower than 0.2 T, the ZFC curves are closer to their conventional shape (below FC). Also, ZFC curves starting from 3 K (where temperature instability lasts shorter), again are closer to their conventional shape, especially when measured at 0.0.5 and 1 T.

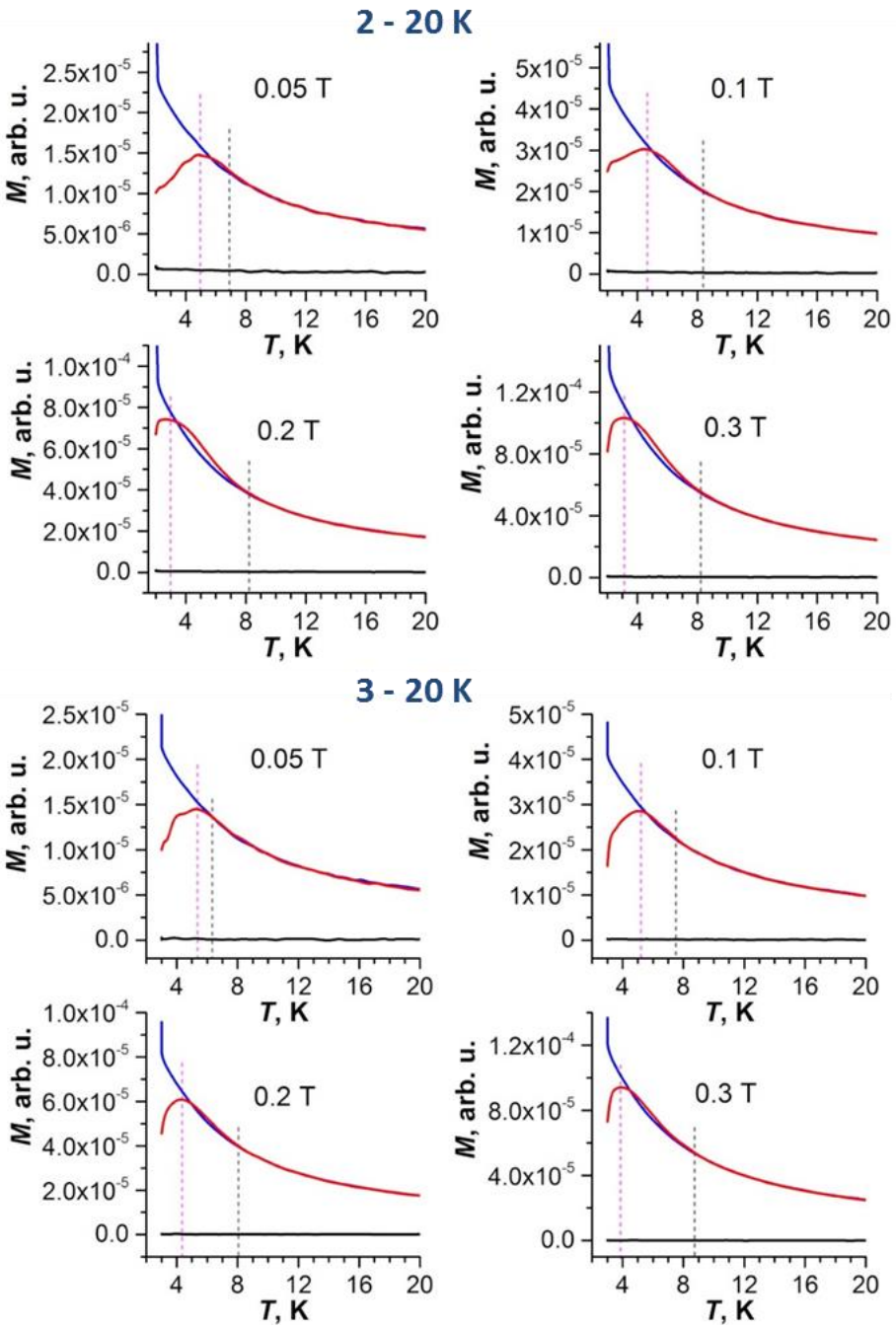

Figure 5.2.2 ZFC and FC measurements for $Dy_2O@C_{72}$ in different magnetic fields. In 3-20 K graphs, the difference from fig. 5.2.1 is that the sample was cooled down to 3 K (instead of 2 K) in a hope to reduce temperature stabilization time. Black curve is magnetization during cooling down in zero field, red curve-magnetization during warming up in the field, blue curve-magnetization during cooling down in the field.

$Dy_2O@C_{72}$ shows relatively broad hysteresis ($H_C \approx 0.2$ T at 1.8 K) which closes at 7 K. This result comes in contrast with the isostructural $Dy_2S@C_{72}$ studied by our group [104], where hysteresis is much narrower and is closing already at 3 K. Thus, Dy_2O cluster is found to be more robust SMM than the Dy_2S analog, despite the same fullerene cage.

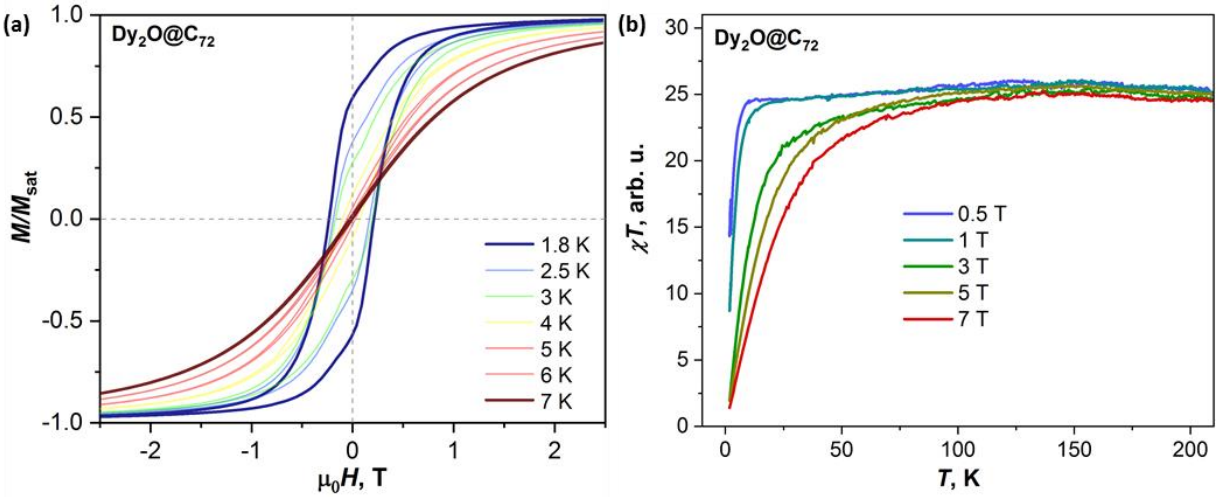

Figure 5.2.3 (a) Magnetic hysteresis curves (field sweep rate: 2.9 mT/s) and (b) χT-T curves of $Dy_2O@C_{72}$.

The ligand-field parameters for Dy ions were computed ab initio at the CASSCF/SO-RASSI level for $DyYO@C_{72}$ molecule. Given the considerable disorder of experimental molecular structures, DFT-optimized atomic coordinates were used. Ab initio calculations showed that Dy^{3+} ions have easy-axis magnetic anisotropy with quantization axes along the corresponding Dy-O bonds, with a deviation of 2°. In $|J, m_J\rangle$ representation, the four lowest energy Kramers doublets (KDs) are almost pure states with m_J of 15/2 (ground state), 13/2 (near 340 cm^{-1}), 11/2 (near 720 cm^{-1}), and 9/2 (near 1030 cm^{-1}) (table 5.2.1). Thus, transition probabilities between these states are very low (fig. 5.2.5). Further KDs have a more mixed nature, and at higher temperatures the relaxation of magnetization following the Orbach mechanism is expected to proceed via the fifth KD at 1180–1200 cm^{-1}, which resembles the situation found experimentally in $Dy_2ScN@C_{80}$ with the Orbach barrier of 1206±15 cm^{-1} [68]. The overall LF splitting is 1337 cm^{-1} in $Dy_2O@C_{72}$.

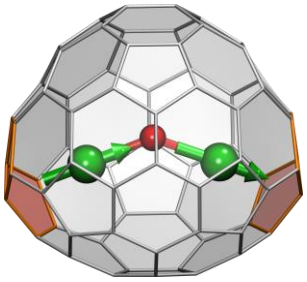

Figure 5.2.4 DFT-optimized molecular structure of $Dy_2O@C_{72}$- C_s, showing alignment of magnetic moment in ferromagnetically-coupled ground-state doublet (Dy is green, O is red, adjacent pentagon pairs are rose; magnetic moments of Dy ions are shown as green arrows). Geometrical angle <Dy–O–Dy is 138.2°.

KD	E, cm^{-1}	**$Dy_2O@C_{72}$**, m_J composition, %
1	0	$99.4\|15/2\rangle$
2	340	$98.0\|13/2\rangle$
3	717	$94.4\|11/2\rangle + 3.8\|9/2\rangle + 1.5\|13/2\rangle$
4	1029	$88.4\|9/2\rangle + 4.8\|7/2\rangle + 3.4\|11/2\rangle$
5	1180	$49.0\|7/2\rangle + 11.8\|-1/2\rangle + 16.5\|-7/2\rangle$
6	1239	$32.9\|5/2\rangle + 24.3\|-1/2\rangle + 21.5\|-5/2\rangle$
7	1284	$51.2\|3/2\rangle + 17.6\|-3/2\rangle + 14.3\|1/2\rangle$
8	1337	$32.0\|5/2\rangle + 21.7\|-1/2\rangle + 12.1\|1/2\rangle$

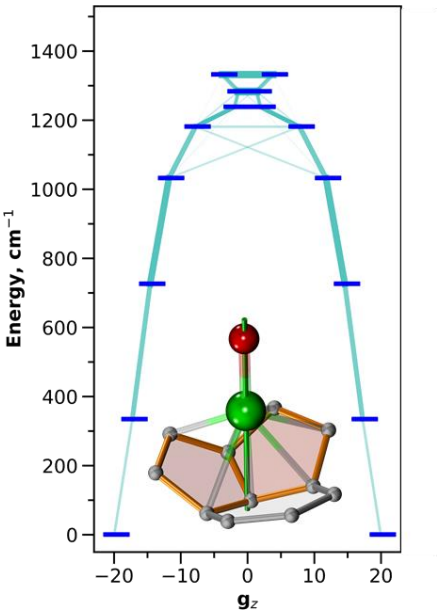

Table 5.2.1. Ab initio computed ligand-field splitting energies for Dy ions in $Dy_2O@C_{72}$-C_s (the two Dy ions are equivalent in this conformer); **Figure 5.2.5** CASSCF/RASSI-computed ligand-field splitting for Dy^{3+} ions in $Dy_2O@C_{72}$-C_s; the thickness of light blue lines corresponds to transition probability. The inset shows Dy-coordinated fragment of the fullerene cage and quantization axis of Dy (green line); Dy-C distances shorter than 2.6 Å are shown as bonds.

Calculations prove that indeed we have a strong LF splitting and the magnetic properties of our system can be described well enough by the spin Hamiltonian of eq. 5.1.1 (at least the lower part of the energy spectrum). Therefore, we can fit the experimental *M-H* and χT-*T* curves with two unknown parameters (j_{12} and α). However, for $Dy_2O@C_{72}$ we have precise knowledge of <Dy-O-Dy angle (138.2°) from X-ray diffraction data. As a result, determination of j_{12} value can be done straightforward by fixing the value of the angle in the data fitting. Best fit was achieved for j_{12} = 0.009±0.002 cm^{-1} (fig. 5.2.6). This j_{12} value gives the energy difference of ΔE_{AFM-FM} = 1.5±0.3 cm^{-1} (weak FM coupling).

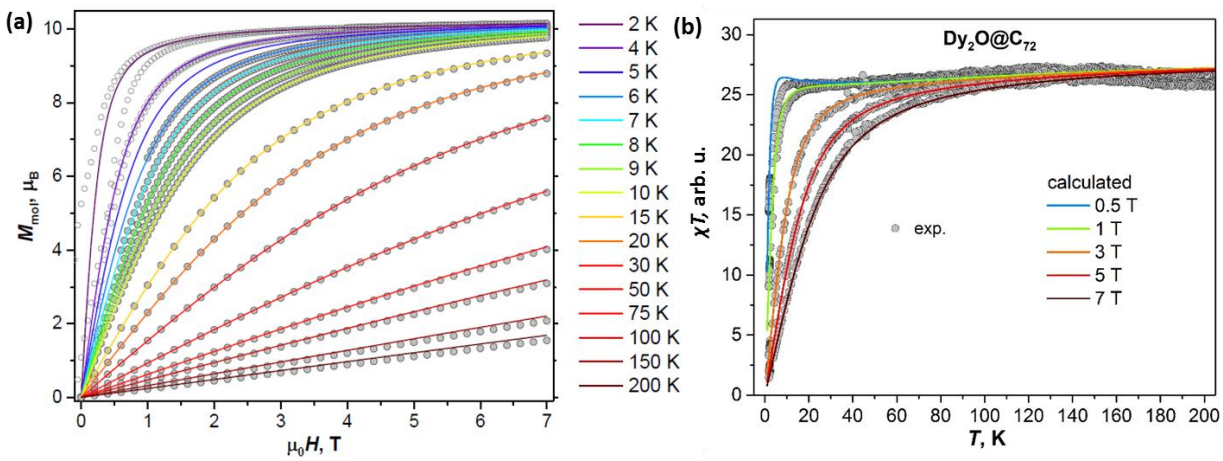

Figure 5.2.6 (a) Exp. magnetization values of $Dy_2O@C_{72}$ (gray dots) measured at different temperatures, compared to the results of the fitting with the spin Hamiltonian of eq. 5.1.1 (colored lines). Experimental values for the fitting were taken only from the regions where hysteresis is closed. For comparison, open dots show exp. magnetization curves with open hysteresis measured at 2 and 4 K; (b) Exp. χT values (grey dots) measured at different fields, compared to the fitting curves (lines). The optimal $j_{1,2}$ value obtained from the fit is 0.0091 cm^{-1};

Relaxation times of magnetization below T_{irrev} (8.6 K) were determined by stretched exponential fitting of magnetization decay curves, recorded after the fast sweep of magnetic field from 5 T to the required value. Fig. 5.2.7a shows the field dependence of τ_m measured at 1.8 K. From 523 s (0 T), τ_m decays fast with field increase down to 95 s (0.4 T) and then tends to level off. The large drop with relatively small field increase is clear indication of direct mechanism of relaxation.

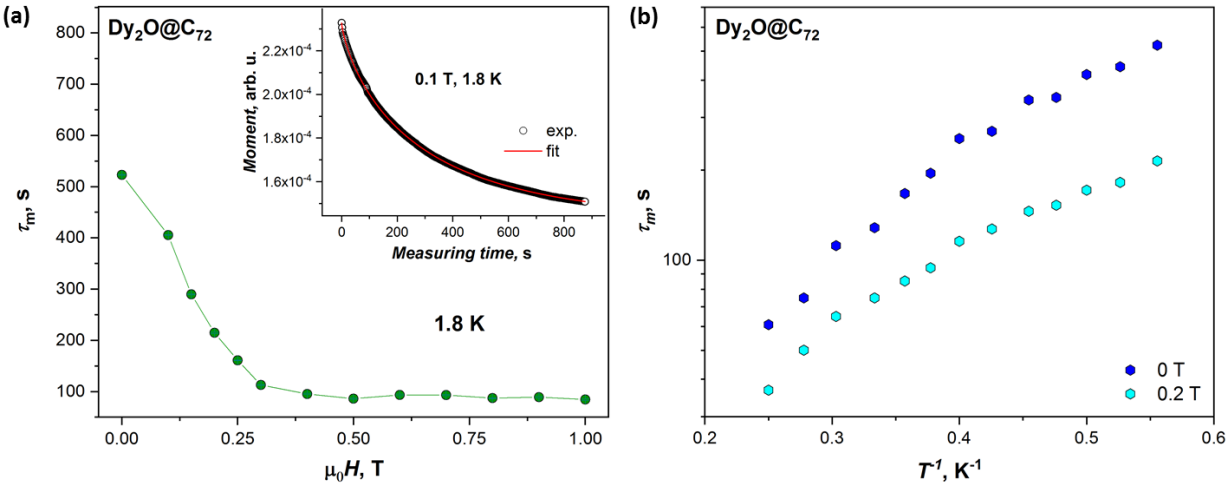

Figure. 5.2.7 Magnetization relaxation times of $Dy_2O@C_{72}$: (a) Field dependence of τ_m at the temperature of 1.8 K; inset: example of a fitted magnetization decay curve measured at 0.1 T, 1.8 K. (b) Temperature dependence of τ_m in two different fields, 0 and 0.2 T.

Temperature dependence of relaxation times were studied in two different constant fields, 0 and 0.2 T (fig. 5.2.7b). The two datasets at each field were fitted jointly either with eq. 5.2.1 (direct and Orbach) or eq. 5.2.2 (direct and Raman) keeping the field-independent parameters identical for both fields.

$$\tau_{\mathrm{m}}^{-1}(T) = C_{\mathrm{d},H} T^{n_{\mathrm{d}}} + \tau_0^{-1} \exp(-U^{\mathrm{eff}}/T) \qquad (5.2.1) \qquad \text{direct + Orbach}$$

$$\tau_{\mathrm{m}}^{-1}(T) = C_{\mathrm{d},H} T^{n_{\mathrm{d}}} + C_{\mathrm{R}} T^{n_R} \qquad (5.2.2) \qquad \text{direct + Raman}$$

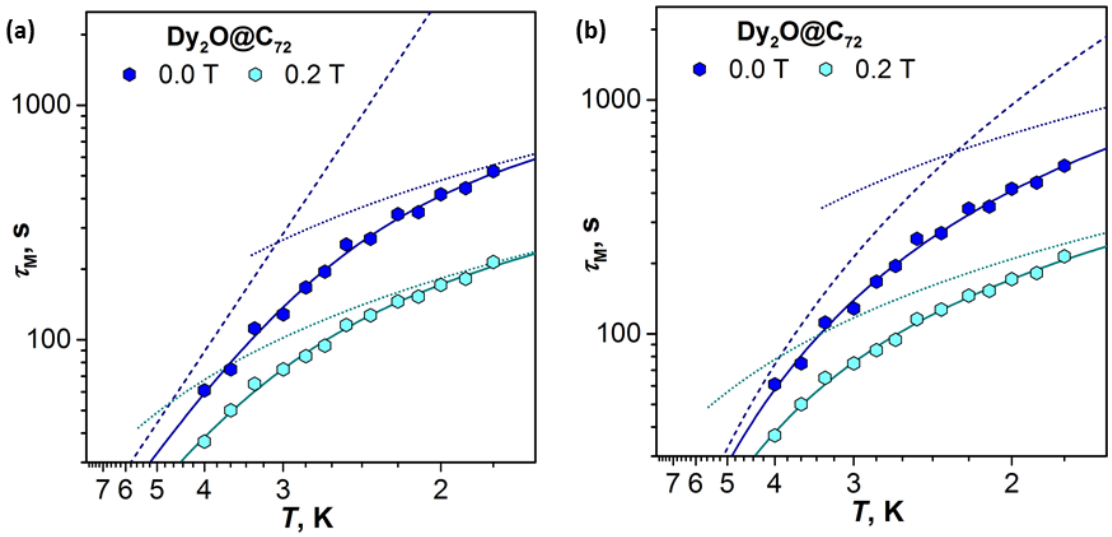

Figure 5.2.8 Magnetization relaxation times of $Dy_2O@C_{72}$ measured in the field of 0 T and 0.2 T (dots); (a) Solid lines are fits with the contribution of Orbach (dashed line) and direct (dotted line) mechanisms (eq. 5.2.1); (b) Solid lines are fits with the model of Raman (dashed line) and direct (dotted line) mechanisms contribution (eq. 5.2.2). Equally good fit is obtained with both equations.

Fitting parameters	Direct + Orbach	Direct + Raman
n_{d}	1.44±0.13	1.43±0.13
$C_{\mathrm{d,0\ T}}$	$(7.7\pm0.6)\cdot10^{-4}$ s^{-1} K$^{-1.44}$	$(5.2\pm0.1)\cdot10^{-4}$ s^{-1} K$^{-1.43}$
$C_{\mathrm{d,0.2\ T}}$	$(2.02\pm0.19)\cdot10^{-3}$ s^{-1} K$^{-1.44}$	$(1.78\pm0.18)\cdot10^{-3}$ s^{-1} K$^{-1.43}$
τ_0	2.7±0.7 s	-
U^{eff}	14±1 K	-
n_{R}	-	3.69±0.36
C_{R}	-	$(8.2\pm4.5)\cdot10^{-5}$ s^{-1} K$^{-3.7}$

Table 5.2.2 Fitting parameters of the two datasets fitted jointly with either eq. 5.2.1 or eq. 5.2.2.

Remarkably, both models give similar parameters for the direct mechanism, which dominates at lowest temperatures. The value of n_{d} is almost 50% higher than 1, which may be due to phonon-bottleneck effect. With temperature increase, field-independent Raman or Orbach process takes over. Effective barrier U^{eff} is calculated to 14±1 K. This value does not correspond to the energy difference between spin states and may be only caused by local vibrations with low frequency.

5.3 $Dy_2O@C_{74}$

The next Dy_2O-clusterfullerene in our list is $Dy_2@OC_{74}$. Measurement of blocking temperature of magnetization showed again the uncommon shape of ZFC curve over the FC but for a different reason from $Dy_2O@C_{72}$. The peak temperature of ZFC curve is near 6.7 K in $Dy_2O@C_{74}$ (fig. 5.3.1), and the bifurcation point (T_{irrev}), after which both curves coincide, is considerably higher than T_B reaching 14 K.

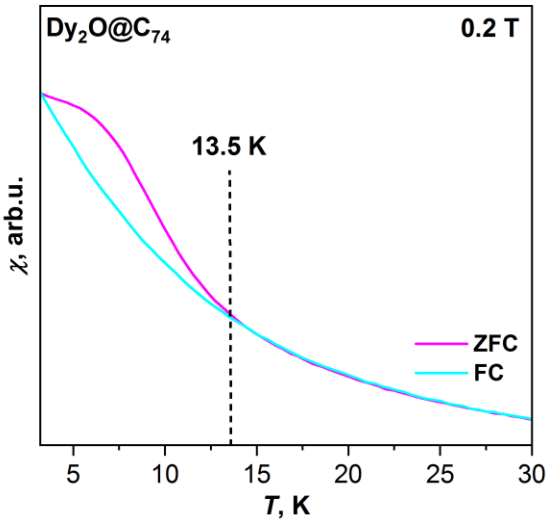

Figure 5.3.1 Comparison of χ_{FC} and χ_{ZFC} curves ($\mu_0 H$ = 0.2 T, temperature sweep rate 5 K/min); dashed black line denotes T_{irrev} (the temperature at which the two curves bifurcate).

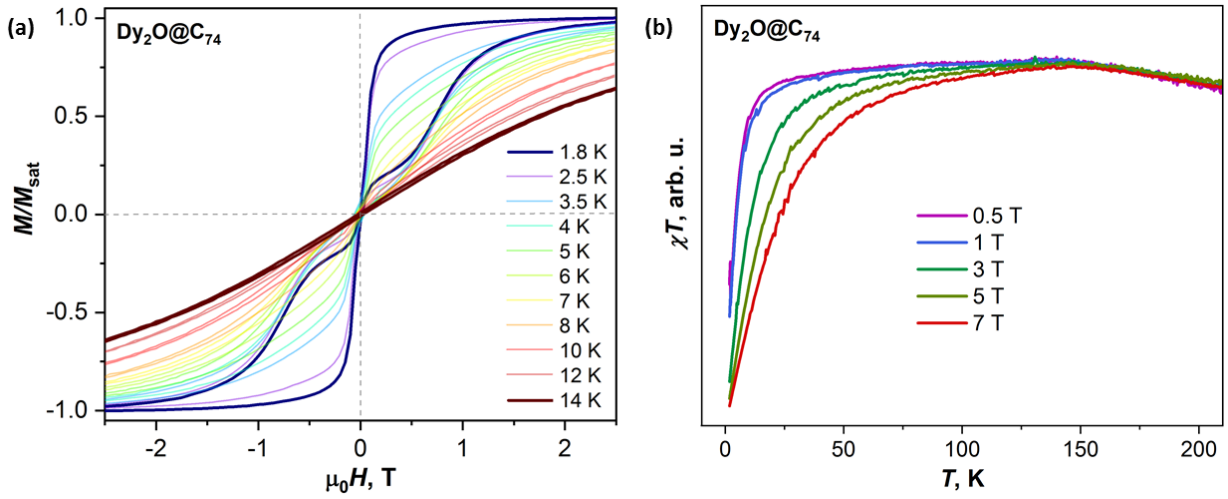

Figure 5.3.2 (a) Magnetic hysteresis curves (field sweep rate: 2.9 mT/s) and (b) χT-T curves of $Dy_2O@C_{74}$.

In agreement with the T_{irrev} value, $Dy_2O@C_{74}$ hysteresis closes at 14 K, the highest temperature for Dy-clusterfullerenes. At 1.8 K, $Dy_2O@C_{74}$ hysteresis appears with the characteristic "butterfly" shape where abrupt decay of magnetization in zero-field occurs. This shape is typical for single-

ion magnets because they experience zero-field QTM, but not for dinuclear SMMs as magnetic interactions lead usually to non-degenerate energy states.

Test measurements of blocking temperature at different fields (0.05, 0.1, 0.2 and 0.4 T) revealed the reason behind the unconventional shapes of ZFC/FC curves. At small fields close to zero (i.e. 0.05 T) where tunneling is still effective, the Dy ions relax fast to equilibrium after the application of the field, and therefore ZFC and FC curves coincide. Increasing the field (0.1 and 0.2 T) QTM is quenched but still relaxation time is small compared to the time scale of the measurement, hence we see the ZFC curve over the FC because it starts from an initial high value of magnetization. At 0.4 T the relaxation slows down considerably and the ZFC/FC curves approach their conventional shapes.

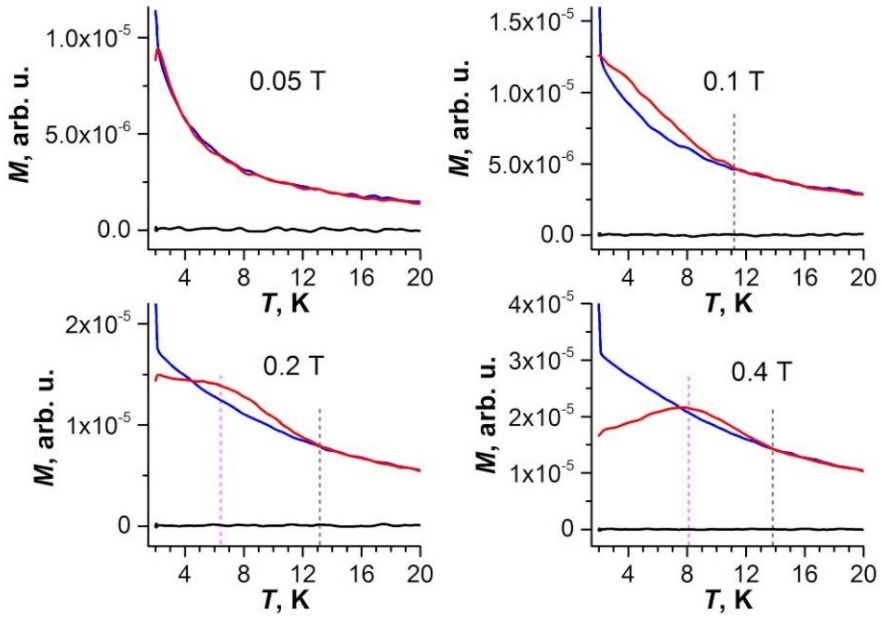

Figure 5.3.3 ZFC and FC measurements for $Dy_2O@C_{74}$ in different magnetic fields, temperature range [2 K, 20 K]. Due to the fast relaxation of magnetization of $Dy_2O@C_{74}$ in small fields caused by the QTM, magnetization of $Dy_2O@C_{74}$ always jumps to a relatively high value during the field ramp from zero to the measurement field. As a result, ZFC/FC curves depend on the magnetic field used in the measurements.

Ab initio calculations for $Dy_2O@C_{74}$ showed that Dy ions have easy-axis magnetic anisotropy with the quantization axes aligned along the corresponding Dy-O bonds with deviation of ca 2^o again. In $|J, m_J\rangle$ representation, the four lowest energy Kramers doublets (KDs) are almost pure states, like in $Dy_2O@C_{72}$ with very similar energies. The overall LF splitting is 1329 cm^{-1} in $Dy_2O@C_{74}$.

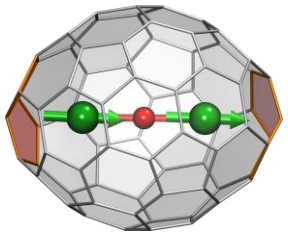

Figure 5.3.4 DFT-optimized molecular structure of $Dy_2O@C_{74}$-C_2, showing absolute alignment of magnetic moments in FM ground-state doublet (Dy is green, O is red, adjacent pentagon pairs are rose; magnetic moments of Dy ions are shown as green arrows). Geometrical angle <Dy–O–Dy is 178°.

KD	E, cm^{-1}	**$Dy_2O@C_{74}$**, m_J composition, %
1	0	$99.5\|15/2\rangle$
2	336	$98.9\|13/2\rangle$
3	716	$97.4\|11/2\rangle + 1.7\|9/2\rangle$
4	1033	$94.7\|9/2\rangle + 2.0\|7/2\rangle$
5	1200	$62.5\|7/2\rangle + 16.2\|-7/2\rangle + 14.4\|1/2\rangle$
6	1261	$54.9\|5/2\rangle + 5.0\|-7/2\rangle + 27.0\|-1/2\rangle$
7	1293	$77.5\|3/2\rangle + 6.5\|5/2\rangle + 4.9\|-3/2\rangle$
8	1329	$45.6\|1/2\rangle + 28.5\|-5/2\rangle + 9.3\|-3/2\rangle$

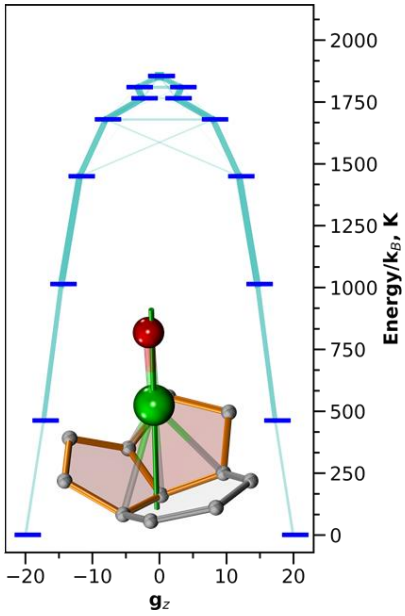

Table 5.3.1. Ab initio computed ligand-field splitting energies for Dy ions in $Dy_2O@C_{74}$-C_2 (the two Dy ions are equivalent in this conformer); **Figure 5.3.5** CASSCF/RASSI-computed ligand-field splitting for Dy^{3+} ions in $Dy_2O@C_{74}$-C_2; the thickness of light blue lines corresponds to transition probability. The inset shows the Dy-coordinated fragment of the fullerene cage and quantization axis of Dy (green line); Dy–C distances shorter than 2.6 Å are shown as bonds.

For $Dy_2O@C_{74}$, the coupling constant j_{12} defining the scale of Dy-Dy interactions is determined by fitting of the experimental magnetization curves. Here the optimal j_{12} is less than 0.001 cm^{-1} with the uncertainty of ±0.002 cm^{-1}. The FM and AFM states in $Dy_2O@C_{74}$ are thus degenerate within $|\Delta E_{FM-AFM}|$<0.4 cm^{-1}, which means that Dy^{3+} moments are essentially decoupled. The optimal $j_{1,2}$ value obtained from the fit is 0.00016 cm^{-1} (if only the T ≤ 14 K is used) and 0.00082 cm^{-1} (if the whole temperature range is used). Variation of j_{12} from -0.002 to +0.002 cm^{-1} does not change the curves noticeably.

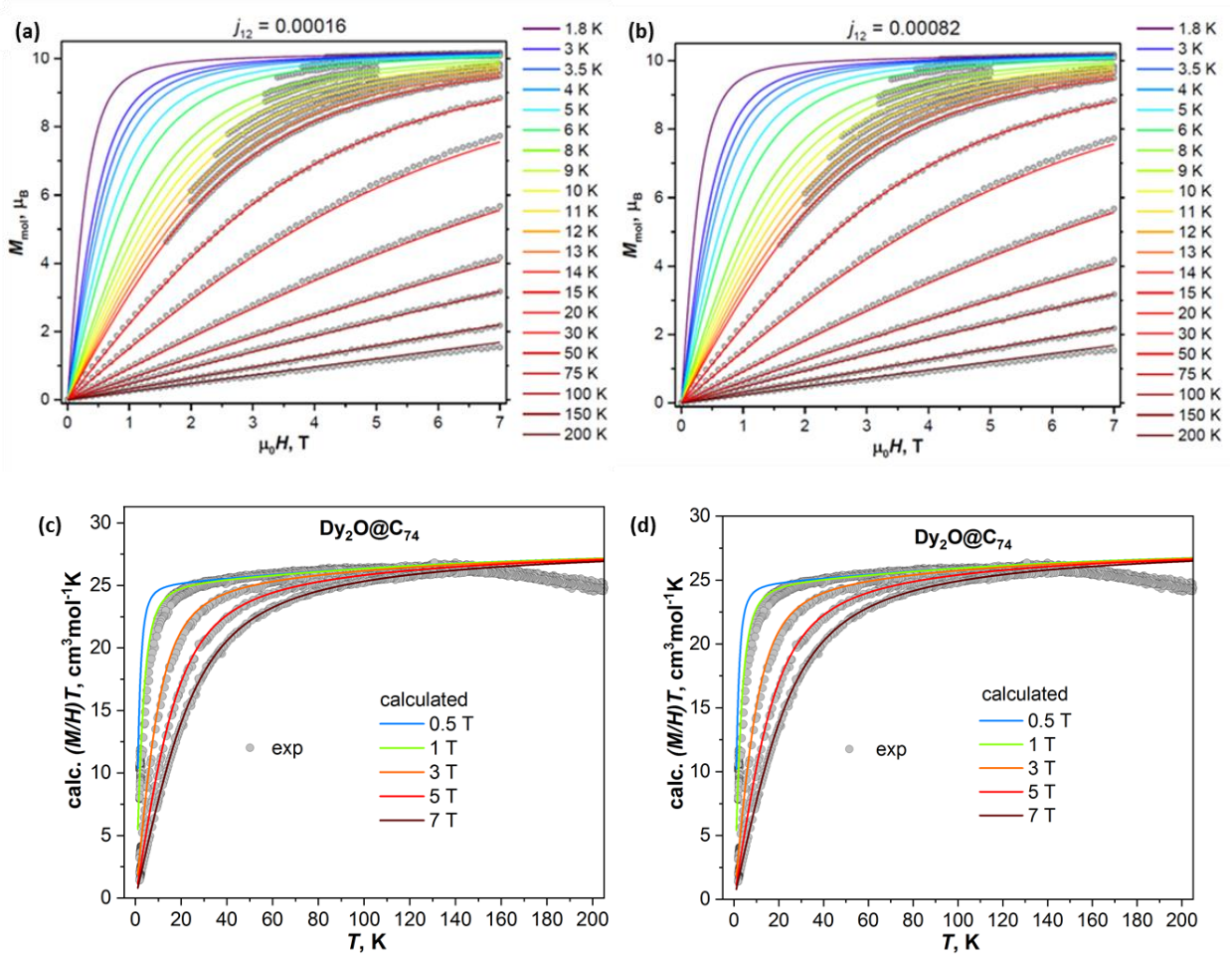

Figure 5.3.6 Experimental *M-H* (a-b) and χT-*T* (c-d) values of $Dy_2O@C_{74}$ (gray dots) compared to the results of the fitting with spin Hamiltonian of eq. 5.1.1 (colored lines). Exp. values for the fitting were taken only from the regions where hysteresis is closed. The optimal $j_{1,2}$ values obtained from fit are 0.00016 cm^{-1} (if only the T≤14 K is used) and 0.00082 cm^{-1} (if the whole temperature range is used.

As long as the FM/AFM states have different energies, the $\Delta E_{\text{FM–AFM}}$ acts as a barrier preventing QTM, because the latter requires degeneracy of the energy levels. $Dy_2O@C_{74}$ is the only dinuclear Dy-clusterfullerene studied up to date to exhibit efficient zero-field QTM, which can be explained by the vanishing of Dy-Dy coupling. The Dy-Dy coupling can be divided into the exchange and dipolar contribution $\Delta E^{exch}_{\text{AFM}-\text{FM}}$ and $\Delta E^{dip}_{\text{AFM}-\text{FM}}$. Dipolar term can be computed when molecular structures and orientations of magnetic moments are known. Using DFT-optimized structures and orientation of quantization axes from ab initio calculations, we obtain 2.56 cm^{-1} in $Dy_2O@C_{74}$. Thus, dipolar interactions favor FM arrangement of Dy^{3+} moments and small overall coupling in $Dy_2O@C_{74}$ results from the cancellation of dipolar coupling by exchange interactions, which are therefore antiferromagnetic. To yield the experimental ΔE energy, $\Delta E^{exch}_{\text{AFM}-\text{FM}}$ value should be

−2.5±0.4 cm^{-1} in $Dy_2O@C_{74}$. Analogous calculations for $Dy_2O@C_{72}$ led to $\Delta E^{dip}_{\mathrm{AFM-FM}}$=2.99 cm^{-1} and $\Delta E^{exch}_{\mathrm{AFM-FM}}$=−1.5±0.3 cm^{-1}.

Magnetization relaxation times τ_m below T_{irrev} were determined by stretched exponential fitting of magnetization decay curves recorded after the fast sweep of magnetic field from 5 T to the required field value. Relaxation rate in 0 T could not be measured because of the fast QTM, and the lowest field studied is 0.05 T.

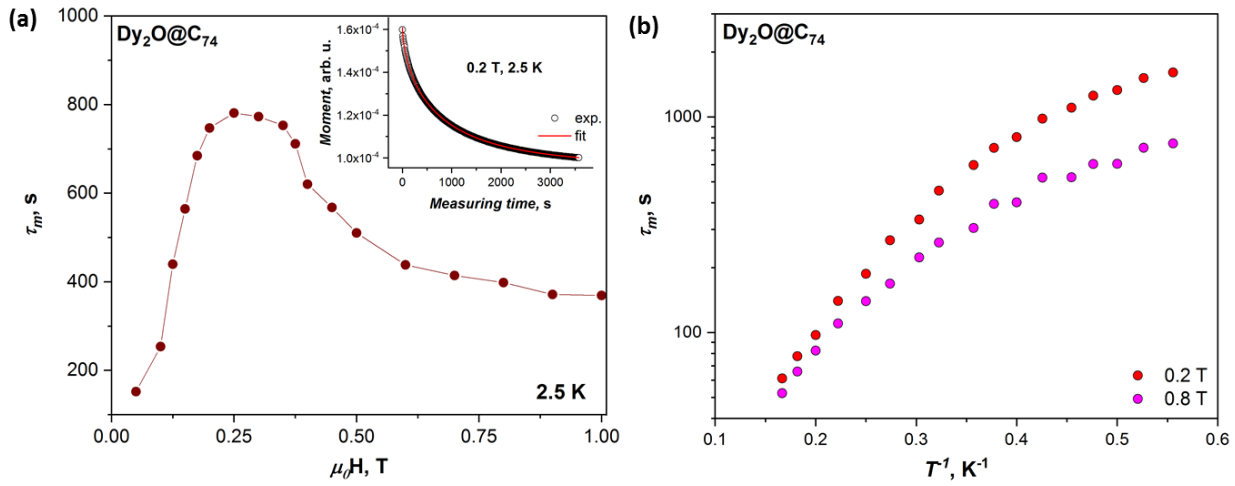

Figure. 5.3.7 Magnetization relaxation times of $Dy_2O@C_{74}$: Field dependence of τ_m at 2.5 K. Note that the smallest field for $Dy_2O@C_{74}$ is 0.05 T since the measurements in zero field are not possible because of the fast QTM process; inset: example of a fitted magnetization decay curve measured at 0.2 T, 2.5 K. (b) Temperature dependence of τ_m in two different fields, 0.2 and 0.8 T.

Field dependence at 2.5 K shows a fast increase of τ_m from 152 s (0.05 T) to 750-780 s (0.2-0.35 T). This corresponds to a gradual quench of QTM by Zeeman splitting increase. With further field increase beyond 0.35 T, relaxation accelerates due to the contribution of the direct mechanism. Similar to $Dy_2O@C_{72}$, temperature dependence of relaxation time was studied in two fields for each clusterfullerene, 0.2 and 0.8 T (fig. 5.3.7b). Then the two datasets were fitted jointly either with eq. 5.3.1 (direct + Orbach) or eq. 5.3.2 (direct + Raman) keeping the field-independent parameters identical. Equally good fit was obtained with both combinations.

$$\text{direct + Orbach} \qquad \tau_{\mathrm{m}}^{-1}(T) = C_{\mathrm{d},H}T^{n_{\mathrm{d}}} + \tau_0^{-1}\exp(-U^{\mathrm{eff}}/T) \qquad (5.3.1)$$

$$\text{direct + Raman} \qquad \tau_{\mathrm{m}}^{-1}(T) = C_{\mathrm{d},H}T^{n_{\mathrm{d}}} + C_{\mathrm{R}}T^{n_R} \qquad (5.3.2)$$

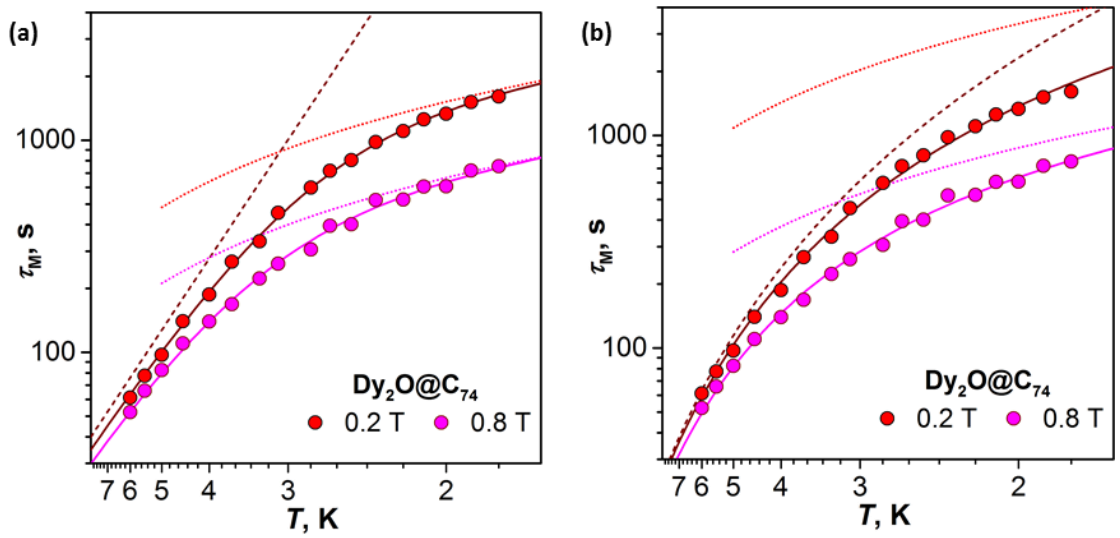

Figure 5.3.8 Magnetization relaxation times of $Dy_2O@C_{74}$ measured in the field of 0.2 T and 0.8 T (dots); (a) Solid lines are fits with the contribution of Orbach (dashed line) and direct (dotted line) mechanisms (eq. 5.3.1); (b) Solid lines are fits with the contribution of Raman (dashed line) and direct (dotted line) mechanisms (eq. 5.3.2). Equally good fit is obtained with both equations.

Fitting parameters	Direct + Orbach	Direct + Raman
n_d	1.25±0.10	1.23±0.14
$C_{d,0.2\ T}$	$(2.77\pm0.17)\cdot10^{-4}$ s^{-1}K$^{-1.25}$	$(1.27\pm0.29)\cdot10^{-4}$ s^{-1}K$^{-1.23}$
$C_{d,0.8\ T}$	$(6.32\pm0.49)\cdot10^{-4}$ s^{-1}K$^{-1.25}$	$(4.88\pm0.51)\cdot10^{-4}$ s^{-1}K$^{-1.23}$
τ_0	5.75±0.45 s	-
U^{eff}	15.5±0.5 K	-
n_R	-	3.28±0.14
C_R	-	$(4.4\pm1.1)\cdot10^{-5}$ s^{-1}K$^{-3.28}$

Table 5.3.2 Fitting parameters of the two datasets fitted jointly with either eq. 5.3.1 or eq. 5.3.2.

Again, both models give similar parameters for the direct mechanism, which dominates at lowest temperatures. The value of n_d is almost 25% higher than 1 this time, which again may be due to phonon-bottleneck effect (for $Dy_2O@C_{72}$ n_d was almost 50% higher than 1). With temperature increase, either field-independent Raman or Orbach process takes over. Effective barrier U^{eff} is calculated to 15.5±0.5 K (compare to 14±1 K for $Dy_2O@C_{72}$). This value does not correspond to the energy difference between spin states and may be only caused by local vibrations with low frequency.

5.4 $Dy_2O@C_{82}$ (three isomers)

The last part of my PhD work is the study of three isomers of $Dy_2O@C_{82}$ (cage symmetry: C_s, C_{3v} and C_{2v}), a very convenient example to understand better the playing role of the carbon cage shape in the SMM properties. So far, we saw for $Dy_2O@C_{72}$ and $Dy_2O@C_{74}$ that the carbon cage size and symmetry affect the angle between the bonds, but the question is what happens when the number of the carbon atoms remains the same and only the cage shape changes? All three $Dy_2O@C_{82}$ isomers show magnetic hysteresis below 10 K with different curves shape and varying temperatures of closing hysteresis, indicating significant dependence of the SMM character on the fullerene type.

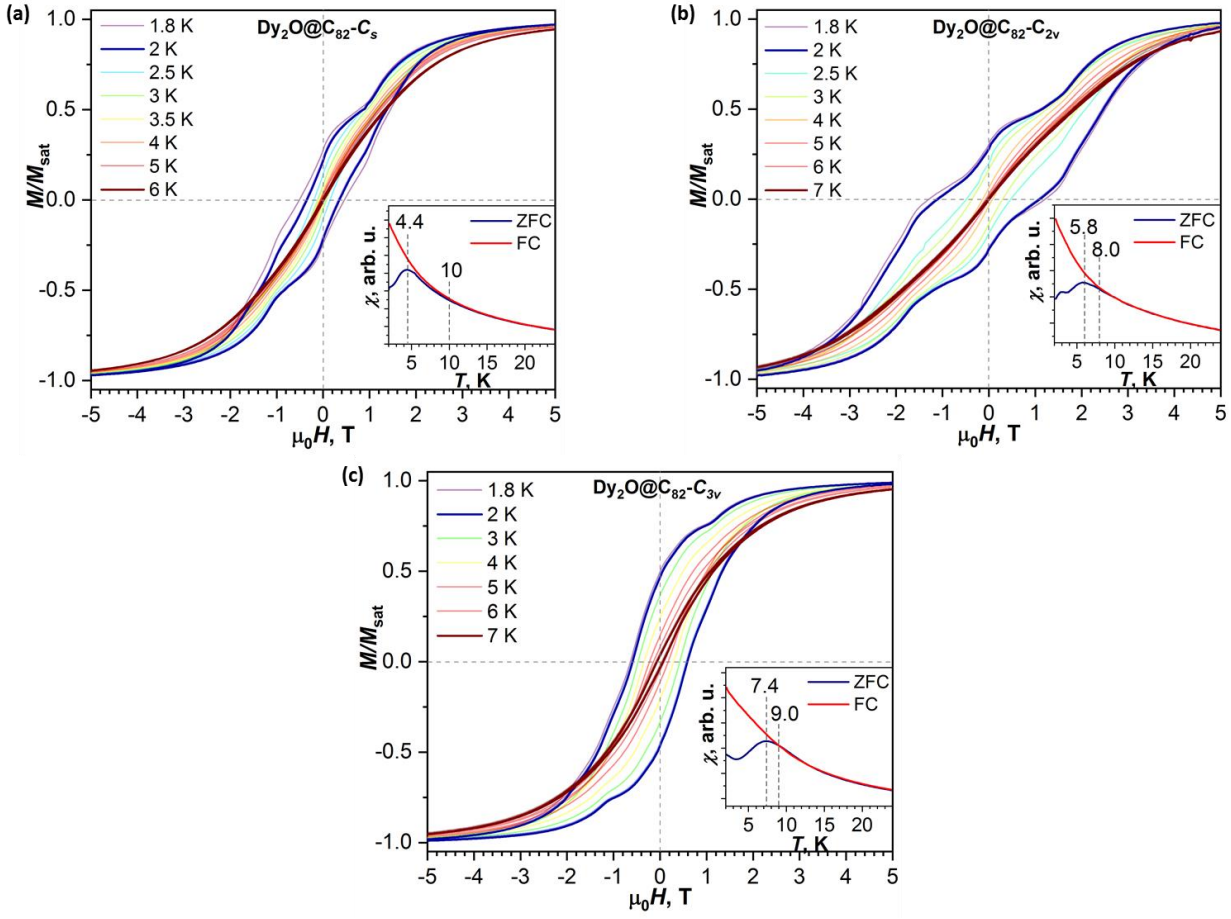

Figure 5.4.1 Magnetic hysteresis of $Dy_2O@C_{82}$ isomers: C_s (a), C_{2v} (b), and C_{3v} (c); magnetic field sweep rate 2.9 mT s^{-1}; inset in each figure shows determination of the blocking temperature T_B.

The ZFC curves measured with temperature sweep rate of 5 K/min have well defined maxima at 4.4 K (C_s), 5.8 K (C_{2v}) and 7.4 K (C_{3v}). At the same time, ZFC and FC curves diverge up to somewhat higher temperatures, 10 K (C_s), 8 K (C_{2v}) and 9 K (C_{3v}). The C_s isomer exhibits comparatively narrow hysteresis loop closing near 6 K. At 2 K, the coercive field H_c is 0.35 T, and the loop remains open

in the range from -3 to 3 T. The C_{2v} isomer shows the broadest hysteresis at 2 K (H_c = 1.1 T, open till 7 T), which is observed up to 8 K. The hysteresis loop of the C_{3v} isomer is also broad (H_c = 0.59 T at 2 K, the loop is open till ca 4 T) and is closing near 8 K. Hysteresis loops of all three compounds have inflections at 1-1.5 T, which are most pronounced for the C_{2v} isomer. The nature of these features is discussed further in the text. The susceptibility curves for all the isomers point clearly to the AFM ground state, because χT-T curves show no maxima at low-temperature regime.

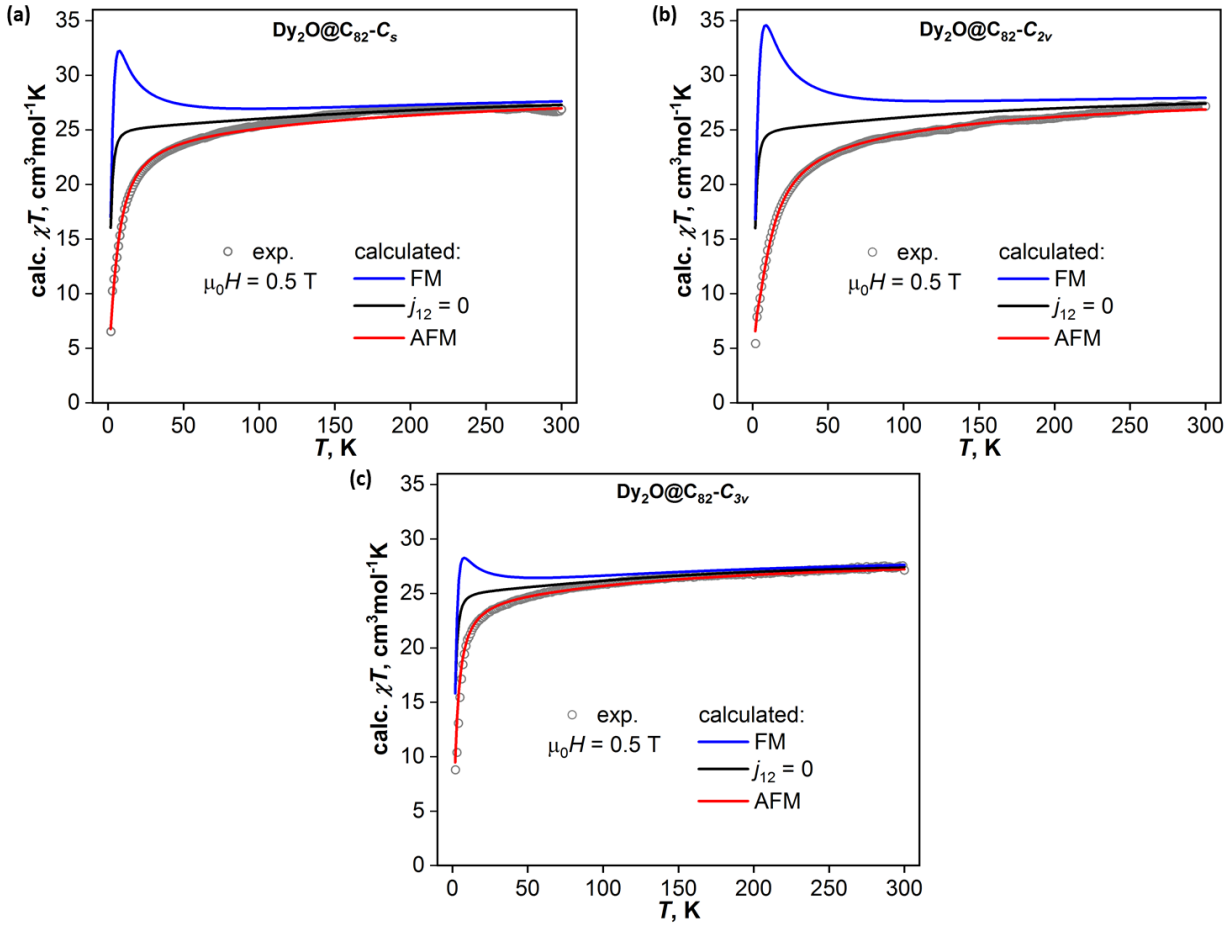

Figure 5.4.2 Magnetic susceptibility of $Dy_2O@C_{82}$ isomers (C_s, C_{3v}, and C_{2v}) measured in the field of 0.5 T. Exp. data (open circles) are compared to the simulations for antiferromagnetic (red lines), ferromagnetic (black lines) coupling and for non-coupled system (blue lines).

Although the fullerene cage structures were unambiguously elucidated by single-crystal X-ray diffraction, the strong disorder in position of Dy atoms did not allow precise determination of the endohedral cluster positions. Therefore, DFT calculations were performed by Dr. Avdoshenko and S. Sudarkova to find the preferable geometries and orientations of the Dy_2O clusters inside the fullerenes. The study resulted in 7 unique conformers for C_s, 5 for C_{3v}, and 8 for C_{2v}.

For $Dy_2O@C_{82}$-C_s isomer, DFT calculations favor one particular conformer, which is more stable than all other six structures. In reasonable agreement with the diffraction data, DFT-optimized Dy–O bond lengths are 2.031 and 2.045 Å, and <Dy–O–Dy angle is 135.7° (136.1° from XRD). Thus, both experiment and theory agree that the C_{82}-C_s cage has two well-defined positions for endohedral metal atoms. For $Dy_2O@C_{82}$-C_{3v}, the calculations located five unique conformers with the cluster easily rearranging between different minima, forming the egg-shaped probability iso-surface closely following the shape of the fullerene cage (fig. 5.4.3). Thus, it comes as no surprise that the metal positions in the $Dy_2O@C_{82}$-C_{3v} crystal were disordered. The DFT-optimized Dy–O bonds length and <Dy–O–Dy angles in the two most stable conformers of $Dy_2O@C_{82}$-C_{3v} are 2.017 Å/2.044 Å/139° and 2.014 Å/2.035 Å/145°. The conformer search for $Dy_2O@C_{82}$-C_{2v} located eight unique structures, two of which are almost iso-energetic. The cluster dynamics in C_{82}-C_{2v} isomer presents an intermediate situation between localized motions as in C_{82}-C_s and almost completely delocalized trajectory as in case of C_{82}-C_{3v}. The DFT-optimized Dy–O bonds length and <Dy–O–Dy angles in the two most stable conformers of $Dy_2O@C_{82}$-C_{2v} are 2.004 Å/2.040 Å/155° and 2.010 Å/2.047 Å/149°.

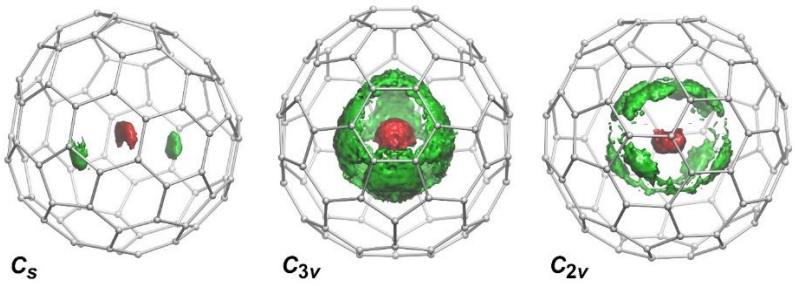

Figure 5.4.3 Spatial distribution of the probability density for Dy and O atoms in $Dy_2O@C_{82}$ isomers as determined from molecular dynamics simulations at T = 300 K. Displacements of carbon atoms are not shown.

Ab initio calculations were performed to get information on the single-ion magnetic anisotropy of Dy ions in $Dy_2O@C_{82}$. For each $Dy_2O@C_{82}$ structure, one of the Dy ions was replaced by Y, and then the multiplet structure for Dy ($^6H_{15/2}$) in $DyYO@C_{82}$ was calculated at the CASSCF(9,7)/SO-RASSI level using SINGLEANISO routine to extract ab initio ligand-field parameters [14, 141]. Calculations for different DFT-optimized conformers of $Dy_2O@C_{82}$ isomers gave similar results. Fig. 5.4.4 visualizes computed LF-splitting, transition probabilities, and Dy-cage coordination sites with the quantization axes of Dy ions for $Dy_2O@C_{82}$-C_s (major conformer). Analogous data for different conformers of other $Dy_2O@C_{82}$ isomers were obtained. The oxide ion at the distance of ca 2 Å from Dy^{3+} imposes a very strong uniaxial anisotropy in the latter. The quantization axes for Dy ions are almost coinciding with corresponding Dy–O bonds, and the overall LF splitting is in the range of 1360–1490 cm^{-1}. The energy of the first excited Kramers doublet (KD) varies from 386 to 515 cm^{-1}. In terms of the $|J, m_J\rangle$ basis, the first KDs have nearly pure composition (near 100% $|\pm 15/2\rangle$ for the first KD, ca 98% $|\pm 13/2\rangle$ for the second KD, ca 90% $|\pm 11/2\rangle$ in the third

KD etc.), and substantial mixing of m_J functions starts from the fifth or sixth KD. Accordingly, transition probabilities within one KD attain significant values only in the fifth-sixth KDs, which shows that the Orbach relaxation via the ligand-field excited states should have a barrier of at least 1200–1300 cm^{-1} (ca 1700–1900 K). Similar findings were reported by Singh and Rajaraman [140] in the computational study of $DyLuO@C_{2n}$ and $DyScO@C_{2n}$ ($2n$ = 72, 76, 82) molecules. Unfortunately, the isolable amount of $Dy_2O@C_{82}$ was not sufficient for AC magnetometry, which is required for the measurement of relaxation times above T_B. At the temperatures accessible for DC magnetometry, the relaxation of magnetization in $Dy_2O@C_{82}$ is not governed by excited ligand-field states.

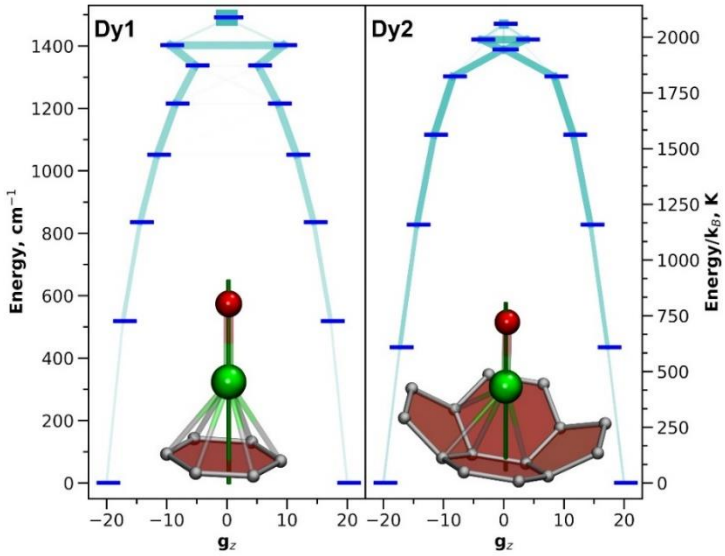

Fig. 5.4.4 Ab initio computed ligand-field states (thick blue dashes) and transition probabilities between them (light blue lines, the thicker the line – the higher the transition probability) for two Dy ions in the lowest-energy conformer of $Dy_2O@C_{82}$-C_s. Also shown are the Dy-cage coordination sites and quantization axes for each Dy ions (dark green lines). Dy – green, O – red, C – gray, Dy–C distances less than 2.60 Å are shown as bonds.

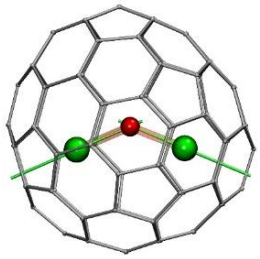

Figure 5.4.5 DFT-optimized molecular structure of $Dy_2O@C_{82}$-C_s, (Dy is green, O is red, quantization axes of Dy ions are shown as green lines). Geometrical angle <Dy-O-Dy: 135.7°. Angle between axes of KD-1 states: 133.8°.

In contrast with $Dy_2O@C_{72}$ and $Dy_2O@C_{74}$, strong disorder of the cluster positions inside the fullerene, did not allow us to have precise knowledge of the angle <Dy-O-Dy between the bonds. As a result, with two unknown parameters (j_{12}, α), fitting of the experimental *M-H* and χT-*T* curves with the Hamiltonian of eq. 5.1.1, becomes rather ambiguous. For that reason, we followed a different strategy to determine the (j_{12}, α) values. We tried to estimate the energy difference $\Delta E_{\text{AFM-FM}}$, by measuring the temperature dependence of relaxation times for the $Dy_2O@C_{82}$ three isomers. The energy gap may correspond to the effective barrier, if relaxation proceeds via exchange excited state as found earlier for $Dy_2ScN@C_{80}$ [110] and $Dy_2S@C_{82}$ [68, 104]. Knowing the energy difference $\Delta E_{\text{AFM-FM}}$, then based on the eq. 5.1.2: $\Delta E_{\text{AFM-FM}} = 225 j_{12}\cos(\alpha)$, we can put an extra limitation on the (j_{12}, α) pair. Relaxation times measured in zero field are plotted in Arrhenius coordinates (log(τ)-*vs*-T^{-1}).

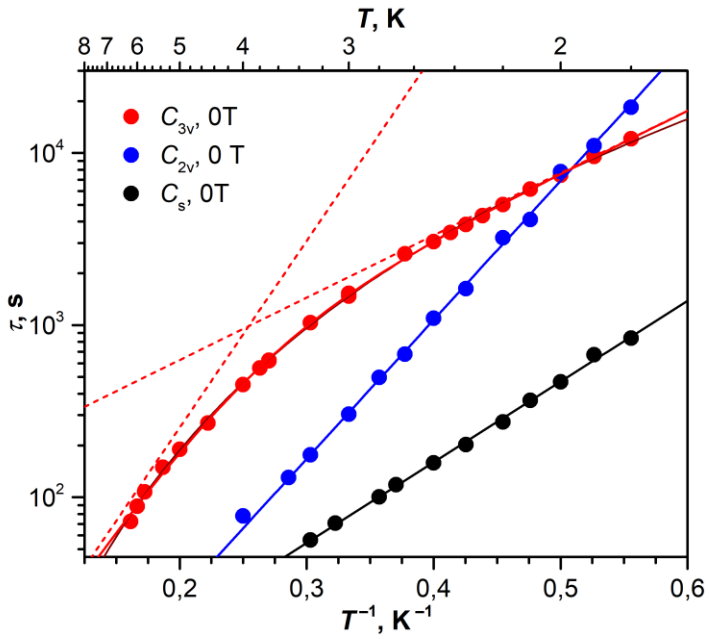

Figure 5.4.6 Magnetization relaxation times of $Dy_2O@C_{82}$ isomers: temperature dependence in zero field (full black, blue and red dots); solid lines are fitting of zero-field dependencies with one (black for C_s, blue for C_{2v}) or two Arrhenius processes (red for C_{3v}). Red dashed lines are contribution of individual processes for the C_{3v} isomer.

We immediately see well-defined linear regimes for C_s and C_{2V} isomers, which can be associated to Orbach relaxation process. Fit of the experimental data with equation $\tau^{-1} = \tau_0^{-1}\exp(-U^{\text{eff}}/T)$ gives U^{eff} = 10.8±0.1 K and τ_0 = 2.1±0.1 s for the C_s isomer and U^{eff} = 18.6±0.2 K and τ_0 = 0.63±0.06 s for the C_{2v} isomer. For C_{3v}, the relaxation times can be best fitted by a combination of two linear processes with U^{eff}/τ_0 parameters of 7.7±0.3 K/165±27 s (prevails at the lowest temperatures) and 22.6±0.8 K/2.63±0.35 s. An onset of another relaxation mechanism can be also seen near 6 K, but shorter relaxation times cannot be measured reliably via DC magnetometry.

The values of the barriers estimated from the fitting are at least one order of magnitude smaller than the LF-splitting of Dy ions predicted by ab initio calculations. Hence, the Orbach relaxation via single-ion LF-excited spin states can be excluded as an explanation of the Arrhenius behavior at low temperatures. Instead, one has to consider the spin states formed by the intramolecular interaction of two Dy ions as had been already found in Dy_2ScN and Dy_2S clusterfullerenes and can prove our assumption correct.

We thus tentatively suggest that the low-temperature relaxation of magnetization in $Dy_2O@C_{82}$ proceeds via exchange excited state. This allows us to determine the $\Delta E_{\mathrm{AFM-FM}}$ energy difference as the U^{eff} value from the temperature dependence of relaxation times. Exploiting the constraint $\Delta E_{\mathrm{AFM-FM}} = 225 j_{12}\cos(\alpha)$ of eq. 5.1.2 on the possible pairs of (j_{12}, α) parameters – they should be on the iso-energy lines plotted in fig. 5.4.7 for the three isomers of $Dy_2O@C_{82}$. These iso-lines correspond to the U^{eff} values of the three isomers (C_s: 10.8 K/7.5 cm^{-1}, C_{2v}: 18.6 K/12.93 cm^{-1} and C_{3v}: 7.7 K/ 5.35 cm^{-1}) determined from the temperature dependence of relaxation times in zero field. Notice that for C_{2v} isomer, the value of the second energy barrier (22.6 K/15.7 cm^{-1}) is rather ambiguous because of the few exp. points (fig. 5.4.6)-shorter times cannot be measured reliably via DC magnetometry, hence we did not select it as the iso-value of $\Delta E_{\mathrm{AFM-FM}}$.

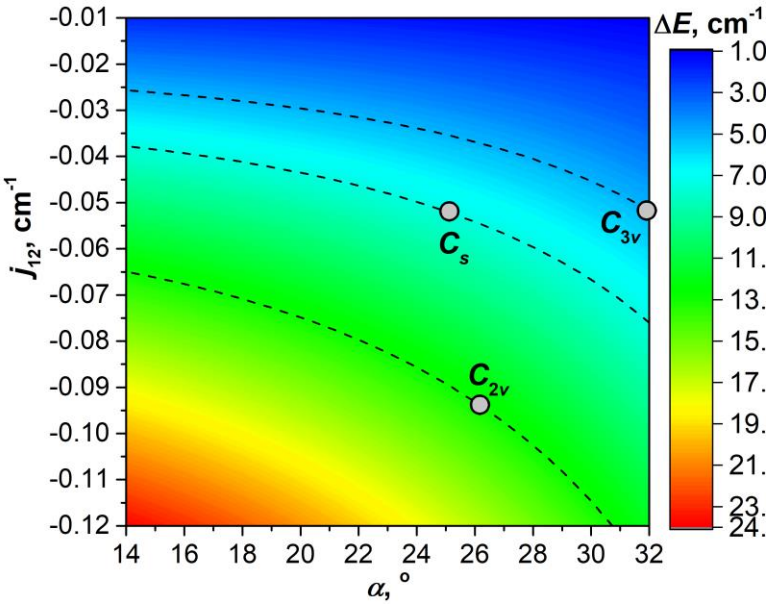

Figure 5.4.7 Energy difference between AFM and FM states (Δ*E*) as a function of the coupling constant j_{12} and the angle α computed with eq. 5.1.2. Dots correspond to the pairs of j_{12}/α parameters giving the best match to the experimental magnetization data as shown in fig. 5.4.8

Using the Hamiltonian of eq. 5.1.1 with ab initio LF parameters to simulate the magnetization curves over blocking temperature with this constraint in mind, we found that the best match to the experimental data is obtained for the following j_{12}/α values: −0.052 cm^{-1}/130° for the C_s isomer, −0.048 cm^{-1}/120° for the C_{3v} isomer, and −0.093 cm^{-1}/128° for the C_{2v} isomer (fig. 5.4.8).

These values and assumption of the AFM ground state also give a perfect match for the χT curves (which were not used in the optimization of parameters) as shown in fig. 5.4.2. Note here that if the sign of j_{12} is reversed (favoring the FM state), χT curves develop a characteristic sharp peak at low temperatures. Such peaks are not observed experimentally, proving that the ground magnetic state of all three $Dy_2O@C_{82}$ isomers is indeed AFM. The optimal angles α should be understood as an average value since there is most probably a distribution of <Dy-O-Dy angles in the real structures. Variation of α within few ^{o} gives small changes in the magnetization curves, and hence the precision of at least ±2–3^o should be assumed. Finally, a good agreement between experimental and simulated magnetization and χT curves confirms the validity of the assumption that the U^{eff} values correspond to $\Delta E_{\text{AFM}-\text{FM}}$ energy differences.

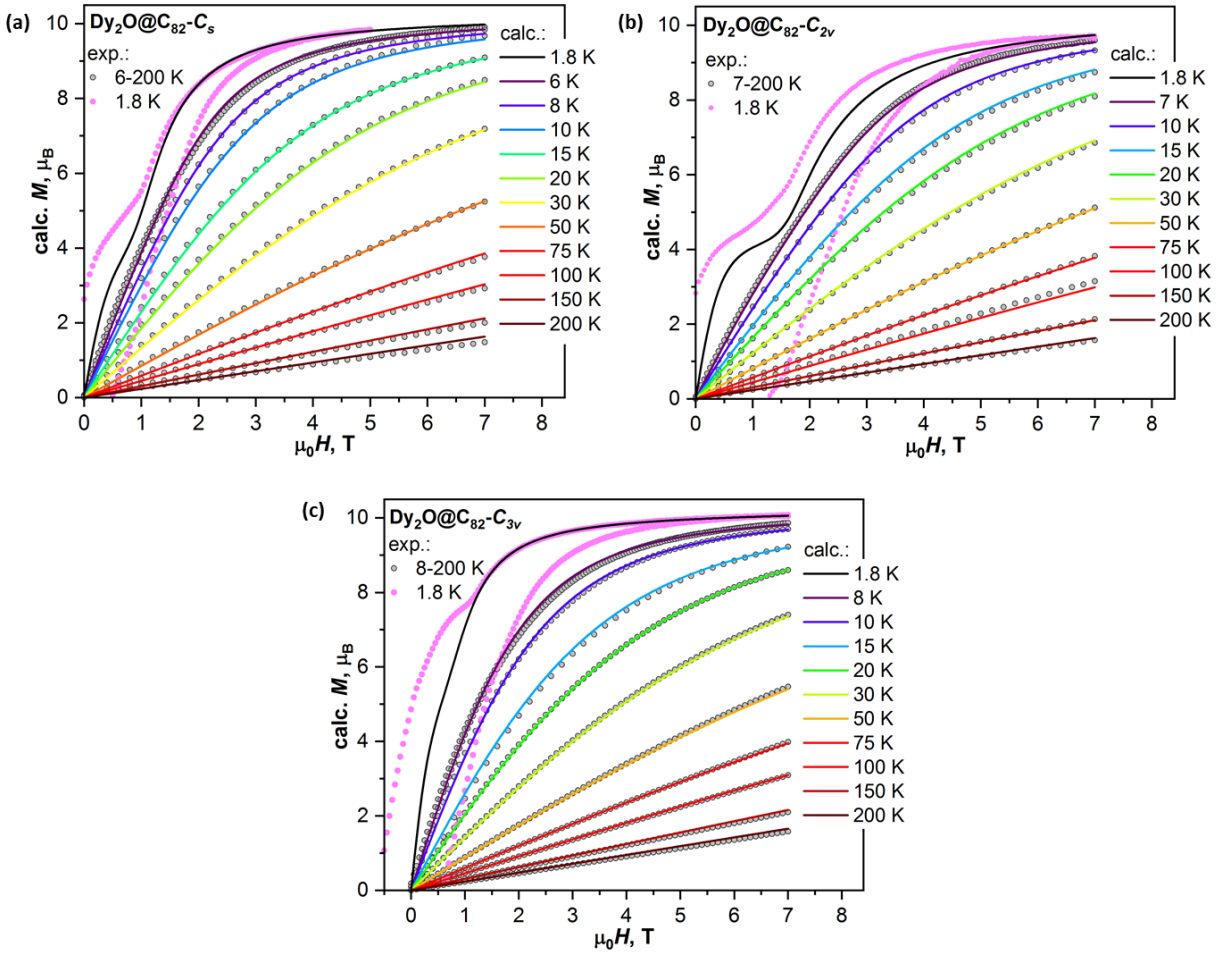

Figure 5.4.8 (a-c) Experimental (dots) and simulated (lines) magnetization curves of $Dy_2O@C_{82}$ isomers at different temperatures above T_B. Simulation parameters are: j_{12} = –0.052 cm^{-1} and α = 130^o for C_s isomer; j_{12} = –0.048 cm^{-1} and α = 120^o for C_{3v} isomer; j_{12} = –0.093 cm^{-1} and α = 128^o for C_{2v} isomer; for comparison, the curves measured at 1.8 K (pink dots) are also shown (they exhibit magnetic hysteresis and hence cannot be directly compared to simulated data).

In zero-field relaxation we can also have QTM as flipping of both Dy magnetic moments, but this is a low-probability process and therefore relaxation through the exchange barrier dominates. However, looking at the *M-H* curves, we notice some inflection areas for each isomer. This may indicate strong QTM between the FM/AFM states at some finite field, due to level crossing. For that reason, we decided to investigate it further by measuring field dependence of relaxation at constant temperature.

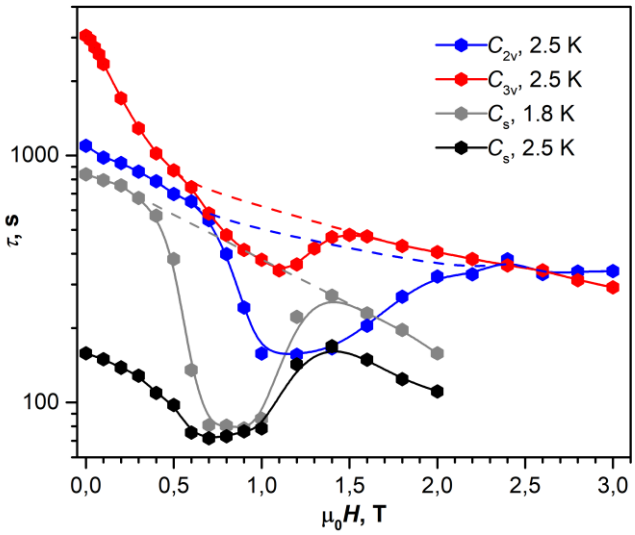

Figure 5.4.9 Magnetization relaxation times of $Dy_2O@C_{82}$ isomers: field dependence at 1.8 K (full grey dots for C_s) and 2.5 K (full black, blue and red dots for C_s C_{2v} and C_{3v} isomers resp.). Dip areas correspond to effective QTM between FM/AFM states at the level crossing.

We see that in low fields, all $Dy_2O@C_{82}$ isomers exhibit a gradual decrease of the relaxation time with the increase of the field. This behavior can be attributed to the increasing contribution of the direct relaxation mechanism, in which the spin flip is caused by the phonon matching the Zeeman splitting. With further increase of the magnetic field, all isomers show an abrupt acceleration of the relaxation. For the C_s isomer the change of the relaxation mechanism starts already at 0.4 T, for the C_{3v} and C_{2v} isomers the changes become apparent at 0.7–0.8 T. At further increase of the field, relaxation times increase again and then turn to a gradual decay. The dips (negative peaks) in the τ-H dependencies are ca 1 T broad and correspond to the positions of inflections observed in the magnetization curves. We propose that they are caused by the QTM at the AFM-FM level crossing. The large width of these "resonances" is caused by the distribution of the molecular orientations in the powder sample as well as by the distribution of dipolar fields. To summarize, we can conclude that Dy ions in all isomers of $Dy_2O@C_{82}$ molecule are coupled antiferromagnetically in the ground state. FM-AFM level crossing results in a special shape of magnetization curves, showing pronounced inflections near the field corresponding to the level crossing. Likewise, relaxation of magnetization near this field accelerates due to the appearance of the QTM mechanism at the crossing.

Comparison to other EMF-SMMs

It is instructive to compare the magnetic properties of $Dy_2O@C_{82}$ to other SMMs based on Dy-clusterfullerenes. Structurally, oxide-clusterfullerenes are similar to sulphide-clusterfullerenes. Both Dy_2O and Dy_2S species transfer 4 electrons to the fullerene cage and hence prefer the same cage isomers, and both clusters have an angular shape (but Dy-S-Dy angles are smaller than Dy-O-Dy angles). Earlier, $Dy_2S@C_{82}$ with C_s and C_{3v} cage isomers were isolated in our group, and their SMM properties were thoroughly studied [104]. C_s isomer of $Dy_2S@C_{82}$ was found to be a softer SMM than the C_{3v} isomer showing a similar effect of the fullerene cage isomer as found in this work for $Dy_2O@C_{82}$.

But in other aspects, magnetic properties of $Dy_2O@C_{82}$ are substantially different from those of $Dy_2S@C_{82}$. As it can be seen from the comparison of magnetic hysteresis curves of $Dy_2O@C_{82}$ and $Dy_2S@C_{82}$ with C_s and C_{3v} cage isomers in fig. 5.4.10, oxide clusterfullerenes are considerably stronger SMMs than their sulfide analogues. They show broader hysteresis and much longer relaxation times (and hence higher blocking temperatures). For instance, T_B/T_{B100} temperatures of the C_{3v} isomer of $Dy_2S@C_{82}$ are 4.0/2.0 K, whereas for $Dy_2O@C_{82}$ they are increased to 7.4/5.9 K. Thus, replacement of S by O in otherwise similar structures results in a dramatic improvement of the SMM performance. The strength of Dy-Dy exchange interactions in Dy_2S cluster is similar to those in Dy_2O but has an opposite sign (the FM state is the ground state in $Dy_2S@C_{82}$). Furthermore, the Dy-S bonds of 2.4-2.5 Å are much longer than Dy-O bonds, and the LF in sulphide clusterfullerenes is almost twice smaller. Ab initio calculations predict that the overall LF splitting in $Dy_2S@C_{82}$ is 880–970 cm^{-1}, whereas the energy of the first excited KD is 220–300 cm^{-1}.

The size of LF splitting in $Dy_2O@C_{82}$ is similar or even higher than in $Dy_2ScN@C_{80}$-I_h. So far, the latter has been the strongest SMM among the clusterfullerenes [142]. T_B of $Dy_2O@C_{82}$-C_{3v} studied in this work is close to that of $Dy_2ScN@C_{80}$, and T_{B100} value of the oxide is even higher than for the nitride clusterfullerene. Apparently, similarity of the LF also results in comparable SMM properties, at least at low temperatures. Both types of EMF-SMMs also exhibit similar spin-relaxation mechanism at low temperature featuring the exchange-excited state of the dinuclear cluster. But in the Dy_2ScN cluster, as in the aforementioned Dy_2S, the ground state is FM [110], whereas Dy_2O favors AFM coupling.

For sulfide and nitride clusterfullerenes we also found a strong influence of the carbon cage on the low-temperature (<10 K) relaxation behaviour [104, 139]. As insignificant variations of the LF are not relevant at these low temperatures, we hypothesized that the fullerene cage contributes to the relaxation of magnetization via the spin-phonon coupling and the energy transfer from the spin system to the lattice. Free motion of the endohedral cluster indicates that the potential energy surface is flat, and that the cluster vibrations are weakly coupled to the fullerene modes. The spin-lattice energy transfer is not very efficient, i.e. the fullerene cage shields the endohedral cluster not only from chemically active environment but also from the lattice phonons. On the

contrary, restricted motion of the endohedral cluster points to the stronger coupling to the cage vibrations, which facilitates the spin-lattice relaxation. As a result, the EMFs with more "isotropic" symmetric cages (I_h for $Dy_2ScN@C_{80}$ or C_{3v} for $Dy_2S@C_{82}$) are better SMMs than the analogous EMFs with less symmetric cages. The results of this work on the three isomers of $Dy_2O@C_{82}$ perfectly follow this trend. The C_{3v} isomer with the most pronounced motions of the Dy_2O cluster is the best SMM in the series, the C_s isomer with the fixed cluster is the weakest SMM, whereas the C_{2v} isomer is in between. Why the exchange interactions in $Dy_2O@C_{82}$ are so much dependent on the fullerene cage isomer and why the coupling in Dy_2O is antiferromagnetic whereas in other dinuclear Dy-EMFs the coupling is ferromagnetic, remain open questions.

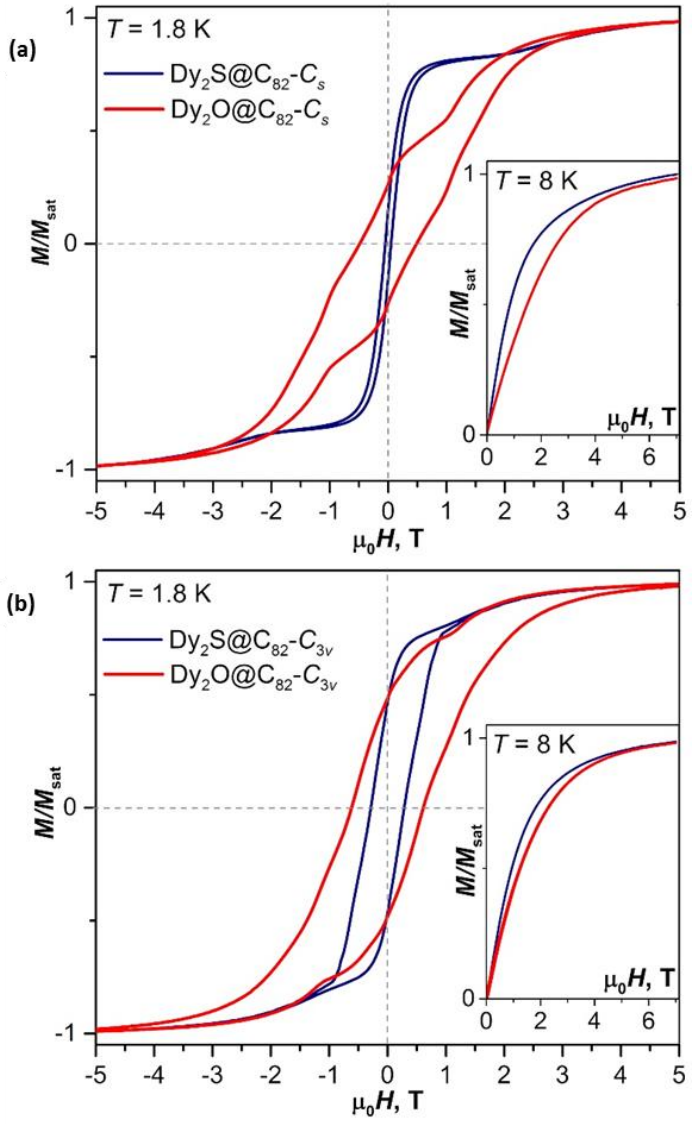

Figure 5.4.10 Comparison of magnetic hysteresis of $Dy_2S@C_{82}$ and $Dy_2O@C_{82}$ at 1.8 K: (a) C_s isomers; (b) C_{3v} isomers (average magnetic field sweep rate 2.9 mT s^{-1}). The insets show magnetization curves measured at 8 K.

5.5 Summary

To conclude, in this part we present the successful characterization of five Dy_2O-clusterfullerenes with all of them showing different magnetic properties. The compact geometry of Dy_2O cluster leads to both strong axial ligand field and strong FM/AFM coupling between the Dy ions.
$Dy_2O@C_{72}$-C_s and $Dy_2O@C_{74}$-C_2 clusterfullerenes violate the isolated pentagon rule. As a result, the shape of the Dy_2O cluster is determined by the form-factor of the carbon cage and location of the pentalene units, leading to the bent cluster in $Dy_2O@C_{72}$ but linear one in $Dy_2O@C_{74}$. Both fullerenes are single molecule magnets showing hysteresis up to 7 and 14 K resp., with the latter being the highest blocking temperature among Dy-clusterfullerenes. Dy-Dy interactions in the Dy_2O cluster are characterized by the ferromagnetic dipolar coupling counterbalanced by the antiferromagnetic exchange. In $Dy_2O@C_{74}$, these two contributions cancel each other leading to effectively decoupled Dy moments and zero-field quantum tunnelling of magnetization.
In case of $Dy_2O@C_{82}$, all three isomers exhibit slow relaxation of magnetization and develop a magnetic hysteresis at low temperatures. In zero field, the relaxation of magnetization follows the Orbach mechanism involving the FM excited state. Thus, the effective barriers determined from Arrhenius plots of the temperature dependence of the relaxation times are equal to the energy difference between AFM and FM coupled states. At the fields corresponding to the AFM-FM level crossing, all isomers of $Dy_2O@C_{82}$ exhibit quantum tunnelling of magnetization, which is apparent from the negative peaks in the field dependence of the relaxation times. The role of the fullerene cage in the magnetic properties of encapsulated Dy_2O clusters, though not fully understood, is quite considerable. First, the size of the exchange coupling constant in the Dy_2O cluster varies considerably with the cage shape and second, the fullerene cage isomerism affects internal dynamics of Dy_2O cluster, which appears to correlate strongly with the relaxation of magnetization. For example, the C_{3v} isomer, in which the cluster is moving almost freely, is found to be the strongest SMM among all three studied structures, whereas the C_s isomer with the fixed position of the endohedral cluster has the shortest magnetization relaxation times. In addition to dynamical properties, the size and the shape of the fullerene cage can also affect the structural parameters of the endohedral cluster, such as Dy–O bond lengths and <Dy–O–Dy angle.

$Dy_2O@C_{2n}$	T_B / T_{irr} (K)	H_C (2.9 mTs^{-1})	$j_{Ln\text{-}e}$ (cm^{-1})	α (deg)
$Dy_2O@C_{72}$-C_s	3 / 8.6	0.2 T (1.8 K)	0.009 ± 0.002	138.2
$Dy_2O@C_{74}$-C_2	6.7 / 13.5	-	<0.001	178
$Dy_2O@C_{82}$-C_s	4.4 / 10	0.35 T (1.8 K)	-0.052 ± 0.005	130 ± 2
$Dy_2O@C_{82}$-C_{2v}	5.8 / 8	1.1 T (1.8 K)	-0.048 ± 0.005	120 ± 2
$Dy_2O@C_{82}$-C_{3v}	7.4 / 9	0.59 T (1.8 K)	-0.093 ± 0.009	128 ± 2

Table 5.5.1 Summary of the most important SMM characteristics of the Dy_2O-clusterfullerenes presented in this work.

Outlook

In this work, we report on the advance of our understanding on the magnetic behavior of various lanthanide-based endohedral metallofullerenes. As we saw, indeed these molecules can play an important role in the field of single-molecule magnetism due to their extraordinary and versatile magnetic properties.

Specifically, we showed that the encapsulation of two lanthanide ions of the same kind, can lead to the stabilization of a single-electron Ln-Ln covalent bond. This situation realizes the idea of 'gluing' together single ion magnetic moments leading to strong anisotropy and in further extent to better SMM properties. The best example is reflected in case of $\{Tb_2\}$ molecules where we observed extremely broad hysteresis and record-high blocking temperatures. On the other hand, deviation from the axial anisotropy like in $\{Ho_2\}$, $\{Er_2\}$ and {TbY} systems, leads to considerable degradation of SMM behavior. However, the common distinct feature of all these magnets is their stability in ambient conditions which is ensured by the protecting environment of the host carbon cage, making them suitable for potential application in devices.

Our studies on Dy_2O-clusterfullerenes, revealed how important role does the carbon cage play in the magnetic properties. Here, the large negative charge of the O ion induces strong ligand-field splitting to both Dy ions. However, the size and shape of the host fullerene seems to play huge role because it affects the shape of the cluster inside (the angle <Dy-O-Dy) and consequently the magnetic properties of the molecule. Exchange interactions between Dy ions vary notably among the Dy_2O-clusterfullerenes. In $Dy_2O@C_{72}$ very weak FM exchange coupling is preferable while in $Dy_2O@C_{74}$ coupling almost disappears because of the canceling dipolar interactions. On the other hand, the three isomers of $Dy_2O@C_{82}$ exhibit AFM exchange coupling as favorable.

In our interest, next magnetic studies would include dimetallofullerenes with lanthanide ions that have not been tested yet (i.e. Ce, Nd etc.) because we know from theory and we expect that the situation will be very different for each case. Other direction of study can be dimetallofullerenes containing different lanthanide elements inside the cage, or even actinides. Regarding the Dy-oxide clusterfullerenes, there are already four more samples to be studied ($Dy_2O@C_{80}$ and three isomers of $Dy_2O@C_{88}$) in order to gain the complete view on this family of endohedral fullerenes.

In the end, I would like to thank again all the people who contributed in this work, from chemical synthesis and characterization to magnetic studies and theoretical interpretation of the results, for our great collaboration during the past 3.5 years.

References

1. *Electronic Structure and Magnetic Properties of Lanthanide Molecular Complexes*, in *Lanthanides and Actinides in Molecular Magnetism*. 2015. p. 1-26.
2. Rinehart, J.D. and J.R. Long, *Exploiting single-ion anisotropy in the design of f-element single-molecule magnets.* Chemical Science, 2011. **2**(11): p. 2078-2085.
3. Bethe, H.A. and E.E. Salpeter, *Quantum Mechanics of One- and Two-Electron Systems*, in *Atoms I / Atome I*. 1957, Springer Berlin Heidelberg: Berlin, Heidelberg. p. 88-436.
4. Dieke, G.H., H.M. Crosswhite, and H. Crosswhite, *Spectra and energy levels of rare earth ions in crystals*. 1968, New York: Interscience Publishers.
5. *Handbook on the Physics and Chemistry of Rare Earths. Herausgeber: K. A. Gschneider, L. Eyring. Vol. I: Metals, 896 Seiten, North Holland Publishing Co. Amsterdam 1978.* Physik in unserer Zeit, 1980. **11**(3): p. 97-97.
6. Stevens, K.W.H., *Matrix Elements and Operator Equivalents Connected with the Magnetic Properties of Rare Earth Ions.* Proceedings of the Physical Society. Section A, 1952. **65**(3): p. 209-215.
7. Benelli, C. and D. Gatteschi, *Magnetism of lanthanides in molecular materials with transition-metal ions and organic radicals.* Chem Rev, 2002. **102**(6): p. 2369-88.
8. Bethe, H., *Termaufspaltung in Kristallen.* Annalen der Physik, 1929. **395**(2): p. 133-208.
9. Liddle, S.T. and J. van Slageren, *Improving f-element single molecule magnets.* Chemical Society Reviews, 2015. **44**(19): p. 6655-6669.
10. Hutchings, M.T., *Point-Charge Calculations of Energy Levels of Magnetic Ions in Crystalline Electric Fields*, in *Solid State Physics*, F. Seitz and D. Turnbull, Editors. 1964, Academic Press. p. 227-273.
11. Wybourne, B.G., *Spectroscopic properties of rare earths.* 1965.
12. Jiang, S.-D. and S.-X. Qin, *Prediction of the quantized axis of rare-earth ions: the electrostatic model with displaced point charges.* Inorganic Chemistry Frontiers, 2015. **2**(7): p. 613-619.
13. Chilton, N.F., et al., *An electrostatic model for the determination of magnetic anisotropy in dysprosium complexes.* Nature Communications, 2013. **4**(1): p. 2551.
14. Chibotaru, L.F. and L. Ungur, *Ab initio calculation of anisotropic magnetic properties of complexes. I. Unique definition of pseudospin Hamiltonians and their derivation.* The Journal of Chemical Physics, 2012. **137**(6): p. 064112.
15. Gatteschi, D., R. Sessoli, and J. Villain, *Molecular Nanomagnets*. Vol. 376. 2006.
16. Tang, J. and P. Zhang, *A Basis for Lanthanide Single-Molecule Magnets*, in *Lanthanide Single Molecule Magnets*. 2015, Springer Berlin Heidelberg: Berlin, Heidelberg. p. 1-39.
17. Bartolomé, E., et al., *Magnetic Relaxation of Lanthanide-Based Molecular Magnets*. 2017.
18. Mironov, V.S., *Generalized superexchange theory of fast energy transfer, cooperative luminescence, and magnetic exchange interactions in exchange-coupled pairs of lanthanide ions.* Spectrochimica Acta Part A: Molecular and Biomolecular Spectroscopy, 1998. **54**(11): p. 1607-1614.
19. Bartolomé, E., et al., *Chapter 1 - Magnetic Relaxation of Lanthanide-Based Molecular Magnets*, in *Handbook of Magnetic Materials*, E. Brück, Editor. 2017, Elsevier. p. 1-289.
20. Bogdanov, A.N., *Magnetic Domains. The Analysis of Magnetic Microstructures.* Low Temperature Physics, 1999. **25**(2): p. 151-152.
21. Humphrey, F.B., *Domain Walls and Wall Structure*, in *Science and Technology of Nanostructured Magnetic Materials*, G.C. Hadjipanayis and G.A. Prinz, Editors. 1991, Springer US: Boston, MA. p. 269-274.

22. Van Vleck, J.H., *Paramagnetic Relaxation and the Equilibrium of Lattice Oscillators.* Physical Review, 1941. **59**(9): p. 724-729.
23. Van Vleck, J.H., *Calculation of Energy Exchange between Lattice Oscillators.* Physical Review, 1941. **59**(9): p. 730-736.
24. Bierig, R.W., M.J. Weber, and S.I. Warshaw, *Paramagnetic Resonance and Relaxation of Trivalent Rare-Earth Ions in Calcium Fluoride. II. Spin-Lattice Relaxation.* Physical Review, 1964. **134**(6A): p. A1504-A1516.
25. Stevens, K., *The theory of paramagnetic relaxation.* Reports on Progress in Physics, 2002. **30**: p. 189.
26. Garanin, D.A., *Spin tunnelling: a perturbative approach.* Journal of Physics A: Mathematical and General, 1991. **24**(2): p. L61-L62.
27. Gatteschi, D. and R. Sessoli, *Quantum Tunneling of Magnetization and Related Phenomena in Molecular Materials.* Angewandte Chemie International Edition, 2003. **42**(3): p. 268-297.
28. Zhang, P., L. Zhang, and J. Tang, *Lanthanide single molecule magnets: progress and perspective.* Dalton Transactions, 2015. **44**(9): p. 3923-3929.
29. McAdams, S.G., et al., *Molecular single-ion magnets based on lanthanides and actinides: Design considerations and new advances in the context of quantum technologies.* Coordination Chemistry Reviews, 2017. **346**: p. 216-239.
30. Kroto, H.W., et al., *C_{60}: Buckminsterfullerene.* Nature, 1985. **318**(6042): p. 162-163.
31. Heath, J.R., et al., *Lanthanum complexes of spheroidal carbon shells.* Journal of the American Chemical Society, 1985. **107**(25): p. 7779-7780.
32. Popov, A.A., S. Yang, and L. Dunsch, *Endohedral Fullerenes.* Chemical Reviews, 2013. **113**(8): p. 5989-6113.
33. Krätschmer, W., et al., *Solid C_{60}: a new form of carbon.* Nature, 1990. **347**(6291): p. 354-358.
34. Djordjevic, A., et al., *Review of Synthesis and Antioxidant Potential of Fullerenol Nanoparticles.* Journal of Nanomaterials, 2015. **2015**.
35. Takabayashi, Y. and K. Prassides, *Unconventional high-T_c superconductivity in fullerides.* Philosophical Transactions of the Royal Society A: Mathematical, Physical and Engineering Sciences, 2016. **374**(2076): p. 20150320.
36. Tanigaki, K., et al., *Superconductivity at 33 K in $Cs_xRb_yC_{60}$.* Nature, 1991. **352**(6332): p. 222-223.
37. Sastri, V.R., *5 - Polymer Additives Used to Enhance Material Properties for Medical Device Applications*, in *Plastics in Medical Devices (Second Edition)*, V.R. Sastri, Editor. 2014, William Andrew Publishing: Oxford. p. 55-72.
38. Zadik, R., et al., *Optimized unconventional superconductivity in a molecular Jahn-Teller metal.* Science Advances, 2015. **1**: p. 1500059.
39. Dunsch, L. and S. Yang, *Metal nitride cluster fullerenes: their current state and future prospects.* Small (Weinheim an der Bergstrasse, Germany), 2007. **3**(8): p. 1298-1320.
40. Zhang, J., S. Stevenson, and H.C. Dorn, *Trimetallic Nitride Template Endohedral Metallofullerenes: Discovery, Structural Characterization, Reactivity, and Applications.* Accounts of Chemical Research, 2013. **46**(7): p. 1548-1557.
41. Dunsch, L., et al., *Metal sulfide in a C_{82} fullerene cage: a new form of endohedral clusterfullerenes.* Journal of the American Chemical Society, 2010. **132**(15): p. 5413-5421.
42. Wang, C.R., et al., *A Scandium Carbide Endohedral Metallofullerene: $Sc_2C_2@C_{84}$.* Angew Chem Int Ed Engl, 2001. **40**(2): p. 397-399.
43. Yang, S., et al., *Fullerenes encaging metal clusters—clusterfullerenes.* Chemical Communications, 2011. **47**(43): p. 11822-11839.
44. Horak, P.D. and U.J. Gibson, *Broad fullerene-ion beam generation and bombardment effects.* Applied Physics Letters, 1994. **65**(8): p. 968-970.

45. Cataldo, F., G. Baratta, and G. Strazzulla, *He+ ion bombardment of C_{60} fullerene: An FT-IR and Raman study.* Fullerenes Nanotubes and Carbon Nanostructures - FULLER NANOTUB CARBON NANOSTR, 2006. **10**: p. 197-206.
46. Cataldo, F., et al., *He+ Ion Bombardment of C_{70} Fullerene: An FT-IR and Raman Study.* Fullerenes, Nanotubes and Carbon Nanostructures, 2003. **11**(3): p. 191-199.
47. Saunders, M. and R.J. Cross, *Putting Nonmetals into Fullerenes*, in *Endofullerenes: A New Family of Carbon Clusters*, T. Akasaka and S. Nagase, Editors. 2002, Springer Netherlands: Dordrecht. p. 1-11.
48. Saunders, M., et al., *Stable compounds of helium and neon: He@c_{60} and Ne@c_{60}.* Science, 1993. **259**(5100): p. 1428-30.
49. Murata, M., Y. Murata, and K. Komatsu, *Surgery of fullerenes.* Chemical Communications, 2008(46): p. 6083-6094.
50. Bloodworth, S., et al., *Synthesis of Ar@C_{60} using molecular surgery.* Chemical Communications, 2020. **56**(72): p. 10521-10524.
51. Dunk, P.W., et al., *Bottom-up formation of endohedral mono-metallofullerenes is directed by charge transfer.* Nature Communications, 2014. **5**(1): p. 5844.
52. Yamamoto, E., et al., *13C-NMR Study on the Structure of Isolated Sc_2@C_{84} Metallofullerene.* Journal of the American Chemical Society, 1996. **118**(9): p. 2293-2294.
53. Saito, Y. and I. Ueta, *Miniaturization for the Development of High Performance Separation Systems.* CHROMATOGRAPHY, 2017. **advpub**.
54. Svitova, A., et al., *A platform for specific delivery of lanthanide-scandium mixed-metal cluster fullerenes into target cells.* ChemistryOpen, 2012. **1**(5): p. 207-210.
55. Yang, S., et al., *A Facile Route to Metal Nitride Clusterfullerenes by Using Guanidinium Salts: A Selective Organic Solid as the Nitrogen Source.* Chemistry – A European Journal, 2010. **16**(41): p. 12398-12405.
56. Liu, F., et al., *A series of inorganic solid nitrogen sources for the synthesis of metal nitride clusterfullerenes: the dependence of production yield on the oxidation state of nitrogen and counter ion.* Inorg Chem, 2013. **52**(7): p. 3814-22.
57. Akasaka, T., et al., *Structural Determination of the La@C_{82} Isomer.* The Journal of Physical Chemistry B, 2001. **105**(15): p. 2971-2974.
58. Wakahara, T., et al., *Characterization of Ce@C_{82} and Its Anion.* Journal of the American Chemical Society, 2004. **126**(15): p. 4883-4887.
59. Yamada, M., et al., *Analysis of Lanthanide-Induced NMR Shifts of the Ce@C_{82} Anion.* Journal of the American Chemical Society, 2006. **128**(5): p. 1400-1401.
60. Szymczak, H. and R. Szymczak, *Magnetic Measurement Techniques*, in *Magnetic Storage Systems Beyond 2000*, G.C. Hadjipanayis, Editor. 2001, Springer Netherlands: Dordrecht. p. 225-242.
61. Pei, G., et al. *A Literature Review of Heat Capacity Measurement Methods*. 2019. Cham: Springer International Publishing.
62. J H Brewer, a. and K.M. Crowe, *Advances in Muon Spin Rotation.* Annual Review of Nuclear and Particle Science, 1978. **28**(1): p. 239-326.
63. Lord, J.S., *Muon spin resonance in ferromagnets.* Journal of Magnetism and Magnetic Materials, 1998. **177-181**: p. 1470-1471.
64. Hao, F.-H., W.-X. Xu, and Y. Wang, *Nuclear Magnetic Resonance Techniques*, in *Plant Metabolomics: Methods and Applications*, X. Qi, X. Chen, and Y. Wang, Editors. 2015, Springer Netherlands: Dordrecht. p. 63-104.
65. Chatterji, T., *CHAPTER 1 - Magnetic Neutron Scattering*, in *Neutron Scattering from Magnetic Materials*, T. Chatterji, Editor. 2006, Elsevier Science: Amsterdam. p. 1-24.

66. Fagaly, R., *Superconducting quantum interference device instruments and applications.* Review of Scientific Instruments, 2006. **77**: p. 101101-101101.
67. Liu, F., et al., *Single molecule magnet with an unpaired electron trapped between two lanthanide ions inside a fullerene.* Nature Communications, 2017. **8**(1): p. 16098.
68. Krylov, D., et al., *Record-high thermal barrier of the relaxation of magnetization in the nitride clusterfullerene $Dy_2ScN@C_{80}$-I_h.* Chem. Commun., 2017. **53**.
69. Cole, K.S. and R.H. Cole, *Dispersion and Absorption in Dielectrics I. Alternating Current Characteristics.* The Journal of Chemical Physics, 1941. **9**(4): p. 341-351.
70. Kahn, O., *Dinuclear Complexes with Predictable Magnetic Properties.* Angewandte Chemie International Edition in English, 1985. **24**(10): p. 834-850.
71. Sessoli, R., et al., *Magnetic bistability in a metal-ion cluster.* Nature, 1993. **365**(6442): p. 141-143.
72. Thomas, L., et al., *Macroscopic quantum tunnelling of magnetization in a single crystal of nanomagnets.* Nature, 1996. **383**(6596): p. 145-147.
73. Ako, A.M., et al., *A Ferromagnetically Coupled Mn19 Aggregate with a Record S=83/2 Ground Spin State.* Angewandte Chemie International Edition, 2006. **45**(30): p. 4926-4929.
74. Milios, C.J., et al., *A Record Anisotropy Barrier for a Single-Molecule Magnet.* Journal of the American Chemical Society, 2007. **129**(10): p. 2754-2755.
75. Sangregorio, C., et al., *Quantum Tunneling of the Magnetization in an Iron Cluster Nanomagnet.* Physical Review Letters, 1997. **78**(24): p. 4645-4648.
76. Powell, A.K., et al., *Synthesis, Structures, and Magnetic Properties of Fe_2, Fe_{17}, and Fe_{19} Oxo-Bridged Iron Clusters: The Stabilization of High Ground State Spins by Cluster Aggregates.* Journal of the American Chemical Society, 1995. **117**(9): p. 2491-2502.
77. Castro, S.L., et al., *Single-Molecule Magnets: Tetranuclear Vanadium(III) Complexes with a Butterfly Structure and an S = 3 Ground State.* Journal of the American Chemical Society, 1998. **120**(10): p. 2365-2375.
78. Murrie, M., *Cobalt(ii) single-molecule magnets.* Chemical Society Reviews, 2010. **39**(6): p. 1986-1995.
79. Murrie, M., et al., *Synthesis and Characterization of a Cobalt(II) Single-Molecule Magnet.* Angewandte Chemie International Edition, 2003. **42**(38): p. 4653-4656.
80. Cadiou, C., et al., *Studies of a nickel-based single molecule magnet: resonant quantum tunnelling in an S = 12 molecule.* Chemical Communications, 2001(24): p. 2666-2667.
81. Wu, D.-Q., et al., *Reversible On–Off Switching of a Single-Molecule Magnet via a Crystal-to-Crystal Chemical Transformation.* Journal of the American Chemical Society, 2017. **139**(34): p. 11714-11717.
82. Shao, D. and X.-Y. Wang, *Development of Single-Molecule Magnets†.* Chinese Journal of Chemistry, 2020. **38**(9): p. 1005-1018.
83. Ishikawa, N., et al., *Lanthanide Double-Decker Complexes Functioning as Magnets at the Single-Molecular Level.* Journal of the American Chemical Society, 2003. **125**(29): p. 8694-8695.
84. Ganivet, C.R., et al., *Influence of Peripheral Substitution on the Magnetic Behavior of Single-Ion Magnets Based on Homo- and Heteroleptic TbIII Bis(phthalocyaninate).* Chemistry – A European Journal, 2013. **19**(4): p. 1457-1465.
85. Stepanow, S., et al., *Spin and Orbital Magnetic Moment Anisotropies of Monodispersed Bis(Phthalocyaninato)Terbium on a Copper Surface.* Journal of the American Chemical Society, 2010. **132**(34): p. 11900-11901.
86. Gonidec, M., et al., *Surface Supramolecular Organization of a Terbium(III) Double-Decker Complex on Graphite and its Single Molecule Magnet Behavior.* Journal of the American Chemical Society, 2011. **133**(17): p. 6603-6612.

87. Candini, A., et al., *Graphene Spintronic Devices with Molecular Nanomagnets.* Nano Letters, 2011. **11**(7): p. 2634-2639.
88. Choudhuri, I., P. Bhauriyal, and B. Pathak, *Recent Advances in Graphene-like 2D Materials for Spintronics Applications.* Chemistry of Materials, 2019. **31**(20): p. 8260-8285.
89. Thiele, S., *Magnetic Properties of $TbPc_2$*, in *Read-Out and Coherent Manipulation of an Isolated Nuclear Spin : Using a Single-Molecule Magnet Spin-Transistor*. 2016, Springer International Publishing: Cham. p. 23-37.
90. Sessoli, R. and A. Powell, *Strategies towards single molecule magnets based on lanthanide ions.* Coordination Chemistry Reviews, 2009. **253**: p. 2328-2341.
91. Mondal, K.C., et al., *Coexistence of Distinct Single-Ion and Exchange-Based Mechanisms for Blocking of Magnetization in a $Co^{II2}Dy^{III2}$ Single-Molecule Magnet.* Angewandte Chemie International Edition, 2012. **51**(30): p. 7550-7554.
92. Qin, L., et al., *Quantum Monte Carlo Simulations and High-Field Magnetization Studies of Antiferromagnetic Interactions in a Giant Hetero-Spin Ring.* Angewandte Chemie International Edition, 2017. **56**(52): p. 16571-16574.
93. Li, H., et al., *A $\{Tb_2Fe_3\}$ Pyramid Single-Molecule Magnet with Ferromagnetic Tb-Fe Interaction.* Chinese Journal of Chemistry, 2019. **37**(4): p. 373-377.
94. Luzon, J., et al., *Spin Chirality in a Molecular Dysprosium Triangle: The Archetype of the Noncollinear Ising Model.* Physical review letters, 2008. **100**: p. 247205.
95. Blagg, R.J., et al., *Magnetic relaxation pathways in lanthanide single-molecule magnets.* Nature Chemistry, 2013. **5**(8): p. 673-678.
96. Ungur, L. and L.F. Chibotaru, *Magnetic anisotropy in the excited states of low symmetry lanthanide complexes.* Physical Chemistry Chemical Physics, 2011. **13**(45): p. 20086-20090.
97. Rinehart, J.D., et al., *A N_2^{3-} Radical-Bridged Terbium Complex Exhibiting Magnetic Hysteresis at 14 K.* Journal of the American Chemical Society, 2011. **133**(36): p. 14236-14239.
98. Goodwin, C.A.P., et al., *Molecular magnetic hysteresis at 60 kelvin in dysprosocenium.* Nature, 2017. **548**(7668): p. 439-442.
99. Guo, F.-S., et al., *Magnetic hysteresis up to 80 kelvin in a dysprosium metallocene single-molecule magnet.* Science, 2018. **362**: p. eaav0652.
100. Funasaka, H., et al., *Magnetic properties of $Gd@C_{82}$ metallofullerene.* Chemical Physics Letters, 1995. **232**(3): p. 273-277.
101. Yamamoto, K., et al., *Isolation of an ESR-Active Metallofullerene of $La@C_{82}$.* The Journal of Physical Chemistry, 1994. **98**(8): p. 2008-2011.
102. Krause, M., et al., *Structure and stability of endohedral fullerene Sc_3NC_{80}: A Raman, infrared, and theoretical analysis.* The Journal of Chemical Physics, 2001. **115**: p. 6596-6605.
103. Westerström, R., et al., *An Endohedral Single-Molecule Magnet with Long Relaxation Times: $DySc_2N@C_{80}$.* Journal of the American Chemical Society, 2012. **134**: p. 9840-3.
104. Chen, C.-H., et al., *Selective arc-discharge synthesis of Dy_2S-clusterfullerenes and their isomer-dependent single molecule magnetism.* Chemical Science, 2017. **8**(9): p. 6451-6465.
105. Valencia, R., A. Rodríguez-Fortea, and J.M. Poblet, *Understanding the Stabilization of Metal Carbide Endohedral Fullerenes $M_2C_2@C_{82}$ and Related Systems.* The Journal of Physical Chemistry A, 2008. **112**(20): p. 4550-4555.
106. Junghans, K., et al., *Methane as a Selectivity Booster in the Arc-Discharge Synthesis of Endohedral Fullerenes: Selective Synthesis of the Single-Molecule Magnet Dy2TiC@C80 and Its Congener $Dy_2TiC_2@C_{80}$.* Angewandte Chemie International Edition, 2015. **54**(45): p. 13411-13415.

107. Liu, F., et al., *Triangular Monometallic Cyanide Cluster Entrapped in Carbon Cage with Geometry-Dependent Molecular Magnetism.* Journal of the American Chemical Society, 2016. **138**(44): p. 14764-14771.
108. Krylov, D., et al., *Magnetization relaxation in the single-ion magnet DySc2N@C80: quantum tunneling, magnetic dilution, and unconventional temperature dependence.* Physical Chemistry Chemical Physics, 2018. **20**.
109. Spree, L., et al., *Single molecule magnets $DyM_2N@C_{80}$ and $Dy_2MN@C_{80}$ (M = Sc, Lu): The impact of diamagnetic metals on the Dy^{3+} magnetic anisotropy, Dy···Dy coupling, and mixing of molecular and lattice vibrations.* Chemistry, 2019. **26**.
110. Westerström, R., et al., *Tunneling, remanence, and frustration in dysprosium-based endohedral single-molecule magnets.* Physical Review B, 2014. **89**(6): p. 060406.
111. Liddle, S.T., *Molecular metal-metal bonds : compounds, synthesis, properties*. 2015, Weinheim: Wiley-VCH.
112. Popov, A., *Redox-active metal-metal bonds between lanthanides in dimetallofullerenes.* Current Opinion in Electrochemistry, 2017. **8**.
113. Zuo, T., et al., *$M_2@C_{79}N$ (M = Y, Tb): isolation and characterization of stable endohedral metallofullerenes exhibiting M-M bonding interactions inside aza[80]fullerene cages.* Journal of the American Chemical Society, 2008. **130**(39): p. 12992-12997.
114. Fu, W., et al., *$Gd_2@C_{79}N$: isolation, characterization, and monoadduct formation of a very stable heterofullerene with a magnetic spin state of S = 15/2.* Journal of the American Chemical Society, 2011. **133**(25): p. 9741-9750.
115. Popov, A.A., et al., *Bonding between strongly repulsive metal atoms: an oxymoron made real in a confined space of endohedral metallofullerenes.* Chemical Communications, 2012. **48**(65): p. 8031-8050.
116. Wang, Z., R. Kitaura, and H. Shinohara, *Metal-Dependent Stability of Pristine and Functionalized Unconventional Dimetallofullerene $M_2@I_h$-C_{80}.* The Journal of Physical Chemistry C, 2014. **118**(25): p. 13953-13958.
117. Yamada, M., et al., *Hiding and recovering electrons in a dimetallic endohedral fullerene: air-stable products from radical additions.* Journal of the American Chemical Society, 2015. **137**(1): p. 232-238.
118. Bao, L., et al., *Crystallographic Evidence for Direct Metal–Metal Bonding in a Stable Open-Shell $La_2@I_h$-C_{80} Derivative.* Angewandte Chemie International Edition, 2016. **55**(13): p. 4242-4246.
119. Singh, M., N. Yadav, and G. Rajaraman, *Record high magnetic exchange and magnetization blockade in Ln2@C79N (Ln = Gd(III) and Dy(III)) molecules: a theoretical perspective.* Chemical communications, 2015. **51 100**: p. 17732-5.
120. Cimpoesu, F., et al., *On exchange coupling and bonding in the $Gd_2@C_{80}$ and $Gd_2@C_{79}N$ endohedral dimetallo-fullerenes.* Molecular Physics, 2015. **113**(13-14): p. 1712-1727.
121. Liu, F., et al., *Single-Electron Lanthanide-Lanthanide Bonds Inside Fullerenes toward Robust Redox-Active Molecular Magnets.* Acc Chem Res, 2019. **52**(10): p. 2981-2993.
122. Velkos, G., et al., *Giant exchange coupling and field-induced slow relaxation of magnetization in $Gd_2@C_{79}N$ with a single-electron Gd–Gd bond.* Chemical Communications, 2018. **54**(23): p. 2902-2905.
123. Velkos, G., et al., *High Blocking Temperature of Magnetization and Giant Coercivity in the Azafullerene $Tb_2@C_{79}N$ with a Single-Electron Terbium-Terbium Bond.* Angew Chem Int Ed Engl, 2019. **58**(18): p. 5891-5896.
124. Liu, F., et al., *Air-stable redox-active nanomagnets with lanthanide spins radical-bridged by a metal-metal bond.* Nat Commun, 2019. **10**(1): p. 571.

125. Kareev, I.E., et al., *Experimental Evidence in Support of the Formation of Anionic Endohedral Metallofullerenes During Their Extraction with N, N-Dimethylformamide.* Fullerenes, Nanotubes and Carbon Nanostructures, 2005. **12**(1-2): p. 65-69.
126. Hafner, J., *Ab-initio simulations of materials using VASP: Density-functional theory and beyond.* Journal of Computational Chemistry, 2008. **29**(13): p. 2044-2078.
127. Chilton, N.F., et al., *PHI: A powerful new program for the analysis of anisotropic monomeric and exchange-coupled polynuclear d- and f-block complexes.* Journal of Computational Chemistry, 2013. **34**(13): p. 1164-1175.
128. Hu, Z., et al., *Endohedral Metallofullerene as Molecular High Spin Qubit: Diverse Rabi Cycles in $Gd_2@C_{79}N$.* Journal of the American Chemical Society, 2018. **140**(3): p. 1123-1130.
129. Mansikkamäki, A., et al., *Interplay of spin-dependent delocalization and magnetic anisotropy in the ground and excited states of $[Gd_2@C_{78}]^-$ and $[Gd_2@C_{80}]^-$.* The Journal of Chemical Physics, 2017. **147**(12): p. 124305.
130. Liu, F., et al., *Single molecule magnet with an unpaired electron trapped between two lanthanide ions inside a fullerene.* Nature Communications, 2017. **8**: p. 16098.
131. Hu, Z., et al., *Endohedral Metallofullerene as Molecular High Spin Qubit: Diverse Rabi Cycles in $Gd_2@C_{79}N$.* Journal of the American Chemical Society, 2018: p. 10.1021/jacs.7b12170.
132. Kanetomo, T., et al., *Giant Exchange Coupling Evidenced with a Magnetization Jump at 52 T for a Gadolinium-Nitroxide Chelate.* Inorganic Chemistry, 2017. **56**(6): p. 3310-3314.
133. Kanetomo, T., T. Yoshitake, and T. Ishida, *Strongest Ferromagnetic Coupling in Designed Gadolinium(III)–Nitroxide Coordination Compounds.* Inorganic Chemistry, 2016. **55**(16): p. 8140-8146.
134. Demir, S., et al., *Exchange Coupling and Magnetic Blocking in Bipyrimidyl Radical-Bridged Dilanthanide Complexes.* Journal of the American Chemical Society, 2012. **134**(45): p. 18546-18549.
135. Meihaus, K.R., et al., *Influence of an Inner-Sphere K+ Ion on the Magnetic Behavior of N_2^{3-} Radical-Bridged Dilanthanide Complexes Isolated Using an External Magnetic Field.* Inorganic Chemistry, 2014. **53**(6): p. 3099-3107.
136. Orbach, R., *Spin-lattice relaxation in rare-earth salts.* Proceedings of the Royal Society of London. Series A. Mathematical and Physical Sciences, 1961. **264**(1319): p. 458-484.
137. Demir, S., et al., *Giant coercivity and high magnetic blocking temperatures for N_2^{3-} radical-bridged dilanthanide complexes upon ligand dissociation.* Nature Communications, 2017. **8**(1): p. 2144.
138. Vieru, V., et al., *Giant exchange interaction in mixed lanthanides.* Scientific Reports, 2016. **6**(1): p. 24046.
139. Schlesier, C., et al., *Strong carbon cage influence on the single molecule magnetism in Dy–Sc nitride clusterfullerenes.* Chemical Communications, 2018. **54**(70): p. 9730-9733.
140. Singh, M.K. and G. Rajaraman, *Acquiring a record barrier height for magnetization reversal in lanthanide encapsulated fullerene molecules using DFT and ab initio calculations.* Chemical Communications, 2016. **52**(97): p. 14047-14050.
141. Aquilante, F., et al., *Molcas 8: New capabilities for multiconfigurational quantum chemical calculations across the periodic table.* Journal of Computational Chemistry, 2016. **37**(5): p. 506-541.
142. Spree, L. and A.A. Popov, *Recent advances in single molecule magnetism of dysprosium-metallofullerenes.* Dalton Transactions, 2019. **48**(9): p. 2861-2871.

Statement of originality

This dissertation was carried out at the Leibniz Institute for Solid State and Materials Research (IFW Dresden) under the supervision of Prof. Dr. Bernd Büchner and Dr. A. Popov.

I herewith declare that I have produced this paper without the prohibited assistance of third parties and without making use of aids other than those specified; notions taken over directly or indirectly from other sources have been identified as such. This paper has not previously been presented in identical or similar form to any other German or foreign examination board.

I accept the doctoral regulations of the Faculty of Mathematics and Natural Sciences dated 23.02.2011.

Dresden, 12.04.2021 Velkos G.